First Principles Investigation of Covalently Immobilised Metalloporphyrins on Carbon Supports for the Electrochemical Reduction of CO_2

OLIVER JAMES CONQUEST

Supervisor: Catherine Stampfl
Associate Supervisor: Tanglaw Roman

A thesis submitted in fulfilment of
the requirements for the degree of
Doctor of Philosophy

School of Physics
Faculty of Science
The University of Sydney
Australia

7 August 2023

I declare that this submission is my own work and that to the best of my knowledge, it contains no material which has been previously published or written by another person, nor material which to a substantial extent has been accepted for the award of any other degree from a university or other institution of higher learning, except where due acknowledgement has been made in the text.

Oliver Conquest

Abstract

Metal-organic molecular catalysts used for CO_2 electroreduction (CO_2ERR) have recently been shown to exhibit remarkable selectivity, high reaction rates, low electrode potentials and good long-term stability (particularly when immobilised). CO_2 electroreduction catalyst design, performance 'tuning' and mechanistic insights are difficult and time consuming to investigate experimentally. *Ab initio* calculations play an important role in complementing experimental results and providing insights into the catalyst reaction mechanisms, intermediates and coordination environments. In this thesis we use *ab initio* calculations to study catalyst immobilisation on carbon supports, focusing on how catalyst immobilisation influences the CO_2ERR performance ultimately serving to guide catalyst design and immobilisation methods.

Theoretically, one indicator of catalyst performance is obtained by calculating the free energy reaction pathways. One of the main challenges, however, is determining accurate entropy values of molecules in the aqueous-phase. We perform a bench marking study of different solvation entropy calculation methods for a set of 56 molecules ranging in size from H_2 (being the smallest) to tetrabutylammonium ($C_{16}H_{36}N$) (being the largest). Particular attention is paid to the cavity packing parameters which are important for calculating accurate cavity formation entropies. The reduced contribution of other entropy values when a molecule is in an aqueous solution is also considered. The most accurate solvation entropy model is determined by comparison with experiment where it is found that our developed approach provides more accurate solvation entropy values of those considered.

Having developed a relatively accurate and efficient method for calculating entropies of molecules in aqueous-phase, we investigate the CO_2ERR performance of immobilised catalysts on carbon supports. We study the impact that intrinsic defects in graphene and carbon nanotube supports have on the CO_2ERR reaction performance of cobalt-centred phthalocyanine (CoPc) and tetraphenylporphyrin (CoTPP) catalysts. We find that up-right

immobilised CoPc on a Stone-Wales defect, and CoTPP on an octagon-pentagon line defect, respectively have the most favourable reaction pathways. The pyridine linker immobilising CoPc (via its Co active site) and the oxygen linker immobilising CoTPP are also studied. The CoPc-pyridine system demonstrates superior CO_2ERR reaction pathway performance compared to all other systems considered due to a large component of unoccupied d_{z^2} states just above the Fermi level. This facilities stronger CO_2 adsorption to the cobalt active site which is shown by its activated/bent geometry.

Finally, we perform a systematic study of the immobilisation of CoPc via its Co active site for eight different atomic-style linkers on a carbon nanotube support. The bonding between the linker and the Co active site can change the d-state ordering and shift components of the d_{z^2} states, which facilitate CO_2 adsorption, to higher energies making them unoccupied and close to the Fermi level. This was found to be the case for the NH, S and PH linkers which exhibited the most favourable reaction free energy pathways indicating best CO_2ERR performance compared to all other linker systems considered. To further investigate the CO_2ERR performance activation barriers for hydrogenated CoPc immobilised using the favourable NH and PH linkers are calculated. It is found that the PH linker has slightly lower activation barriers and remains bonded to the catalyst, unlike the NH linker. We therefore propose that the NH, S and PH linkers or their derivatives would be promising candidates for future experimental studies.

List of Publications

The following is a list of chapters in this thesis which are based on manuscripts that have either been published or accepted to scientific journals. This means each chapter is a self contained body of work and follows the usual structure of a scientific publication starting with an abstract and followed by an introduction, results, discussion and conclusion.

Chapter 3: *Calculating Entropies of Large Molecules in Aqueous Phase*, O. J. Conquest, T. Roman, A. Marianov, A. Kochubei, Y. Jiang, C. Stampfl, J. Chem. Theory Comput. 17, 12, 7753–7771 (2021)

Chapter 4: *Ab Initio Investigation of Covalently Immobilized Cobalt-Centered Metal–Organic Catalysts for CO_2 Reduction: The Effect of the Substrate on the Reaction Energetics*, O. J. Conquest, T. Roman, A. Marianov, A. Kochubei, Y. Jiang, C. Stampfl, J. Phys. Chem. C 126, 24, 10081–10100 (2022)

Chapter 5: *Ab Initio Investigation of Cobalt-Phthalocyanine Active Site Tuning via Atomic Linker Immobilization for CO_2 Electroreduction*, O. J. Conquest, T. Roman, A. Marianov, A. Kochubei, Y. Jiang, C. Stampfl, J. Catal. 422, 43-55 (2023)

In the above list of publications I am the first author and therefore primarily responsible for the project. I took the lead role in researching and planning the projects, I conducted all the calculations and was responsible for preparing the manuscripts. I have also contributed to publications for which I am a co-author. These publications are listed below but are not included in this thesis.

(1) *Resolving Deactivation Pathways of Co Porphyrin-Based Electrocatalysts for CO_2 Reduction in Aqueous Medium*, A. Marianov, A. Kochubei, T. Roman, O. J. Conquest, C. Stampfl, Y. Jiang, ACS Catal. 11, 6, 3715–3729 (2021)

(2) *Modeling and Experimental Study of the Electron Transfer Kinetics for Non-ideal Electrodes Using Variable-Frequency Square Wave Voltammetry*, A. Marianov, A. Kochubei, T. Roman, O. J. Conquest, C. Stampfl, Y. Jiang, Anal. Chem. 93, 29, 10175–10186 (2021)

As supervisor for the candidature upon which this thesis is based, I can confirm that the authorship attribution statements above are correct.

Catherine Stampfl

Tanglaw Roman

Conferences that I attend as part of my PhD are listed below.

- Royal Australian Chemical Institute (RACI) National Congress in Brisbane between 3-8 July 2022 were I presented a poster.
- Australian Institute of Physics (AIP) congress in Adelaide between 12-16 December 2022 were I conducted a 15 minute oral presentation.

Acknowledgements

I would like to start by thanking my supervisors Professor Cathy Stampfl and Dr. Tanglaw Roman. Cathy provided steadfast support, thoughtful guidance, and encouragement throughout my PhD. I am deeply grateful for Cathy's support and the fantastic opportunities she has provided me, which included organising the funds for my PhD scholarship and support for attending two domestic conferences in Brisbane and Adelaide. Cathy's initial efforts welcoming me to Sydney University and the Condensed Matter Theory group paved the way for my PhD and this body of work. I am also deeply grateful to Tanglaw for his continued support, guidance and technical expertise in density functional theory and condensed matter physics from which I learned a lot and had many interesting and insightful discussions. Even though Tanglaw moved jobs from Sydney to Adelaide he still found time to conduct regular meetings and provide thoughtful guidance until the completion of my PhD. I would also like to thank the remaining members of the condensed matter theory group for their support who are Keri, El-Abed, Naiyuan and Luke.

I would also like to thank the chemical engineering group at Macquarie University for their guidance in chemistry related matters, our collaboration on various projects and their support throughout my PhD. In particular, Aleksei was key to providing a chemist's point of view when it came to checking our work and provided continued support and encouragement throughout my PhD. I would also like to thank Yijiao for her support both financially for providing scholarship funds and her guidance and expertise in chemistry related matters. Finally, I wish to thank Alena for her support and expertise in experimental chemistry.

I wish to acknowledge financial support from the Australian research council and the Sydney Nano Institute, Grand Challenge, CO_2 Zero. These funds provided my scholarship and the financial support required to undertake my PhD. I also acknowledge the Australian National Computational Infrastructure (NCI) and the Sydney Informatics Hub for access to

computational resources on their Gadi and Artemis high-performance computing facilities, respectively.

I wish to thank my friends and family for their support throughout my PhD. In particular my parents for their support through the past three and a half years.

Contents

CHAPTER 1

Introduction

Carbon dioxide (CO_2) is the most common product of any combustion reaction and is the most populous greenhouse gas in our atmosphere. Greenhouse gases are causing a general increase in global temperatures which will have a negative impact on certain human population settlements. In order to reduce the amount of CO_2 we release into the atmosphere new technologies are required that make it desirable and cost effective not to do so. One such technology is the electroreduction of CO_2 which if made efficient and powered via renewable energy sources would create a 'true' carbon neutral production cycle.

The electroreduction of CO_2 into valuable feedstocks and fuels motivates the development of a carbon neutral production cycle with low production costs [**1**]. The challenge lies in making the electroreduction of CO_2 energy efficient. Direct reduction of CO_2 requires large electrode potentials, so various catalysts have been studied which lower the required electrode potential improving the energy efficiency. These catalysts exist on the electrode surface making the interface between the electrode and the bulk solution the region of activity. Modelling this region is, however, quite difficult given the solid-liquid interface and cation and anion interactions. Creating models of these systems that efficiently and accurately simulate these systems is an active field of study [**2**]. The catalysts studied in this body of work are molecular metal complexes which are metal-organic in character.

Metal-organic complexes are a molecule with a single central metal species situated inside a macro-cycle nitrogen (N_4) complex, which is surrounded by an organic structure. These complexes can exists with a range of metal centres which include most 4^{th} row transition metals from Cr to Zn and some rare earth metals such as Ru, Rh [**3**]. The outer organic structure can have various configurations, common ones include porphyrin and phthalocyanine

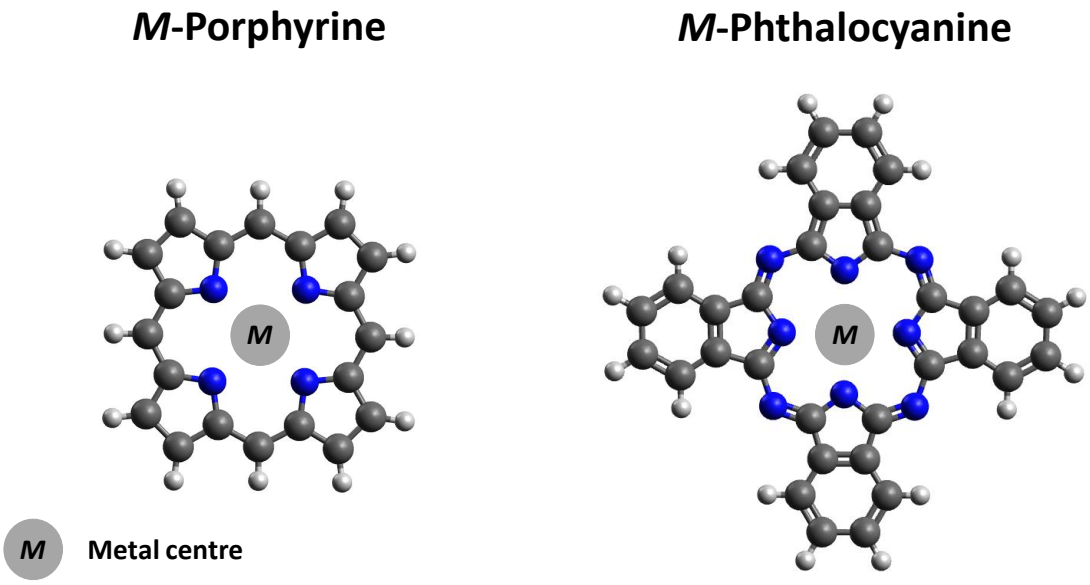

FIGURE 1.1. Geometries of metal centred porphyrine and phthalocyanine. Blue atoms are nitrogen, grey atoms are carbon and white atoms are hydrogen.

structures, shown in figure 1.1 below. The ligand structure of these complexes can be modified with additional structures such as phenyl and methoxy groups [**4**].

These metal-organic molecules, in recent years, have been shown to be remarkable CO_2 electroreduction reaction (CO_2ERR) catalysts with exceptional product selectivity, reaction rates and low electrode overpotentials [**5**–**11**]. This is owed to a single metal active site; the metal species and surrounding organic structure influence the electronic properties of the active site governing the catalysts CO_2ERR performance. The most common active site species are Co and Fe, where the latter has shown superior CO_2ERR performance as a homogeneous catalyst while Co presented similar; if not better, performance compared to Fe as a heterogeneous catalyst [**12**–**16**]. In this thesis we focus entirely on Co centred porphyrin (CoP) and phthalocyanine (CoPc) catalysts. Currently there is no agreement in the literature regarding the active anionic state of CoPc which is important in establishing the CO_2ERR mechanism of CoPc [**17**–**20**]. Heterogeneous catalysts which are immobilised directly to the electrode surface facilitate faster electron transfer required to reduce (charge $-1e/-2e$) the catalyst making it active for CO_2ERR [**21**]. This improves the performance, in particular

the reaction rate measured as turn over frequency (TOF). Covalent immobilisation of the catalyst also greatly improves its stability by removing the potential of catalyst leaching, but is experimentally difficult to achieve [**9**, **21**].

For metal-organic complexes covalent immobilisation depends on both the electrode type (e.g. glassy carbon or carbon nanotube) and the character of the immobilisation itself. Carbon nanotube functionalised electrodes have been shown to improve the CO_2ERR performance of catalysts owning to their higher surface conductivity [**22**]. The bonding between the catalyst and electrode provides a overall improvement in electron transfer but can also influence the energies and ordering of the active site d-state orbitals depending on the catalyst-electrode coordination [**21**, **23**–**26**]. The local environment of the catalyst surface is expected to have defect sites, which facilitate catalyst immobilisation.

This thesis investigates these aforementioned electronic and structural properties using density functional theory (DFT) and determines their impact on the catalyst performance through reaction pathway calculations. In particular we attempt to explain how these catalysts are directly immobilised to carbon supports and to ascertain whether defects play an important role as immobilisation sites. The effect on catalyst performance when immobilising directly to the active site is expected to significantly impact the performance of the catalyst but remains both computationally and experimentally unexplored [**23**, **25**–**27**].

DFT calculations, as implemented in the Vienna Ab initio Simulation Package (VASP) have been used to simulate the systems investigated in this thesis [**28**, **29**]. Most DFT calculations have been conducted using the generalised gradient approximation (GGA) functional of Perdew-Burke-Ernzerhof (PBE) to account for the exchange-correlation energy [**30**]. The D3 dispersion correction is also included to account for weaker adsorption interactions [**31**–**33**]. The relaxed geometries of catalysts, intermediates and catalyst-support systems are calculated also allowing us to calculate adsorption energies. Free energies are obtained using the computational hydrogen electrode method of Nørskov *et al.* which allows us to determine the reaction pathways accounting for thermodynamic, electrode and proton concentration contributions [**34**].

One of the challenges associated with calculating free energies is determining accurate solvation entropy terms. Accurate entropy terms can be obtained from *ab initio* molecular dynamics (MD) but these calculations are computationally too expensive [**35**–**41**]. Ideally we would have an approximate method that efficiently calculates entropies within, or close to, chemical accuracy (i.e. within 0.04 eV of experimental values). The difficulty comes when calculating the cavity formation entropy. Early attempts used scaled particle theory, while others simply scaled gas-phase entropy values, which were not always accurate [**42**–**46**]. More recent methods have attempted to solve this by accounting for solvation effects in the translational, rotational and cavitational entropy contributions [**47**]. More work is still required in this field with simple accurate models for solvent ordering for cavity formation and entropies of molecules at the surface-solution interface still to be developed [**48**].

In chapter 2 we describe the theory behind the DFT calculations conducted using VASP. Chapter 3 benchmarks different methods of calculating solvation entropies which is important for obtaining accurate reaction free energies. We found the solvation entropy method of Garza gave the most accurate aqueous phase entropy values compared to the other common approaches, which matched the experimental size dependence [**47**]. The other entropy methods tested included scaled gas-phase, the dipole method of ChemSol 2.1 and vibrational entropy only, which were tested on a bench marking set of 56 molecules [**49**–**51**]. Chapter 4 investigates how intrinsic defects in graphene and carbon nanotubes supports affect catalyst immobilisation and their impact on CO_2ERR performance. We found up-right catalyst immobilisation on Stone-Wales defect and octagon-pentagon line defect improve the reaction performance but immobilisation via the pyridine linker showed superior reaction performance by comparison of the determined free energy reaction pathways. In Chapter 5 is a series of eight atomic-style linkers that directly immobilise CoPc on a carbon nanotube support is investigated in order to determine if any specific linker species exhibited superior CO_2ERR performance. We found that both the NH and S linkers likely had similar CO_2ERR performance to each other and the pyridine linker, and significantly better performance compared to homogeneous CoPc. The PH linker is predicted to have better reaction rate performance compared to the NH and S linker systems but at a higher electrode potential. Finally, an

outlook is presented, where we summarise the main findings of this thesis and provide a view for future work in this area.

CHAPTER 2

Background Theory

2.1 Schrödinger Equation

Density functional theory (DFT) was born out of the computational necessity to treat multi-atomic systems accurately and efficiently, with the option of tailoring the accuracy/cost ratio to ones computational needs. Before we go into detail about DFT we discuss the Hartree-Fock method [**52–54**], a 'foundational' method of DFT which finds solutions to the Schrödinger equation using the wave function, as opposed to the charge density used in DFT [**55**].

Starting with the wave function in equation 2.1

$$\Psi(x,t) = e^{i(kx-\omega t)} \tag{2.1}$$

and then taking the derivative with respect to time and substituting the energy quantisation equation $E = hf$ into $\omega = 2\pi f$, we get equation 2.2.

$$\frac{\partial \Psi(x,t)}{\partial t} = -i\frac{E}{\hbar}e^{i(kx-\omega t)} \tag{2.2}$$

Equation 2.2 can be simplified and rearranged to give equation 2.3. The H term is the Hamiltonian operator and constitutes the sum of kinetic energy and potential energy giving equation 2.4 which includes the momentum operator.

$$i\hbar\frac{\partial \Psi(x,t)}{\partial t} = H\Psi(\mathbf{x},t) \tag{2.3}$$

$$\hat{H} = \frac{i\hbar}{2m}\frac{\partial}{\partial x} + V(x) \tag{2.4}$$

However, the both Hartree-Fock and DFT are not time dependant since they calculate incrementally the electronic and position changes of static systems. Equation 2.3 needs to become time independent. This can be achieved by a separation of variables using $\Psi(x,t) = e^{i(kx)}e^{-i(\omega t)} = \Psi(x)\Psi(t)$, substituting this and H into equation 2.3 we obtain equation 2.5.

$$i\hbar\frac{1}{\Psi(t)}\frac{\partial\Psi(t)}{\partial t} = -\frac{\hbar^2}{2m}\frac{1}{\Psi(x)}\frac{\partial^2\Psi(x)}{\partial x^2} + V(x) \tag{2.5}$$

In equation 2.5 the left hand side (LHS) only depends on time and the right hand side (RHS) only depends on spatial coordinates. Since we have a form in which the time dependence is equal to the spatial dependence both sides of equation 2.5 are equal to the same constant, C, which we call $E = i\hbar\frac{1}{\Psi(t)}\frac{\partial\Psi(t)}{\partial t} = C$. If we include E and multiply by $\Psi(x)$ we obtain equation 2.6.

$$E\Psi(x) = -\frac{\hbar^2}{2m}\frac{\partial^2\Psi(x)}{\partial x^2} + V(x)\Psi(x) \tag{2.6}$$

Arguments surrounds whether one can actually ‘derive’ the Schrödinger equation since there is no absolute starting axiom. We assume that the particles have wave-like motion and this is what experiments where showing at the time Schrödinger developed his equation. Feynman also asked this question stating: "It came from the mind of Schrödinger". Feynman later demonstrated a way to derive the Schrödinger equation using his path integral method [**56**]. More recent derivations have proposed that the Schrödinger equation can be derived from the average energy relation analogous to ‘total energy’ in a classical sense [**57**].

2.2 Many Body Schrödinger Equation

In the previous section we derived the time independent Schrödinger equation for a single particle, equation 2.3. This, however, needs to be expanded to include all energy contributions of a many body atomic system. These contributions are kinetic energies of electrons and nuclei, electron-electron repulsion, nuclei-nuclei repulsion and electron-nuclei interaction. The many body Schrödinger equation is given by equation 2.7 [**58**].

$$\hat{H} = \sum_{A=1}^{M} \frac{-\hbar^2}{2M_A} \nabla_A^2 + \sum_{A=1}^{M} \sum_{B>A}^{M} \frac{Z_A Z_B}{R_{AB}} - \sum_{A=1}^{M} \sum_{i=1}^{N} \frac{Z_A}{r_{iA}} + \sum_{i=1}^{N} \frac{-\hbar^2}{2M_e} \nabla_i^2 + \sum_{i=1}^{N} \sum_{i<j}^{N} \frac{1}{r_{ij}} \tag{2.7}$$

On the RHS of equation 2.7, the first term and second terms are the nuclei kinetic energy and nuclei-nuclei repulsion. The third term describes the electron-nuclei attraction. The fourth and fifth terms describe the electron kinetic energy and electron-electron repulsion, respectively. The variables M_A and M_e are the nuclei and electron masses respectively. The atomic number of the A^{th} atomic species is given by Z_A. The distance between the A^{th} and B^{th} nuclei is R_{AB}. Similarly r_{ij} is the distance between the i^{th} and j^{th} electrons.

The many body Schrödinger equation forms the basis of density functional theory providing a "complete" energy description of atomic systems. We will come back to this equation in later sections.

2.3 Born-Oppenheimer Approximation

The Born-Oppenheimer approximation is fundamental to all modern quantum mechanical methods of solving complex atomic systems [**59**]. The nuclei of an atom is at least three orders of magnitude (or 2000 times) heavier compared to an electron. This means electrons will have larger velocities compared to the nuclei and can therefore be treated separately. This is usually achieved by assuming the ansatz in equation 2.8.

$$\Psi(\boldsymbol{r}, \boldsymbol{R}) = \Phi_e(\boldsymbol{r}, \boldsymbol{R})\Phi_N(\boldsymbol{R}) \tag{2.8}$$

In equation 2.8, $\Phi_e(\boldsymbol{r}, \boldsymbol{R})$ is the electron wavefunction which is dependant on nuclei position since the electron is assumed to move with its respective nuclei. $\Phi_N(\boldsymbol{R})$ is the nuclei wavefunction.

This separation of electron and nuclei contributions allows us to define an electronic and nuclear Schrödinger equation from the terms in equation 2.7. The electronic Schrödinger equation is given by equation 2.9 and the nuclear Schrödinger equation is given by equation 2.10 [**59**, **60**].

$$\hat{H}_e\Phi_e(\boldsymbol{r}, \boldsymbol{R}) = \left(\sum_{A=1}^{M}\sum_{i=1}^{N}\frac{-Z_A}{r_{iA}} + \sum_{i=1}^{N}\frac{-\hbar^2}{2M_e}\nabla_i^2 + \sum_{i=1}^{N}\sum_{i<j}^{N}\frac{1}{r_{ij}}\right)\Phi_e(\boldsymbol{r}, \boldsymbol{R}) \tag{2.9}$$

$$\hat{H}_N\Phi_N(\boldsymbol{R}) = \left(\sum_{A=1}^{M}\frac{-\hbar^2}{2M_A}\nabla_A^2 + \sum_{A=1}^{M}\sum_{B>A}^{M}\frac{Z_AZ_B}{R_{AB}}\right)\Phi_N(\boldsymbol{R}) \tag{2.10}$$

These two equations are reflective of how DFT software works with solutions to the electronic Schrödinger equation found before a solution to the nuclear Schrödinger equation can be determined. These equations and the process of finding their solutions are explored in the next chapters.

2.4 Hartree-Fock Method

An exact general solution to the Schrödinger equation is limited to the hydrogen atom (a two body system) due to the complex nature of formulating a solution of an interacting system in three dimensions. No such solution exists for the helium atom which involves a system of three interacting bodies, two electrons and a nucleus. Historically, attempts have been made to find a general solution to the three body problem with figures such as Henri Poincaré and Heinrich Bruns concluding there was no algebraic solution [**61**]. Hope was not lost however,

as Karl Sundman discovered a series which if summed would give a solution to the three body system, but this series converges so slowly and with so many terms that no meaningful solution could be found [**62–64**]. Work on the three body problem is still on going with special case solution families being discovered and more recently machine learning has been used to improve the computation efficiency and accuracy of numerical solutions [**65**]. This explains why approximate, instead of exact, solutions to the Schrödinger are found for the helium atom [**66**]. This leads us to the question how do we get accurate solutions to the Schrödinger equation for systems containing many atoms/electrons?

This is where the method of Hartree and Fock comes into play [**52**,**53**,**67**,**68**]. The fundamental assumption of the Hartree-Fock method is the wavefunction describing the multiple electrons of the system can be described as a product of single-electron wavefunctions (the Hartree product shown in equation 2.11). Essentially, electrons are assumed to move independently of each other and therefore can be treated separately just like the nuclei under the Born-Oppenheimer approximation. Electrons do however experience Coulomb repulsion with respect to an average contribution of all other electrons, helping to keep calculations within the framework of separate two body calculations for each component of the N-body system.

$$\Psi(\boldsymbol{r}_1, \boldsymbol{r}_2, ..., \boldsymbol{r}_n) = \Phi_1(\boldsymbol{r}_1)\Phi_2(\boldsymbol{r}_2)...\Phi_n(\boldsymbol{r}_n) \tag{2.11}$$

In equation 2.11, $\boldsymbol{r}$ is the electronic coordinates and $\Phi_i(\boldsymbol{r}_i)$ is the one-electron wavefunction (spatial orbital) of the i$^{\text{th}}$ electron. To satisfy the anti-symmetry principle (and Pauli exclusion principle) for electrons, which states that an electron that changes in spin must correspond to a change in sign of the wavefunction we use equation 2.12. The one-electron wavefunction can be rewritten as spin orbital $\chi_i(\boldsymbol{x}_i) = \sigma(\omega)\Phi_i(\boldsymbol{r}_i)$, where $\sigma(\omega)$ is the spin function and ω is the spin coordinate. This allows us to generalise the N electron wavefunction as a matrix of orbitals whose Slater determinant is the wavefunction of the system [**54**], see equation 2.13. An example for the two electron case is given in equation 2.12.

$$\Psi(\boldsymbol{x}_1, \boldsymbol{x}_2) = \frac{1}{\sqrt{2}}[\chi_1(\boldsymbol{x}_1)\chi_2(\boldsymbol{x}_2) - \chi_1(\boldsymbol{x}_2)\chi_2(\boldsymbol{x}_1)] \tag{2.12}$$

$$\Psi(\boldsymbol{x}_1, \boldsymbol{x}_2) = \frac{1}{\sqrt{2}} \det \begin{vmatrix} \chi_1(\boldsymbol{x}_1) & \chi_1(\boldsymbol{x}_2) \\ \chi_2(\boldsymbol{x}_1) & \chi_2(\boldsymbol{x}_2) \end{vmatrix} \tag{2.13}$$

Coming back to the time independent Schrödinger we need to define the energy components of the electrons in our system. These can be expressed as the electronic Hamiltonian (only contains electron energy contributions) in equation 2.14 with the first term describing the electron-electron repulsion, second term describes the electron kinetic energy and the last term is the electron-nucleus interaction. The number of electrons and the the number of nuclei are given by N and M, respectively.

$$H_e = \sum_{i=1}^{N} \sum_{i<j}^{N} \frac{1}{r_{ij}} - \sum_{i=1}^{N} \frac{1}{2} \nabla^2 - \sum_{i=1}^{N} \sum_{A=1}^{M} \frac{Z_A}{r_{iA}} = \sum_{i=1}^{N} h_i \tag{2.14}$$

Equation 2.14 is the electronic Hamiltonian operator (also written as $\hat{H}_e$) in the Schrödinger equation which is now easier to represent in bra-ket notation, see equation 2.15. This can be rearranged into equation 2.16.

$$E_{\mathrm{e}} \left|\Psi_e\right\rangle = \hat{H}_e \left|\Psi_e\right\rangle \tag{2.15}$$

$$E_{\mathrm{e}} = \langle \Psi_e | \hat{H}_e | \Psi_e \rangle \tag{2.16}$$

To put equation 2.14 into context, the total energy of the many electron/nucleus system is given in equation 2.17. The first term (E_e) is sometimes called the Hartree-Fock energy (H_{HF}).

$$E_{\mathrm{tot}} = E_e + \sum_{A=1}^{M} \sum_{B>A}^{M} \frac{Z_A Z_B}{R_{AB}} \tag{2.17}$$

Substituting equation 2.11 into equation 2.15 we obtain equation 2.18.

$$E_e = \langle \chi_1 \chi_2 ... \chi_n | \hat{H}_e | \chi_1 \chi_2 ... \chi_n \rangle \tag{2.18}$$

In order to solve equation 2.18 the *variational principle* is used to approximate the ground state (lowest) energy of the wave function. In effect this is an optimisation problem with certain parameters kept fixed. In this case the positions of nuclei and core electrons are fixed while valence region electrons experience a change in their spin and orbital energies and positions until a minimum (ground state) energy is found. In other words, the expectation value of the Hamiltonian is always greater than or equal to the ground state energy [**69**, **70**]. This method is iterative starting with a trial wave function which by definition can only have an energy greater than or equal to the ground state energy.

To avoid unnecessarily long and arduous equations and derivations we do not derive the Hartree-Fock equation (see equation 2.19) here. A derivation can be found in the appendix of the textbook *Orbital Interaction Theory of Organic Chemistry* [**71**].

$$\hat{f}(x_i)\chi(x_i) = \epsilon\chi(x_i) \tag{2.19}$$

$$\hat{f}(x_i) = -\frac{1}{2}\nabla^2 - \sum_{A=1}^{M} \frac{Z_A}{r_{iA}} + V^{NN} \tag{2.20}$$

In equation 2.19 $\hat{f}(x_i)$ is the Fock operator as defined in equation 2.20 and ϵ is a diagonal matrix of spin-orbital energies. The average electron-electron potential is given by V^{NN} in equation 2.20. This equation contains the desired eigenvalues and is solved using the iterative self-consistent field (SCF) method [**53**]. Roothaan equations are solved via the SCF process and provide the expansion coefficients of equation 2.24. Equation 2.19 can be written as equation 2.21 when we include spin (restricted closed-shell, unrestricted open-shell and restricted open-shell) and spatial orbitals as basis functions.

$$\hat{f}(r_i)\sum_n C_{ni}\Phi_n(r_i) = \epsilon_i \sum_n C_{ni}\Phi_n(r_i) \tag{2.21}$$

In equation 2.21 C_{ni} are the expansion coefficients and $\Phi_n(r_i)$ are the spatial orbitals (see equation 2.11) and r_i is the spatial coordinate of the i^{th} electron. Referring back to the Fock operator (equation 2.20) we see equation 2.21 is an integro-differential equation. This means equation 2.21 can be represented in matrix form as shown in equation 2.22.

$$\sum_n C_{ni}\int \Phi_n^*(r_i)\hat{f}(r_i)\Phi_n(r_i)\mathrm{d}r_i = \epsilon_i \sum_n C_{ni}\int \Phi_n^*(r_i)\Phi_n(r_i)\mathrm{d}r_i \tag{2.22}$$

$$\sum_n C_{ni}F_{nk} = \epsilon_i \sum_n C_{ni}S_{nk} \tag{2.23}$$

In equation 2.22 the integrals are the Fock matrix (F_{nk}) and overlap matrix (S_{nk}) as shown in equation 2.23. The transformed Fock matrix ($F^{'}$) of equation 2.19 when in matrix form ($FC = C\epsilon$) is given by equation 2.24 [**72**, **73**].

$$F^{'}C^{'} = C^{'}\epsilon \tag{2.24}$$

Finally, the Hartree-Fock method uses a density matrix derived from the electronic charge density of the system. The electronic charge density is given in equation 2.25 and the density matrix which also contains the expansion coefficients in equation 2.26.

$$\rho(\mathbf{r}) = \sum_{nk} D_{nk}\Phi_n\Phi_k^* \tag{2.25}$$

$$D_{nk} = 2\sum_{\alpha}^{N/2} C_{n\alpha}C_{k\alpha} \tag{2.26}$$

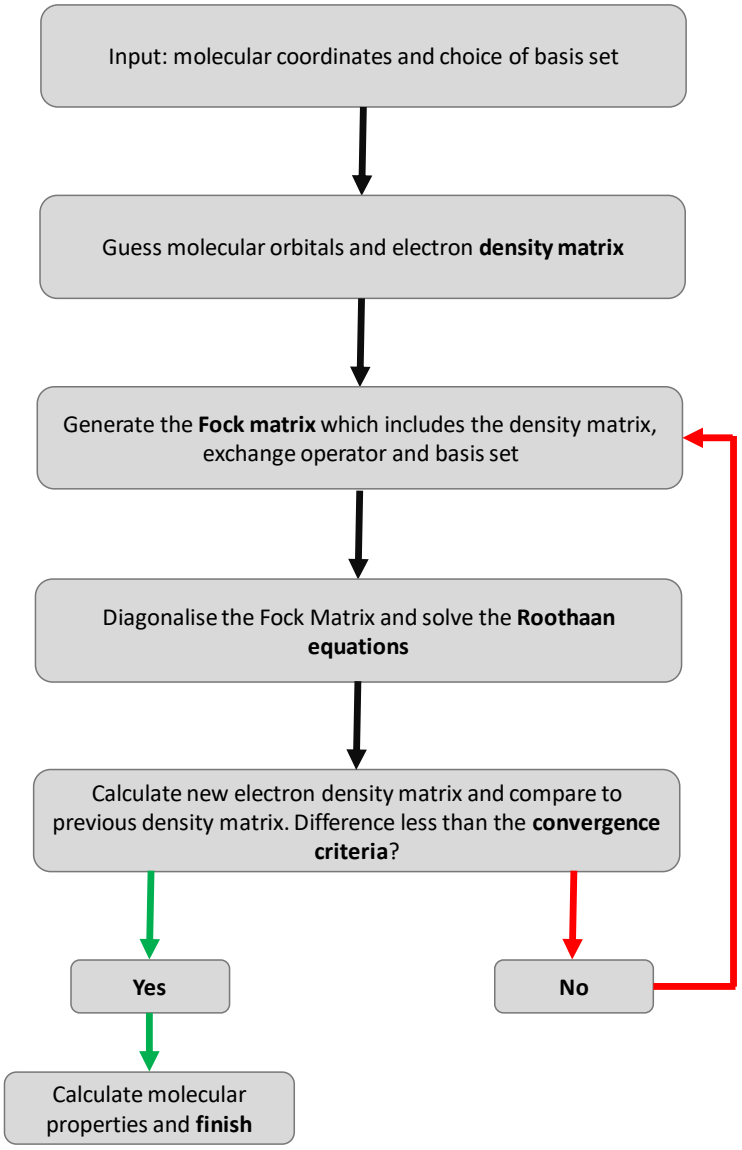

FIGURE 2.1. Flow diagram of the Hartree-Fock calculation procedure. The SCF method occurs between steps three to six.

We have not covered every step of the Hartree-Fock method derivation here in detail due to tedious calculations but these are easy to find in any computational physics or chemistry textbook [**55**, **71**, **74**]. The Hartree-Fock method is a precursor to modern DFT with similar

methods and algorithms. Having an understanding of the Hartree-Fock method will make understanding the Hohenberg-Sham method in the next section much easier.

2.5 Density Functional Theory

The Hartree-Fock method uses single-electron wavefunctions to solve the many body Schrödinger equation. We can see from equation 2.11 that as we scale to many electron systems the electron wavefunction will become increasing complex. In-fact the Hartree-Fock method is only efficient at calculating small systems [**74**]. The computational time of Hartree-Fock approximately scales as $\mathcal{O}(N^4)$ compared to $\mathcal{O}(N^3)$ for modern DFT (where N is the number of plane waves/basis functions) using either the local density approximation or generalised gradient approximation exchange-correlation functionals (these are discussed further in section 2.5.3) [**75**]. However, some DFT exchange-correlation functionals include Hartree-Fock mixing which causes the computational efficiency to scale as $\mathcal{O}(N^4)$.

How does DFT achieve this improvement in computational efficiency without sacrificing accuracy? As mentioned in the start of this section, charge or electron density is used to solve the Schrödinger equation. The charge density only has three dimensions compared to the $3N$ dimensions for the wavefunction, this means that DFT reduces the problem to N different three-dimensional problems.

The functional in density functional theory refers to a function that takes another function as an input, e.g. $F[g(x)]$. In the case of DFT we have an energy functional based on the many body Schrödinger equation which takes the charge density as the input function and is given by equation 2.27.

$$E_0[\rho_0(\mathbf{r})] = E_e[\rho_0(\mathbf{r})] + T[\rho_0(\mathbf{r})] + E_{\mathrm{Ne}}[\rho_0(\mathbf{r})] \tag{2.27}$$

In equation 2.27 $E_e[\rho_0(\mathbf{r})]$ is the electron-electron electrostatic repulsion, $T[\rho_0(\mathbf{r})]$ is the electron kinetic energy and and E_{Ne} is the electrostatic attraction between the nucleus and the

electron. The ground state energy is E_0 and $\rho_0(\mathbf{r})$ is the ground state charge density, both of which are formally defined by the Hohenberg-Kohn theorems in the next section.

2.5.1 Hohenberg-Kohn Theorems

We have defined charge density in equation 2.25, and it is given by the sum of the absolute square of the non-interacting occupied orbitals. The reason we can use the charge density as a solution to solve the Schrödinger equation is given by two theorems proven by Hohenberg and Kohn in 1964 [**76**].

The first theorem (to paraphrase) states: *The external potential $V_{\text{ext}}(\boldsymbol{r})$ is a unique functional of the charge density $\rho(\boldsymbol{r})$ and therefore uniquely determines the Hamiltonian $\hat{H}$ operator. Therefore, the ground state E_0 of the many-particle system is a unique functional of the charge density*. This theorem can be proven by contradiction, i.e. assuming $V_{\text{ext}}(\mathbf{r})$ is not unique which allows us to define another external potential $V_{\text{ext}}^{'}(\mathbf{r})$ (different by more than just a constant) which has the same ground state charge density $\rho(\mathbf{r})$ as $V_{\text{ext}}(\mathbf{r})$.

The second theorem follows on from the first and states: *The true ground state charge density, ρ_0, gives the lowest energy and therefore the ground state energy of the system. In other words for an external potential V_{ext}, and associated trial charge density, $\tilde{\rho}(\boldsymbol{r})$, the energy from the functional in equation 2.27 is an upper bound to the true ground state energy*. This theorem can simply be represent by equation 2.28 and in-fact represents the variational principle.

$$E_0[\rho_0(\mathbf{r})] \leq E_e[\tilde{\rho}(\mathbf{r})] + T[\tilde{\rho}(\mathbf{r})] + E_{\text{Ne}}[\tilde{\rho}(\mathbf{r})] \tag{2.28}$$

We have not provided a detailed proof of these theorems here as they can be found in many textbooks such as *A Chemists Guide to Density Functional Theory* [**77**]. The Hohenberg-Kohn theorems create the formal mathematical foundation on which Kohn and Sham develop their formulism for density functional theory.

2.5.2 Kohn-Sham Equations

Using the theorems established in the previous section Kohn and Sham, with inspiration from the Hartree-Fock method, developed what they called '*...approximation methods for treating an inhomogeneous system of interacting electrons.*' [**78**]. The 'approximation' occurs due to a separation in the kinetic energy treatment of electrons, i.e. an exact kinetic energy term is calculated for the non-interacting component while the interacting component is unknown and is approximated as part of the exchange-correlation energy. This allowed Kohn and Sham to start off by showing that for the non-interacting kinetic energy term (see equation 2.14) one can define and non-interacting Hamiltonian and therefore a 'Kohn-Sham' operator analogous to the Fock operator equation 2.20. All that is left is to apply the second Hohenberg-Kohn theorem by which we find the V_{ext} that gives the ground state ρ_0 which is equal to sum of the Kohn-Sham orbitals (ϕ_i) multiplied by their respective conjugate shown in equation 2.25 and is rewritten in terms of Kohn-Sham orbitals in equation 2.29.

$$\rho(\mathbf{r}) = \sum_{ij} \phi_i \phi_j^* \tag{2.29}$$

Using the Kohn-Sham approach and the fact that we cannot account exactly for the interacting component (called the 'exchange-correlation' energy) we can define what Kohn and Sham called the universal functional, given by equation 2.30. The exact kinetic energy of the non-interacting system of electrons is given by $T_{\text{non-int}}[\rho(\mathbf{r})]$, while the the interacting or exchange-correlation components are grouped together in the $E_{\text{XC}}[\rho(\mathbf{r})]$ term. To be clear, $T[\rho(\mathbf{r})] = T_{\text{non-int}}[\rho(\mathbf{r})] + T_{\text{int}}[\rho(\mathbf{r})]$ meaning $T[\rho(\mathbf{r})]$ in equation 2.27 and equation 2.28 is the total electronic kinetic energy of the system. We will have a more rigorous discussion of the exchange-correlation energy in the next section, but for now we look at defining the Kohn-Sham energy equations.

$$G[\rho(\mathbf{r})] = T_{\text{non-int}}[\rho(\mathbf{r})] + J_e[\rho(\mathbf{r})] + E_{\text{XC}}[\rho(\mathbf{r})] \tag{2.30}$$

Now we can combine equation 2.27 and equation 2.30 giving us a 'complete' energy description of our system. The $J_e[\rho(\mathbf{r})]$ term is the classical component of $E_e[\rho(\mathbf{r})]$ (electron-electron repulsion) such that $E_e[\rho(\mathbf{r})] = J_e[\rho(\mathbf{r})] + J_{\text{XC}}[\rho(\mathbf{r})]$. However, $J_{\text{XC}}[\rho(\mathbf{r})]$ is not known but accounts for the quantum energy contributions to electron-electron repulsion. Therefore, we can write the exchange-correlation energy as $E_{\text{XC}}[\rho(\mathbf{r})] = T_{\text{int}}[\rho(\mathbf{r})] + J_{\text{XC}}[\rho(\mathbf{r})]$. The $E_{\text{XC}}[\rho(\mathbf{r})]$ term would ideally be 'complete' giving an exact solution to the Schrödinger equation but in actuality it must be approximated. The energy description of our system is given by equation 2.31 and is analogous to equation 2.14 of section 1.4 but in the Kohn-Sham charge density formulism.

$$E[\rho(\mathbf{r})] = T_{\text{non-int}}[\rho(\mathbf{r})] + J_e[\rho_0(\mathbf{r})] + E_{\text{XC}}[\rho(\mathbf{r})] + E_{\text{Ne}}[\rho_0(\mathbf{r})] \tag{2.31}$$

Using the Kohn-Sham orbitals we know the exact form of each term in equation 2.31 except for $E_{\text{XC}}[\rho(\mathbf{r})]$. Substituting the exact forms for each term we get equation 2.32.

$$\begin{aligned} E[\rho(\mathbf{r})] = & -\frac{1}{2}\sum_{i}^{N}\phi_i\nabla^2\phi_i^* + \frac{1}{2}\iint\frac{\rho(\mathbf{r})\rho(\mathbf{r}')}{|\mathbf{r}-\mathbf{r}'|}\mathrm{d}\mathbf{r}\mathrm{d}\mathbf{r}' \\ & + E_{\text{XC}}[\rho(\mathbf{r})] - \int\sum_{A}^{M}\frac{Z_A}{|\mathbf{r}-\mathbf{r}_A|}\rho(\mathbf{r})\mathrm{d}\mathbf{r} \end{aligned} \tag{2.32}$$

Equation 2.32 shows that all terms except the $E_{\text{XC}}[\rho(\mathbf{r})]$ term can be calculated exactly. All that is left to do is to apply the variational principle allowing us to minimise the energy of equation 2.32. To do this we follow the variational principle we used for the Hartree-Fock method, i.e. we want the Hartree-Fock equation (equation 2.19) but in terms of Kohn-Sham orbitals and the Kohn-Sham energy formulism. One can start off with the constraint that the Kohn-Sham orbitals must be orthonormal as per equation 2.33, where δ_{ij} is the Kronecker delta function.

$$\int\phi_i(\mathbf{r})\phi_j^*(\mathbf{r})\mathrm{d}\mathbf{r} = \delta_{ij} \tag{2.33}$$

Then, as shown in Parr & Yang 1995, one can develop the Kohn-Sham orbital equations as shown in equations 2.34-2.35 [**79**]. In equation 2.34 ϵ_i are the i^{th} element of the ϵ_{ij} diagonal Hermitian matrix of orbital energies. In equation 2.35, the δ symbols indicate a functional derivative of E_{XC} with respect to $\rho(\mathbf{r})$.

$$\left(-\frac{1}{2}\nabla^2 + V_{\text{eff}}\right)\phi_i = \epsilon_i\phi_i \tag{2.34}$$

$$V_{\text{eff}}(\mathbf{r}) = \int \frac{\rho(\mathbf{r}')}{|\mathbf{r} - \mathbf{r}'|}\mathrm{d}\mathbf{r}' + \frac{\delta E_{\text{XC}}}{\delta\rho(\mathbf{r})} - \sum_A^M \frac{Z_A}{|\mathbf{r} - \mathbf{r}_A|} \tag{2.35}$$

Equation 2.35 comes about by needing to minimise equations 2.31 & 2.32 which is achieved by calculating the functional derivative of equation 2.30. All that's left to do is substitute equation 2.35 into the Kohn-Sham version of equation 2.20 (the Fock operator) which gives equation 2.36.

$$\hat{f}_{\text{KS}} = -\frac{1}{2}\nabla^2 + V_{\text{eff}} \tag{2.36}$$

Equation 2.36 is then applied to each orbital as per equation 2.19 giving us the orbital energies which per equation 2.29 gives us the charge density and thus the total energy from equation 2.32. This process is still iterative but instead of using a trial wavefunction we use trial charge densities until we find the minimum total energy of the system. However, our process is not yet complete we still need to decide how we are going to include the exchange-correlation energy contribution which we have assumed to be unknown.

2.5.3 Exchange-Correlation Energy

In the previous section we found that we can only calculate exact energy contributions for the non-interacting kinetic energy and classical electrostatic repulsion with the interacting kinetic energy and nonclassical components relegated to an'exchange-correlation' functional, defined

in equation 2.37. The $E_{\mathrm{X}}[\rho(\mathbf{r})]$ and the $E_{\mathrm{C}}[\rho(\mathbf{r})]$ are the electron exchange and correlation energies respectively.

$$E_{\mathrm{XC}}[\rho(\mathbf{r})] = T_{\mathrm{int}}[\rho(\mathbf{r})] + J_{\mathrm{XC}}[\rho(\mathbf{r})] + ... = E_{\mathrm{X}}[\rho(\mathbf{r})] + E_{\mathrm{C}}[\rho(\mathbf{r})] \tag{2.37}$$

Before we outline approximations to equation 2.37 its important to define the electron exchange and correlation components. Electron exchange energy is the attractive energy gained by the system when we account for the Pauli exclusion principle which means it only applies to electrons with the same spin, since by the Pauli exclusion principle they cannot occupy the same orbital. The exchange energy can be calculated exactly using equation 2.38 but computationally this brings us back to similar situation as the Hartree-Fock method with this contribution being computationally too expensive for large systems. With respect to charge density, accounting for the electron exchange causes regions of charge density depletion which in turn reduces the repulsive energy between same spin electrons since they cannot get too close to each other. These regions of charge density depletion are referred to as 'exchange holes'.

$$E_{\mathrm{X}} = -\frac{1}{2}\sum_{ij}^{N}\iint \frac{\phi_i^*(\mathbf{r})\phi_j^*(\mathbf{r}')\phi_i(\mathbf{r}')\phi_j(\mathbf{r})}{|\mathbf{r}-\mathbf{r}'|}\mathrm{d}\mathbf{r}\mathrm{d}\mathbf{r}' \tag{2.38}$$

On the other hand we have the correlation energy contribution, which in the Hartree-Fock approach is omitted. This is the energy contribution between electrons of both the same and opposite spin but occurs over a much shorter distance compared to the electron exchange interactions [**74**, **80**, **81**]. This means the correlation energy contribution is much smaller compared to the exchange contribution. However, for a system of sparsely populated electrons it becomes more significant since the exchange contribution which occurs over larger distances is smaller [**82**]. Just like with the 'exchange hole' we have a 'correlation hole' which applies to electrons in the same orbital (i.e. a spin-up and spin-down electron) resulting in a zero charge density node between the two electrons [**74**]. The exchange correlation charge density is then the sum of the two exchange and correlation contributions.

2.5.3.1 Local Density Approximation

The most simple method of calculating the exchange correlation contribution is the local density approximation (LDA) as first proposed by Kohn and Sham [**83**]. The LDA method assumes the system has a charge density that varies slowly with position. This means we can define a neutral system of a homogeneous electron gas in a uniform positive background charge. Here the positive background charge is essentially the average charge of the atomic nuclei covering all points in space. Based on this model Hohenburg, Kohn and Sham were able to derive a simple form for the LDA functional shown in equation 2.39 [**76**, **83**]. The single-electron approximation to the exchange-correlation energy is given by $\epsilon_{\mathrm{XC}} = \epsilon_{\mathrm{X}} + \epsilon_{\mathrm{C}}$.

$$E_{\text{XC-LDA}}[\rho(\mathbf{r})] = \int \rho(\mathbf{r})\epsilon_{\mathrm{XC}}[\rho(\mathbf{r})]\mathrm{d}\mathbf{r} \tag{2.39}$$

Only the exchange energy ϵ_{X} has a known explicit expression but the correlation energy ϵ_{C} is determined numerically from Monte Carlo simulations [**84**]. The exchange energy is given by equation 2.40 which is referred to as the Slater or Dirac exchange [**77**, **79**].

$$\epsilon_{\mathrm{X}}(\rho(\mathbf{r})) = -\frac{3}{4}\left(\frac{3\rho(\mathbf{r})}{\pi}\right)^{\frac{1}{3}} \tag{2.40}$$

In terms of the correlation energy there are two main results used, the one by Vosko, Wilk and Nusair [**85**] and more recently the one by Perdew and Wang (PW92) [**86**]. Most methods approximate the electron correlation energy using the random phase approximation (RPA) which is optimised numerically via fitting parameters. For example, the PW92 correlation energy function is parameterised for low and high charge densities and then fitted to numerical quantum Monte Carlo simulation results [**84**, **86**]. The PW92 correlation energy is given by equation 2.41.

$$\epsilon_{\mathrm{C}} = -2A(1+\alpha_1 r_s)\ln\left(1 + \frac{1}{2A(\beta r_s^{1/2} + \beta_2 r_s + \beta_3 r_s^{3/2} + \beta_4 r_s^{P+1})}\right) \tag{2.41}$$

In equation 2.41 A, α_1, β_1, β_2, β_3, β_4 are all fitting parameters and $P = \frac{3}{4}$. This leaves r_s, the Wigner-Seitz radius, which is related to the charge density by $r_s = \frac{1}{\sqrt[3]{4\pi\rho/3}}$, meaning low and high r_s refer to high and low charge densities, respectively [**86**].

Now we have both the single-electron approximation to the exchange and correlation energies, all that is left to do is to combine equation 2.40 and the analytical expression for ϵ_{C} in equation 2.39. This gives us the exchange correlation which can be used in equations 2.34-2.35 to find the orbitals, ground state charge density and therefore the minimum energy.

The LDA exchange-correlation functional is the most basic and computationally efficient functional. However, the LDA tends to suffer from an over binding issue which is apparent when e.g. comparing the cohesive energies of metals with respect to experiment [**87**]. The LDA functional has also been found to give poor descriptions of hydrogen bonding and errors in bond lengths twice as large compared to more advanced exchange-correlation functionals. To address this issue higher order exchange-correlation functionals where developed using the LDA as a foundation.

2.5.3.2 Generalised Gradient Approximation

We can think of the LDA exchange-correlation functional as the first term in a functional Taylor expansion that can be expanded to the n^{th} order term. This was the next development; a first order gradient term for the charge density was included and after some 'practical' adjustments, in the form of exchange and correlation hole constraints, the Generalised Gradient Approximation (GGA) functional was developed. The general form of the GGA functional is shown in equation 2.42 and in equation 2.43 the charge density has been split into its spin up and spin down components.

$$E_{\text{XC-GGA}}[\rho(\mathbf{r})] = \int f(\rho, \nabla\rho)\mathrm{d}\mathbf{r} \tag{2.42}$$

$$E_{\text{XC-GGA}}[\rho(\mathbf{r})_\uparrow, \rho(\mathbf{r})_\downarrow] = \int f(\rho_\uparrow, \rho_\downarrow, \nabla\rho_\uparrow, \nabla\rho_\downarrow)\mathrm{d}\mathbf{r} \tag{2.43}$$

Just like for the LDA, the GGA electron exchange and correlation components are calculated separately. This means we can write the exchange component of equation 2.43 explicitly, in particular the first order gradient term as shown in equation 2.44. The $E_{\text{X-LDA}}$ is given by the exchange component in equation 2.39 from the previous section.

$$E_{\text{X-GGA}} = \sum_{\uparrow,\downarrow} \int \epsilon_{\text{X-LDA}} F(S) \rho_{\uparrow,\downarrow}(\mathbf{r}) \mathrm{d}\mathbf{r} \tag{2.44}$$

In equation 2.44 $F(S)$ is called the reduced density gradient functional and has been developed in to two main forms, P86 and B88 [**88–90**]. The S term is an inhomogeneity parameter which is large for both large gradients and small charge density regions as shown by equation 2.45.

$$S = \frac{1}{[24\pi^2 \rho_{\uparrow,\downarrow}(\mathbf{r})]^{\frac{1}{3}}} \frac{|\nabla \rho_{\uparrow,\downarrow}(\mathbf{r})|}{\rho_{\uparrow,\downarrow}(\mathbf{r})} \tag{2.45}$$

The P86 form of the GGA functional has become the most commonly used, given its implementation in the Perdew, Burke, and Ernzerhof (PBE) exchange-correlation functional [**30**]. The alternative is the Perdew, Burke and Wang (PW91) functional using the B88 form of the reduced density gradient [**91**]. In this thesis we utilise the PBE functional so all our calculations utilise the P86 form of $F(S)$, which is given by equation 2.46.

$$F(S) = 1 + \kappa - \frac{\kappa}{1 + \mu S^2 / \kappa} \tag{2.46}$$

In equation 2.46 $\kappa = 0.804$ and $\mu = 0.21951$ are empirical factors determined such that $F(0) = 1$ recovers equation 2.40 while increasing for larger S until $F(S) \leq 1.804$ as $S \longrightarrow \infty$ [**30**]. Substituting equation 2.46 into equation 2.44 gives us an explicit term for the GGA exchange energy used by the PBE functional.

The general form for the GGA correlation used by the PBE functional is given in equation 2.47 where $\epsilon_{\text{C-LDA}}$ is equation 2.41 and $\epsilon_{\text{C-GGA}}$ is defined in equation 2.48

$$E_C = \int [\epsilon_{\text{C-LDA}} + \epsilon_{\text{C-GGA}}]\rho_{\uparrow,\downarrow}(\mathbf{r})\mathbf{dr} \tag{2.47}$$

$$\epsilon_{\text{C-GGA}} = \gamma\phi^3 \ln\left(1 + \frac{\beta}{\gamma}t^2\left[\frac{1+At^2}{1+At^2+A^2t^4}\right]\right) \tag{2.48}$$

Equation 2.48 was determined based on three conditions (1) $\epsilon_{\text{C-GGA}} \longrightarrow \beta\phi^3t^2$ as $t \longrightarrow 0$, (2) $\epsilon_{\text{C-GGA}} \longrightarrow \epsilon_{\text{C-LDA}}$ as $t \longrightarrow \infty$ and (3) $\epsilon_{\text{C-GGA}} \longrightarrow$ constant value as $\gamma \longrightarrow \infty$ [**30**, **91**]. Here $\beta = 0.066725$ and $\gamma = \frac{1-\ln(2)}{2} \approx 0.031091$ which are empirically determined values. While ϕ defined in equation 2.49 accounts for the spin polarisation, t defined in equation 2.50 is a density gradient terms similar to equation 2.45 and lastly A is defined by equation 2.51 [**30**].

$$\phi = \frac{1}{2}[(1 + \frac{\rho_\uparrow - \rho_\downarrow}{\rho})^{2/3} + (1 - \frac{\rho_\uparrow - \rho_\downarrow}{\rho})^{2/3}]/2 \tag{2.49}$$

$$t = \frac{|\nabla\rho|}{2\phi[\frac{4}{\pi}(3\pi^2\rho)^{1/3}]^{1/2}} \tag{2.50}$$

$$A = \frac{\beta}{\gamma e^{\epsilon_{\text{C-LDA}}/(\gamma\phi^3)} - 1} \tag{2.51}$$

Substituting equations 2.49, 2.50 and 2.51 into equation 2.48 and then substituting back into equation 2.47 gives us an explicit form for the electron correlation energy used by the PBE functional. Now we have a complete picture for the PBE exchange-correlation functional which is used along with a dispersion correction (see section 2.5.3.4) for DFT calculations in chapters 3-5.

However, the GGA exchange-correlation functional is not the end of exchange-correlation functional development. Higher order contributions and Hartree-Fock mixing have been developed creating a new class of exchange-correlation functional called the hybrid and metaGGA classes of functionals.

2.5.3.3 Meta-GGA and Hybrid Functionals

Functional complexity is associated with the biblical analogy of Jacobs ladder which leads to heaven and we the angels choose our rung on the ladder (Genesis 28.10-12) [**92**]. Here the Earth represents the Hartree-Fock (exact) method, then the first rung of the ladder is DFT-LDA, the second rung is DFT-GGA, the third rung is DFT-meta-GGA, the fourth rung is DFT-hybrid and the fifth rung is DFT-RPA (random phase approximation). Beyond the fifth rung is the ideal realm (heaven) of chemically accurate calculations which are yet to be realised and if found would constitute the 'perfect' functional.

The meta-GGA functional includes an additional level of complexity above the GGA functional and is given by equation 2.52.

$$E_{\text{XC-metaGGA}}[\rho(\mathbf{r})_{\uparrow}, \rho(\mathbf{r})_{\downarrow}] = \int f(\rho_{\uparrow}, \rho_{\downarrow}, \nabla\rho_{\uparrow}, \nabla\rho_{\downarrow}, \tau_{\uparrow}, \tau_{\downarrow})\mathrm{d}\mathbf{r} \tag{2.52}$$

In equation 2.52 τ is the kinetic energy density which is given by equation 2.53 and is the sum of the Laplacian over all the Kohn-Sham orbitals. The kinetic energy density is used instead of taking the Laplacian of the charge density ($\nabla^2\rho(\mathbf{r})$) because of slow energy convergence [**93**, **94**].

$$\tau(\mathbf{r}) = \frac{1}{2}\sum_{i}^{N} |\nabla^2\phi_i(\mathbf{r})|^2 \tag{2.53}$$

A recently developed meta-GGA functional called the Strongly Constrained and Appropriately Normed semilocal density functional (SCAN) has demonstrated GGA levels of efficiency with excellent accuracy in calculating lattice constants and weakly interacting systems [**95**]. Further refinements of the SCAN functional have been developed such as the SCAN+rVV10 and regularised SCAN (rSCAN), with the SCAN+rVV10 utilised in this work in Appendix A [**96**, **97**].

Finally there are the hybrid functionals which are a mix of Hartree-Fock (exact) and GGA or LDA levels of theory. The motivation behind their conception was the splitting of the

exchange and correlation energies as assumed in the previous sections are not completely representative of the physical picture but a simplification to aid in calculation. A more accurate method would be to calculate the exchange correlation energy 'together' which is what hybrid functionals aim to achieve [**98**].

Some common hybrid functionals include the Becke 3-parameter Lee-Yang-Parr (B3LYP) functional and the Heyd-Scuseria-Ernzerhof (HSE06) functional [**99**, **100**]. The B3LYP function has historically be the most utilised Hybrid functional given the accuracy in calculating molecular systems [**101**]. The HSE06 functional has proven very successful in calculating accurate band gap energies [**102**]. We however do not utilise hybrid functionals in our study due our large systems and the significantly increased computational cost associated with using them. In section 2.5.3.5 we discuss our choice of functional and how we decide on the right accuracy and computational cost trade-off.

2.5.3.4 Dispersion Corrections

One final contribution which neither the exact DFT contribution, nor the exchange-correlation contribution accounts for, is the medium to long range intermolecular dispersion contributions. Dispersion interactions around the medium range interaction region, typically 3-4 Å (should be checked for each system), includes an overlap with the shorter range exchange-correlation interactions [**103**]. Accuracy of dispersion corrections in this region garners the most attention, while long range dispersion interactions converge asymptotically as $1/r^6$.

There are four main classes of dispersion correction, these include the vdW, Parameterised, Dispersion (D/D2/D3) and one electron potential dispersion corrections ($-1e$POT) [**103**]. In this thesis we have utilised the Dx dispersion correction, in particular the D3 dispersion correction with Becke-Johnson damping, D3(BJ) [**31–33**]. The D3 dispersion correction is semi-empirical and takes the general form shown in equation 2.54 and this is added to equation 2.32 as an additional energy contribution after the electronic optimisation is complete (it is not calculated during the self-consistent electronic optimisation cycle). E_2 in equation 2.55 is the two atom dispersion correction [**104**, **105**]. The scaling factor is given by s_i, C_i is the dispersion correction coefficient for atoms A and B, R^i_{AB} is the distance between atoms

A and B, and $F_{\text{damp}}(R^i_{AB})$ is the damping function used to constrain the dispersion function at short-medium ranges. E_3 shown in equation 2.56 is the three atom dispersion correction and includes the same damping function as equation 2.55 [**32**, **106**].

$$E_{\text{disp}} = E_2 + E_3 \tag{2.54}$$

$$E_{\text{disp}} = -\sum_{AB}\sum_{i=2n+6} s_i \frac{C_i}{R^i_{AB}} F_{\text{damp}}(R^i_{AB}) \tag{2.55}$$

$$E_3 = \sum_{ABC} F_{\text{damp}}(R^i_{ABC}) \left(\frac{C_9[3\cos(\theta_A)\cos(\theta_B)\cos(\theta_C) + 1]}{(R_{AB}R_{AC}R_{BC})^3} \right) \tag{2.56}$$

The E_2 dispersion correction includes two terms for $n = 1, 2$ giving the C_6 and C_8 dispersion coefficients as per equation 2.58. The C_6 dispersion coefficient requires the dipole polarizability (from the charge density) averaged in all three directions for each atom pair using the Casimir-Polder formula [**107**]. The C_8 dispersion correction is calculated using $C_8 = 3C_6\sqrt{Q_A Q_B}$, where $Q_{A/B}$ are calculated using empirical factors and the DFT charge density [**108**]. The s_6 factor is set to one while the s_8 factor is depends on the choice of functional and is determined empirically. In equation 2.56 the C_9 dispersion coefficient is approximated as $C_9 = -\sqrt{C_6^{AB} C_6^{BC} C_6^{AC}}$ as opposed to using the Casimir-Polder formula for a three atom system since it accounts for less than 10% is of the dispersion correction [**32**].

Typical damping functions are given in references [**109–111**], but for the work in this thesis the BJ damping function from equation 2.55 is given in equation 2.57 [**33**].

$$F_{\text{damp}}(R^i_{AB}) = \frac{s_i R^i_{AB}}{R^i_{AB} + (a_1 R_0 + a_2)^i} \tag{2.57}$$

In equation 2.57 a_1 and a_2 are fitting parameters while $R_0 = \sqrt{\frac{C_8}{C_6}}$ as approximated from previous work on using higher order dispersion coefficients for post-Hartree-Fock methods [**33**, **112**].

$$
\begin{aligned}
E_{\text{D3}} = &-\sum_{AB}\left(s_6\frac{C_6}{R_{AB}^6}F_{\text{damp}}(R_{AB}^6)+s_8\frac{C_8}{R_{AB}^8}F_{\text{damp}}(R_{AB}^8)\right)\\
&-\sum_{ABC}F_{\text{damp}}(R_{ABC}^i)\left(\frac{C_9[3\cos(\theta_A)\cos(\theta_B)\cos(\theta_C)+1]}{(R_{AB}R_{AC}R_{BC})^3}\right)
\end{aligned}
\tag{2.58}
$$

Therefore, considering equation 2.32, equation 2.44, equation 2.58 we can write our complete electronic energy functional as explicitly as possible which is shown in equation 2.59. E_{C-GGA} is the GGA correlation term, which as discussed in section 1.5.3.2 is determined numerically.

$$
\begin{aligned}
E_0[\rho(\mathbf{r})] = &-\frac{1}{2}\sum_i^N\phi_i\nabla^2\phi_i^*+\frac{1}{2}\iint\frac{\rho_0(\mathbf{r})\rho_0(\mathbf{r}')}{|\mathbf{r}-\mathbf{r}'|}\mathrm{d}\mathbf{r}\mathrm{d}\mathbf{r}'\\
&+\int\rho_0(\mathbf{r})\epsilon_{\text{XC}}[\rho_0(\mathbf{r})]\mathrm{d}\mathbf{r}+\sum_{\uparrow,\downarrow}\int F(S)\rho_0(\mathbf{r})^{\frac{4}{3}}\mathrm{d}\mathbf{r}+E_{C-GGA}\\
&-\int\sum_A^M\frac{Z_A}{|\mathbf{r}-\mathbf{r}_A|}\rho_0(\mathbf{r})\mathrm{d}\mathbf{r}\\
&-\sum_{AB}\left(s_6\frac{C_6}{R_{AB}^6}F_{\text{damp}}(R_{AB}^6)+s_8\frac{C_8}{R_{AB}^8}F_{\text{damp}}(R_{AB}^8)\right)\\
&-\sum_{ABC}F_{\text{damp}}(R_{ABC}^i)\left(\frac{C_9[3\cos(\theta_A)\cos(\theta_B)\cos(\theta_C)+1]}{(R_{AB}R_{AC}R_{BC})^3}\right)
\end{aligned}
\tag{2.59}
$$

For most of the density functional theory calculations in this thesis our ground state electronic energies (E_0) will be calculated using equation 2.59. This means the dispersion correction energy is only included after the electronic states have been optimised (determined $\rho_0(\mathbf{r})$ giving E_0). There will be some variation with the occasional use of different exchange correlation functionals and dispersion corrections. We now have a complete mathematical description of our energies, in section 2.5.4 we consider how it is practically implemented.

2.5.3.5 Choice of Exchange-Correlation Functional

When choosing an exchange-correlation functional the size of the system and properties we are calculating guide our decision. The GGA exchange-correlation functionals have been

found to be a factor of ten faster compared to hybrid functionals [**105**]. DFT calculations of GaAs have shown a HSE06 is slower by a factor of 30 to 100 (depending on the system size) compared to PBE [**113**]. Given the large systems studied in chapters 3, 4 and 5, and the large number of calculations that are required, it is not feasible to use hybrid functionals. We have chosen to use the PBE exchange-correlation functional throughout the present work, which is one of the most commonly used GGA functionals today in conjunction with dispersion corrections as explained below [**30**, **114**].

The PBE exchange-correlation functional used by itself underestimates the interaction energy of weakly adsorbed systems, for example benzene physisorption on an Ag(111) surface is experimentally measured to be -0.63 eV, while using PBE and SCAN (meta-GGA) functionals it is calculated to be -0.07 eV and -0.27 eV, respectively [**115**]. This is because the PBE functional by itself (with out dispersion corrections) does not accurately describe intermediate to long range van der Waals interactions [**103**]. As discussed in section 2.5.3.5 we need to take into account van der Waals contributions. Therefore, we use the D3(BJ) dispersion correction with the PBE functional (PBE+D3(BJ)) [**32**, **33**].

An extensive benchmarking study by Blaha *et al.* was performed for systems of strongly and weakly bound solids ranging from non-metallic, transition metal and rare earth metal solids [**116**]. The PBE+D3(BJ) functional shows almost identical performance to common meta-GGA and hybrid functionals such as PBE0+D3, TPSSh+D3 for lattice constant and cohesive energies. It was also shown to give accurate interlayer spacing and interlayer binding energies for graphite and hexagonal-boron nitride, within 2% and 12% of the benchmark (random phase approximation calculations), respectively. In this case PBE+D3(BJ) outperforms almost all of the meta-GGA and hybrid functionals which also include the D3 dispersion correction. Grimme *et al.* showed that for weak interactions the difference between PBE+D3 and the best performing functional (B2PLYP) was only 0.02 eV [**32**]. This is backed up by a more recent study by Pettersson *et al.* who showed PBE+D3 had similar MAE values for physisorption and chemisorption, within 0.03 eV and 0.13 eV, respectively, compared to the SCAN (meta-GGA) functional which captures intermediate van der Waals interactions [**117**, **118**]. This shows PBE+D3 is a sound choice of functional for solids and two dimensional layered materials.

In this thesis we investigate cobalt-porphyrin and cobalt-phthalocyanine (see figure 1.1) systems. DFT and/or coupled cluster singles and doubles theory (CCSD(T)) benchmark studies of these exact systems do not seem to have been reported as of the writing of this thesis. However, DFT benchmarking of experimentally studied metal-organic frameworks including $Co_2C_8N_{12}$ have been reported by Sholl *et al.* and Truhlar *et al.* [**119**, **120**]. Sholl benchmarked against other GGA functionals (PBE, PW91, PBE+D2, PBE+D3 and more) and found that PBE+D3 showed an improvement of around 70% for bond length and bond angle, while the partial (atomic) charges showed less significant differences between functionals. Truhlar found that PBE+D3 bond lengths were on average < 0.02Å compared to all the meta-GGA functionals and gave the most accurate bond angles to within 1^{o}. Therefore, PBE+D3/D3(BJ) are found to accurately describe the structural parameters of metal-organic systems.

A recent study by Nava *et al.* investigated spin state energy difference for various metal-organic cobalt systems (e.g. CpCo(C_4H_4) and CpCo(C_6H_8)) in singlet and triplet states using hybrid (TPSSh+D3, PBE0+D3, B3LYP+D3), meta-GGA and GGA functionals benchmarked against CCSD(T) calculations [**121**]. Spin difference values for the PBE+D3 along with other GGA and meta-GGA functionals were closer to the benchmark CCSD(T) values compared to the hybrid functionals investigated. All GGA and meta-GGA spin differences where within 0.04 eV of each other and within 0.15 eV of the CCSD(T) benchmark. The best performing hybrid functional (TPSSh+D3) was within 0.2 eV of the CCSD(T) benchmark and on average the hybrid functionals were within 0.5 eV of the benchmark. This means we expect the PBE+D3 functional to give relatively accurate spin states for our cobalt-porphyrin and cobalt-phthalocyanine systems.

Lastly, a recent study by Lytken *et al.* benchmarked the experimentally determined adsorption energies of MgTPP, ZnTPP and CoTPP on MgO(100) as compared to DFT adsorption energies calculated using the PBE functional with a modified D3 dispersion correction [**122–124**]. The difference between the calculated and experimental benchmark adsorption energies of MgTPP, ZnTPP and CoTPP is 0.08 eV, 0.23 eV and 0.12 eV, respectively. The calculated and experimental adsorption energies also showed the same trend with MgTPP having the largest

adsorption energy while ZnTPP and CoTPP had similar adsorption energies. The calculated adsorption energies are close to the experimental values demonstrating PBE+D3 can be used to reliably determine adsorption energies.

2.5.4 Implementation of Density Functional Theory

In our work we use the Vienna *Ab initio* Simulation Package (VASP) DFT code. VASP is a periodic boundary condition code meaning our systems which are contained in a supercell are repeated in all three directions. This allows us to efficiently simulate semi-infinite and infinite systems such as surfaces and bulk materials, and also isolated structures such as clusters and molecules in gas-phase, provided the supercell includes a large enough vacuum region. One then uses Bloch's theorem to solve the Schrödinger for these periodic systems [**125**].

2.5.4.1 Bloch's Theorem

For a lattice with a periodic pattern all the information required to periodically construct a solid is contained in the primitive unit cell. We can define a conventional unit cell, which unlike the primitive unit cell, is not necessarily an irreducible representation of the lattice in real space, but is easier to work with (e.g. may have orthogonal unit vectors). As mentioned periodic boundary DFT codes take a supercell to define the system geometry. In terms of size we have the primitive unit cell $\leq$ conventional unit cell $\leq$ supercell, where the 'supercell' can simply be the unit cell, but more often than not, it is taken to be much larger such that defect, doping, adsorption of atoms or other molecules, or other properties can be studied. However, periodic DFT codes use reciprocal space this means the primitive unit cell defined in real space becomes the Brillouin zone in reciprocal space.

Bloch's theorem uses the symmetry of a periodic lattice and thus the periodic nature of its potential to define the electron plane wave basis functions who's behaviour is consistent with the lattice periodicity [**125**]. If we consider the one dimensional periodic lattice shown in figure 2.2 the potential at 0 is the same as the potential at a, or $V(x) = V(x + a)$ where x can be taken as any position between $-\frac{1}{2}a$ and $\frac{1}{2}a$ (the first primitive unit cell). Then we

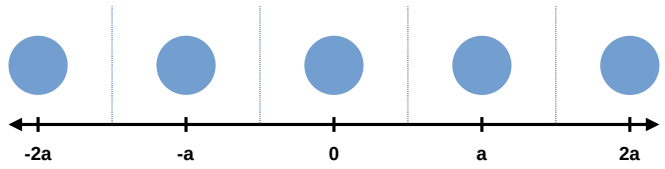

FIGURE 2.2. Illustration of periodic boundary conditions for a one dimensional lattice. Primitive unit cell boundaries are indicated by the vertical dashed lines.

can describe our electron basis functions as plane waves in the form $\psi(x) = e^{ikx}$ in the first primitive unit cell, $\psi(x+a) = e^{ika}\psi(x)$ in the second primitive unit cell and for the N^{th} primitive unit cell we have equation 2.60.

$$\psi(x+Na) = (e^{ika})^N \psi(x) \tag{2.60}$$

Equation 2.60 is a general form of Bloch's theorem. However, if we rearrange equation 2.60 and multiply both sides by e^{-ikx} we get equation 2.61.

$$u(x) = e^{-ikx}\psi(x) = e^{-ikx}e^{-ikNa}\psi(x+Na) = e^{-ik(x+Na)}\psi(x+Na) \tag{2.61}$$

Equation 2.61 is clearly periodic for any value integer value of N such that $u(x) = u(x+Na)$. Therefore, we can write the general form of the one dimensional Bloch theorem as equation 2.62.

$$\psi(x) = e^{ikx}u(x) \tag{2.62}$$

We can extend equation 2.62 into three dimensions, as per equation 2.63, by replacing x with a three dimensional position vector $\mathbf{r}$ in real space and $\mathbf{k} = m_1\mathbf{b_1} + m_2\mathbf{b_2} + m_3\mathbf{b_3}$ is the position vector in reciprocal space where m_j are integers and $\mathbf{b_j}$ are the reciprocal lattice vectors.

$$\psi(\mathbf{r}) = e^{i\mathbf{kr}}u(\mathbf{r}) \tag{2.63}$$

Since electrons can occupy multiple energy bands for each $\mathbf{k}$ vector we can write equation 2.63 as a linear combination of n plane wave basis functions. We also know that a periodic function can be expressed as a Fourier series which means $u_{n\mathbf{k}}(\mathbf{r}) = \sum_{\mathbf{G}} C_{n\mathbf{k}} e^{i\mathbf{Gr}}$, where $C_{n\mathbf{k}}$ are the Fourier coefficients and $\mathbf{G}$ is a reciprocal lattice vector. Typically, $\mathbf{k}$ is taken to be in the first Brillouin zone (in reciprocal space and is analogous to the first primitive unit cell in real space) while $\mathbf{G}$ differs from $\mathbf{k}$ by an integer multiple of the lattice constant. Substituting into equation 2.63 we get an expression for Bloch's theorem as a linear combination of plane wave basis functions, shown in equation 2.64 [**126**].

$$\psi_{n\mathbf{k}}(\mathbf{r}) = e^{i\mathbf{kr}}u_{n\mathbf{k}}(\mathbf{r}) = \sum_{\mathbf{G}} C_{n\mathbf{k}+\mathbf{G}} e^{i(\mathbf{k}+\mathbf{G})\mathbf{r}} \tag{2.64}$$

If we invoke the Born-von Karman boundary conditions which states that plane wave basis functions remains unchanged for N translations of the lattice, $\psi_{n\mathbf{k}}(\mathbf{r}) = \psi_{n\mathbf{k}}(\mathbf{r} + N_i\mathbf{a}_i)$ [**126**]. Here N_i are integer multiples of $\mathbf{a}_i$ indicating N_i primitive cells in the $\mathbf{a}_i$ direction, where $\mathbf{a}_i$ are primitive lattice vectors with $i = 1, 2, 3$ for all three directions. Taking the relation from equation 2.60 and extending it to three dimensions we have $\psi(\mathbf{r} + N_i\mathbf{a}_i) = e^{i\mathbf{k}N_i\mathbf{a}_i}\psi(\mathbf{r})$, following the Born-von Karman boundary conditions we must have equation 2.65.

$$e^{i\mathbf{k}N_i\mathbf{a}_i} = e^{2\pi i N_i m_i} = 1 \tag{2.65}$$

From equation 2.65 m_i is the integer multiple of the reciprocal lattice vector $\mathbf{b}_i$ and we have $m_i = \frac{l_i}{N_i}$ since any integer choice for l_i gives $e^{2\pi i l_i} = 1$. Now $\mathbf{k}$ is restricted to the first Brillouin zone and is given by equation 2.66.

$$\mathbf{k} = \sum_{i=1}^{3} \frac{l_i}{N_i}\mathbf{b}_i \tag{2.66}$$

Equation 2.66 shows that when we take $N_i \longrightarrow \infty$ for an infinite lattice in all three dimensions we still have a countably infinite number of $\mathbf{k}$. However, we can not calculate an infinite number of plane wave basis functions so we choose a discrete number of sampling points in reciprocal space called 'k-points' [**127**]. In this thesis we deal with large supercells which transform into a small Brillouin zones in reciprocal space given the volume relation $V_{\text{BZ}} = \frac{2\pi}{V_{cell}}$, where V_{BZ} and V_{cell} are the Brillouin zone and supercell volumes, respectively. Therefore, we only choose the Γ point which is located at the centre of the Brillouin zone a point of high symmetry, where $\mathbf{k} = 0$. The calculations in this thesis are conducted in large supercells in real space meaning they are transformed into very small volumes in reciprocal space making sampling only at the Γ point adequate for capturing the electronic properties of the system.

Finally we need to limit the range of the $\mathbf{G}$ vectors, otherwise equation 2.64 will be an infinite Fourier sum over $\mathbf{G}$. This is achieved by defining a kinetic energy cutoff for the plane wave basis functions. We know $|\mathbf{k} + \mathbf{G}|$ is the plane wave momentum so the electron plane wave kinetic energy cutoff can be defined by equation 2.67. Therefore, only plane wave basis functions with kinetic energies less than E_{cut} are considered meaning equation 2.64 is now a finite Fourier sum within the range of $\mathbf{G} = 0$ to $\mathbf{G} = \mathbf{G}_{\text{max}}$.

$$E_{\text{cut}} = \frac{\hbar}{2m_e}|\mathbf{k} + \mathbf{G}_{\text{max}}|^2 \tag{2.67}$$

If $|\psi(\mathbf{r})|^2$ is periodic then so is the charge density $\rho(\mathbf{r})$. For DFT calculations all that happens is the charge density is Fourier transformed from real space to reciprocal space such that the periodic behaviour of the plane wave basis functions is consistent with that of real space. This Fourier transform is conducted over a discrete number of plane wave basis functions controlled by our choice of 'k-point' sampling and energy cutoff range.

2.5.4.2 PAW Pseudopotentials and VASP

Here we arrive at the final piece of the DFT implementation. We have been treating all electrons the same until this point but not all electrons contribute equally to bonding and interactions between atoms. These all electron potentials can be used but they are computationally expensive especially for systems involving large atoms. This is where pseudopotentials come in, they improve the computational efficiency by approximating the net electrostatic contribution for the nucleus and the region of electrons close to the nucleus [**128**]. The region containing those core electrons is called the augmentation region [**129**]. This means the core electrons (H and Li excepted) are taken to be frozen and are pre-calculated as part of the pseudopotential. A high density of plane wave basis functions in reciprocal space are needed to accurately resolve features close to the atomic core in real space requiring computationally more expensive to do fast Fourier transforms (FFTs) [**129**].

This method can be clearly defined in terms of the total charge density as shown in equation 2.68 [**128**].

$$n_{\text{total}} = n_{\text{v}} + n_{\text{c}} + n_{\text{Z}} \tag{2.68}$$

In equation 2.68 n_{v} is the charge density of the valence electrons outside the augmentation region. n_{c} is the net charge density of the frozen core electrons and is therefore the same inside and outside the augmentation region. n_{Z} is the point charge densities of the atomic nucleus. The PAW pseudopotential method can be thought of as another layer of approximation on top of those already fundamental to DFT and required for the exchange correlation functionals.

As mentioned at the start of this section all DFT calculations are conducted using VASP which uses PAW pseudopotentials. This means the orbitals we are calculating are not the exact KS orbitals but psuedo-orbitals under the PAW approximation. A screening study on the total energy errors associated with the PAW approximation found a maximum error of only 0.4 meV, well with the chemical accuracy region of 0.04 eV [**130**].

We now know how to calculate the total electronic ground state energy of our system in equation 2.59, shown how to calculate our system for a finite number of plane wave basis functions and efficiently handle core electrons. Now we can describe the DFT calculation procedure followed by VASP. We start by choosing a trial plane wave basis functions $\psi_{\text{initial/in}}(\mathbf{r})$ and charge density $\rho_{\text{initial/in}}(\mathbf{r})$. These are used to set up an initial Hamiltonian and effective potential using equation 2.34 and equation 2.35, respectively. Then the plane wave basis functions ψ_n are iteratively optimised via matrix diagonalisation of the Hamiltonian applied to each plane wave basis function for each state n. Once we have optimised ψ_n we get a new $\rho_{\text{out}}(\mathbf{r}) = |\psi_n|^2$ which we can use to calculate the total energy in equation 2.59 (excluding the dispersion terms for now) and the electron occupancies for each band n. Then total energy convergence is checked, if convergence is not satisfied a new $\rho_{\text{in}}(r)$ is calculated by combining $\rho_{\text{initial}}(r)$ and $\rho_{\text{out}}(r)$ restarting the calculation cycle.

Once we have optimised our electronic states such that they meet the total energy convergence we include the dispersion correction contribution from equation 2.58 and the atomic positions are optimised. We discuss the geometry optimisation process in the next section.

2.5.4.3 Geometry Optimisation

Up until now we have only considered the electronic optimisation which assumes the atomic cores are fixed which is the case since electronic optimisation precedes any geometry optimisation steps. As discussed before it is due to electron interactions occurring much faster than ionic interactions (see section 1.5.3.1). The geometry optimisation steps attempt to minimise the forces between ions by finding the position where the ions are in an electronic potential energy minimum. The forces on the ions are calculated using the Hellman-Feynman theorem which calculates the force by calculation of the energy gradient [**131**]. The Hellman-Feynman theorem in terms of charge density is given by equation 2.69 which includes the electron-nucleus and nucleus-nucleus terms (only electrostatic forces) first introduced at the start of this chapter in equation 2.7.

$$F_{X_i} = \frac{\partial E}{\partial X_i} = \int \rho(\mathbf{r}) \frac{Z_i(x - X_i)}{|\mathbf{r} - \mathbf{R}_i|^3} \mathrm{d}\mathbf{r} - \sum_{i,j} \frac{Z_i Z_j (X_j - X_i)}{|\mathbf{R}_j - \mathbf{R}_i|^3} \tag{2.69}$$

Equation 2.69 is given for forces in the x-direction as an example, but this equation is true for forces in the x, y and z directions. **r** refers to the location of electrons (x is the x-component of **r**) while **R** refers to location of nuclei. The variables X_i and X_j are the x coordinates of the i^{th} and j^{th} nuclei. Z_i and Z_j are charge of the i^{th} and j^{th} nucleus.

Using equation 2.69 to calculate the forces in the electronic ground state, there are two primary algorithms implemented in VASP that search for the ionic potential minimums. These are the gradient descent algorithm (using Newtons method) and the conjugate gradient algorithm [**132**]. The gradient descent algorithm looks for the direction of steepest decline and will move the ions in that direction with the movement distance based on a user defined step size. The conjugate gradient algorithm is a bit more complex but is more reliable for larger complex systems. The conjugate gradient algorithm differs in that it has an inner loop that automatically adjusts the step size, which helps to reduce the number of ionic movement iterations.

Now we have an understanding of how DFT is able to efficiently calculate the energies, approximate orbitals and relax the geometries of many atom systems. In the next chapters these methods are applied to investigate molecular and surface interface catalytic systems used in CO_2 electroreduction.

CHAPTER 3

Calculating Entropies of Large Molecules in Aqueous Phase

Entropy benchmarking of different sized molecules in aqueous phase is carried out for known solvation models where we compare geometry and solvation cavity packing parameters which allows us to improve the accuracy of the obtained entropy values using empirical corrections. A comparison of solvation entropy models is conducted for a benchmarking set of 56 molecules, showing how an accurate description of cavitation entropy and its hindrance on other entropy values is important for large sized solute molecules. Finally, we compare reaction free energies with entropies calculated using the most accurate solvation model considered, where we demonstrate a significant improvement in the accuracy relative to experimental values.

3.1 Introduction

Accurate calculation of entropy is necessary for reliable determination of reaction free-energy pathways. Reaction entropies can provide a sizable contribution to reaction free energy values in aqueous solutions [**133**], this has been shown to be of particular importance for homogeneous O_2 reduction catalysis [**134**, **135**] (one can envisage this being extended to other reduction systems such as catalytic CO_2 reduction). Although for reactions involving enzymes, entropies have been shown to be overestimated [**136**,**137**]. The method of Ref. [**136**] has been used in many studies in the literature including the evaluation of binding entropy of protein-ligand complexes which found entropy contribution to be small, suggesting entropy may not be significant for determining the binding free energies for some or most enzyme reactions [**137**]. Benchmarking of solvation entropy models is usually limited to small -

medium sized molecules, while large molecules are not considered due to tedious calculations of certain properties such as moments of inertia, Van der Waals (vdW) volumes and the solvation-solute packing factor (the ratio of the number of solvent molecules that coordinate around the solute and solvent molecule) [**47**, **138**, **139**]. We categorise the molecules into small (2-9 atoms), medium (10-19 atoms) and large (20 atoms or more).

Values of solvation entropies within chemical accuracy (< 1 kcal/mol or < 0.043 eV) has been demonstrated using molecular dynamics (MD) calculations with various solvation models [**35**–**41**]. MD calculations are computationally expensive and require multiple runs in order to obtain accurate statistical averages of system properties such as entropy and free energy. Accurate solvation-dependent empirical corrections between established solvation-phase entropy models and experiment have not been reported to the best of our knowledge. However, scaling of calculated gas-phase entropies by factors of around 0.5 have been adopted [**43**,**44**], as well as approaches that consider only the vibrational entropy (translational and rotational entropies are excluded) [**45**, **46**] to predict the entropy loss from the gas-phase to solvation-phase. The methods used in references: [**43**–**46**] albeit convenient, do not provide a physically accurate description of molecular entropy in aqueous medium.

Attempts have been made to create models that approximate entropies of solute/solvent systems by including a cavity entropy term which accounts for rotational and translational entropy hindrance of the solute molecule inside the solvent cavity and the formation entropy of the solvent cavity itself. The solvent cavity is a space within the solvent medium which is occupied by the solute molecule and is not accessible to any solvent molecule. Early studies that involve entropy and free energy calculations involving solvent cavities include the works of Tomasi and co-workers [**140**], Barone and co-workers [**141**] and Rauk and co-workers [**142**]. The latter of whom focus on entropic contributions and the cavity entropy term was determined using an isodensity surface of the solute molecule along with enthalpy (H) and free energy (G) equations from Pierotti's study of SPT for aqueous and non-aqueous solutions [**143**]. Two approaches to calculating solvation cavity entropies have been recently proposed by Garza [**47**] utilising the statistical mechanics of rigid spheres [**144**] with the Pitzer Acentric Factor (ω) which relates molecular polarity and shape to non-ideal behaviour,

while the second method is based on scaled particle theory (SPT) similar to Rauk and co-workers [**142**] but relates the density of the solvent to its relative permittivity and isobaric thermal expansion coefficient. A detailed explanation of these methods are given in the method section.

Another approach has used the Langevin dipole (LD) model [**49**, **50**] which was developed in 1976 for the study of enzyme reactions in water [**145**] and was built upon in subsequent studies [**146**–**148**], although this method is not limited to enzyme applications. The LD model generates a dipole grid around the solute molecule and calculates the electrostatic interaction between this grid and the solute polarisation (determined by point charges at the atomic nuclei), a dielectric continuum for bulk contribution of the solvent is also included. This method has been implemented in a program called ChemSol version 2.1 [**49**–**51**] which is popular in the biochemical field and has been employed in recent studies [**149**, **150**]. A similar electrostatic solvation model by Marenich et al uses dielectric medium for the solvent while the solute molecules are defined using the complete electron density (no partial charges) and surface tension at its boundary [**151**].

In this study we investigate methods of calculating entropy when extending entropy models to large solute molecule systems with a focus on Garza's most recent solvation model [**47**]. We show how solute-solvent packing varies with molecular size and geometry, i.e. packing of water molecules around the cavity structure of the solute molecule which can be optimally defined for individual molecules. The behaviour of the entropy model is studied for the large molecule regime with a focus on model limitations and error sources. These include methods for calculating the van der Waals volumes of molecules and the previously mentioned packing factors. The entropy models are applied to the catalytic reduction reaction of CO_2 involving the large cobalt centred porphyrin (CoP) and the cobalt-centred tetraphenylporphyrin (CoTPP) catalyst molecules. Molecule geometries and vibrational frequencies are determined by density functional theory (DFT) calculations.

3.2 Method

The density functional theory (DFT) calculations are performed using the Vienna Ab initio Software Package (VASP) version 5.4.4 [**28**, **29**]. All calculations are carried out including spin-polarisation, using the generalised gradient approximation (GGA) of Perdew, Burke and Ernzerhof (PBE) for the exchange-correlation functional [**30**] from default pseudo-potentials. We include dispersion corrections using Becke-Johnson damping (D3(BJ)) [**31**–**33**] and a polarised continuum model (PCM) to include the effect of implicit water is implemented in the VASPSol extension [**152**, **153**]. The energy cut-off is 500 eV which was determined by convergence tests of the cobalt formation energy in porphyrin (see figure A1 in appendix A). The **k**-point sampling is the Γ point and a large supercell size of $30 \times 33 \times 35$ $\mathring{\text{A}}^3$ is used which is more than sufficient to eliminate interactions between supercells (see figure A2 in appendix A). The atomic positions are relaxed until the forces on all atoms are less than 0.01 eV/$\mathring{\text{A}}$, with the electronic convergence criterion set to 10^{-6} eV. The Methfessel-Paxton scheme for Fermi level smearing is used for systems involving metal ions; otherwise Gaussian smearing is used. Vibrational frequencies are calculated for three degrees of freedom with initial displacements set to 0.015 $\mathring{\text{A}}$. Entropies calculated using the ChemSol program (version 2.1) require atomic charge input; the Voronoi Deformation Density (VDD) method [**154**–**156**] is used for the charge densities calculated in VASP to determine atomic charge values.

The change in reaction free energy (ΔG) [**34**] is given in equation 3.1.

$$\Delta G = \Delta E + \Delta E_{\text{ZPE}} - T\Delta S + neU + \Delta G_{\text{pH}} \tag{3.1}$$

In equation 3.1, ΔE is the reaction energy or the energy difference between the adsorbed and isolated intermediates (similarly used to define adsorption energy in the application section). The term ΔE_{ZPE} is the change in the calculated zero point energy (ZPE) from DFT vibration calculations between the adsorbed and isolated intermediates and ΔS is the change in entropy between the adsorbed and isolated molecules. The number of electrons transferred to the system is given by n, e is the charge of an electron and U is the applied electrode potential.

This gives the effect of a bias potential due to the electron transferred from the electrode. We have $\Delta G_{\text{pH}} = k_{\text{B}}T\ln(10\text{pH})$ where k_{B} is the Boltzmann constant, T is the temperature in Kelvin and pH is the pH number of the system; this term corrects for the concentration dependence of H^+ ions on entropy. In this study we only consider the neutral pH system, or pH = 7, which means for all our free energy calculations in the application section we have $\Delta G_{\text{pH}} = 0.11$ eV.

The ZPE (E_{ZPE}) is the energy of all atomic vibrations of the system at a temperature of 0 K and is calculated using DFT and is given in equation 3.2.

$$E_{\text{ZPE}} = \frac{1}{2}\sum_i h\nu_i \tag{3.2}$$

Equation 3.2 sums the energy of each vibrational mode i, where ν_i is the vibrational frequency and h is Planck's constant. The term E_{ZPE} is the ZPE of a single system, while ΔE_{ZPE} is the ZPE energy difference between the reactants and products.

3.2.1 Gas-phase Entropy

For the free-energy calculations we take into account all entropic contributions of a single system within the harmonic approximation (HA) and assume an ideal gas [**157**].

$$S = S_{\text{elec}} + S_{\text{tran}} + S_{\text{rot}} + S_{\text{vib}} \tag{3.3}$$

In equation 3.3, S_{elec}, S_{tran}, S_{rot} and S_{vib} are the electronic, translational, rotational and vibrational entropies. Each of these terms can be described using partition functions which are based on spin multiplicity, molecular mass, principal moment of inertia, vibrational frequency and temperature [**157**]. The entropy terms are given in equations 3.4 - 3.8.

$$S_{\text{elec}} = R\ln(\gamma) \tag{3.4}$$

$$S_{\text{tran}} = R\left(\ln\left[\left(\frac{2\pi m k_B T}{h^2}\right)^{\frac{3}{2}} V\right] + \frac{5}{2}\right) \tag{3.5}$$

$$S_{\text{rot-linear}} = R\left(\ln\left[\frac{8\pi^2 I k_B T}{h^2 \sigma_r}\right] + 1\right) \tag{3.6}$$

$$S_{\text{rot-nonlinear}} = R\ln\left[\frac{\pi^2}{\sigma_r}\prod_j^n \left(\frac{8\pi^2 I_i k_B T}{h^2}\right)^{\frac{1}{2}}\right] + \frac{3}{2}R \tag{3.7}$$

$$S_{\text{vib}} = R\sum_i \left(\frac{h\nu_i}{k_B T(e^{h\nu_i/k_B T} - 1)} - \ln\left[1 - e^{-h\nu_i/k_B T}\right]\right) \tag{3.8}$$

In equation 3.4, γ is the spin multiplicity of the system at 0 K. In equation 3.5, m is the mass of the molecule and V is the volume of the 'container' which we can define as $V = k_B T/P$ where P is the pressure, taken to be 1 atm (1.01×10^5 Pa). In equation 3.6 and 3.7, I is the principal moment of inertia and σ_r is the rotational symmetry number of the system which is the number of indistinguishable rotations of a molecule's symmetry or the number of rotational symmetry operations [**158**]. This symmetry relation holds for $T > 0$ K since the 'topology' of the molecule is preserved even under thermal agitation [**159**]. In equation 3.8, ν_i is the frequency of the i^{th} normal mode and in equation 3.7 n is the number of independent axes of rotation. In all the equations mentioned R is the ideal gas constant.

3.2.1.1 Moment of Inertia

The moment of inertia (*I*) for linear molecules is determined by:

$$I = \sum_i m_i r_i^2 \tag{3.9}$$

where m_i is the atomic mass and r_i is the distance of the i^{th} atom from the centre of mass. The centre of mass is calculated for isolated solute molecules in gas phase. Linear molecules are described by a single rotational constant so *I* is a singular value. However, non-linear molecules such as asymmetric rotors have two or three rotational constants, thus *I* will have

two or three principal values. An example of how rotational entropy scales with moments of inertia for linear and nonlinear molecules is shown in figure 3.1. We expect that the moment of inertia will not be less than 10^{-48} kg m^2 for any molecule as shown for H_2. For larger molecules, such as lactose and sucrose which have 45 atoms, we can expect a moment of inertia between 10^{-44} to 10^{-42} kg m^2.

We also observe an order of magnitude difference in rotational entropy when comparing small and large molecules such as H_2 to CO_2 and CO_2 to lactose.

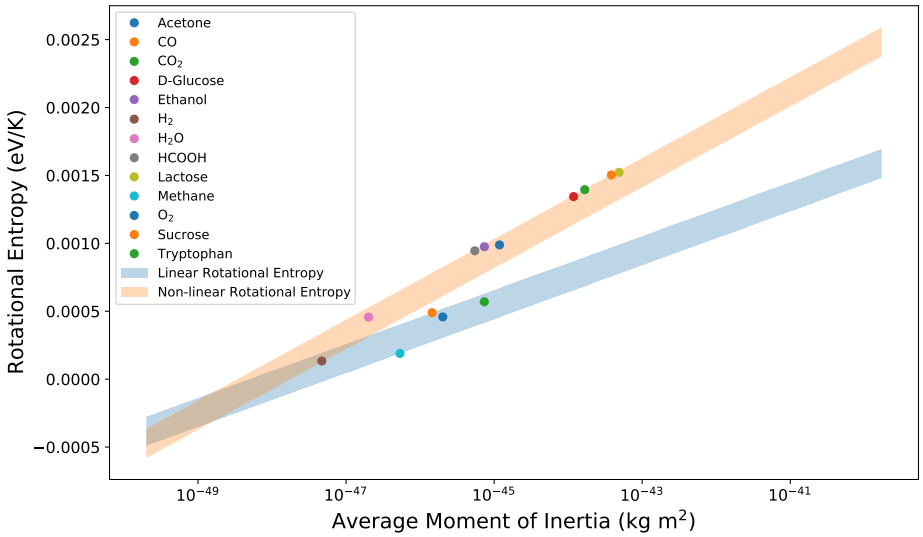

FIGURE 3.1. Calculated rotational entropy for a subset of molecules investigated in this study versus *I* for linear (blue region) and non-linear (orange region) molecules. The regions are bounded by the entropy lines for symmetry numbers (σ_r) ranging between 1 to 12.

3.2.1.2 Vibrational Entropy Damping

For low-frequency modes the HA method (see equation 3.8) fails to properly describe S_{vib} for low values because as $\nu \longrightarrow 0$, $S_{\text{vib}} \longrightarrow \infty$. A method to address low frequency modes has been proposed by Grimme [**160**] which includes a damping term $w(\nu)$ and combines vibrational, and a redefined rotational, entropy term.

$$S = w(\nu)S_{\text{vib}} + (1 - w(\nu))S_{\text{rot}} \tag{3.10}$$

$$w(\nu) = \frac{1}{1 + (\nu_0/\nu)^\alpha} \tag{3.11}$$

Equation 3.10 is the corrected entropy term described by Grimme [**160**] and equation 3.11 is the Head-Gordon damping equation [**161**] used by Grimme. The low-frequency reference value is ν_0, and is usually set within the limits of 50-150 cm^{-1} (we set it to 100 cm^{-1} in this study), while $\alpha = 4$ is the usual value for this parameter which is an exponent governing the rate of damping [**160**]. The damping method by Grimme interpolates between the harmonic oscillator and free rotor entropy depending on the value given for ν_0. The free rotor entropy can be used to describe vibrations where the barrier to rotation is thermodynamically favourable (less than $k_B T$).

The redefined rotational entropy for low-frequency modes is given in equation 3.12.

$$S_{\text{rot}} = R \left[\frac{1}{2} + \ln \left[\left(\frac{8\pi^3 \mu' k_{\text{B}} T}{h^2} \right)^{1/2} \right] \right] \tag{3.12}$$

$$\mu' = \frac{\mu I_{\text{avg}}}{\mu + I_{\text{avg}}} \tag{3.13}$$

$$\mu = \frac{h}{8\pi^2 \nu} \tag{3.14}$$

Equation 3.13 is the reduced moment of inertia with I_{avg} being the average molecular moment of inertia calculated via the Parallel Axis theorem and μ is the moment of inertia for a free rotor with frequency ν as shown in equation 3.14. A comparison of vibrational entropy with frequency cut-off value ν_0 ranging between 50-350 cm^{-1} is shown in figure 3.2 for the example of the sucrose molecule (when $\nu_0 = 0$ there is no damping so equation 3.10 becomes equation 3.8).

In addition to using the low frequency damping model we also cutoff frequencies less than 100 cm^{-1} similar to that used by Truhlar and co-workers [**139**,**162**]. We expect larger molecules to

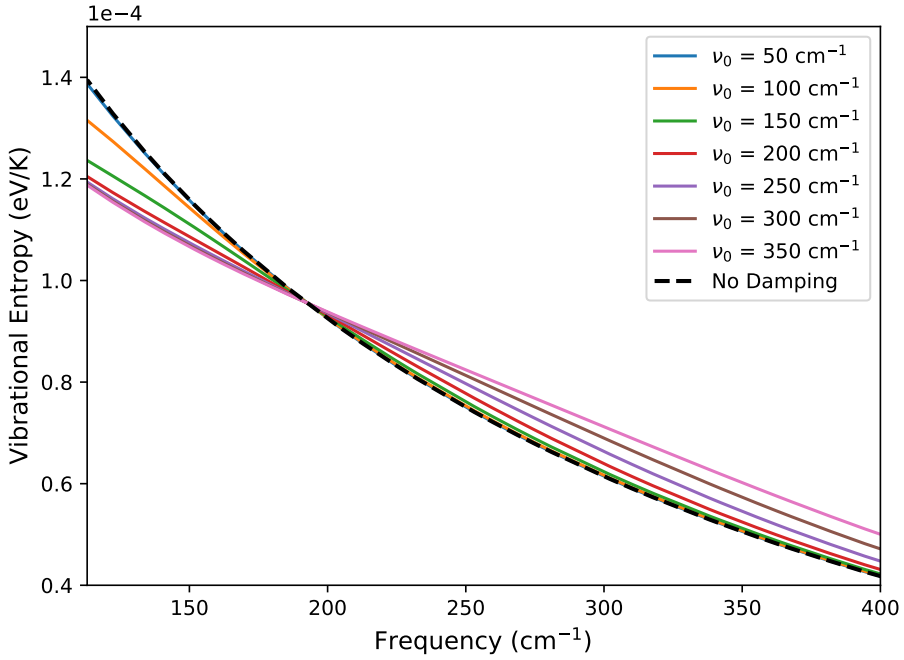

FIGURE 3.2. Vibrational entropy of a sucrose molecule as a function of frequency for several values of the low frequency cut-off (ν_0). This is based on the low frequency damping method by Grimme [**160**].

benefit from the vibrational damping model as they are more likely to have lower frequencies around 100 cm^{-1}.

An alternative to the method just described is the hindered rotor method [**163–165**] which in principle provides a more accurate description but would be too computationally expensive.

3.2.2 Solvation-Phase Entropy

Vibrational modes calculated using DFT in gas-phase or solvation-phase are expected to give qualitatively similar results [**139**]. Therefore, in this study we calculated vibrational modes based on the gas-phase geometries. As described in the introduction, until recently, methods for calculating entropy for solvation systems relied on scaling factors, excluding translational and rotational entropy contributions, or have been limited to continuum solvation models which are parameterised against experimental free energy results [**43–46**, **136**, **142**]. The method by Garza [**47**] utilises known values of the acentric factor (ω) and relative permittivity

(ϵ_0) constants, this method is summarised in the subsequent acentric factor and scaled particle theory sections.

Calculation of the molecular volumes is carried out using consistently determined van der Waals radii [**166**] and methods based on tables of pre-determined volume contributions for common molecular group elements [**167**], statistically determined corrections [**168**], the accurate flood-fill algorithm freely available in the *Protein Volume* program [**169**] and by determining the convex hull of a molecule. The statistically corrected van der Waals volume [**168**] is calculated using equation 3.15.

$$V_{\text{vdW}} = \left(\sum V_{\text{atom}}\right) - 5.92N - 14.7R_{\text{A}} - 3.8R_{\text{NA}} \tag{3.15}$$

Where V_{atom} is the atomic van der Waals volume, $N = N_{\text{atom}} - 1 + R_{\text{A}} + R_{\text{NA}}$, where N_{atom} is the number of atoms making up the molecule, R_{A} is the number of aromatic rings in the molecule and R_{NA} is the number of non-aromatic rings in the molecule. The coefficients (volume elements) out the front of the N, R_{A} and R_{NA} terms have units of Å^3. The correction terms in equation 3.15 (the terms outside the summation) are statistically determined volume corrections which attempt to correct for overlap between van der Waals spherical volumes between bonded atoms in a molecule. This method of calculating van der Waals volumes provides a generalised description easily applied to any molecule, in particular large molecules. However, this method differs from the one used in the solvation entropy model by Garza [**47**], who used the method of Bondi [**167**] which relies on tables of pre-calculated volumes of common molecular group elements, but some large molecules have bond configurations which are not accounted for in Bondi's volume tables.

Both generalised and accurate, the *Protein Volume* program (using the flood-fill algorithm) [**169**] provides accurate van der Waals volumes for small to large molecules alike, with calculation resolution down to 0.02 Å. The flood fill algorithm uses two types of probe, a solvation probe is used to determine the accessibility of voids and cavities in the solute molecule to the solvent molecules, while volume probes of size 0.02Å fill the area of the solute molecule traced out by the solvent probe which are then summed up to give the volume

of the solute molecule. This method calculates the volume of the molecular surface available to a solvent molecule, which is analogous to the Solvent Excluded Surface (SES) [**170**] by inclusion of void regions within the molecules not accessible by the solvent. A comparison of these methods is given in the benchmarking entropies subsection of the results and discussion section with an analysis of errors for small, medium, and large molecules.

In this study, the standard state concentration for solutes in aqueous solution (mixtures) is 1 mol/L. It must be assumed that the mixing of solutes in solution is dilute to minimise the chance of solute-solute interactions. For example, pure concentrated/bulk water has a concentration of around 55.5 mol/L, so mixing with the standard solute molecule concentration would means 55.5 mol's of water molecules for each mol of solute molecule per unit volume.

Changes in entropy due to changes in concentration can be calculated using equation 3.16.

$$\Delta S_{\text{con}} = k\ln(C_{\text{i}}/C_{\text{f}}) \tag{3.16}$$

In equation 3.16 C_{i} is the concentration of the initial state and C_{f} is the concentration of the final state. Therefore, solvation entropies can be adjusted for bringing 1 M of molecules from standard state gas phase to standard state solvation phase. Using the ideal gas equation with the standard states we get $V_{\text{gas}} = 24.5$ L, then the initial and final concentrations are $C_{\text{i}} = 1/24.5$ mol/L and $C_{\text{f}} = 1$ mol/L respectively, which gives $T\Delta S_{\text{con}} = -0.08$ eV at a temperature of 298.15 K.

Given the standard gas-phase entropy, standard solvation-phase entropy, and concentration entropy it's easy to calculate the solvation entropy [**171**]. In this study, focus is given to the accurate calculation of absolute standard state entropy values and reaction entropies and free energies.

Conformational Entropy: Conformational (or configurational) entropy accounts for the number of different structural minima for which a molecule may exist. Differences in conformers may include bond rotations or changes in dihedral angles, but calculations of conformers usually involve molecular dynamics (MD) calculations which are not conducted in this study. However, it should be mentioned that conformation entropy can provide a non-negligible

contribution to total entropy particularly for large flexible molecules [**172**, **173**]. When going from gas-phase to solvation-phase the dominant conformer structure can change, this has been shown to result in errors of free energy values up to 0.085 eV [**172**].

A recent method by Pracht & Grimme has improved the efficiency and automation for calculating configurational entropy in both gas-phase and solvation-phase by combining DFT calculations to determine the lowest energy conformer and force-field (or semi-empirical quantum mechanics) calculations to determine other possible conformers [**173**]. This method still uses MD calculations to get snap-shots of conformer structures over a specified run time and is likely to still require large amounts of computational time and resources. For these reasons only single conformer systems will be considered in this study.

3.2.2.1 Acentric Factor Method

A summary of Garza's solvation entropy model [**47**] is given in this section for the Acentric Factor method and the next section for the SPT method. For translational entropy, the partition function is defined as usual with the HA description (see equation 3.5) except for the volume V which is ambiguously defined for an ideal gas. Here the volume V of a solute is defined in equation 3.17.

$$V = N_c v_c \tag{3.17}$$

Here, N_c is the average number of accessible cavities in the solute, which for dense and/or non-bulky solutes such as water, is usually $N_c = 1$. The solute cavity volume v_c is described in equation 3.18.

$$v_c = \left(V_M^{\frac{1}{3}} + \left(\frac{M_S}{N_A \rho} - V_S \right)^{\frac{1}{3}} \right)^3 \tag{3.18}$$

Here, V_M is the volume of the solute molecule and V_S is the volume of the solvent molecule which are calculated from the van der Waals radii. N_A is Avogadro's number, ρ is the mass density of the solvent medium and M_S is the molecular weight/molar mass of the solvent

molecule. Solvent specific constants used in this study are outlined in (table A1 of appendix A). Translational entropy is given by equation 3.19 which is similar to its gas-phase form (see equation 3.5) except the N_c and v_c terms which incorporate solvent cavity effects. In this study it is assumed the solvent cavity restricts the translational and rotational motion of the solute molecule to within the cavity volume resulting in a reduction in translational and rotaional entropy [**142**, **171**, **174**].

$$S_{\text{tran-sol}} = R\left(\ln\left[\left(\frac{2\pi m k_B T}{h^2}\right)^{\frac{3}{2}} N_c v_c\right] + \frac{5}{2}\right) \tag{3.19}$$

For rotational entropy in solvation phase, the translational entropy terms are introduced to account for the loss of translational entropy during rotation when the molecule is restricted inside the solvation cavity.

$$S_{\text{rot-sol}} = S_{\text{rot}} + S_{\text{tran-sol}}(T, r_c - r_g) - S_{\text{tran-sol}}(T, r_c) \tag{3.20}$$

In equation 3.20, $S_{\text{tran-sol}}$ is the solvation-corrected translational entropy which is defined by equation 3.19. The term $r_c = (3v_c/(4\pi))^{1/3}$ is the radius of the cavity and $r_g^2 = 1/N \sum_{k=1}^{N}(r_k - r_{\text{mean}})^2 = \frac{r_1^2+r_2^2+\ldots+r_N^2}{N}$ is the radius of gyration squared for the solute and N is the number of atoms in the solute. The v_c spherical cavity volume term in equation 3.19 is dependant on a radius which is why the last two terms in equation 3.20 are a function of the cavity radius r_c and the radius reduced by gyration $r_c - r_g$. Specific cases regarding values of $r_c - r_g$ refer to Garza's original paper [**47**].

Cavity entropy (equation 3.21) is based on differences between ideal and real vaporisation entropies, correcting for the loss of rotational entropy upon condensation. The cavity formation entropy is defined by the probability of empty site existence in the solvent medium which is accessible by the solute molecule.

$$S_{\text{c}}^{\omega} = \frac{k_{\text{B}} V_{\text{M}}}{V_{\text{S}}} \ln(1 - V_{\text{S}} N_{\text{A}} \rho / M_{\text{S}}) - [5.365\omega k_{\text{B}} + S_{\text{tran-sol}}(T, r_c - r_g) - S_{\text{tran-sol}}(T, r_c)] G_{\text{p}} \tag{3.21}$$

The first term in equation 3.21 describes the entropy of a reference ideal liquid, while the other terms account for the non-ideal behaviour of the solute-solvent system. The translational entropy terms account for the loss in rotational entropy between phase transitions. The $5.365k_{\mathrm{B}}$ constant comes from the corresponding states theorem and ω is the acentric factor for the solvent (see table A1 of appendix A) which are known for common solvents. Here $G_{\mathrm{p}} = N_{\text{solute}}/N_{\text{solvent}}$ is defined as the ratio of the number of solvent molecules that coordinate around the solute and the solvent itself. This is a packing problem and is approximated as $G_{\mathrm{p}} = \frac{A_{\mathrm{M}}\Phi_{\mathrm{S}}}{A_{\mathrm{S}}\Phi_{\mathrm{M}}}$ for $\Phi_{\mathrm{X}} = A_{\mathrm{X}}/A_{\mathrm{X_{Box}}}$ (X being M or S, the solute or solvent molecule respectively) which is the ratio of the surface area, A, of the 'effective' spheres. The surface areas of 'effective' spheres are found by back-calculating the radius from the total vdW volume of the solvent and solute molecules. We then calculate the surface area of the minimum bounding boxes ($A_{\mathrm{M/S_{Box}}}$) which encloses the 'effective' spheres of the solute and solvent molecules giving us the approximation for G_{p}. This packing method will be referred to here on in as the *box packing method*. However, for larger molecules we would expect G_{p} and the cavity surface area to be more sensitive to molecular geometry because the error associated with fitting poorly defined cavities are amplified. Figure 3.3 illustrates some examples of the cavity structures we investigate.

In the present paper, we provide alternative packing approximations (see Figure 3.3) for G_{p} in which we attempt to describe the cavity structures more accurately; in particular for large molecules, but we also compare the accuracy of the entropy model for simpler solvation cavity structures.

Spherical Packing: Instead of describing the solute molecule cavity using the van der Waals volumes (as previously reported [**47**]) we fit an approximate 'minimum' bounding sphere which encloses the solute molecule's structure defined by points on van der Waals spheres of atoms making up the molecule. The bounding sphere has been calculated based on the Welzl algorithm [**175**] which provides an iterative approach to determining the bounding circle or sphere for planar and non-planar molecules respectively, with run time $\mathcal{O}(n)$, given a set of points. We implemented this algorithm in Python with the following conditionals to deal with specific geometries:

- For molecules constituting of two atoms or less, we calculate a minimum bounding circle and use the radius to define the minimum bounding sphere.
- Planar molecules consisting of three or more atoms are mapped to a fitted plane and a minimum bounding circle is calculated with its radius used to determine the minimum bounding sphere. Planar 'like' molecules are determined by fitting a plane to the molecular coordinates and checking if 75% or more of the atomic coordinates are within a distance of 0.1 Å of the fitted plane.
- For non-planar molecules with four or more atoms, we calculate the equation of the sphere giving us the centre and radius of the minimum bounding sphere. A sphere is uniquely defined by four points, so for molecules with more than four atoms, we iteratively calculate intermediate spheres until the bounding sphere is found.

The G_{sphere} packing term is then approximated by $G_{\text{sphere}} = \frac{R_{\text{solute}}}{R_{\text{solvent}}}$ where $R_{\text{solute}} = \frac{SA_{\text{Solute}}}{A_{\text{Solvent}}}$, where $R_{\text{solvent}} = 12$. We set $R_{\text{solvent}} = 12$, based on the number of unit spheres which can be ideally packed around a central unit sphere [**176**]. The SA_{Solute} term is the surface area of the bounding sphere for the solute molecule and A_{Solvent} is the average area of one side of the solvent molecule based on the minimum bounding rectangle.

Rectangular Packing: We determine the minimum bounding rectangular prism for solute and solvent molecules. This is done by first determining the convex hull of the points making up the van der Waals surface of the molecule which has the atomic coordinates at its centre. Each plane of the convex hull is then iteratively rotated onto the $x - y$ plane which allows us to simply calculate a minimum bounding rectangular prism based on the minimum and maximum extremal points in each direction, where by the rectangular prism with the minimum surface area is then returned.

In this case $G_{\text{rect}} = \frac{R_{\text{solute}}}{R_{\text{solvent}}}$ is approximated by $R_{\text{solute}} = \frac{SA_{\text{Solute}}}{A_{\text{Solvent}}}$ and $R_{\text{solvent}} = \frac{SA_{\text{solvent}}}{A_{\text{Solvent}}}$. As before determining the ratio of solvent molecules that coordinate around the solvent compared to the solute, with A_{Solvent} being the average side area of the solvent.

Convex Hull Packing: The convex hull is determined by generating surface points of the atomic van der Waal spheres and then determining the vertex points which define planes (simplices)

making up the convex hull structure. The Convex Hull function in the SciPy Spatial library was used to generate the convex hull structures surrounding our molecules; this function is an implementation of the 'Quick Hull' Algorithm [**177**]. This method provides more accurate molecular surface areas compared to the previous two methods, but overestimation of surface area and volume still occur for molecules with complex geometries such as sucrose because simplices are calculated for the 'bounding' vertices with no length/size limiting condition, meaning cavities in the molecule are essentially 'cocooned' over which otherwise might be accessible to the solvent molecules.

The method of approximating G_{convex} is identical to the rectangular prism case, except SA_{Solute} is the surface area of the convex hull.

Solvent-Excluded Surface (SES) Packing: Algorithms which provide an exact analytical solution to the surface area of overlapping spheres (modelling a molecule) do exist, but involve complex integrals over parameterised arcs and are not widely implemented [**178**, **179**]. However, the Jmol software package provides a molecular probing method similar to [**169**] and is analogous to rolling a spherically approximated solvation molecule over the surface of the solute molecule, tracing out the surface area accessible by the solvent probe. This method has the advantage of excluding surface area components of the solute molecule such as cavities and voids that might otherwise not be accessible to the solvent molecule.

The term G_{SES} is approximated using the same method as the convex hull and rectangular packing schemes except SA_{SES} is the SES surface area.

3.2.2.2 Scaled Particle Theory Method

An alternative method also proposed by Garza [**47**] for calculating the cavity entropy is based on scaled particle theory which relies on ϵ_r the relative permittivity. The cavity contribution to entropy is calculated using equation 3.22.

$$S_{\text{c}}^{\epsilon\alpha} = \frac{G_{\text{c}}}{T} \tag{3.22}$$

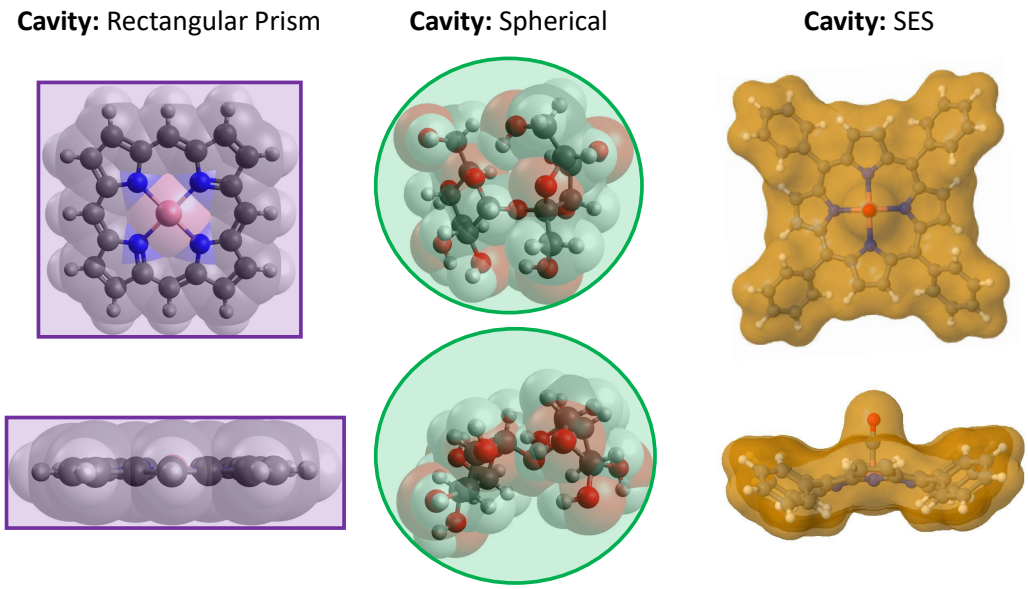

FIGURE 3.3. Some of the proposed solvation cavity geometries for different molecules, namely cobalt porphrine (CoP) (left), sucrose (centre) and cobalt tetraphenylporphyrin with CO adsorbed on the cobalt centre (CoTPP-CO) (right). Left (purple) shows a rectangular prism cavity, centre (green) shows a spherical cavity and right (orange) assumes an solvent excluded surface (SES) type cavity. The ball and stick structures show the atomic positions while the translucent overlapping spheres represent the van der Waals spheres for each atom.

$$G_{\mathrm{c}} = k_{\mathrm{B}}T\left[-\ln(1-y) + \frac{3y}{1-y}R_v + \left[\frac{3y}{1-y} + \frac{9}{2}\left(\frac{y}{1-y}\right)^2\right]R_v^2\right] \tag{3.23}$$

$$y = \frac{3}{4\pi}\frac{\epsilon_r - 1}{\epsilon_r + 2} \tag{3.24}$$

In equations 3.22 and 3.23 G_{c} is the free energy of the cavity formation used in polarisable continuum models (PCM) [**42**, **47**, **143**]. Equation 3.22 is the cavity entropy based on the relative permittivity (in equation 3.24). In equation 3.22 we have excluded a thermal expansion term since in most cases the thermal expansion coefficient of the solvent is usually much less than the free energy term. In equation 3.23 $R_v = \left(\frac{V_{\mathrm{M}}}{V_{\mathrm{S}}}\right)^{1/3}$ is the ratio of scaled radii of the solute and solvent van der Waals volumes.

3.2.3 ChemSol 2.1

Solvation entropies for the benchmarking set are also calculated using ChemSol 2.1 [**49–51**] for comparison purposes (see Comparison to Previous Methods section). The iterative mode in ChemSol is used with parameters remaining unchanged from the default except for van der Waals radii which are explicitly chosen to match those used in the acentric factor and scaled particle theory methods for consistency. For further details about how the ChemSol 2.1 program works and the theory behind the Langevin Dipoles model refer to ref. [**49–51**].

3.2.4 Benchmarking Data Set

A data set of 56 molecules is used for benchmarking and has been determined based on studies which present experimentally determined aqueous standard molar entropy values [**180–184**] or estimated aqueous standard molar entropy values based on experimental free energies and enthalpies [**185**]. We only consider aqueous standard molar entropy values since benchmarking in this study is mostly limited to water solvation systems. Molecules have also been selected based on size, with an attempt to select an even spread of small (2-10 atoms), medium (10-20 atoms) and large (20 or more atoms) sized molecules. Sugar structures have been calculated in their cyclical configuration with the exception of D-Ribulose which is calculated in its linear configuration.

Where both experimentally determined and estimated aqueous standard molar entropy values are found, we have chosen the experimentally determined value as the benchmark because estimated values overestimate the standard entropies in some cases. For example, sucrose is found to have a aqueous standard molar entropy value of 435.4 J K^{-1} mol^{-1} based on experimentally observed ΔG and ΔH values [**182**], while a value of 504.3 J K^{-1} mol^{-1} is estimated using a table of experimentally determined constants to determine ΔG, ΔH and ΔS [**185**].

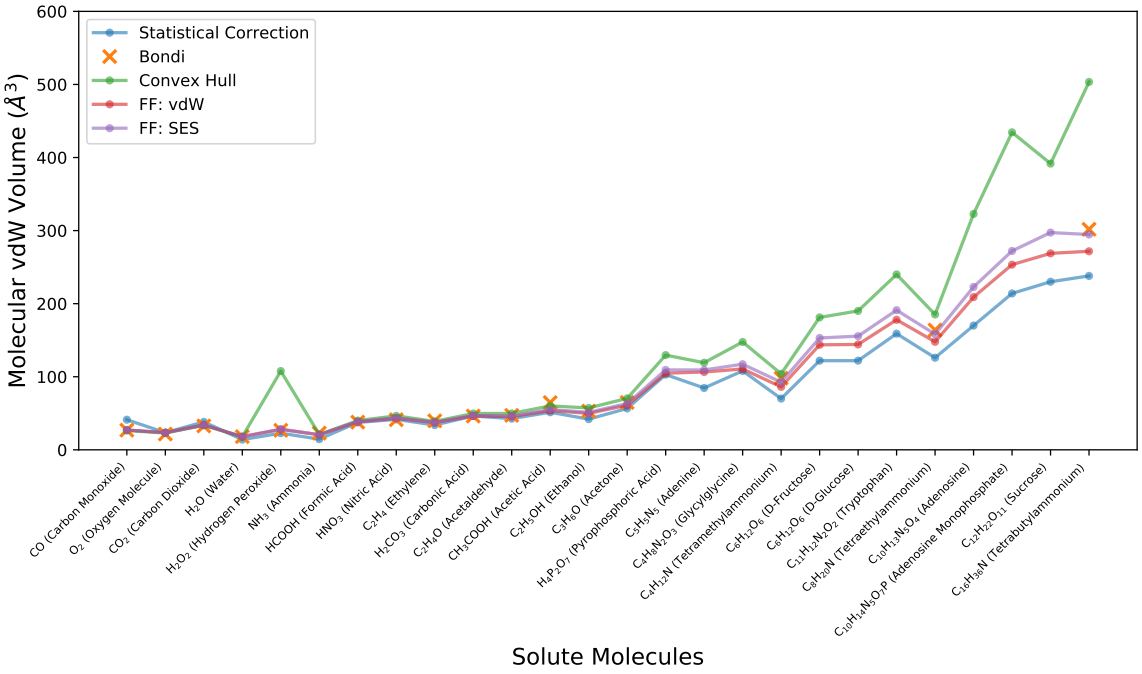

FIGURE 3.4. Comparison of van der Waals volumes for a selection of solute molecules, listed in order of number of atoms. Van der Waals volumes are calculated using the convex hull (green), pre-determined volume components [**167**] (orange cross), statistical correction method (blue) [**168**], flood-fill (FF) method excluding void volumes (red) and the flood-fill method including void volumes similar to the SES (purple) [**169**].

3.3 Results and Discussion

3.3.1 Benchmarking Entropies

3.3.1.1 Van der Waals Volume Method Comparison

The results in figure 3.4 show that all methods give similar volumes for small molecules (molecules with a volume of 50 Å^3 or less), but a noticeable discrepancy in volumes is observed with medium to large molecules (volumes of 50 Å^3 or more). In the regime of medium to large molecules, it is likely the convex hull method will overestimate volumes of molecules with complex geometries. The statistical correction method from equation 3.15 [**168**] is shown to slightly underestimate the vdW volumes in the medium-large molecule regime. The method of Bondi [**167**], which uses volume contributions of common bonding elements (e.g.

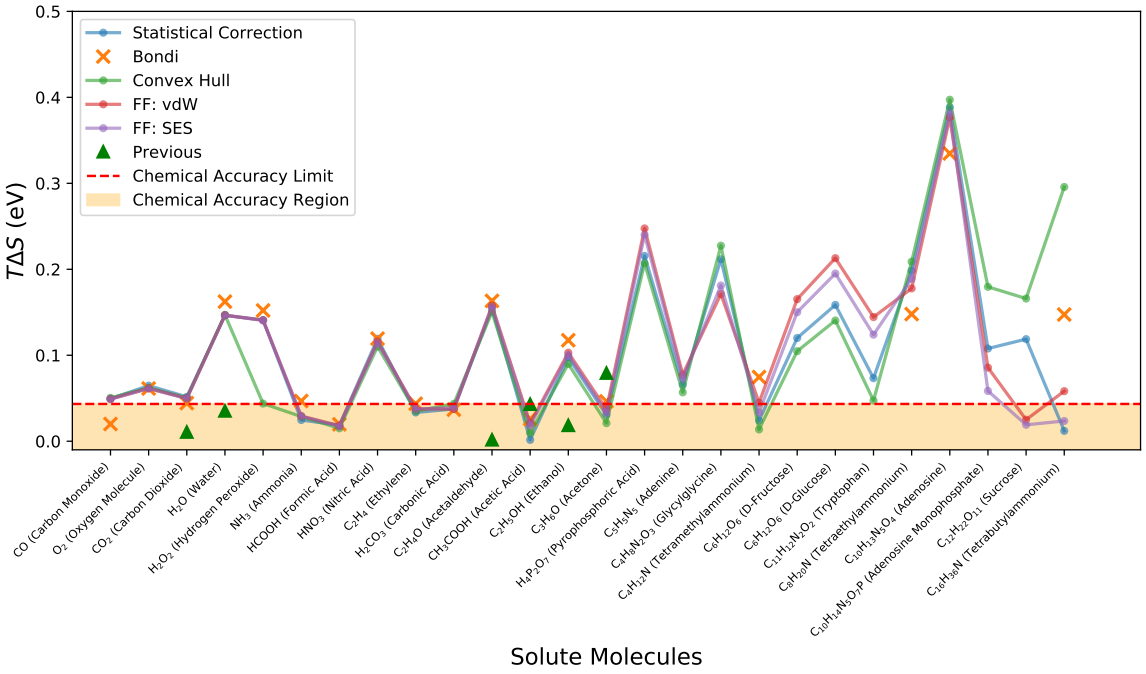

FIGURE 3.5. Calculation of absolute entropic energy deviation from experimental values for a representative subset of the full benchmarking set using the acentric factor method with the box packing scheme for the different vdW volume calculation methods. The *previous* entropy values (green triangles) were determined by Garza in a previous study [**47**]

double carbon-carbon bonds or oxygen-hydrogen bonds) to estimate the volumes of small molecules and some large molecules accurately, but is limited in it applicability, with some large molecules having bonding elements which have not been considered in Bondi's tables. The SES volume is the volume of the molecular surface traced out by a spherical solvent probe and should be considered the most accurate representation of the molecular volume. For larger molecules we would consider the van der Waals volume (also calculated using the *Protein Volume* program) to slightly underestimate the 'effective' volume of the molecule as it may include cavities/voids not accessible by the water probe.

In figure 3.5 we observe a general increase in the entropy deviation from experiment with molecular size, in particular, for the convex-hull method. Comparing figures 3.4 and 3.5, we see the choice of vdW calculation method is not as important for small molecules as it is for medium-large molecules, where for the latter molecules, we find significant accuracy

Molecule Set	Statistical	Bondi	FF: vdW	FF: SES	Convex Hull
All (56)	0.12	0.09	0.1	0.09	0.1
Small (20)	0.07	0.06	0.06	0.06	0.06
Medium (18)	0.12	*0.07*	0.1	0.1	0.09
Large (18)	0.19	*0.15*	0.13	0.12	0.14

TABLE 3.1. Mean absolute error (MAE) values of $T\Delta S$ (eV) for the entire set of 56 molecules (see table A2 of appendix A), along with the subsets of small, medium and large molecules. The numbers in brackets in column 1 are the number of molecules considered. FF stands for the flood-fill volume calculations. The values in *italics* have been calculated using Bondi's method which gives smaller sample sizes because some bonding elements found in medium to large molecules are not considered in Bondi's volume tables [**167**]. For reference, the value of chemical accuracy is 0.04 eV.

differences between the methods. For example sucrose shows entropy within chemical accuracy for both the flood-fill algorithms (SES, vdW) methods [**169**], but the statistical and convex hull methods deviate from chemical accuracy by 3 and 4 times, respectively. The calculated SES volume is expected to give the most accurate entropy values since it includes volume contributions of cavities which are not accessible by the solvent molecule.

In figure 3.5 a comparison is also made with entropy values from a previous study by Garza [**47**] (who uses the box packing method for cavity entropy), where agreement is demonstrated for some of the molecules, but for others, such as water or acetaldehyde, our values do not achieve chemical accuracy. The difference in entropy values could in part be caused by the different geometry and frequency calculation methods; we use DFT calculations with the PBE functional and D3(BJ) dispersion correction, while the Garza uses the GFN2-XTB semiempirical quantum mechanical (SQM) calculations [**186**].

In order to calculate entropies using the solvation model and compare the performance of van der Waals volume methods, we used the box packing method to calculate the packing term G in equation 3.21.

Table 3.1 shows relatively little change in the mean absolute error (MAE) for the set of small molecules, with a maximum difference of 0.009 eV at a temperature of 298.15 K, between vdW calculation methods. The table also tells us that entropic energy deviations from experiment of small molecules are on average $\sim 50\%$ above the chemical accuracy

value (of 0.04 eV at 298.15 K). For the set of large molecules, we obtain a minimum MAE of 0.12 eV using the SES method, values in red have been excluded, and the SES performance for medium sized molecules are just behind the Convex Hull method with a difference of 0.01 eV. Medium and large molecules have, on average, entropy deviations of 2.4 and 3.5 times the chemical accuracy value. The MAE of the entire set is also included in the table, with the SES method having the lowest error value, but this metric is less sensitive to changes for molecules in a specific size group.

Even though none of the vdW methods achieve chemical accuracy, we find the SES method for calculating the molecular volume can be generalised to any molecule and provides good performance across molecular size groups and the lowest error values for the large molecule subset, and the entire set of molecules. Therefore, the results from figure 3.4, figure 3.5 and table 3.1 shows that the best all-round performance for entropy calculations is given by the SES method which will be used here to calculate the vdW volumes of molecules.

3.3.1.2 Packing Method Comparison

The packing methods described in the acentric method section have been applied to the entire set of 56 molecules with experiment - calculation ($\Delta S = S_{\text{expt}} - S_{\text{calc}}$) entropy differences shown in the top plot of figure 3.6 plotted as $T\Delta S$. This figure shows that the box and SES packing methods have the best performance. In the bottom plot of figure 3.6 we show the mean absolute error (MAE) for each packing method for which none of the packing methods or subsequent size categories achieve chemical accuracy, but we find the box and SES packing methods have the best performance. We find in figure 3.6 that the difference between the box, rectangular prism, convex hull and SES packing methods are subtle, but the box packing method provides the lowest MAE values across all categories. We do observe an increase in the MAE value going from the small, medium and large categories for almost all packing methods as expected, since there is a larger possibility for errors to enter into geometry and other related calculations of larger molecules. Both the SES and convex hull methods show values close to the box packing method in the large molecule category with a difference of only 0.003 eV at 298.15 K and could be suitable alternatives for large molecule calculations.

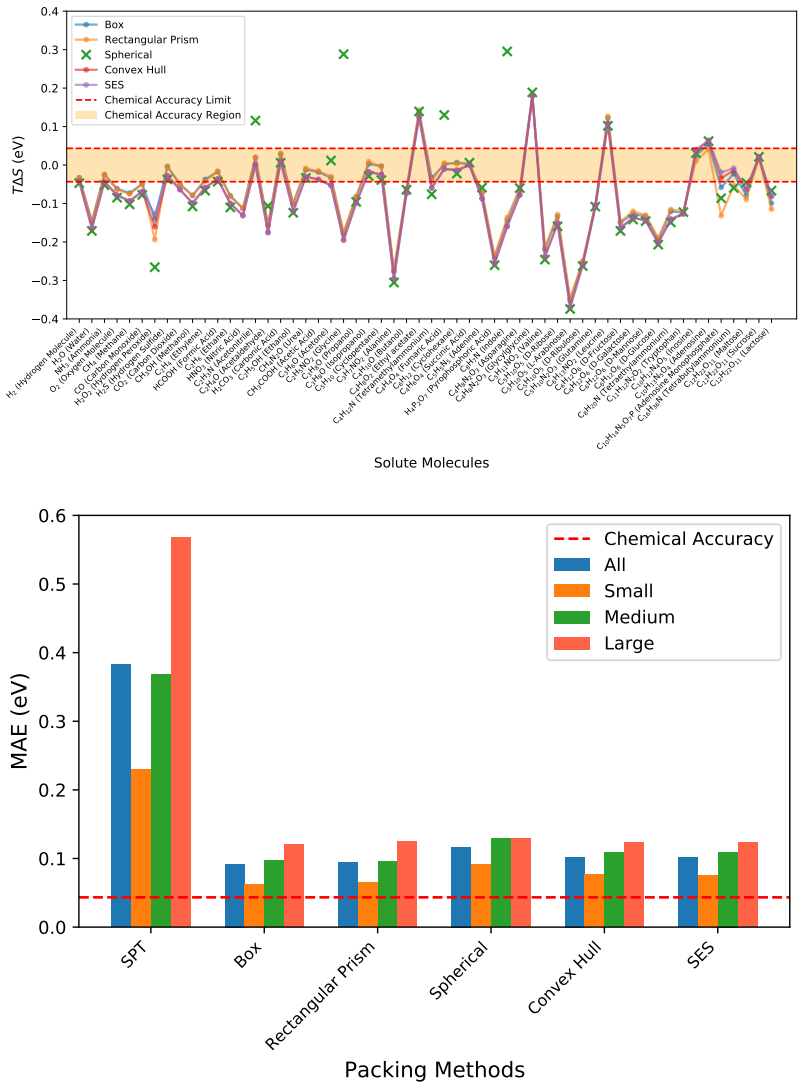

FIGURE 3.6. Top plot is the calculated entropy deviation from experiment ($T\Delta S = T(S_{\text{Expt}} - S_{\text{Calc}})$), with $T = 298.15$ K, for the listed packing methods for the entire benchmarking set (see table A3 in appendix A). Bottom plot is the MAE of the different packing methods of the entire benchmarking set split into categories of the entire benchmarking set, small (< 10 atoms), medium (between 10-19 atoms) and large (≥ 20 atoms) molecules. Values of the bottom plot are shown in table A4 of appendix A. The red dashed lines in both plots represent the chemical accuracy; any value between the lines for (a) or below the line for (b) are entropy values which are considered chemically accurate.

However, for small and medium size categories, we find either the box or rectangular prism packing methods are likely the most suitable with the smallest MAE values.

The spherical packing method yields overestimated entropies for some molecules, and could be caused by a poor estimation of the spherical cavity size and thus the G packing term. However, on closer inspection we find molecules with overestimated entropies have planar or semi-planar geometries in which case a sphere is determined by calculating the radius of a circle by mapping the molecular geometries in three dimensions onto a plane of best fit, and therefore overestimating the cavity size of a molecule that would have its cavity best described using a rectangular shaped (or more detailed shape such as the one described for the SES method) cavity.

It is interesting that the box packing method provides the best performance across all categories considering it simplifies the geometry of all molecules to a single sphere using the vdW volume radii. It maybe anticipated that the SES method would give the lowest MAE values because in 'theory' it provides the most detailed description of the molecular surface accessible to the solvent. To resolve this, in the next section we will investigate empirical correction values to the box and SES packing methods with the aim of minimising the MAE values and improving the accuracy of the calculated entropy values.

For amino acids and sugars considered to be outliers such as L-arabinose and glycylglycine in figure 3.6, further analysis is conducted in figure A5 of appendix A looking at the zwitterionic structures of amino acids and the cyclic and linear structures of sugars in implicit water. It is found that in all cases only a slight accuracy gain in entropy is achieved by including implicit water and using the zwitterionic structures for amino acids and cyclical structures for sugars. This implies that other entropic contributions not included in this study such as conformation entropy may be required to achieve better accuracy for certain molecules.

The computational costs of these packing methods are not significant. The slowest method is the convex hull and rectangular prism methods because for large molecules with many generated surface points (points that lie on the van der Waals sphere of each atom) the triangulation is more significant. Since the rectangular prism packing method requires the

convex hull, it has a similar computational cost. The computational cost of the SPT, Box, Spherical and SES packing methods are negligible.

3.3.1.3 Empirical Correction

Empirical correction terms have been calculated for the box and SES packing methods by minimising the overall MAE of the data set as shown in figure A4 of appendix A. The determined empirical correction values are $S_{\text{corr-box}} = -0.000212$ eV/K and $S_{\text{corr-SES}} = -0.000248$ eV/K for the box packing and SES packing methods respectively, which have been accurately calculated to within 10^{-8} eV/K. Updated total entropies (S_{Total}) given the new correction factors, are shown in equations 3.25 and 3.26.

$$S_{\text{Total-Box}} = S_{\text{elec}} + S_{\text{tran}} + S_{\text{rot}} + S_{\text{vib}} + S_{\text{cav}} + S_{\text{corr-box}} \tag{3.25}$$

$$S_{\text{Total-SES}} = S_{\text{elec}} + S_{\text{tran}} + S_{\text{rot}} + S_{\text{vib}} + S_{\text{cav}} + S_{\text{corr-SES}} \tag{3.26}$$

A comparison between the box packing and SES packing results with no empirical correction and those with the correction are shown in figure 3.7. As expected the corrected values are shifted up or down by their empirical correction value which in general reduces the maximum and minimum errors and on average brings the calculated values closer to being chemically accurate. With the correction factor, chemical accuracy is achieved for 11/20 and 11/20 small molecules, 6/18 and 6/18 medium molecules and 4/18 and 3/18 large molecules for the box packing and SES packing methods, respectively. For the entire set, 21 out of the 56 molecules achieve chemical accuracy for both packing methods, while for the uncorrected calculations, 19 and 17 molecules out of the set of 56 achieve chemical accuracy for the box and SES packing methods, respectively.

This means achieving chemical accuracy for medium to large molecules is unlikely even with an empirical correction term, but if we relax the accuracy criterion to twice the chemical accuracy value which has been done for free energy values in previous studies [**187**], we obtain

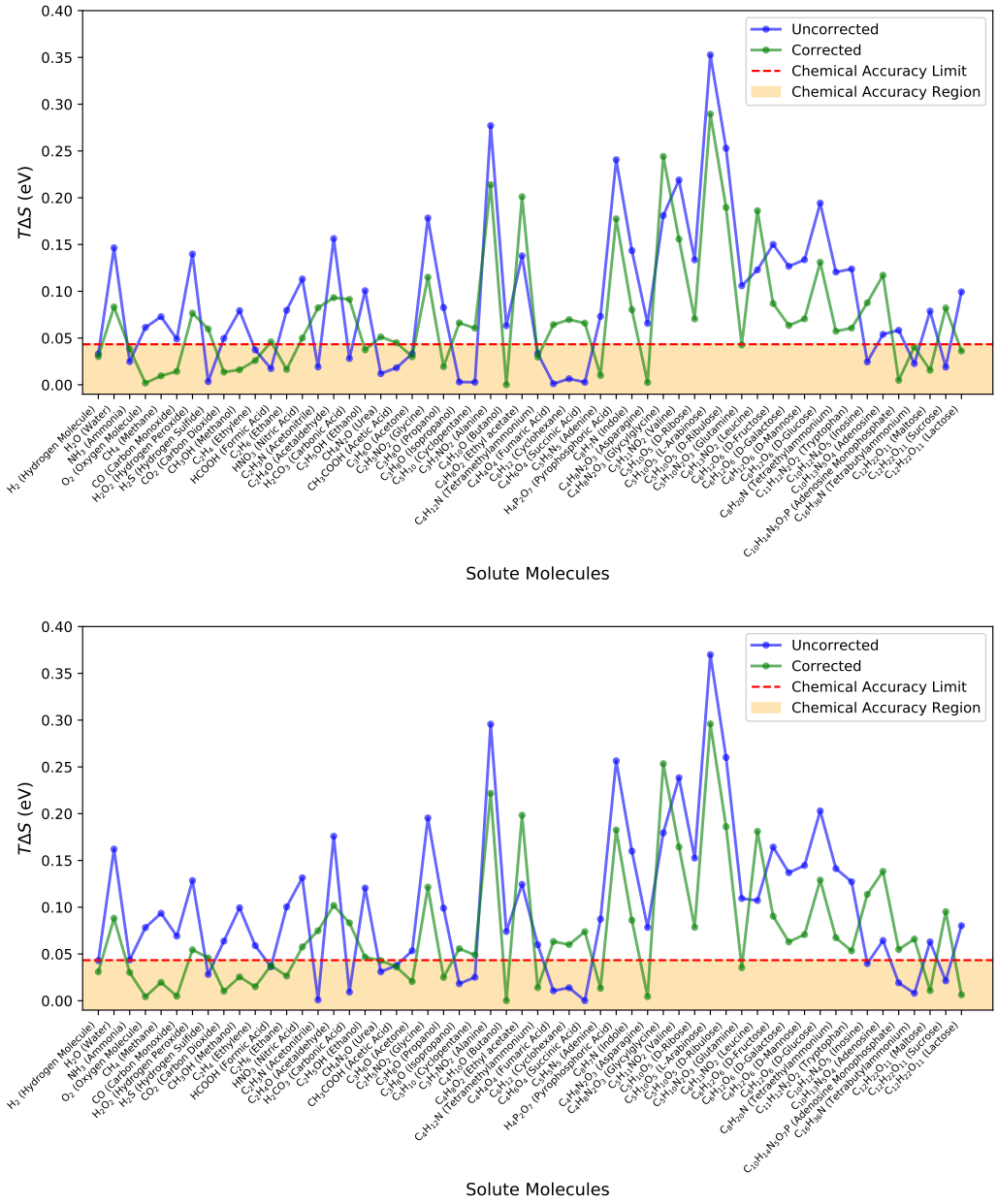

FIGURE 3.7. Comparison of MAE values between uncorrected and corrected entropy values for the box packing (top plot) and SES packing (bottom plot) methods. Values below the red dashed line are considered chemically accurate. The correction is determined by shifting the calculated entropy values relative to the experimental entropy values such that the MAE value is minimised (see figure A3 of appendix A).

44/56 and 41/56 molecules being considered accurate. A summary of chemical accuracy numbers is given in table 3.2, which shows an increase in the number of molecules with entropies considered chemically accurate for entropy values calculated with the empirical correction term. When the accuracy parameter is relaxed to twice the chemical accuracy value we see the largest increase in the number of molecular entropies achieving accuracy for the corrected entropies; for the entire set we have 52-57% achieving twice chemical accuracy for the uncorrected entropy values and 73-79% achieving twice chemical accuracy for the empirically corrected entropy values.

When comparing molecular sizes in table 3.2, the uncorrected entropy values show a reduction in the number of entropies achieving either of the accuracy criteria when going from small to medium and medium to large. The number of entropy values achieving the accuracy criterion for medium sized molecules does not change significantly between uncorrected or corrected entropy values. Comparing the uncorrected and corrected entropy values we obtain approximately twice the number of entropy values achieving the accuracy criterion for large molecules when using the corrected entropies compared to the uncorrected entropies. Therefore, including the empirical correction term improves the accuracy of entropy values for large molecules.

The inclusion of the empirical correction term in the entropy calculations show a slight improvement in the number of molecular entropies achieving chemical accuracy but we find an $\sim$25% improvement in the number of entropies achieving twice chemical accuracy. The empirical correction value has been applied to entropies calculated using the Meta-GGA SCAN+rVV10 [**95**,**96**] functional (see table A6 in appendix A) and is shown to be not sensitive to the type of functional used. The box packing method provides the best performance with more entropy values achieving the accuracy criterion, but the SES method also performs well, in particular for small molecular entropies. Therefore, in the next sections we will focus on the box packing method for simplicity and plot readability but comparison with the SES method is still conducted for reaction entropies and free energies.

Model:	Molecular Size	Box Packing		SES Packing	
		CA	2CA	CA	2CA
Uncorrected	All	19	32	17	29
	Small	10	15	8	12
	Medium	7	11	5	10
	Large	3	6	4	7
Corrected	All	21	44	21	41
	Small	11	18	11	19
	Medium	6	12	6	11
	Large	4	13	3	11

TABLE 3.2. The number of molecules in each size category which fall under the accuracy criterion. There are 56 molecules, with 20 small, 18 medium and 18 large. CA means chemical accuracy and 2CA is twice the chemical accuracy value. Uncorrected refers to entropies with no empirical correction, while corrected values have the empirical correction included. The number of molecules considered in each size category are the same as those shown in table 3.1.

Molecular Size	MAE					
	Solvation Model	Solvation Model with Correction	Gas-Phase Scaling	Vibrational	Gas-Phase	ChemSol
All	0.09	0.07	0.08	0.43	0.39	0.32
Small	0.06	0.045	0.06	0.38	0.3	0.22
Medium	0.1	0.09	0.08	0.47	0.38	0.32
Large	0.12	0.09	0.1	0.45	0.51	0.43

TABLE 3.3. Summary of the $T\Delta S$ MAE values (eV) for the methods shown in figure 3.8. *Solvation Model* is the solvation entropies calculated using the box packing method and *Solvation Model with Correction* includes the empirical correction from the previous section. *Gas-Phase Scaling* is the gas-phase entropies scaled by a factor of 0.62. *Vibrational* is only the vibrational component of the entropy. *Gas-Phase* is the gas-phase entropy values. *ChemSol* is the entropy values calculated using the ChemSol 2.1 program.

3.3.1.4 Comparison to Previous Methods

Figure 3.8 shows the solvation entropy will take a value between the gas phase entropy and vibrational entropy values, with vibrational entropy values significantly underestimating the solvation entropy. This means neglecting translational and rotational entropies for solvation systems should not be considered accurate because even though the contributions are reduced relative to gas-phase entropies, they still contribute significantly to the total entropy value in solvation-phase. We also find an optimal scaling value for the gas phase entropies of 0.62,

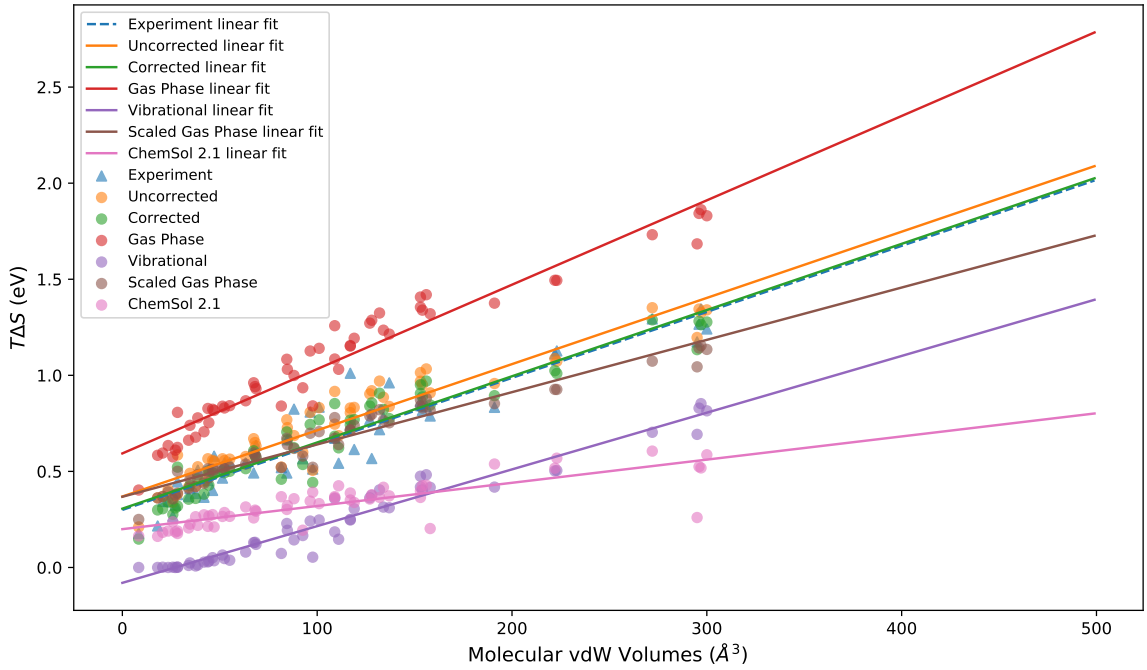

FIGURE 3.8. A comparison between experimental and gas phase entropies, the gas phase entropy scaling method, vibrational entropies, entropies calculated using ChemSol 2.1 and the calculated solvation entropies with and without the empirical correction. Lines of best fit have been included for all seven entropy data sets and predicted to volumes of 450 $\mathring{A}^3$. See table A5 for the list of entropy values calculated using each method. The correction is determined by shifting the calculated entropy values relative to the experimental entropy values such that the MAE value is minimised (see figure A3 of appendix A).

which is found by minimising the MAE value with a scaling value between 0-1 (see figure A5 of Appendix A). The scaled gas phase entropy values follow the calculated solvation entropies (with and without empirical correction) closely for small and medium sized molecules, but starts to underestimate entropies for larger molecules. This is supported by the MAE results in table 3.3, which shows the solvation model with the empirical correction term provides slightly better overall performance with an MAE value of 0.07 eV compared to 0.08 eV for the optimally scaled gas phase entropies. In particular, entropy values of small and large molecules are best described using the solvation model with the empirical correction term which shows an improvement of 10-25% compared to the scaled gas phase entropies.

It is clear from table 3.3 that the vibrational entropy contribution by itself significantly underestimates the entropy of a solvation system with MAE values an order of magnitude larger compared to the scaled gas phase entropies and solvation model entropies. Solvation model entropies without the empirical correction show MAE values larger than both the scaled gas phase and empirically corrected solvation model MAE values by 15% and 25% respectively. As expected, the solvation model with the empirical correction term provides the smallest overall error and smallest error across the molecular size categories.

Calculations using the ChemSol program are seen to systematically underestimate the solvation entropy values relative to experimental values in figure 3.8. However, the ChemSol solvation entropy values are more accurate for small and medium sized molecules compared to the vibrational entropy, but for larger molecules we find a divergence in results and worse performance relative to vibrational entropy values. The results for the ChemSol calculations in figure 3.8 mirror the MAE results in table 3.3 with small and medium sized molecules having MAE values of 0.22 eV and 0.32 eV respectively for ChemSol solvation entropies compared to 0.38 eV and 0.47 eV for small and medium sized molecules calculated using vibrational entropy. For large molecules the MAE values show similar performance between ChemSol solvation and vibration entropies with a difference of only 0.02 eV. We checked several molecules and found good agreement with the solvation entropy values calculated using ChemSol in Ref. [**50**].

In figure 3.8 we predict our entropy results for larger molecules using lines of best fit for each entropy method (including experiment) because as the volume of a molecule increases, other indirectly related variables also increase such as molecular mass, moment of inertia, number of vibrational modes and the packing number. We observe that total solvation entropy vs molecular volume follows an approximately linear trend.

We find both the corrected and uncorrected solvation models follow the fitted line to the experimental data quite closely with the uncorrected line being slightly offset. The fitted line for scaled gas phase entropy is seen to be accurate for the small molecule size regime but begins to diverge from the experimental line for larger molecule sizes. This means even though we get relatively low MAE values for the scaled gas phase method in table 3.3, it does

Reaction	Experiment (eV/K)	Previous (eV/K)	Solvation Model BP (eV/K)	Solvation Model SES (eV/K)
(1): H + $CH_3OH \rightarrow H_2 + CH_2OH$	-0.00032	-0.00026	-0.00031	-0.00028
(2): H + $CH_3CH_2OH \rightarrow H_2 + CH_3CHOH$	-0.00034	-0.00021	-0.00039	-0.00036
(3): H + $(CH_3)_2CHOH \rightarrow H_2 + (CH_3)_2COH$	-0.00027	-0.00020	-0.00037	-0.00034
(4): H + $CH_2(OH)_2 \rightarrow H_2 + CH(OH)_2$	-0.00013	-0.00017	-0.00034	-0.00030
(5): H + $(CH_2OH)_2 \rightarrow H_2 + HOCH_2CHOH$	-0.00045	-0.00026	-0.00043	-0.00040
(6): $CH_3SH + CH_3 \rightarrow CH_3S + CH_4$	-0.00060	-0.00033	-0.00019	-0.00019
(7): $CH_3SH + CH_2OH \rightarrow CH_3S + CH_3OH$	-0.00082	-0.00063	-0.00026	-0.00026
(8): $CH_3SH + (CH_3)_2COH \rightarrow CH_3S + (CH_3)_2CHOH$	-0.00069	-0.00077	-0.00020	-0.00020

TABLE 3.4. Comparison of reaction entropies between calculated and experimental values. Reaction entropies are calculated by subtracting the entropy of the reaction products by their reactants ($\Delta S_{\text{Reaction}} = S_{\text{Products}} - S_{\text{Reactants}}$). *Solvation Model* is the solvation reaction entropies calculated with the box packing method (BP) and the solvent excluded surface method (SES). *Previous* is reaction entropies from Garza's study, while *Experiment* is experimental entropy values which are known for these reactions [**47**, **142**, **187**]. Entropies are calculated for a concentration of 1 mol/L.

not follow the expected trend of the experimental values as closely as the solvation model methods.

Computational Efficiency

Most of the computational cost in calculating the entropy values is in the ab initio calculation of vibrations, particularly for large molecules. Atomic relaxation is an order of magnitude faster compared to vibration calculations and the final analytical calculation of entropy is an order of magnitude faster again. When comparing with other analytical methods such as vibration only entropy, scaling factors or ChemSol [**49–51**] we expect similar calculation costs because all these methods require 1. *ab initio* structural relaxation, 2. *ab initio* vibration or atomic charge calculation and 3. post *ab initio* analytical entropy calculation utilising the structure and vibration or charge output. This method and other analytical methods are expected to have lower computational costs possibly by an order of magnitude or more compared *ab initio* molecular dynamics (AIMD) methods since they require multiple runs over long time scales.

Reaction Entropy Comparison

In table 3.4 we find our calculated solvation reaction entropy values and those calculated by Garza in a previous study (who calculates frequencies and geometries using Gaussian) [**47**] are close to experimental values for the first five hydrogen reactions. The gas-phase entropy of the hydrogen atom (H) is used because we expect little hindrance from solvent molecules due to its relatively small size. For the last three reactions involving Methanethiol (CH_3SH) we calculate reaction entropies 3-4 times smaller compared to experimental values, but the differences between these three reactions followed the same trend as the experimental entropies with reaction 7 having the largest reaction entropy followed by reaction 8 then reaction 6. Reaction entropies from the previous study do not follow this trend but are closer to the experimental values. The translational and cavitational entropy almost completely cancel out for reactions 6-8, leaving only rotational and vibrational entropy contributions. Differences between the box packing (BP) and solvent excluded surface (SES) are limited to -0.00004 eV/K or 0.01 eV at 298.15 K for the first five reactions, with reactions 6-8 being the same for both methods. These reactions involve radicals (unstable molecules) which may not be accurately described using DFT and/or the solvation model. It is possible dipole contributions to entropy would be required for an accurate determination of these reaction entropies. Therefore, the solvation entropy model is suited to calculating reaction entropies, but one should keep in mind the treatment of specific radicals by DFT and the solvation model may not be accurate.

Ideally a comparison of reactions not involving radicals would provide a better performance benchmark for reaction entropies using the solvation model. However, experimental values of reaction entropies in aqueous solution are scarce with the reactions chosen here being used in previous studies [**187**].

Solute Polarity and Type

The polarity of a molecule in water will determine whether it interacts with the surrounding water molecules through hydrogen bonding. The magnitude of the dipole moment of a molecule defines its polarity, but the point at which a molecule becomes more polar than non-polar (or vice versa) is not clearly defined. In figure 3.9 rather than looking at dipole

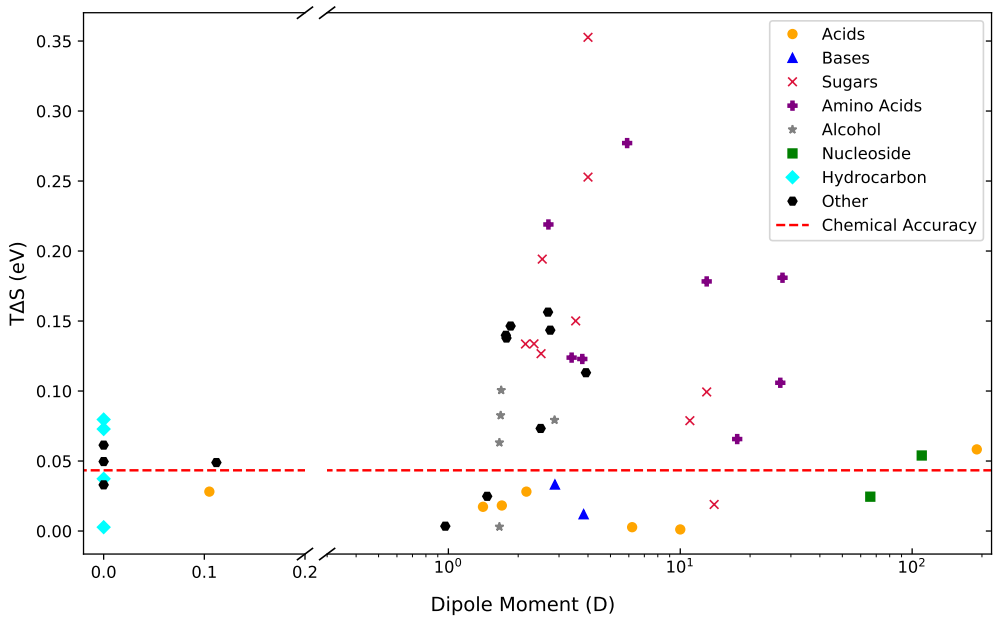

FIGURE 3.9. Comparison of entropy deviations from experiment ($\Delta S = |S_{\text{expt}} - S_{\text{calc}}|$) with molecular dipole moment (in units of Debye). Molecules are ordered based on their dipole moment and categorised as follows: Acids (orange), bases (blue), sugars (dark red), amino acids (purple), alcohol (grey), nucleoside (green), Hydrocarbon (cyan) and other (black). Values below the red line are considered chemically accurate. The x-axis has been broken into a linear section (left) and log scale section (right) for the purposes of visualisation.

moment vs entropy alone we will also categorise molecules based on their type, such as acids, bases, amino acids, sugars, hydrocarbons, alcohols etc.

We see from figure 3.9 that acids, bases and nucleosides almost all achieve chemical accuracy, but sugars and amino acids show the largest deviations from experiment. Sugars and amino acids present the largest spread of entropy difference values from experiment, with some of these values achieving chemical accuracy. Hydrocarbon entropies are predicted relatively accurately with all entropy values within twice the chemical accuracy criterion, and have zero dipole moments. Similarly, alcohol molecules mostly fall within the twice chemical accuracy criterion while those molecules in the 'Other' category, molecules that don't fall under the

Reaction	ΔG_{vib}	ΔG_{sol} **(BP)**	ΔG_{sol} **(SES)**	ΔE	ΔG_{lit}	ΔE_{lit}	**Ref.**
(1): $Co^{II}P + e \longrightarrow Co^{I}P$	-3.68	-3.67	-3.67	-3.62	-3.13†	-3.07†,-1.88††	[**188**]†, [**189**]††
(2): $Co^{I}P + e \longrightarrow Co^{0}P$	-2.21	-2.23	-2.23	-2.21	-2.47	-2.28	[**188**]
(3): $Co^{I}P + CO_2 \longrightarrow Co^{I}P\text{-}CO_2$	-0.44	-0.07	-0.08	-0.44	0.09†	-0.16††	[**190**]†, [**189**]††
(4): $Co^{II}P+CO_2+H \longrightarrow Co^{II}P\text{-}COOH$	-0.44	0.01	0.003	-0.57	-0.43	None	[**190**]
(5): $Co^{I}P\text{-}CO_2+H \longrightarrow Co^{I}P\text{-}COOH$	0.72	0.76	0.76	0.69	-1.01	None	[**190**]

TABLE 3.5. Comparison of calculated CO_2 reduction reaction steps in implicit water with those reported in the literature. All values in this table are in units of eV. Free energy values are calculated using $\Delta G = \Delta E + \Delta E_{\text{ZPE}} - T\Delta S$ instead of equation 3.1. ΔG_{vib} is the free energy calculated using vibrational entropy, ΔG_{sol} is the free energy calculated using the solvation entropy model with water, with values calculated using the box packing (BP) and solvent excluded surface packing (SES) methods. ΔE is the reaction energy, ΔG_{lit} and ΔE_{lit} is the calculated free energy and reaction energy respectively, previously reported in the literature. The superscript † indicates which reference matches the literature value being compared. Ref. [**188**] and Ref. [**190**] uses the vibrational entropy contribution and Ref [**189**] uses entropy values based on statistical thermodynamics [**191**] to determine their free energy values. All free energy values are calculated at a temperature of 298.15 K with a concentration of 1 mol/L.

previous mentioned categories, fall within twice chemical accuracy for small dipole moments and within for times chemical accuracy for large dipole moments.

3.3.2 Application to Catalytic CO_2 Reduction

We use our entropy values to calculate the free energy values (G) for CO_2 reduction using cobalt porphrine (CoP). The difference between the box packing method and the SES is small, but for comparison we calculate free energy values using both methods. We then compare free energy values with previous solvation entropy methods described in the introduction, ΔG_{sol}, along with our values obtained using only the vibrational contribution to the free energy, ΔG_{vib}, and the reaction energy, ΔE (no entropy), with those reported in the literature. The results are shown in table 3.5 for systems in aqueous solution. The literature values in table 3.5 have been selected based on similar functional types i.e. RPBE and PBE.

We firstly discuss the electron transfer reactions in table 3.5 (reactions 1 and 2). For both reactions the values for ΔG_{sol} are larger in magnitude compared to ΔE, with a maximum deviation of 0.05 eV for reaction 1. Our results give similar values to the reaction free energies,

ΔG_{lit}, and reaction energy, ΔE, of Ref. [**188**], and the same trend between ΔG to ΔE, is obtained: we obtain $\Delta E - \Delta G = 0.05$ eV, 0.02 eV for reaction 1 and 2, while Ref. [**188**] finds $\Delta E - \Delta G = 0.06$ eV, 0.19 eV. The slight discrepancy in reaction 2 could possibly be caused by differences in entropy calculation methods: Ref. [**188**] only accounts for vibrational entropy (calculated using the B3LYP [**192, 193**] functional in FHI-aims [**194**] code). The result obtained by Ref. [**189**] of -1.88 eV differs quite substantially from both the present results as well as those of Ref. [**188**]. Ref. [**189**] includes an entropy contribution based on a previous method which estimates the entropy values from statistical thermodynamics [**191**]. In the 'ΔG_{lit}' column of table 3.5 and the 'Ref. [**189**]' values of table 3.6 free energies associated with Ref. [**189**] are calculated using the PBE or B3LYP functionals in Gaussian03 [**195**] with the 6-31G* basis set [**196–199**]. The free energy calculated using vibrational entropy (ΔG_{vib}) alone for reaction 2 gives calculated values closer to the reaction energies (ΔE) compared to the free energies calculated using the solvation entropy model (ΔG_{sol}).

For reaction 3 we find $\Delta G_{\text{sol}} = -0.07$ and -0.08 eV for the box and SES packing methods respectively, which is in good agreement with that of Ref. [**190**] of $\Delta G_{\text{lit}} = 0.09$ eV, while that of Ref. [**189**] differs qualitatively with a value -0.16 eV. When we consider only the vibrational contribution to the entropy it yields a value greater in magnitude, namely, $\Delta G_{\text{vib}} = -0.44$ eV, which is equal to the reaction energy ($\Delta E = -0.44$ eV). This highlights the importance of including full entropic effects, although for reaction 4 a difference between the reaction free energy ($\Delta G_{\text{sol}} = 0.01$ and 0.003 eV for the box and SES packing methods) and reaction energy ($\Delta E = -0.57$ eV) is up to 0.58 eV which is larger than 0.01 eV for the reaction entropy calculated using vibration entropy. For reaction 4 our calculated reaction free energy values using solvation entropy show approximately a 0.4 eV difference with the literature calculations, presumably caused by calculation differences such as functional, basis set or solvation treatments used by Ref. [**190**] (which is calculated using the Amsterdam density functional program (ADF) [**200**] with the RPBE functional [**201**] and D3 dispersion correction). The free energy values we obtain for reaction 5 show a difference of approximately 1.7 eV using both the solvation entropy model and vibrational entropy compared that of Ref. [**190**], the increase in differences between reaction 4 and reaction 5 could presumably be caused by different charge treatments between VASP and ADF.

Study	DFT Functional & Experiment	Entropy Model	Reaction Values (ΔG_{ads}, ΔE_{ads}) (eV)
This Study	PBE+D3(BJ)	Solvation Model (BP)	$\Delta G_{\text{ads}} = -0.48$
		Solvation Model (SES)	$\Delta G_{\text{ads}} = -0.49$
		Vibration	$\Delta G_{\text{ads}} = -0.9$
		-	$\Delta E_{\text{ads}} = -1.14$
	PBE	Solvation Model (BP)	ΔG_{ads} = -0.30 (-0.24)
		Solvation Model (SES)	ΔG_{ads} = -0.31 (-0.23)
		Vibration	$\Delta G_{\text{ads}} = -0.72$
		-	ΔE_{ads} = -1.12 (-1.33)
Ref. [189]	PBE	Estimated	$\Delta G_{\text{ads}} = -0.70$
		-	$\Delta E_{\text{ads}} = -1.27$
	B3LYP	Estimated	$\Delta G_{\text{ads}} = 0.24$
		-	$\Delta E_{\text{ads}} = -0.44$
	Experiment	-	$\Delta G_{\text{ads}} = -0.26$

TABLE 3.6. *Solvation Model* is the adsorption free energy calculated using the solvation entropy model for the CH_2Cl_2 solvent, BP refers to the box packing method and SES refers to the solvent excluded surface packing method. *Vibration* is the free energy calculated by just using the vibrational entropy. *Estimated* is the adsorption free energy calculated using a statistical thermodynamics estimation of entropy [**191**]. ΔG_{abs} is the adsorption free energy and ΔE_{abs} is the adsorption energy direct from DFT calculations, with all values in this table are in units of eV. The values for *This Study* are for the adsorption of CO on Co^{III}TPP, expect for values in brackets which are for CO adsorption on Co^{III}P. The values for *Ref.* [**189**] are for the adsorption of CO on Co^{III}P, except for the experimental free energy which is for CO adsorption on Co^{III}TPP. For free energy calculations the temperature is chosen to be 298.15 K with a concentration of 1 mol/L.

We also compare our calculated value of the adsorption free energy of CO on Co^{III}TPP in CH_2Cl_2 (-0.48 eV for box and -0.49 eV for SES packing methods) (see method section for definition) with the experimental value, which is -0.26 eV [**189**], and with previously calculated values, as shown in table 3.6. Our calculated value of ΔG_{ads} is -0.48 eV, obtained including entropy using the solvation entropy model with the box packing method, is in good agreement with the experimental value, and in closer agreement to experiment than that obtained using the vibrational free energy only for the entropy contribution (-0.9 eV).The Solvation model packing methods (box packing and SES packing) show marginal differences of 0.01 eV with the best performance from the box packing method, this is corroborated with the packing method comparison from table 3.4. CO adsorption using the PBE functional is

known to produce over binding adsorption energies which have been shown to be between 0.24-0.34 eV [**202**, **203**] larger. This could account for the 0.22 eV difference between ΔG_{ads} using the solvation model and the experimental ΔG_{ads} value. With regard to comparison with previous theoretical values [**189**], the free energy of adsorption has been calculated for CO on $Co^{III}P$ (not $Co^{III}TPP$) using the PBE (-0.7 eV) and B3LYP (0.24 eV) functionals, and are also included in table 3.6. The free energy of adsorption using the PBE functional in this study is -0.72 eV, close to the -0.7 eV value from previous theoretical calculations [**189**]. It has been shown in earlier work that the adsorption energy for CO on $Co^{III}TPP$ and $Co^{III}P$ is very similar [**189**], which is also verified here, thus we compare these systems. The close similarity of these structures can be seen from figure 3.10, so it is not surprising that there is not a significant difference in the adsorption free energy. Both these literature results (PBE and B3LYP [**189**]) are obtained without including dispersion corrections, unlike the present work. Therefore, to enable a more consistent comparison with the former results, we provide our corresponding values also without including the dispersion corrections for CO on both $Co^{III}TPP$ (-0.30 eV) and $Co^{III}P$ (-0.24 eV), given in parenthesis in table 3.6. On consideration of these values, it can be concluded that the present results, either with or without dispersion forces included, are closer to experiment than previous theoretical studies. In particular, the values previously calculated using the B3LYP functional indicate that adsorption of CO on $Co^{III}P$ is endothermic, which is likely to be echoed if applied to $Co^{III}TPP$ and is not representative of the behaviour reflected experimentally. It is found in the previous study [**189**] that the difference between Gaussian and VASP adsorption energies is 0.06 eV for the $Co^{III}P$-CO system, which is confirmed in the present work when comparing $\Delta E_{\text{ads}} = -1.27$ eV calculated using Gaussian [**189**] and our obtained values of $\Delta E_{\text{ads}} = -1.33$ eV using VASP, both using the PBE functional. These values are also included in table 3.6. Comparing our calculated values of the adsorption energy given in table 3.6 of $\Delta E_{\text{ads}} = -1.14$ eV with the free energy of adsorption, $\Delta G_{\text{ads}} = -0.48$ eV (solvation model with box packing) and -0.9 eV (vibration), highlights again the significant contribution due to entropy.

This means for systems in solvation-phase, an accurate description of entropy is important to accurately determine free energy values and reaction pathways. The cavity formation entropy

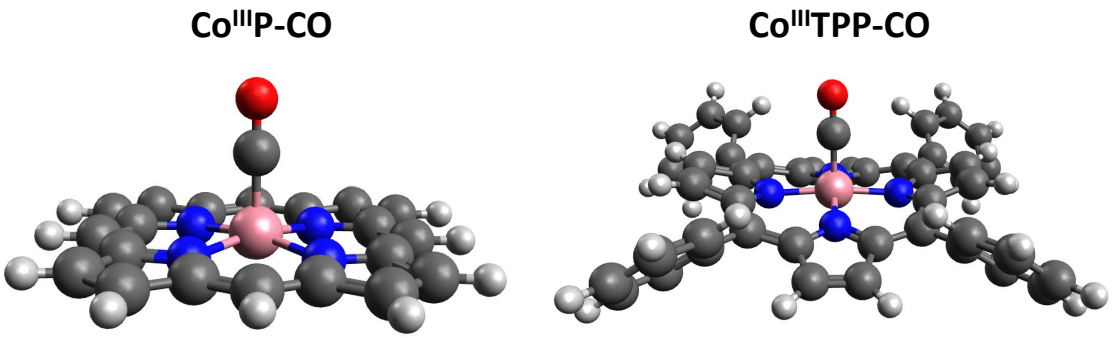

FIGURE 3.10. The relaxed geometries of CO adsorbed on, positively charged cobalt porphrine ($Co^{III}P$) (left) and, positively charged cobalt tetraphenylporphyrin ($Co^{III}TPP$) (right). The grey, white, red, blue and pink spheres represent carbon, hydrogen, oxygen, nitrogen and cobalt atoms respectively.

and hindered translational and rotational entropies go a long way to improving adsorption free energy calculations relative to experimental values.

3.4 Summary

We investigated current methods for determining entropies of different sized molecules in aqueous medium with a particular focus on larger sized molecules. Density functional theory calculations have been utilised to calculate optimal molecular structures, vibrational frequencies and atomic charges necessary for calculating solvation entropy values. Benchmarking of solvation entropy model parameters against a set of 56 molecules was conducted, showing: molecular volumes calculated using the solvent excluded surface and solvation cavity geometries (used to describe the packing of solvent molecules around a solute molecule) described using a box structure approximation, give the most accurate calculated entropy values relative to experimental values. Empirical corrections for the solvent excluded surface and box packing methods were calculated by minimisation of the mean absolute error between calculated entropies using the solvation model and experimental entropies. The empirically corrected solvation model shows a 25% increase in the number of molecules in the entire benchmarking set being considered accurate, while a 50% increase in large molecules being

considered accurate is also found. A comparison to previously reported solvation entropy calculation methods show the solvation entropy model follows a similar trend to experiment for molecules of increasing volume, while the scaled gas-phase, vibration only and ChemSol solvation entropy values show divergent trends from experiment. Therefore, we find a significant improvement in accuracy for entropy values in aqueous medium calculated with the solvation model compared to other methods.

Finally, the solvation entropy model was applied to the well-studied catalytic reduction reaction of CO_2 using molecular cobalt porphrine and cobalt tetraphenylporphyrin; reaction free energies are shown to be in good agreement with the experimental value of CO adsorbed on positively charged cobalt tetraphenylporphyrin. Compared to previous calculated results, the present solvation entropy model provides more accurate reaction free energy values compared to experiment. Thus, the results of the present study indicate that this is a promising, accurate and fast approach to include solvation entropy effects, and thus to obtain more accurate reaction free energies.

CHAPTER 4

Ab Initio Investigation of Covalently Immobilised Cobalt-Centred Metal-Organic Catalysts for CO_2 Reduction: Effect of Substrate on the Reaction Energetics

---

Recently, experimental studies of covalently immobilised CO_2 reduction metal-organic catalysts have reported remarkable activity, however, the reason for this and the underlying mechanisms are not currently understood. To advance understanding of such systems, we perform ab initio calculations investigating how covalent immobilisation of such molecular catalysts and the substrate geometry affects the reaction pathways. We address this as realistically as possible by doing a survey of possible structures including common surface defects and nanotubes, as well as linkers. In particular we study covalently immobilised cobalt-centred phthalocyanine (CoPc) and tetraphenylporphyrin (CoTPP), as used in CO_2 electroreduction reactions (CO_2ERR), immobilised on pristine and defective graphene and single walled carbon nanotubes (SWCNT), with and without linkers. The bonding energies of the CoPc and CoTPP catalysts to the different substrates are found to be consistently stronger on the SWCNTs and on defect sites, suggesting such structures will be the anchoring sites for these immobilised molecular catalysts. Covalently immobilised CoPc and CoTPP catalysts show improved CO_2ERR reaction pathway performance compared to their homogeneous analogues. Favourable reaction pathways are found for the upright-bonded CoPc and CoTPP on Stone-Wales defect and octagon-pentagon line defect respectively, in graphene. CoPc immobilised via pyridine linker is found to have the most favourable reaction pathway due to strong exothermic behaviour of CO_2 adsorption and COOH formation while having a weak endothermic final step for CO desorption, consistent with its excellent experimental performance. We attribute this to unoccupied d_{z^2} states just above the Fermi level. On comparing the

calculated free energy reaction pathways with corresponding available experimental results of catalyst performance, we find consistent agreement. The present study provides new detailed understanding into the covalent immobilisation and function of these metal-organic catalysts and the role that charge, defects and structure has on the free energy reaction pathways for the CO_2ERR.

4.1 Introduction

Covalent immobilisation of metal-organic complexes is currently a highly active field of research [**8**–**11**]. For experimental investigations of covalent immobilisation (or anchoring) of metal-organic complexes, complementary *ab initio* calculations such as through density functional theory (DFT) are not always performed, presumably due to the computational cost of calculating such large systems. This means a detailed and systematic theoretical understanding of the intermediate adsorption, structural and electronic properties of covalently immobilised metal-organic complexes is lacking.

Metal-organic complexes are promising candidates as molecular catalysts in the CO_2 electroreduction reaction (CO_2ERR) with Fe (Iron), Co (Cobalt) and Rh (Rhodium)-centred complexes showing the highest activity [**3**, **204**–**206**]. Rhodium is a rare earth metal with a cost of currently about $350 per gram, while the same amount of cobalt or iron is just a few cents, thus rhodium is economically unfavourable. Furthermore, rhodium porphyrin complexes can be prone to poisoning at the metal centre by axial ligation [**204**]. For Fe-porphyrin and Co-porphyrin or porphyrin-like structures, Fe-porphyrin has been shown to outperform Co-porphyrin under homogeneous conditions with a relatively higher CO product turnover by 30× [**12**–**15**]. However, comparisons have shown similar CO_2ERR performance between Fe-porphyrin and Co-porphyrin structures when immobilised on substrates such as carbon nanotubes (CNT) or carbon black (CB) [**9**, **15**, **16**].

The stability of a catalyst over time is just as important as its efficiency since long-lived catalysts improve economies of scale and time between catalyst replacement or regeneration. Experimental studies have shown Co-phthalocyanine (another metal-centred complex) shows

better stability over long operational times compared to Co-porphyrin complexes. Immobilised Co-phthalocyanine on CNT has been shown to maintain a steady efficiency and current density curve over a 24 hour run [**207**], while immobilised Co-tetraphenylporphyrin shows a slight reduction in performance after a few hours and a significant reduction after 20+ hours [**4**, **21**]. The deactivation of Co-tetraphenylporphyrin which accounts for its loss of performance over time is given by two mechanisms. The first is reductive, and involves off-centre binding of CO_2 on a ligand carbon site of Co-tetraphenylporphyrin in the $-2e$ charge state (two electrons are transferred from the electrode to the Co-tetraphenylporphyrin). The second is oxidative, adsorption of OH^- on the Co-centre resulting in a poor performing catalyst since CO_2 no longer forms a covalent bond [**4**].

Substrates used to immobilise metal-organic complexes should be electrically conducting or semi-conducting such that electron transfer can occur via the immobilisation site. Carbon cloth (CB) and large CNTs (> 20 Å in diameter) are common immobilisation platforms and are best represented by graphene (considered a conductor [**208**]) at the scale of first-principles (DFT) calculations. Experimental studies have compared the effect that different carbon substrates have on metal-organic complexes used in CO_2ERR such as CoPc which found CNTs outperformed graphite with regards to long term stability and CO product production [**22**]. CNTs smaller than 20 Å in diameter are best represented by the CNT itself and those larger by a graphene surface in DFT calculations. The zig-zag oriented CNT has electronic properties that are semiconducting for diameters larger than 5 Å, so smaller diameter CNTs can be considered as metallic in nature [**209**].

The smallest carbon nanotubes created experimentally have a diameter of 4 Å and were discovered encapsulated inside larger carbon nanotubes [**210**], while the smallest free-standing SWCNTs experimentally created had a diameter of 4.3 Å. The experimental discovery of 4 Å sized carbon nanotubes was backed by theoretical calculations which predicted carbon nanotubes down to a diameter of 4 Å were energetically stable and carbon nanotubes with a diameter of 5 Å or more had a stronger cohesive energy compared to finite graphene sheets [**211**]. Early (DFT) calculations showed zig-zag (n,0) single-walled carbon nanotubes became metallic for tubes with $n = 6$ and below, corresponding to a diameter of less than 5

Å [**209**]. The calculated density-of-states (DOS) of zig-zag, armchair and chiral CNT's have been verified experimentally [**212**, **213**].

At room temperature the structure of a surface will not be perfect but contain some defects due to entropy, in-fact defect sites are considered active sites for surface reactions, meaning a realistic interpretation of carbon electrodes should reflect this [**214**]. Defect sites on graphene and CNTs have been shown in most cases to be more reactive compared to perfect sites, meaning defects could assist in the immobilisation of metal-organic complexes [**214**–**221**]. Common defects include the Stone-Wales (SW) defect which is a C-C bond rotated 90^{o}, single vacancy (SV) and double vacancy (DV) defects which result from carbon atoms being removed from the lattice structure (see figure 4.1) [**213**, **222**, **223**]. For CNTs (and possibly graphene as well) SW and DV defects are expected to have the highest concentration [**222**] since they have the smallest formation energies (see table B1 in appendix B) and high migration energies making them stable even at temperatures well above room temperature [**223**]. Non-localised defects in graphene include line (grain boundary) defects of pentagon, heptagon and octagon structures and have been proposed as 'one-dimensional wire' candidates [**224**–**226**]. There are subtle differences between favoured defect configurations for graphene and CNTs; in-fact for CNTs defect formation energies are related to the CNT size due to curvature. The DV defect in graphene has the lowest formation energy for the 555-777 configuration, while for CNTs the 5-8-5 configuration has the lowest formation energy (see table B1 of appendix B).

The covalent immobilisation of phthalocyanine (Pc) metal-organic complexes on substrates such as CNTs has been studied for some time, facilitated by amino-substituted linkers [**227**–**230**]. These studies have shown the process of covalent immobilisation is more complicated, and historically did not garner much attention. However, recent experimental studies have demonstrated covalent immobilisation of cobalt porphyrin (CoP), cobalt tetraphenylporphyrin (CoTPP) and cobalt phthalocyanine (CoPc) on graphene and CNT substrates via linkers or substrate defects. In particular, Marianov *et al.* demonstrated covalent immobilisation of CoTPP via a phenylene linker on a carbon cloth electrode which showed an approximately two-fold increase in CO production and a 20% increase in Faradaic efficiency (FE) relative to non-covalently immobilised CoTPP under the same conditions [**21**]. An atomic linker

method for immobilising CoP has been demonstrated by Zhu *et al.* by which Cl bonded to the cobalt centre of CoP reacts with OH bonded on the CNT resulting in CoP-O-CNT via the cobalt centre and ·HCl. The resulting FE in this study is shown to be 98% which at the time of publication was one of the highest values using cobalt porphyrin [**23**]. Another study by Zhu *et al.* demonstrates immobilisation of CoPc by its cobalt centre on CNT via a pyridine linker. The FE is shown to be 98% with an impressive turn over frequency (TOF) of 34.5 s^{-1} (turn over frequency is the amount of product produced per site per second) [**24**]. Ma *et al.* investigated the immobilisation of CoPc over combinations of single and double vacancy defect sites, which due to dangling bonds form C-C or Co-C bonds with CoPc, and determined that CoPc immobilised by two C-C bonds at ligand locations gave the most efficient performance with an onset potential for CO_2ERR of -0.32 V [**231**]. Other studies have also investigated how different substrates can facilitate covalent immobilisation, but this is beyond the scope of this study which focuses on carbon-based substrates [**232**–**234**]. A summary of immobilised catalyst performances is given in table B2 of appendix B.

In this study extensive DFT calculations have been done to provide detailed insight into immobilised metal-organic catalysts for CO_2ERR, shedding light on the nature of the immobilisation, including the role of charge, substrate and structure. We investigate the aforementioned properties for covalently upright and linker immobilised CoTPP and CoPc catalysts. Focusing on the effect that immobilisation over defect sites on graphene and CNTs has on the CO_2ERR reaction performance. By doing a survey of possible carbon electrodes including defect sites and CNTs we address as realistically as possible the immobilisation of CoPc and CoTPP. For CNTs we use single-walled CNTs (SWCNT) close to the smallest SWCNTs experimentally created, in particular the (4,0) zig-zag and (4,4) armchair are used in this study as substrates and are investigated to determine if they provide any performance benefits compared to larger CNTs or graphene. The choice of such a small SWCNT and a large graphene sheet as substrates are examples of two extremes and will encompass all other SWCNTs and localised ripples and dimples in the graphene sheet. Charge difference and partial charge calculations are conducted to help explain changes in the CO_2ERR caused by defects and linkers, along with interesting results for the electronic behaviour between the immobilised catalyst and substrate. Many reaction pathways are determined, compared

and discussed in depth to help establish the best combination of defect, linker and catalyst for CO_2ERR. This new knowledge will be valuable for, and aid in, the design of future immobilised metal-organic catalysts for carbon dioxide reduction and transformation.

The paper is organised as follows: In the *Method* section the calculation method is presented; in the *Benzene Bonding* section we identify favourable bonding sites for CoPc and CoTPP using benzene as a computationally efficient probe; the *Covalent Catalyst Immobilisation* section compares the bonding of CoPc, CoTPP and benzene on different substrates and defect sites; the *Partial Charge Analysis* section compares calculated atomic charges for upright immobilised systems for different, charge states, substrates and defect sites; the *Intermediate Adsorption* section compares and discusses adsorption energies of CO, CO_2 and COOH adsorption intermediates on the various immobilised CoPc and CoTPP systems including linker systems; the final section *Reaction Pathways* provides a free energy reaction pathway comparison between the immobilised systems and determines the best performing systems.

4.2 Method

The DFT calculations are performed using the Vienna Ab initio Software Package (VASP) version 5.4.4 [**28**, **29**]. All calculations are conducted using the generalised gradient approximation (GGA) of Perdew, Burke and Ernzerhof (PBE) for the exchange-correlation functional [**30**]. In addition, dispersion corrections are included using the Becke-Johnson damping D3(BJ) [**31**–**33**]. All calculations are spin-polarised with an energy cut-off of 500 eV which is determined from convergence tests. The Γ-point is used for the **k**-point sampling owing to the large systems investigated in this study. For graphene systems hexagonal close packed (HCP) supercells are used with the exception of the line defect in graphene, and are the following sizes: $24.7 \times 22.2 \times 30$ Å for HCP, and $19.6 \times 18.95 \times 30$ Å for orthorhombic. CNT systems have an orthorhombic supercell with sizes $A \times 25 \times 30$ Å where A depends on the chirality/orientation (i.e. armchair or zig-zag) of the CNT used and is around 24-25 Å. For systems containing metal ions the Methfessel-Paxton scheme for smearing at the Fermi level is used, otherwise Gaussian smearing at the Fermi level is used. The atomic positions

are relaxed until the forces on all atoms are less than 0.01 eV/Å and electronic convergence criterion is set at 10^{-6} eV. For charged systems additional charge is included in the supercell by increasing the number of valence electrons. Atomic charges are calculated using the Voronoi deformation density (VDD) method [**154–156**] with charge densities calculated in VASP. Implicit water is implemented using the VASPSol extension for VASP [**152**, **153**].

4.3 Results & Discussion

4.3.1 Benzene Bonding

Benzene immobilisation is used to efficiently identify favourable bonding sites on defective graphene and different SWCNT types (size and orientation). We expect benzene to approximate the phenyl group ligand structure of cobalt tetraphenylporphyrin (CoTPP) and cobalt phthalocyanine (CoPc), which is the catalyst we investigate in later sections and the main subject of the present paper. Bonding sites of benzene and dissociated hydrogen (from the benzene molecule creating phenyl group) on Stone-Wales (SW), single vacancy (SV), double vacancy (DV), octagon-pentagon and heptagon-pentagon line defects are shown in figure 4.1. The bonding energies of benzene are shown in table 4.1. Geometries of favourable bonding systems are shown in figure B1 of appendix B and a comparison to larger molecules (CoPc) is shown in table B3 of appendix B, which demonstrates that CoPc exhibits the same site preference and trends as benzene. For the situation when H adsorbs on the graphene surface instead of forming H_2 see table B4 of appendix B. Benzene (C_6H_6) becomes phenyl group (C_6H_5) when a hydrogen is removed but for simplicity, we will refer to immobilised C_6H_5 as bonded benzene.

The bonding energy of benzene on graphene is defined in equation 4.1, where the H atom dissociated from benzene is taken to go into gas-phase H_2. The reason for including H dissociation in the bonding energy is to avoid calculating radical intermediates, as a result we can expect bonding energies to be systematically increased by the H dissociation process which is strongly endothermic. However, this will have no impact on the relative accuracy of

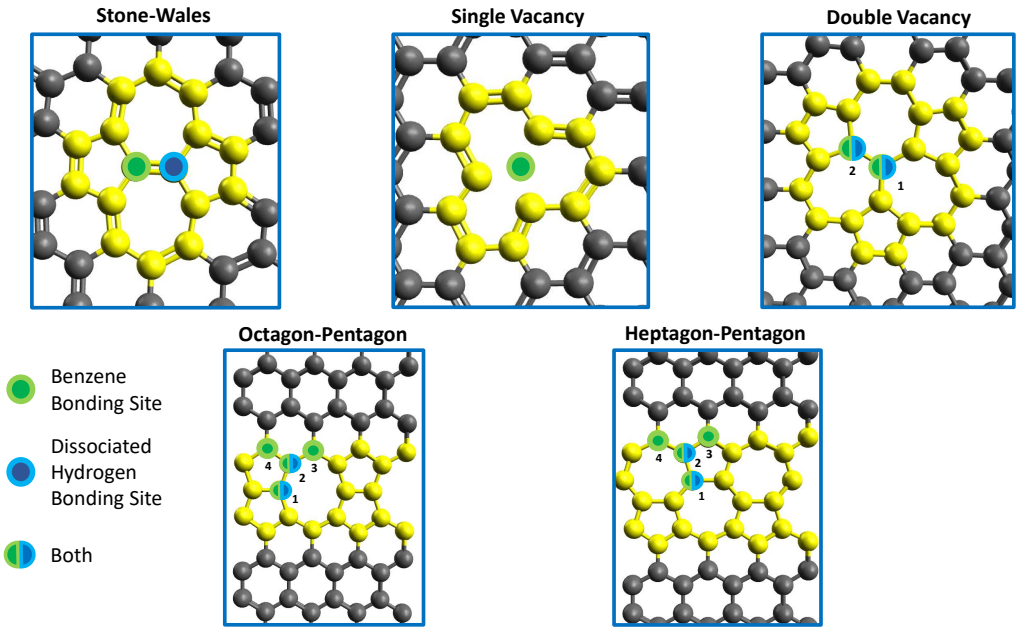

FIGURE 4.1. Benzene and dissociated Hydrogen bonding sites on Stone-Wales (SW), single vacancy (SV), double vacancy (DV), octagon-pentagon and heptagon-pentagon line defects. Atoms highlighted green, blue, and both green and blue are benzene, hydrogen and benzene and hydrogen bonding sites, respectively. Yellow atoms make up the defect site.

the bonding energies.

$$E_{\text{bond}} = E_{\text{graphene-benzene}} - E_{\text{graphene}} - E_{\text{benzene}} - E_{0.5\text{H}_2} \tag{4.1}$$

Benzene bonded to the SV defect which is the least stable defect considered, shows the strongest bonding energy (-1.33 eV) even when taking into account the energy required to remove one of the benzene hydrogen atoms, and forming H_2 elsewhere. Benzene bonding on the SW defect is found to be slightly more favourable by ~ 0.1 eV when H adsorbs on the defect next to benzene rather than forming H_2 (see table B4 of appendix B). This is also found for the DV and line defects. For the DV defect we find bonding at site 2 (defect off-centre) more favourable compared to site 1 (defect centre) for the free H_2 scenario, while the H surface adsorption scenario shows little difference between bonding sites. Similar to the SW defect, the line defects also show similar bonding energies for both H adsorption scenarios.

Defect	Bonding site	Bonding energy (eV)
Pristine	-	**1.96**
Stone-Wales	On-defect	**0.67**
	Off-defect	1.87
Single Vacancy	-	**-1.33**
Double-vacancy	Site 1	1.64
	Site 2	**0.49**
Line: octagon-pentagon	Site 1	**0.76**
	Site 2	0.9
	Site 3	1.79
	Site 4	1.09
	Off-defect	2.07
Line: heptagon-pentagon	Site 1	**1.29**
	Site 2	1.4
	Site 3	1.88
	Site 4	1.82
	Off-defect	2.2

TABLE 4.1. Benzene bonding energies on pristine and defective graphene, with bonding sites indicated in figure 4.1. Favourable bonding energies are shown in **bold** and is defined as the lowest bonding energy for each defect. Bonding energies are calculated using equation 4.1 with the H atom of the benzene molecule going to a free H_2 molecule.

The octagon-pentagon line defect shows lower (stronger) bonding energies for all the sites compared to the heptagon-pentagon line defect. The octagon-pentagon line defect is known to have a high density-of-states close to the Fermi level and bands crossing the Fermi level so it is expected to have properties of an 'electric wire' [**226**]. The heptagon-pentagon line defect has a semiconducting character, meaning the bonding or grafting of molecules such as benzene on the heptagon-pentagon line defect is expected to be weaker compared to the octagon-pentagon line defect, consistent with the calculated bonding energies. The atomic geometry of all the favourable benzene bonding structures are shown in figure B1 of appendix B.

Based on the results from table 4.1 and table B4 in appendix B we find that in most cases only slight differences in benzene bonding energy are observed between the two H treatment scenarios (adsorbing on the graphene surface or combining with another H atom to form free H_2) and so calculations from here on in involving H desorption will be taken to form free H_2.

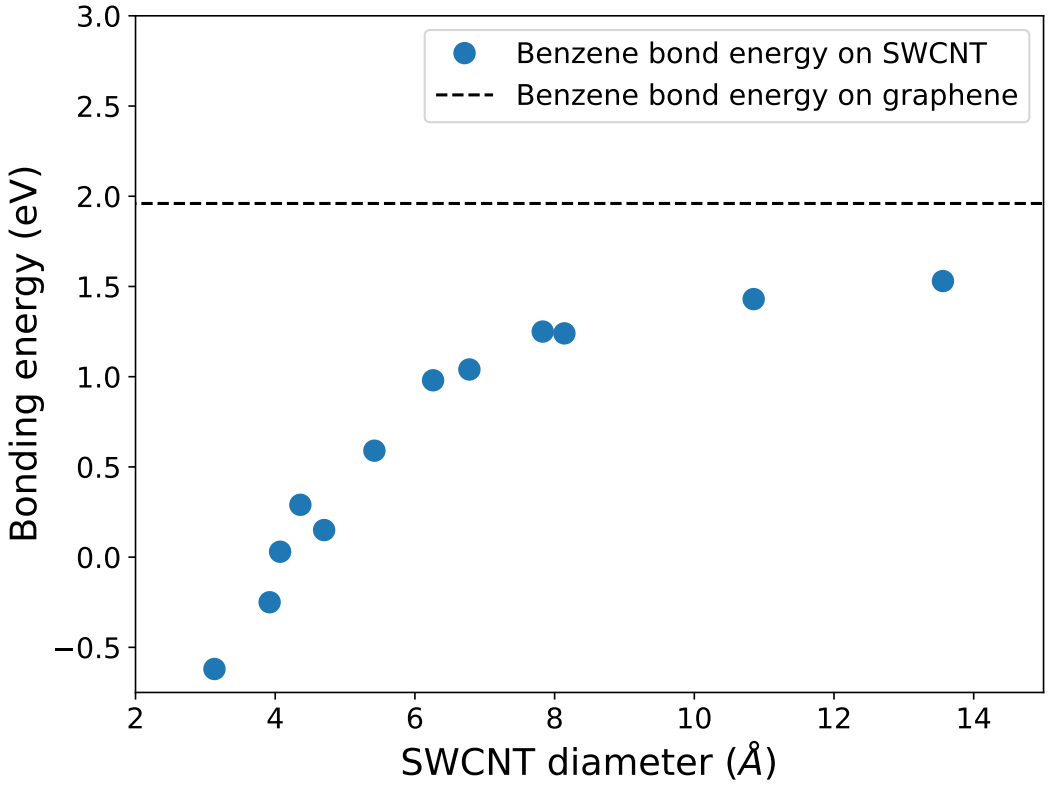

FIGURE 4.2. Benzene bonding on different sized non-chiral single-walled carbon nanotubes (SWCNTs). The black dashed line indicates the bonding energy of benzene on pristine graphene. Adsorption energy values are listed in table B5 of appendix B.

Also, H adsorption on the graphene surface is unlikely to be realised experimentally under normal room temperature CO_2ERR conditions.

Figure 4.2 shows the bonding energy of benzene on different sized non-chiral, single-walled carbon nanotubes (SWCNT). Smaller diameter SWCNTs are shown to be more reactive, with diameters less than 4Å having favourable benzene bonding energies. Benzene bonding on larger diameter SWCNTs gradually trends towards the bonding energy of benzene on pristine graphene. As stated in the introduction in this study we investigate the performance of the (4,0) zig-zag and (4,4) armchair SWCNTs as immobilisation substrates for the CoTPP and CoPc CO_2ERR catalysts. The (4,0) SWCNT has a diameter of 3.1 Å, slightly smaller than the experimentally created (3,3) and (5,0) SWCNTs [**210**, **235**] which have diameters of 4.0 Å

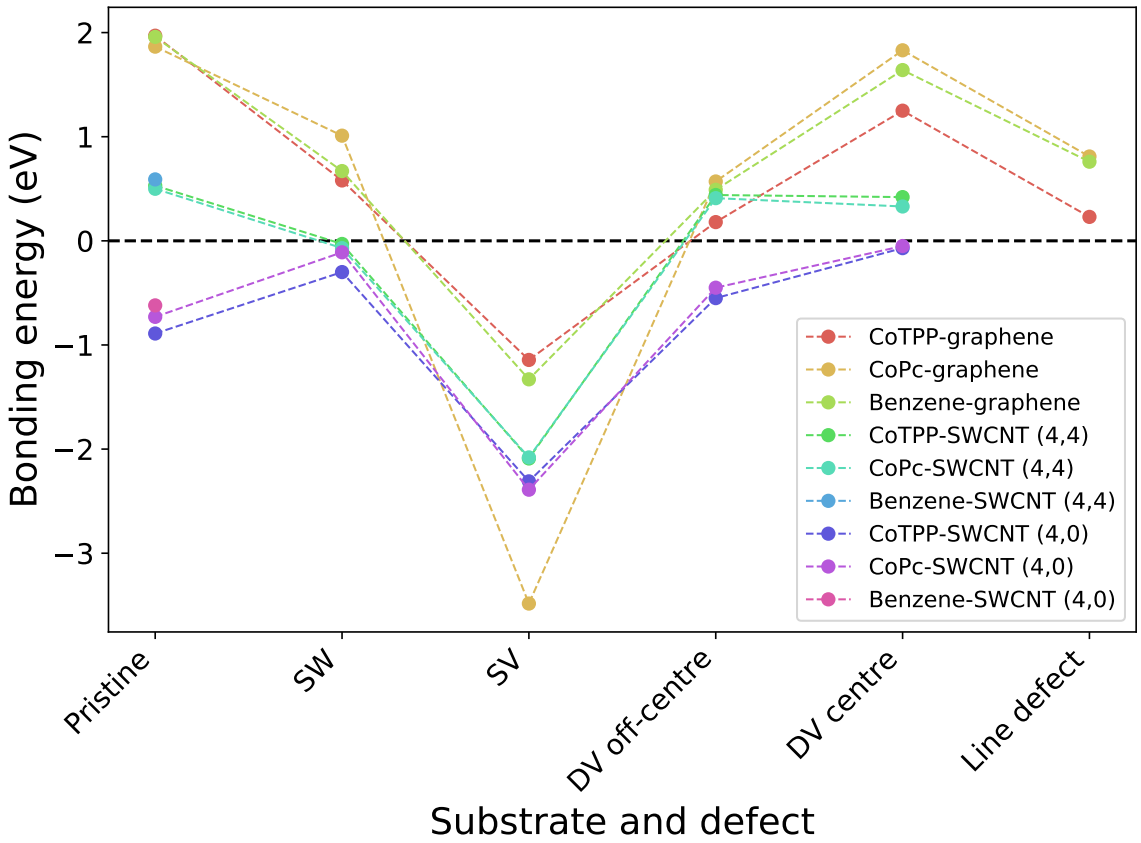

FIGURE 4.3. Bonding energy comparison of neutral upright cobalt-tetraphenylporphyrin (CoTPP), cobalt-phthalocyanine (CoPc) and benzene on pristine and defective graphene and single-walled carbon nanotube (SWCNT) substrates. The line defect considered is in the octagon-pentagon configuration. Bonding energies have been calculated assuming that the dissociated H from CoTPP/CoPc/benzene goes to form H_2 elsewhere (see equation 4.1).

and 3.9 Å respectively. We also find that the bonding energy of benzene on these SWCNTs are -0.62 eV for (4,0) SWCNT, -0.25 eV for the (5,0) SWCNT, 0.03 eV for the (3,3) eV and 0.59 of the (4,4) SWCNT. The idea of using such a small SWCNT is to amplify the bond curvature of a 'rolled up' graphene sheet and to investigate its effect on the intermediate adsorption energies and reaction pathways.

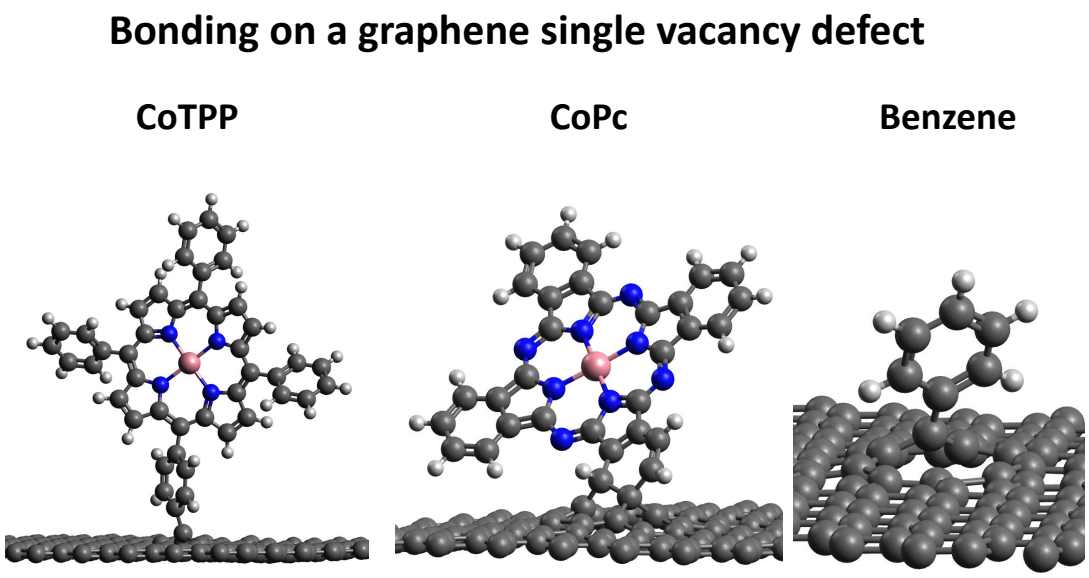

FIGURE 4.4. Relaxed geometries of CoTPP, CoPc and benzene bonded on a single vacancy (SV) defect on graphene. Gray atoms are carbon, white atoms are hydrogen, blue atoms are nitrogen and pink atoms are cobalt.

4.3.2 Covalent Catalyst Immobilisation

To determine if there are any differences between the bond strength of CoTPP, CoPc and benzene to the substrate we compare their bonding energies and relaxed geometries. Figure 4.3 shows the bonding energy of CoTPP, CoPc and benzene on pristine and defective graphene and SWCNTs (benzene bonding energies are only calculated for pristine SWCNT) of type (4,0) and (4,4) (zig-zag and armchair, respectively). The bonding energies in figure 4.3 are also listed in table B6 in appendix B. We find benzene, CoPc and CoTPP all have similar bonding energies on pristine graphene which is due to similar C-C bonds and a stable pristine graphene substrate. For pristine SWCNT substrates there is again little difference between CoPc, CoTPP and benzene bonding energies but bonding energies relative to graphene are stronger, a result of the reactive nature of small SWCNTs due to their high bond curvature [**211**, **236**]. We also observe that the smaller diameter zig-zag (4,0) SWCNT shows consistently stronger bonding energies compared to the larger armchair (4,4) SWCNT as expected.

The SW and DV (centre and off-centre or site 1 and site 2 in figure 4.1) defect sites have similar bonding energies for CoTPP, CoPc and benzene with the DV off-centre site being slightly stronger (an average of 0.4 eV between CoTPP, CoPc and benzene). The SW and DV centre defect sites have average bonding energies (for CoTPP, CoPc and benzene) of approximately 0.75 eV and 1.6 eV respectively. For the line defect (octagon-pentagon configuration) in graphene we have an average bonding energy of 0.6 eV between CoTPP, CoPc and benzene which is only slightly weaker compared to DV off-centre bonding. As expected the strongest bonding energy comes from the single vacancy defect which has bonding energies of -1.14 eV, -3.48 eV and -1.33 eV for CoTPP, CoPc and benzene, respectively. The strong nature of these bonds is due to the highly reactive dangling bond associated with the SV defect [**223**]. The bonding of CoPc on SV defective graphene shows a much more favourable bonding energy compared to CoTPP and benzene because it forms three C-C bonds with the graphene substrate for two of its carbon ligand atoms, unlike CoTPP and benzene which both form one C-C bond with the graphene substrate, see figure 4.4. In general, stable defects such as SW, DV and Line defects show little difference between bonding energies for CoTPP, CoPc and benzene, on the other hand the SV defect which can be considered relatively unstable, yields a large difference in the bonding energies between CoTPP, CoPc and benzene.

For the SWCNT substrates, just like the graphene substrate, the SV defect shows the strongest bonding energy for CoTPP, CoPc and benzene on any pristine of defective SWCNT site. Although for CoTPP and CoPc the bonding energies are similar on the SWCNT SV defect, unlike for graphene which has a 2.9 eV difference between bonding energies for CoTPP and CoPc. We observe similar bonding energies for pristine, SW and DV off-centre defect bonding of CoTPP and CoPc on both zig-zag and armchair SWCNTs. The SW and DV centre defect sites show slightly negative bonding energies between -0.05 and -0.10 eV on both SWCNTs indicating favourable bonding given H is dissociated from CoPc/CoTPP to form free H_2. For pristine and DV off-centre defect sites on SWCNT (4,0) bonding energies are found to be stronger with bonding energies between -0.4 and -0.9 eV. Therefore, as shown by the dark blue and purples lines on figure 4.3, we find SWCNT substrates show the most favourable bonding energies compared to graphene for the covalent immobilisation of CoTPP, CoPc and benzene.

Overall, its clear from figure 4.3 that defect sites in general facilitate surface adsorption (which indicates as to why defect sites are considered active sites [**214**]) and thus facilitate the covalent immobilisation of CoPc and CoTPP catalysts. The graphene substrate consistently shows immobilisation on a defect site is preferred compared to a pristine site, however, exceptions to this trend are found for the SWCNT substrates the smaller (4,0) SWCNT shows pristine sites are favoured compared to SW, and DV defect sites.

4.3.3 Partial Charge Analysis

Atomic charge analysis allows us to establish how much charge is localised on each atom which can allude to the role charge plays in both the immobilisation of CoPc and CoTPP and the respective intermediate adsorption behaviour. Table 4.2 lists the net Voronoi charges [**154–156**] for the CoTPP- and CoPc-graphene systems investigated which are compared to the non-immobilised homogeneous CoTPP and CoPc catalysts. The *Co* column is the charge on the cobalt atom at the centre of the CoPc and CoTPP structures. The *CoPc/CoTPP* column is the total charge of the immobilised CoPc and CoTPP molecules. The *Defect* column is the total charge of the graphene defect as highlighted in figure 4.1 in yellow. The *Graphene* column is the charge of the graphene sheet including the defect. The *Homogeneous* charge values are for 'free' (not immobilised) CoPc and CoTPP molecules. In the *CoPc/CoTPP* column we see the additional charge included in the supercell for the homogeneous case is completely localised on the CoPc and CoTPP molecules, while for the immobilised systems the additional charge is shared between the CoTPP/CoPc catalyst and graphene substrate shown in the *Graphene* column. For homogeneous CoTPP [**4**, **21**] and CoPc [**19**, **23**, **231**] there is consensus that the CO_2ERR is facilitated when in the reduced $-1e$ charge state (Co^{I}TPP), our calculations however for the adsorption of CO_2 on homogeneous CoPc in implicit water shows a weak adsorption energy (-0.13 eV) in the $-1e$ charge state and stronger adsorption energy (-0.35 eV) in the $-2e$ charge state. CO_2 adsorption for the $-2e$ charge state shows good agreement with the previously reported adsorption free energies (~ -0.5 eV) of CO_2 on homogeneous CoPc calculated in explicit water with a small amount of hydronium for charge transfer [**18**]. It has been proposed more rigid ligand structures such as those for

Graphene Defect	Catalyst	Total charge (e)	Co (e)	CoPc/CoTPP (e)	Defect (e)	Graphene (e)
Homogeneous	CoPc	Neutral	0.99	0.00	N/A	N/A
		-1	0.86	-1.00	N/A	N/A
		-2	0.84	-2.00	N/A	N/A
	CoTPP	Neutral	0.98	0.00	N/A	N/A
		-1	0.82	-1.00	N/A	N/A
		-2	0.82	-2.00	N/A	N/A
Pristine	CoPc	Neutral	0.97	-0.41	N/A	0.41
		-1	0.91	-0.73	N/A	-0.27
		-2	0.83	-1.16	N/A	-0.84
		-3	0.81	-1.29	N/A	-1.71
	CoTPP	Neutral	0.99	-0.24	N/A	0.24
		-1	0.94	-0.49	N/A	-0.51
		-2	0.86	-0.91	N/A	-1.08
		-3	0.81	-1.25	N/A	-1.75
Stone-Wales	CoPc	Neutral	0.98	-0.42	0.13	0.42
		-1	0.92	-0.98	0.04	-0.29
		-2	0.83	-1.20	-0.01	-0.80
		-3	0.81	-1.35	-0.08	-1.65
	CoTPP	Neutral	0.99	-0.18	0.07	0.18
		-1	0.95	-0.38	-0.04	-0.62
		-2	0.86	-0.84	-0.08	-1.16
		-3	0.80	-1.17	-0.13	-1.83
Line: Oct-Pent	CoPc	Neutral	0.99	-0.34	0.41	0.34
		-1	0.93	-0.65	0.19	-0.35
		-2	0.86	-1.00	-0.02	-1.00
		-3	0.81	-1.35	-0.24	-1.65
	CoTPP	Neutral	0.99	-0.17	0.13	0.17
		-1	0.89	-0.40	-0.13	-0.60
		-2	0.88	-0.75	-0.34	-1.25
		-3	0.82	-1.13	-0.53	-1.87
Single Vacancy	CoPc	Neutral	0.97	-0.40	0.14	0.40
		-1	0.92	-0.70	0.05	-0.31
		-2	0.85	-1.12	-0.01	-0.88
		-3	0.84	-1.22	-0.06	-1.78
	CoTPP	Neutral	0.99	-0.15	0.07	0.15
		-1	0.95	-0.45	0.00	-0.55
		-2	0.87	-0.85	-0.06	-1.15
		-3	0.82	-1.18	-0.09	-1.82
Double Vacancy: centre	CoPc	Neutral	0.99	-0.32	0.17	0.32
		-1	0.93	-0.60	0.05	-0.40
		-2	0.86	-0.95	-0.06	-1.05
		-3	0.82	-1.28	-0.16	-1.72
	CoTPP	Neutral	1.00	-0.17	0.14	0.17
		-1	0.96	-0.37	-0.01	-0.63
		-2	0.90	-0.71	-0.11	-1.28
		-3	0.84	-1.06	-0.22	-1.94
Double Vacancy: Off-centre	CoPc	Neutral	1.00	-0.35	0.19	0.35
		-1	0.93	-0.61	0.07	-0.39
		-2	0.82	-1.17	0.03	-0.83
		-3	0.81	-1.28	-0.10	-1.72
	CoTPP	Neutral	0.98	-0.22	0.08	0.22
		-1	0.89	-0.44	-0.05	-0.56
		-2	0.87	-0.87	-0.12	-1.13
		-3	0.81	-1.20	-0.21	-1.80

TABLE 4.2. Net Voronoi charges (in units of e) of atoms and structures of interest for the immobilised CoPc and CoTPP molecules on defective graphene. Charge analysis has been done for the neutral, $-1e$, $-2e$ and $-3e$ charge states of the immobilised systems and neutral, $-1e$, $-2e$ charge states for the homogeneous systems.

CoPc facilitate an increase in nucleophilicity and thus facilitate a $-2e$ charge state [**237**]. We are interested in finding the charge on the active cobalt site (*Co* column) and CoTPP molecule (*CoPc/CoTPP* column) of the CoTPP immobilised systems that compares with the homogeneous $-1e$ charge state (0.82e and $-1e$ charge for the Co centre and CoTPP molecule). Due to some uncertainty around the ideal charge state of homogeneous CoPc we will use the same net system charge as determined for CoTPP.

In almost all cases of CoTPP immobilised on graphene (pristine and defective) we find the $-3e$ charge state has similar or identical charge on the cobalt centre compared to the same charge on the cobalt centre of the homogeneous CoTPP in the $-1e$ and $-2e$ charge states. The $-3e$ charge state for both CoPc and CoTPP immobilised on graphene shows the total charge on the CoPc and CoTPP catalysts to be slightly larger than the $-1e$ charge for the homogeneous systems. A slight decrease in the charge localised on immobilised CoPc and CoTPP (by approximately 0.1-0.2e) is found for defective graphene substrates meaning these defects can be thought of as charge sinks, which is confirmed in the *Defect* column. Interestingly the charge sink behaviour seems more apparent for CoTPP compared to CoPc since CoPc immobilised over defective sites attracts more of the charge compared to pristine graphene, but defective sites seem to draw charge away from immobilised CoTPP. A charge density comparison for CoPc and CoTPP is shown in figure 4.5 which illustrates defect and immobilisation sites gaining charge which would otherwise be localised on the CoPc/CoTPP catalysts in their homogeneous state. Charge densities for the other systems are shown in figure B2 of appendix B.

Comparing bonding of CoPc and CoTPP on graphene defect sites for the $-3e$ charge state, we see little to no difference in the net charge of CoPc when it is bonded on either the SW or line (octagon-pentagon) defect ($1.35e$ on both defects), the same is true for CoTPP with only a slight difference in net charge ($0.04e$) between SW and the line defect. A more significant difference is found for CoTPP bonded on SV and DV defects with CoTPP bonded to a DV off-centre site showing the highest net charge value for CoTPP on a defect site of $-1.20e$, followed by $-1.18e$ for CoTPP on a SV site. This is about $-0.13e$ to $-0.15e$ more compared to bonding at the centre of the DV defect which shows the lowest net charge value for CoTPP

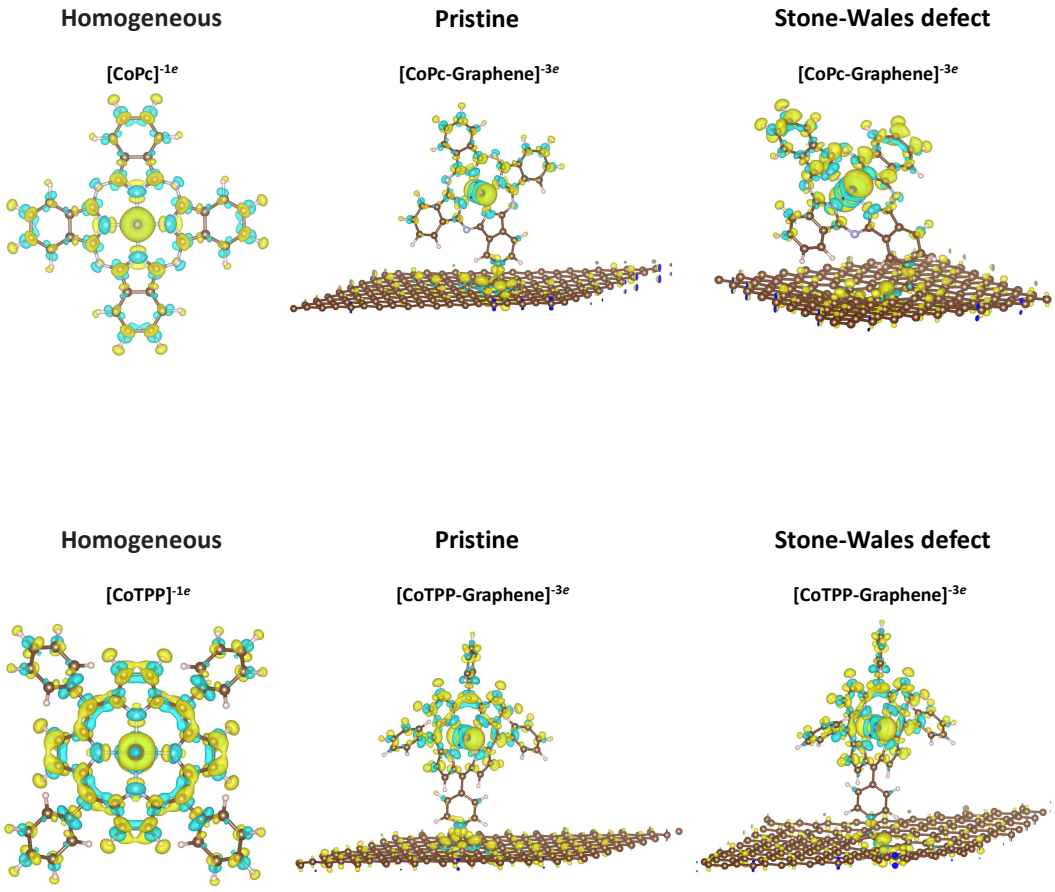

FIGURE 4.5. Charge density difference of CoPc (top) and CoTPP (bottom) in their reduced states. Regions which gain charge population are shown in yellow and those of charge depletion are shown in blue. An isosurface value of 0.01 electrons/Å^3 is used. The charge difference is determined by subtracting the neutral charge density from the $-1e$ (homogeneous) or $-3e$ (immobilised) charge densities.

of $-1.06e$. However, CoTPP bonded on a pristine graphene substrate still shows the highest net charge value of $1.25e$ localised on CoTPP. We also find that the CoPc molecule has a tendency to attract more charge compared to CoTPP, and to some extent the defective graphene substrate (with exception of the DV defect). This is because the CoPc molecule bonded on graphene defect sites is able to attract more charge compared to when it is bonded on pristine graphene which is in agreement with previous studies [**237**]. In particular CoPc

bonded to the SW and octagon-pentagon line defect show a net charge of $-1.35e$ is localised on the CoPc molecule compared to $-1.29e$ for the pristine site, $-1.28e$ for both DV sites and $-1.22e$ for the SV site. Therefore, all but the pristine and SV defect systems show an increase of $\sim -0.2e$ localised on CoPc compared to CoTPP bonded on the same defect sites.

SWCNT Defect	**System**	**Total Charge** (e)	**Co** (e)	**CoTPP** (e)	**Defect** (e)	**SWCNT** (e)
Pristine	CoPc	Neutral	1.00	0.16	N/A	-0.15
		-1	0.97	-0.29	N/A	-0.71
		-2	0.87	-0.74	N/A	-1.26
		-3	0.82	-1.13	N/A	-1.87
	CoTPP	Neutral	0.96	0.31	N/A	-0.31
		-1	0.98	-0.14	N/A	-0.86
		-2	0.90	-0.56	N/A	-1.44
		-3	0.84	-0.95	N/A	-2.05
Stone-Wales	CoPc	Neutral	1.00	0.09	0.15	-0.09
		-1	0.97	-0.34	0.05	-0.66
		-2	0.88	-0.73	-0.05	-1.27
		-3	0.83	-1.13	-0.16	-1.87
	CoTPP	Neutral	0.98	0.21	0.13	-0.21
		-1	0.98	-0.16	-0.03	-0.85
		-2	0.90	-0.55	-0.13	-1.45
		-3	0.84	-0.93	-0.25	-2.07

TABLE 4.3. Net Voronoi charges (e) for atoms and structures of interest in the immobilised CoPc/CoTPP molecule on pristine and defective SWCNT (4,0). Charge analysis has been done for the neutral, -1e, -2e and -3e charge states of all the systems.

Table 4.3 lists the net Voronoi charges for CoPc and CoTPP covalently immobilised on pristine and SW sites of a (4,0) zig-zag SWCNT. The *Co* column is the charge on the cobalt atom at the centre of the CoPc/CoTPP molecule. The *CoPc/CoTPP* column is the total charge of the immobilised CoPc/CoTPP molecule. The *Defect* column is the total charge of the SWCNT defect. The *SWCNT* column is the charge of the graphene sheet including the defect.

As per the graphene case we also find that $-3e$ charge state is required to match the cobalt charge for the homogeneous $-1e$ charge state. A standout difference between the graphene and SWCNT Voronoi charges is more charge becomes localised on the SWCNT substrate compared to graphene for all CoPc/CoTPP systems and defect cases. For example, the charge localised on CoTPP immobilised on pristine SWCNT is -0.95e which is $-0.3e$ less compared to the same system on a pristine graphene substrate. This charge attraction behaviour could

possibly be explained by the metallic nature and/or the unique sp^2-sp^3 hybridisation of such a small SWCNT, but the charge localised on the cobalt centre (see the *Co* column) is only slightly less by ~ 0.02 compared to the comparative graphene systems. For CoPc there is no significant difference in charge localisation when comparing immobilisation on a pristine SWCNT and a SW defective SWCNT. However, we do see a slight change for CoTPP in which $-0.02e$ less charge is localised on the CoTPP which is gained by the SWCNT substrate; this would be caused by the defect charge sink behaviour, although it is significantly less prominent compared to graphene. The results show that the electronic character of the small (4,0) SWCNT dominates how charge is localised with defect sites shown to have little to no effect on the charge localisation.

4.3.4 Intermediate Adsorption

The CO_2ERR involves CO_2, COOH and CO intermediates adsorbed on the cobalt centre of CoPc or CoTPP. The adsorption energy of these intermediates is calculated using equation 4.2.

$$E_{\text{ads}} = E_{\text{graphene-CoPc/CoTPP-COxx}} - E_{\text{graphene-CoPc/CoTPP}} - E_{\text{COxx}} \tag{4.2}$$

In equation 4.2 $E_{\text{graphene-CoPc/CoTPP-COxx}}$ is the energy of the covalently immobilised CoPc/CoTPP system with adsorbed COxx intermediate, $E_{\text{graphene-CoPc/CoTPP}}$ is the energy of the covalently immobilised CoPc/CoTPP system and E_{COxx} is the energy of the CO, CO_2 or COOH intermediate. For intermediate adsorption on the homogeneous system, equation 4.2 is used but without the substrate contribution, i.e. the terms $E_{\text{graphene-CoPc/CoTPP-COxx}}$ and $E_{\text{graphene-CoPc/CoTPP}}$ become $E_{\text{CoPc/CoTPP-COxx}}$ and $E_{\text{CoPc/CoTPP}}$ respectively.

4.3.4.1 Direct Covalent Immobilisation

Figure 4.6 summarises the adsorption energies of the CO, CO_2 and COOH intermediates on immobilised CoPc and CoTPP for the $-1e$ and $-3e$ charge states of the system. These adsorption energies are listed in table B7 of appendix B. We observe for the $-1e$ charge state,

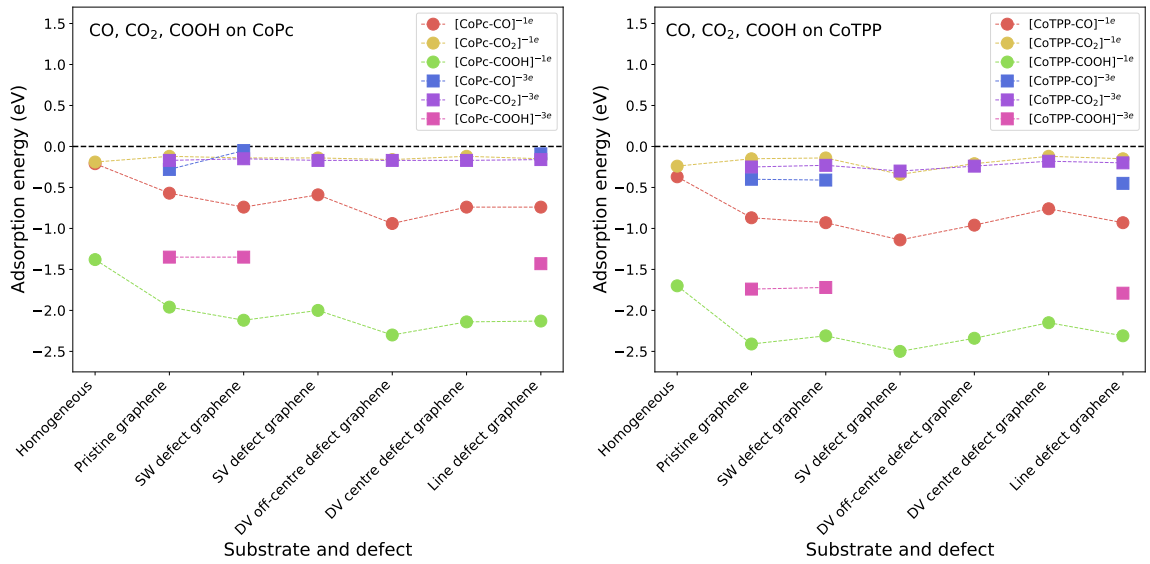

FIGURE 4.6. Adsorption energies of CO, CO_2 and COOH on CoPc and CoTPP which are immobilised on pristine and defective graphene substrates. The *Homogeneous* case is when CoPc and CoTPP are not immobilised (free molecule). The $-1e$ charge state and $-3e$ charge state (one and three electrons added to the supercell respectively) are investigated based on the results from table 4.2.

adsorption energies for CO_2 on CoPc and CoTPP are not strongly influenced by the presence of a defect site on graphene on which CoPc and CoTPP are covalently immobilised. For CoPc increasing the charge state of the system does not significantly affect the adsorption energy of CO_2 on the cobalt centre. This is because CO_2 tends to be weakly bonded to the cobalt centre of CoPc particularly in gas-phase, which these calculation are (see figure B3 in appendix B). For CoTPP we find adsorption of CO_2 is slightly more favourable in the $-3e$ charge state compared to the $-1e$ charge state, this is because CO_2 forms a stronger C-Co bond, with the bond length changing from 3.26 Å to 2.03 Å, becoming covalently bonded. This is shown in figure 4.7. Adsorption energies of CO_2 have been tested for a range of charge states from neutral to $-6e$ as shown in table B8 of appendix B. We find that adsorption energies of CO_2 do not change significantly (only by 0.02 eV) for charge states higher than $-3e$.

The difference in adsorption energy of the homogeneous and immobilised CoPc/CoTPP in the $-1e$ charge state is likely related to the charge localised on the cobalt centre of CoPc/CoTPP and the entire CoPc/CoTPP molecule (see table 4.2), with more positive charge (less electron

charge density) showing stronger adsorption energy for CO and COOH intermediates. A strong adsorption energy for CO would indicate that the CoPc/CoTPP complexes would be prone to CO poisoning, but previous studies for CoTPP have shown CO poisoning is an unlikely deactivation process [**4**]. We observe for the covalently immobilised systems in the $-3e$ charge state, adsorption energies for CO (-0.28 eV for CoPc and -0.40 eV for CoTPP on pristine graphene) and COOH (-1.35 eV for CoPc and -1.74 eV for CoTPP on pristine graphene) are close to the homogeneous adsorption energies in the $-1e$ charge state (CO: -0.21 eV for CoPc and -0.37 eV for CoTPP; COOH: -1.38 eV for CoPc and -1.70 eV for CoTPP). This is expected given the charge on the cobalt centre in table 4.2 is similar for the homogeneous systems in the $-1e$ charge state and the immobilised systems in the $-3e$ charge state. In particular CO adsorption on CoPc immobilised over defect sites (SW and line defects) in the $-3e$ charge state is weaker by ~ 0.2 eV compared to pristine sites. Different defect sites (particularly for the $-1e$ charge state) are also found to cause slight changes in the adsorption energy of CO and COOH which does not follow the relation found for the cobalt centre charge. For example, in the $-1e$ charge state immobilisation on the DV off-centre defect shows one of the strongest adsorption energies for CO and COOH but the cobalt centre charges are generally more negative compared to other defect sites, except the line defect. This could be caused by electronic changes in the substrate; it is known that the line defect and double vacancy defect in the 555-777 configuration have a high density of states close to the Fermi level compared to pristine graphene and other graphene defects considered here [**226**, **238**].

In table B9 and figure B4 of appendix the CO, CO_2 and COOH adsorption energies are shown for different sized and oriented SWCNTs (4,0) zig-zag and (4,4) armchair, along with pristine and SW defect immobilisation sites. The differences in adsorption energies show the same relation as figure 4.6 with the $-3e$ charge state being required to achieve similar adsorption energies to the homogeneous case in the $-1e$ charge state (i.e. the Co^{I} charge state of the cobalt centre). The (4,0) SWCNT systems show similar and in some cases stronger intermediate adsorption energies compared to the larger (4,4) SWCNT systems. For CoPc and CoTPP immobilised on (4,0) SWCNT we find defect sites cause slight changes in the CO, CO_2 and COOH adsorption energies as a result of differences in the electronic structure

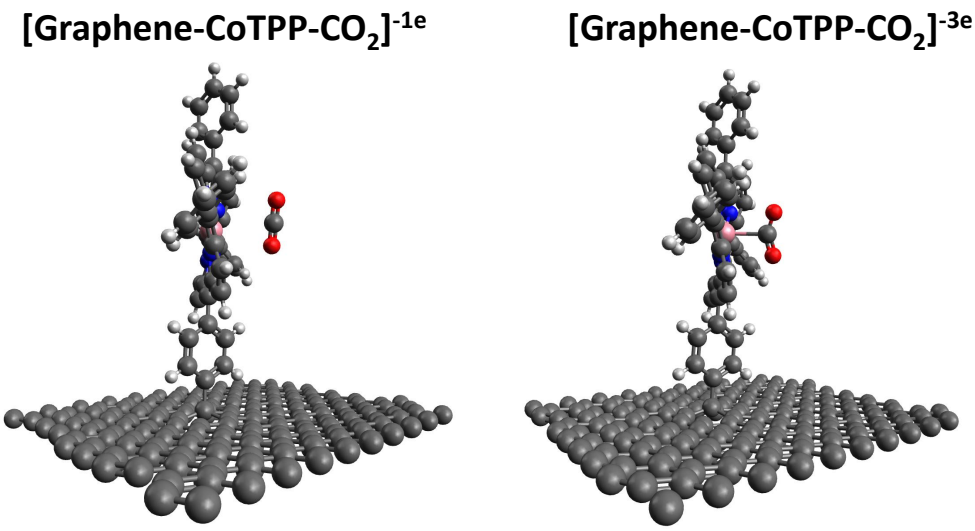

FIGURE 4.7. The relaxed geometries of immobilised CoTPP on pristine graphene with CO_2 adsorbed for the $-1e$ and $-3e$ charge states, shown on the left and right respectively. White atoms are hydrogen, grey atoms are carbon, blue atoms are nitrogen, red atoms are oxygen and the pink atom is cobalt.

of the substrate and/or differences in the charge localisation particularly on the cobalt centre active site.

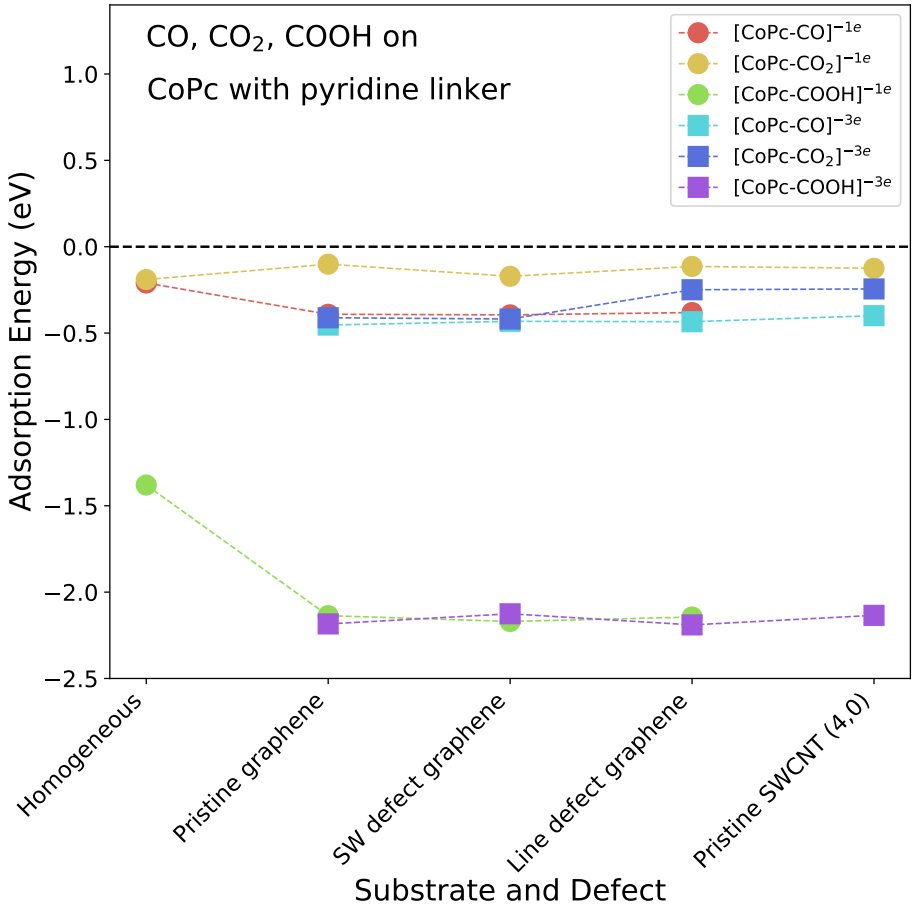

FIGURE 4.8. Adsorption energies of CO, CO_2 and COOH intermediates on CoPc that is immobilised via pyridine linker on both pristine and defective graphene and pristine SWCNT (4,0). The homogeneous case is when CoPc is considered a 'free molecule'.

4.3.4.2 Immobilisation via Linkers

Figure 4.8 shows the adsorption energies of the aforementioned intermediates on CoPc that have been immobilised on graphene using a pyridine linker bonded to the cobalt centre of the CoPc catalyst (see figure 4.9). Adsorption energy values are listed in table B10 of appendix B. We find that in the $-3e$ charge state CO_2 has a larger adsorption energy of -0.4 eV for CoPc immobilised via pyridine linker on graphene (pristine and SW sites) compared to analogous systems in figure 4.6 which have adsorption energies of CO_2 on CoPc to be between -0.1 and -0.2 eV. For CoPc immobilised via pyridine linker on the graphene line defect and pristine SWCNT in the $-3e$ charge state we obtain adsorption energies of -0.25 eV for CO_2 which is

similar to adsorption energies of CO_2 on CoTPP immobilised on graphene. Figure 4.10 shows that the charge density of the additional $-3e$ charge is localised to a higher extent on the line defect compared to pristine graphene meaning we can assume less charge localised on the immobilised CoPc molecule and/or connecting structures. This is confirmed by the Voronoi charge analysis shown in table B11 of appendix B where we find $0.2e$ and $0.3e$ more charge is localised on the line defect graphene substrate compared to the SW and pristine graphene substrates respectively. The charge on the CoPc molecules is similar between the substrates but the net charge on the N atom of the pyridine linker which bonds to the cobalt centre of CoPc is about $0.2e$ less for the line defect compared to the SW and pristine substrates. This difference in charge localisation could account for the difference in CO_2 adsorption energies between the line defect substrate ($-2.06e$), SW ($-1.96e$) and pristine ($-1.86e$) substrates shown in figure 4.8. We find the pyridine immobilised cobalt centre of CoPc shows a reduced nucleophilic character with a net charge of $\sim 1.03e$, which is about $0.2e$ less compared to upright-immobilised CoPc as seen in table 4.2 but the total net charge of the pyridine nitrogen atom and cobalt centre (which are bonded) is $0.34e$. This is indicates that the net charge on the cobalt centre alone may not represent the 'true' nucleophilicity for systems with active site linker immobilisation and would then be in agreement with experimental observations that these systems are found to be relatively more nucleophilic [**24**, **237**]. The adsorption energies are reflected by the atomic structure shown in figure 4.9 with the leftmost geometry representing CO_2 adsorption for the $-3e$ charge state which shows a physisorbed system, while the centre and right geometries are for CO_2 adsorption on pyridine-immobilised CoPc which forms a stronger covalent bond with the cobalt centre.

The adsorption of COOH on pyridine-immobilised CoPc in the $-3e$ charge state shows similar adsorption energies and behaviour to the systems in figure 4.6 due to its high reactivity, which is also the case for CO adsorption. We find that the adsorption energy for CO matches the adsorption energy for CO_2 on CoPc immobilised via pyridine on pristine and SW-defective graphene with a slight difference ($\sim 0.2 - 0.15$ eV) for the line defect in graphene and SWCNT substrates. The adsorption energy for CO on pyridine-immobilised CoPc is similar to the pristine graphene value in figure 4.6 where the adsorption energy is close to -0.4 eV. The relatively small adsorption energy for CO indicates that the pyridine linker system is

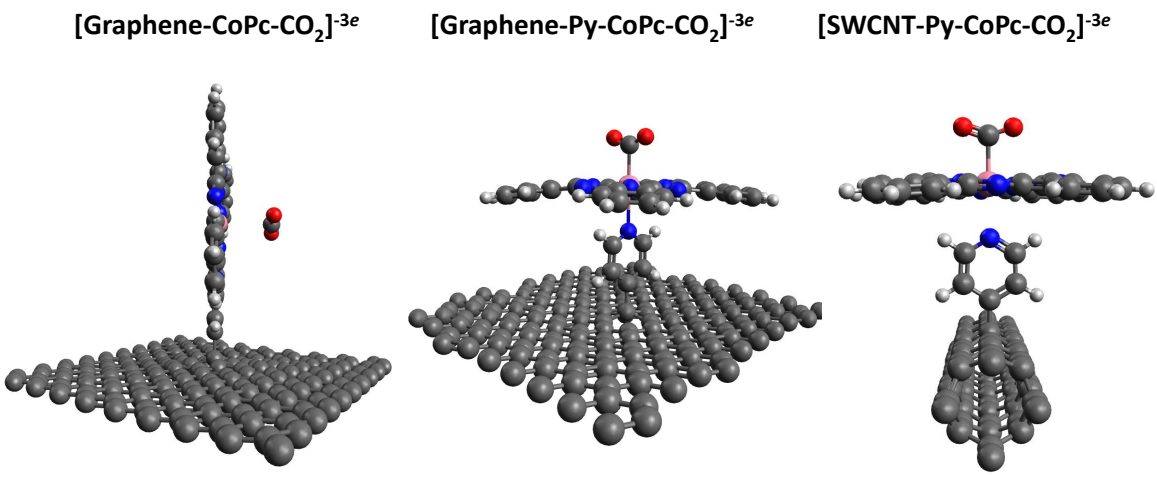

FIGURE 4.9. The relaxed geometries of charged (-3e) CoPc-CO_2 systems immobilised on pristine graphene and SWCNT (4,0) substrates with and without the pyridine linker. The C-Co bond lengths between CO_2 and CoPc for the left, middle and right systems are 3.11 Å, 2.19 Å and 2.22 Å, respectively. The N-Co bond lengths in the middle and right systems are 2.41 Å and 2.47 Å, respectively. White atoms are hydrogen, grey atoms are carbon, blue atoms are nitrogen, red atoms are oxygen and the pink atoms are cobalt.

just as unlikely to experience CO poisoning compared to the upright-immobilised CoPc and CoTPP systems since previous studies have reported CO adsorption energies of -1 eV or more for poisoned systems [**239**, **240**]. It it also observed that CO adsorption energies in the $-1e$ charge state show little difference compared to the $-3e$ charge state for the pyridine systems but for the upright-immobilised CoPc system the difference is significant, ~ 0.3 eV between the charge states. This is possibly caused by difference in bonding orbitals and/or a more positive (by $\sim 0.2e$ compared to upright-immobilised CoPc) and consistent atomic charge state maintained on the Co centre which only changes by $0.01e$ between the $-1e$ and $-3e$ charge states since the additional charge that facilitates the strong CO_2 adsorption is localised on the pyridine N atom which bonds to the central Co atom of CoPc.

We also consider the CoTPP system covalently immobilised at its cobalt centre by an atomic oxygen-linker on a SWCNT (4,0) substrate. There is a significant difference in adsorption

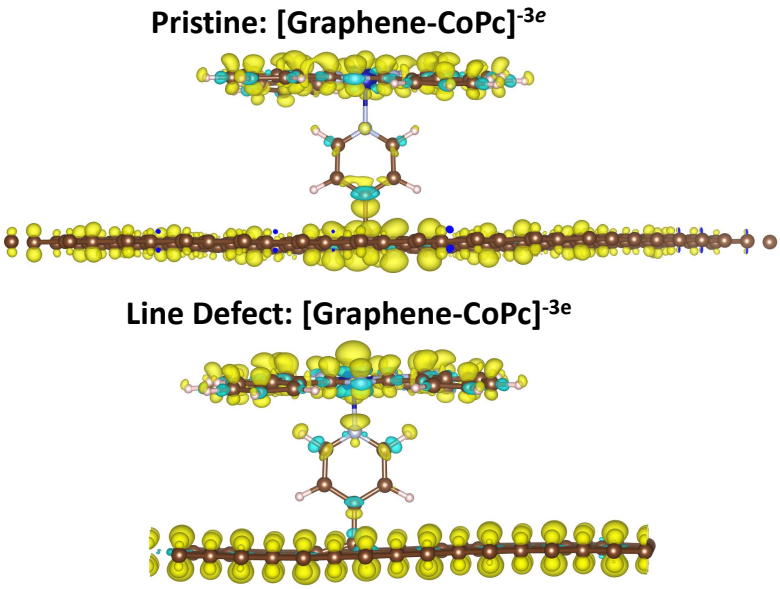

FIGURE 4.10. Charge density difference of CoPc in the Co^{I} charge state, immobilised on graphene via a pyridine linker. An isosurface value of 0.01 electrons/$\mathring{A}^3$ is used. Regions of charge gain are shown in yellow and regions of charge depletion are shown in blue. The charge density difference was calculated by subtracting the charge density of the $-3e$ system with the charge density of the neutral system.

energies of CO and COOH for the $-1e$ charge state between adsorption on a pristine SWCNT and over a SW defect site on an SWCNT. As listed in table B12 of appendix B and shown in figure 4.11, the $-1e$ charge state shows that CO has an adsorption energy of -1.33 eV for the pristine SWCNT and -0.93 eV for a SW defective SWCNT, a 0.4 eV difference. For COOH we observe a similar trend except in the opposite direction for the $-1e$ charge state, i.e. the pristine system has an adsorption energy of -1.72 eV and the SW defect system has an adsorption energy of -2.25 eV showing an ~ 0.5 eV difference. When considering the $-3e$ charge state, these differences between CO and COOH adsorption energies for pristine and SW defect systems disappear meaning they are not significantly effected by the substrate. There is also little difference in the CO_2 adsorption energies which are -0.19 eV and -0.21 eV for pristine and SW defective substrates respectively. The strong CO adsorption energies of -0.89 eV to -0.75 eV for pristine and SW systems, respectively, alludes to possible CO poisoning issues, although experimental results show long term stability over a 12 hour

cycle [**23**]. Given such similar adsorption energies for CO_2 it is interesting we find significant differences in adsorption behaviour as illustrated in figure 4.12, which shows that CO_2 is not bonding strongly to CoTPP on pristine SWCNT, but does show stronger bonding over the SW-defective site. This is because CoTPP does not bond covalently with the oxygen linker over the SW defect, which instead forms two bonds on a bridge site. The strong electronegativity of the oxygen atom causes charge to accumulate on the oxygen linker as shown in figure 4.13, drawing charge away from the cobalt centre of CoTPP and the CoTPP molecule itself, with light blue regions indicating charge depletion and yellow charge accumulation. The Voronoi analysis in table B13 of appendix B supports this conclusion with the total charge on the CoTPP molecule for the $-3e$ charge state being $-0.63e$ for pristine SWCNT and $-0.85e$ for the SW defective SWCNT (which is not covalently bonded), meaning less charge is localised on the CoTPP molecule compared to upright immobilisation on pristine SWCNT, which is $-0.95e$ as shown in table 4.3. Therefore, the relatively low experimental ToF of 2 s^{-1} [**23**] (compared to upright immobilised CoTPP which was measured to be 8.3 s^{-1} [**21**]) can in part be explained by the electronegative nature of the atomic oxygen linker acting as an inefficient conduit for electron transfer from the substrate to the cobalt centre and the CoTPP molecule itself.

Overall, the adsorption energies provide a glimpse into the behaviour and performance of the different immobilised systems with upright-immobilised CoPc and CoTPP systems and CoPc immobilised via pyridine linker systems showing adsorption energies ideal for CO_2ERR, i.e. strongly bound CO_2 for fast COOH formation and weakly bound CO to avoid CO poisoning. Although based on adsorption energies alone it is difficult to say which system provides the best CO_2ERR performance as it is the free energy that is relevant. It is clear that CoTPP immobilised via oxygen linker would have relatively poor performance based on weak CO_2 adsorption energy and a strong CO adsorption, a result of the electronegative nature of oxygen. Defect sites have a greater impact on the weakly binding intermediates (i.e. CO and CO_2) on immobilised CoPc compared to immobilised CoTPP. While graphene and SWCNT substrate systems show similar adsorption energy trends which is also seen between the (4,0) zig-zag and (4,4) armchair SWCNT substrates. To gain further insight into the performance and the

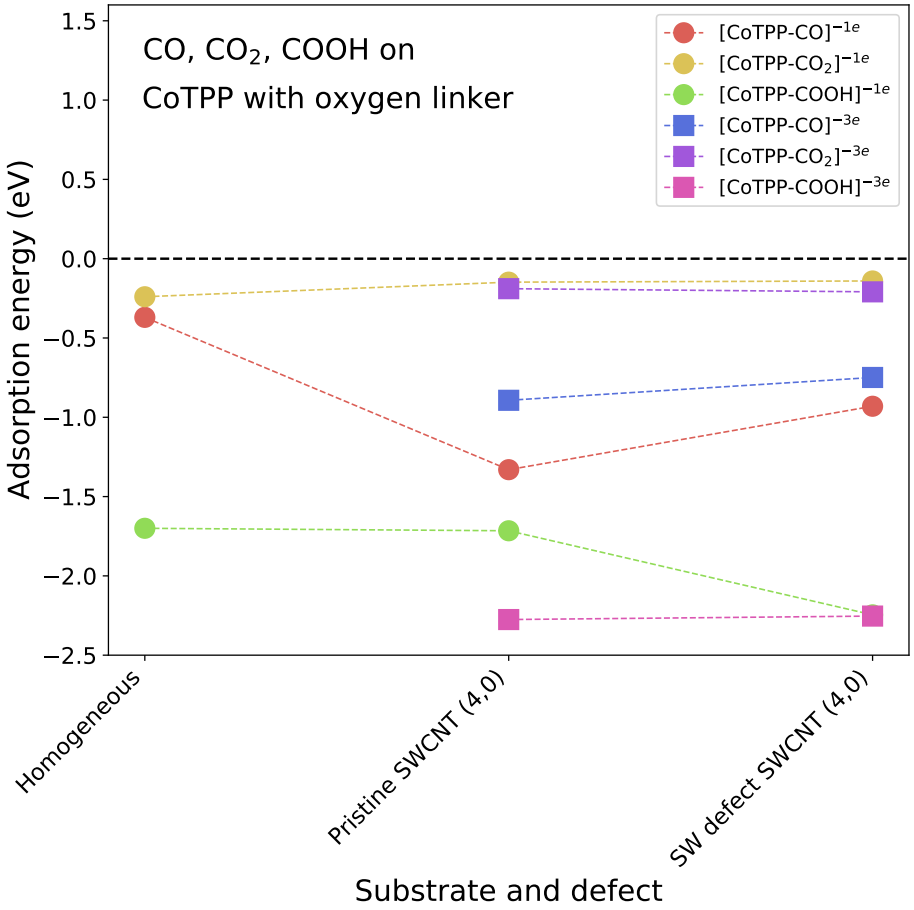

FIGURE 4.11. The adsorption energy of the CO, CO_2 and COOH intermediates on CoTPP immobilised via oxygen linker on SWCNT (4,0). Both the $-1e$ and $-3e$ charge states are considered. The homogeneous case is when CoTPP is considered a 'free molecule'. Adsorption energy values are listed in table B12 of appendix B.

effect of different defects and substrates we investigate the free energy reaction pathways for these systems in the reaction pathway section.

4.3.4.3 Density of States

We find that charge density of the cobalt centre and/or the immobilised CoPc/CoTPP molecule itself does not correlate in all cases to strongly and weakly bound intermediates. To investigate why CO_2 bonds more strongly to CoPc when immobilised via a pyridine linker on graphene we consider the d-orbital states of the CoPc cobalt centre which are shown in figure 4.14.

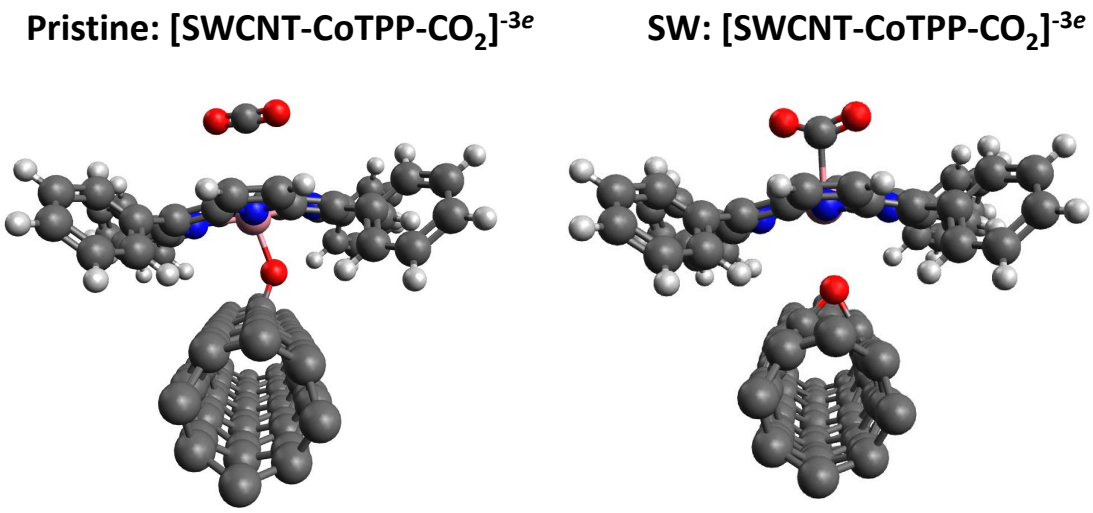

FIGURE 4.12. The relaxed geometries of CoTPP-CO_2 systems immobilised on pristine and SW defective SWCNT (4,0) substrates via an atomic oxygen linker. The O-Co bond length of the pristine system (left) is 1.97 Å while the same distance for the SW system (right) is 2.64 Å. White atoms are hydrogen, grey atoms are carbon, blue atoms are nitrogen, red atoms are oxygen and the pink atoms are cobalt.

The d-orbital PDoS of the pyridine immobilised cobalt centre shows a shift in the spin up states to below the Fermi level, while the spin down states have a large population above the Fermi level, in particular the states for the d_{z^2} orbital. This asymmetry results from the magnetic spin polarisation of the pyridine system which is found to be in a triplet state, and is not found for the upright-immobilised CoPc system since it is in a singlet state and shows a symmetric spin polarised PDoS plot. Figure B6 of appendix B shows that the spin charge density for the CoPc-pyridine system is primarily located on the CoPc cobalt centre and bonded pyridine nitrogen atom. This indicates that the spin down states of the d_{z^2} orbital facilitates stronger CO_2 bonding to the cobalt active site compared to other CoPc systems, such as upright-immobilised CoPc on graphene. This trend in the d_{z^2} orbital is also reported in an experimental investigation of pyridine-immobilised CoPc, where they find the d_{z^2} orbital is 'raised' in energy upon CO_2 adsorption [**24**]. Another study points to this same mechanism explaining NH_3 adsorption on Fe(110) with the spin down d-orbital showing strong binding

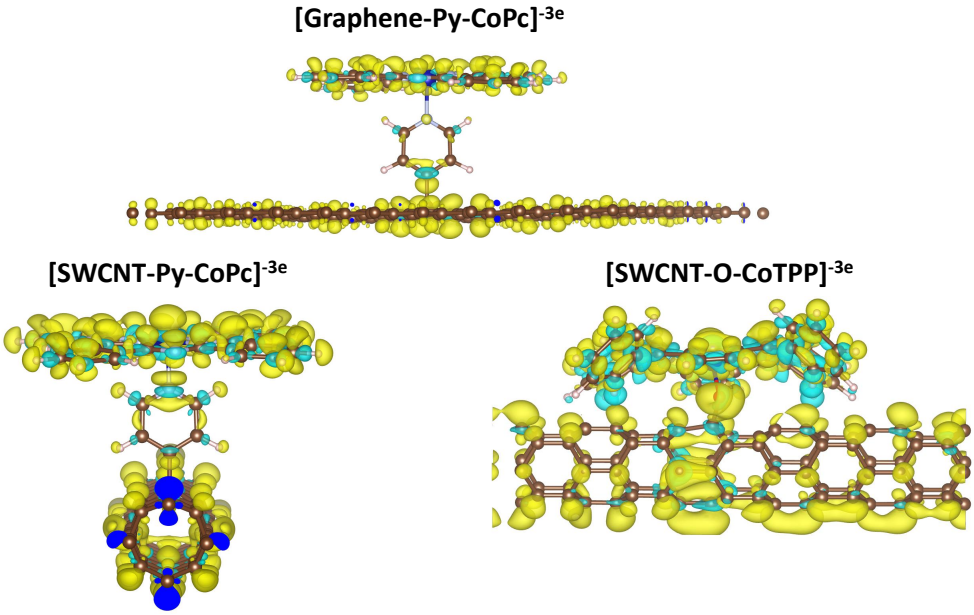

FIGURE 4.13. Charge density difference of pyridine and oxygen linker systems for CoPc and CoTPP immobilisation on graphene and a single-walled carbon nanotube (SWCNT). An isosurface value of 0.01 electrons/Å^3 is used. Regions of charge gain are shown in yellow and regions of charge depletion are shown in light blue (Dark blue indicates discontinuation of the isosurface at the super cell boundary). Charge density differences have been calculated by subtraction of the charge density of the neutral system.

while the spin up d-orbital shows weaker binding [**241**]. Therefore, an investigation of the d-orbital for transition metal catalysts can indicate whether strong bonding will occur for CO_2 which is involved in the rate determining step (COOH formation on CoPc/CoTPP) of CO_2ERR.

4.3.5 Reaction Pathways

To calculate accurate reaction pathways we need to determine the free energy values for each reaction step. Reaction steps that do not include a H^++e^- transfer can be calculated as usual using equation 4.3, but for steps that include a H^++e^- transfer, we use the method of Norskov [**34**] shown in equation 4.4.

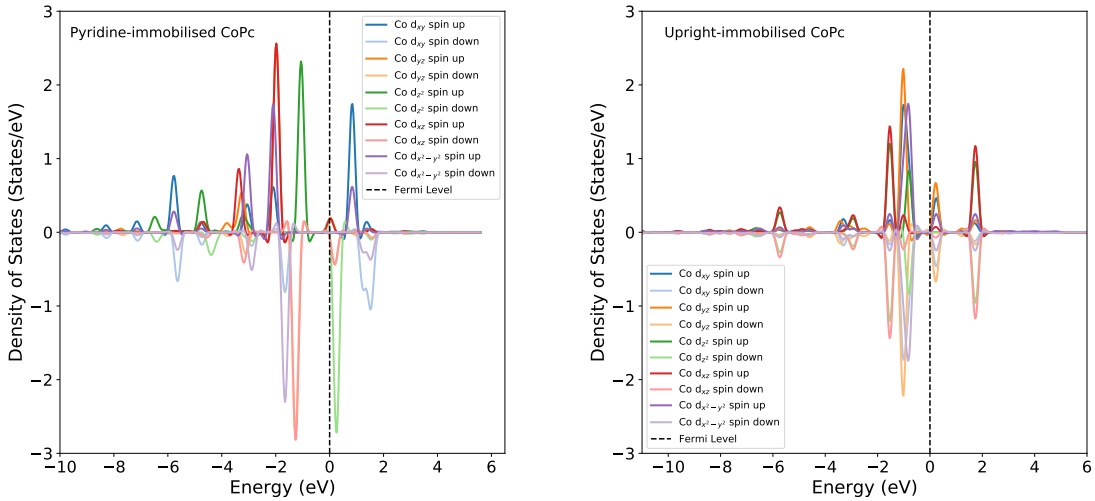

FIGURE 4.14. Partial density of states (PDoS) plots for the cobalt centre for CoPc immobilised on graphene via pyridine linker and CoPc directly immobilised upright to graphene via its ligand. The separated components of the d-orbital PDoS are shown. Spin polarised d-orbitals PDoS are shown for the cobalt centre (active site) since these are the transition metal bonding orbitals. The plots have been zeroed to the Fermi level indicted by dashed black lines. Both systems have a net charge of $-3e$. Total PDoS plots are shown in figure B5 of appendix B.

$$\Delta G = \Delta E_{\text{DFT}} + \Delta E_{\text{ZPE}} - T\Delta S \tag{4.3}$$

$$\Delta G = \Delta E_{\text{DFT}} + \Delta E_{\text{ZPE}} - T\Delta S - eU + G_{\text{pH}} \tag{4.4}$$

For equations 4.3 and 4.4, E_{DFT} is the ground state energy from DFT calculations, E_{ZPE} is the zero point energy calculated from DFT vibration calculations, T is temperature and is set to $T = 298.15$ K (room temperature) for all free energy calculations, and S is the entropy of the system. The Norskov method for calculation of reaction free energies includes the eU term, which is the electrode potential relative the standard hydrogen electrode (SHE) in units of eV and $G_{\text{pH}} = k_{\text{B}}T\ln(10\text{pH})$ is the term which corrects for pH values greater than 0.

In this section we treat H^++e^- transfer steps as coming from a H_2 molecule instead of hydronium radical (H_3O^+) and e^- in the bulk solution to avoid calculating radicals and providing additional charge to the immobilised systems as this may facilitate undesirable adsorption behaviour and/or geometries.

4.3.5.1 Defining Our Entropy Contribution

One of the challenges associated with free energy calculations is determining accurate and consistently defined entropy values. Here we have decided to use only the vibrational entropy contribution for immobilised systems as we expect translational and rotational entropy contributions to be less significant and difficult to determine accurately. There is no simple method for calculating solvation entropy components (shown in equation 4.5) such as cavitational entropy for immobilised catalysts on a substrate without doing computationally expensive molecular dynamics calculations. For small free molecules, such as CO and CO_2, vibrational entropy by itself significantly underestimates the entropy contribution [**242**]. However, in figure 4.15 the vibration free energy reaction pathway (shown in green) are calculated using only vibrational entropy components. The free energies in subsequent figures such as figure 4.16 include both vibrational and solvation entropy. In particular, vibration entropy is used to calculate free energies of the substrate immobilised CoPc/CoTPP systems and solvation entropy (which also includes vibration entropy as one of its components, see equation 4.5) is used to calculate free energies of the small intermediate molecules such as CO and CO_2. For Homogeneous CoPc/CoTPP in figure 4.15 and figure 4.16 and intermediates such as CO, CO_2, H_2O and H_2 solvation entropies have been calculated using water as the solvent [**47**, **242**].

$$S_{\text{sol}} = S_{\text{elec}} + S_{\text{trans}} + S_{\text{rot}} + S_{\text{vib}} + S_{\text{cav}} \tag{4.5}$$

Equation 4.5 shows provides an efficient and accurate method [**47**,**242**] of calculating solvation entropy where S_{elec} is the electronic entropy, S_{trans} is the solvation corrected translational entropy, S_{rot} is the solvation corrected rotational entropy, S_{vib} is the vibrational entropy and

S_{cav} is the cavity formation or cavitational (cavity of solvent molecules around the solute molecule) entropy.

A comparison of the CoPc and CoTPP (homogeneous) free energy reaction pathway for different entropy calculation methods is shown in figure 4.15. We find entropy plays a significant role in understanding the reaction pathway behaviour of CoTPP and CoPc for CO_2ERR. For CoTPP the free energy pathways calculated using DFT energy or vibrational entropy follow a strong exothermic path until the final CO desorption step which requires approximately 0.4 eV to 0.6 eV for CO desorption, suggesting the Co centre may experience some deactivation due to CO poisoning. This has been found to be unlikely with OH^- binding to the Co centre and CO_2 off-centre binding being better contenders for the CoTPP catalyst deactivation [**4**]. The free energy calculated using solvation entropy without implicit water shows a much smaller CO desorption energy of ~ 0.1 eV, while free energy calculated using solvation entropy with implicit water shows a slight exothermic energy difference of -0.06 eV for CO desorption making it spontaneous, which is what we would expect for efficient CO_2ERR. This reduction in CO desorption free energy granted by using solvation entropy corresponds well to results from a previous study in which CO adsorption free energy on CoTPP in the $+1e$ charge state was found to be largely over estimated when using vibrational entropy while solvation entropy showed a marked improvement [**242**]. The first step however becomes endothermic as a result of the solvation entropy model, which is discussed in more detail below. Finally, a significant difference in the free energy for the CoTPP + CO + H_2O step between vibration entropy and the solvation entropy with implicit water free energies is found to be 0.34 eV, with the solvation entropy being the lower free energy value. A similar degree of change is also found for different free energy calculation methods for the CoPc reaction pathway.

A detailed look at CoTPP reaction pathways in figure 4.15 shows a slight difference in CO_2 adsorption energies between DFT energy and vibrational entropy reaction pathways for CoTPP; this is due to a 0.09 eV $T\Delta S$ contribution at $T = 298.15$ K for the vibrational entropy. A more significant difference is observed for the solvation entropy reaction pathways with the solvation entropy contribution ($T\Delta S$ at $T = 298.15$ K) being ~ -0.6 eV which

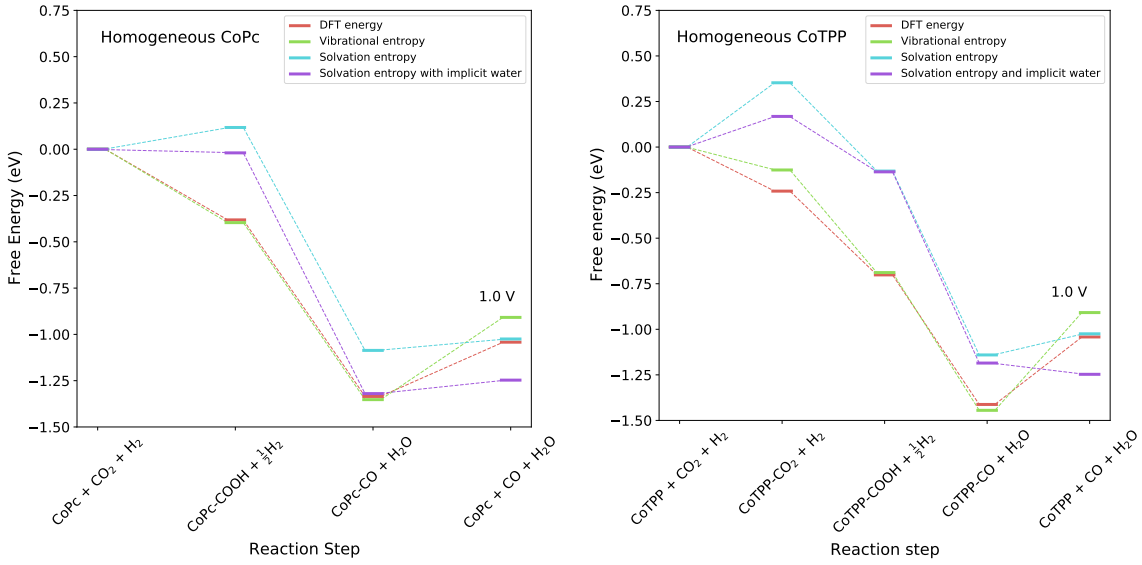

FIGURE 4.15. Free energy reaction pathway of homogeneous CoPc and CoTPP at 1 V electrode potential for different entropy methods and phases (gas or solvation). Each system being homogeneous is in the $-1e$ charge state. DFT energy is the ground state energy from the gas-phase DFT calculations with the electrode and pH terms included. For vibrational entropy free energy the $T\Delta S$ term only includes the entropy contribution from the DFT vibration calculations in gas-phase. The free energy with solvation entropy without implicit water includes solvation corrected entropy terms along with a cavitational entropy contribution but geometries are still calculated in gas-phase. Finally Free energy calculated using solvation entropy with implicit water has the same entropy has before but geometries are calculated in implicit water.

means the $-T\Delta S$ contribution in equation 4.3 and 4.4 will be positive, causing energies to be shifted up by this amount. When comparing the solvation entropy reaction pathways in gas-phase (light blue) and solvation-phase (purple) we find implicit water facilitates CO_2 adsorption with a -0.24 eV adsorption energy in gas-phase and a -0.43 eV adsorption energy in solvation-phase (implicit water); this in-turn reduces the endothermic energy of CO_2 adsorption. The CoTPP-COOH free energy shows negligible differences between DFT energy and vibrational entropy, also between the solvation entropy pathways, this is due to the highly reactive nature of COOH resulting in consistent geometries between gas-phase and solvation-phase. Again for CoTPP-CO + H_2O we see slight differences between free energies calculated for DFT only and vibration only entropies which is caused by a 0.02 eV difference in the zero point energy (ZPE) value, ΔE_{ZPE} in equations 4.3 and 4.4; the entropy contribution

in this case almost entirely cancels. Looking at the solvation entropy values for the same system we see a slightly larger difference in free energy values caused by the implicit water contribution of -0.04 eV. Interestingly, the final step of CO desorption is found to be close, or lower in energy, for the solvation entropy reaction pathways compared to DFT energy and vibrational entropy free energies. This is in part due to different entropy contributions between vibrational only and solvation entropy which have $T\Delta S$ values of -0.22 eV and 0.19 eV for vibrational and solvation entropies respectively. The difference between the two solvation entropy pathways (light blue and purple markers) for CO desorption is again resulting from the implicit water contribution with a value of -0.18 eV. Therefore, entropy is found to play a significant role for some reaction steps (likely those steps that experience significant geometry changes) and for others it shows a negligible contribution. This means a detailed description of entropy should be used for each step of the reaction pathway to minimise uncertainty in the free energy values.

Figure 4.15 includes the same entropy comparison for homogeneous CoPc which shows similar trends between the entropy methods and phases, except for CoPc-COOH calculated in solvation-phase using solvation entropy which shows similar free energy values to vibrational entropy and DFT energy values. This is caused by the implicit water contribution of -0.1 eV resulting in similar energies to DFT energy and vibration entropy free energy values since the vibrational entropy contribution ($T\Delta S$ at $T = 298.15$ K) is only 0.06 eV. The final CO desorption step shows almost identical behaviour and trends compared to homogeneous CoTPP.

4.3.5.2 Substrate Comparison

A favourable reaction pathway is determined by identifying the reaction pathway with the closest behaviour to a ‘downhill’ (exothermic) reaction. For example in figure 4.15 homogeneous CoTPP at 1 V potential and calculated with solvation entropy and implicit water shows consistent ‘downhill’ behaviour (excluding the CO_2 adsorption step which is slightly ‘uphill’) until the final CO desorption step which is also ‘downhill’. If a step is ‘uphill’ (endothermic)

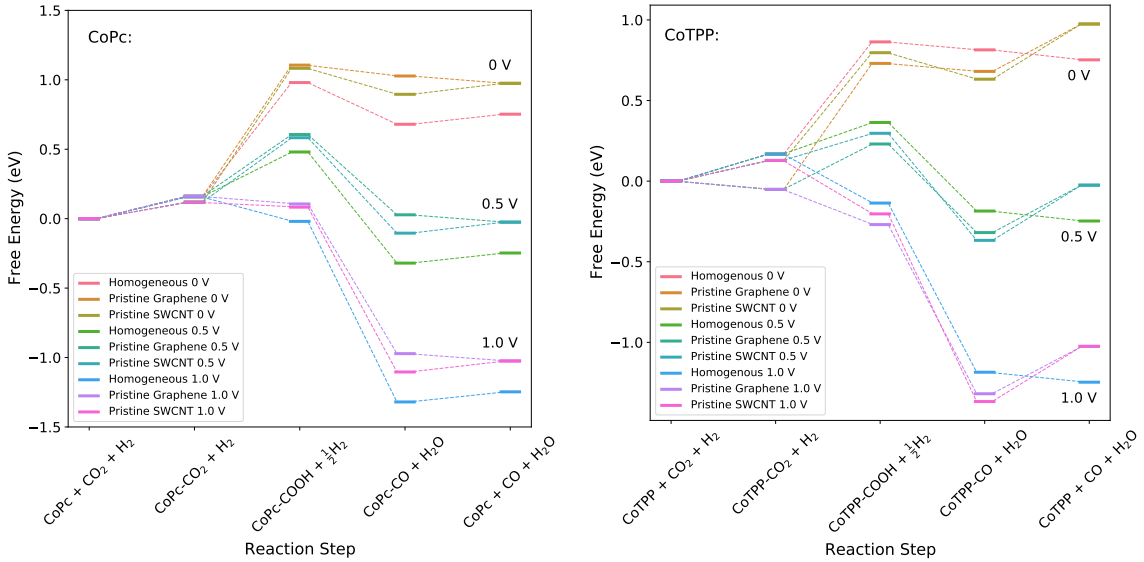

FIGURE 4.16. Reaction pathways of the CO_2ERR reaction for homogeneous and upright immobilised CoPc and CoTPP. The reaction pathways are calculated for the 0 V, 0.5 V and 1 V electrode potentials. *Homogeneous* indicates a non-immobilised or free CoPc/CoTPP molecule calculated in implicit water and using solvation entropy. The Homogeneous systems have a net charge of $-1e$ and the immobilised systems have a net charge of $-3e$. A pH value of 7 has been assumed for all H^++e^- transfer steps. Free energies of immobilised systems are calculated using vibrational entropy while intermediates such as CO and H_2O have their free energies calculated using solvation entropy. Both immobilised and free systems are calculated in gas-phase.

for all systems then the system with the smallest 'uphill' step is the most favourable; for example the CO desorption step for solvation entropy (light blue) and vibrational entropy (green) in figure 4.15 shows a smaller 'uphill' step for solvation entropy compared to vibrational entropy and is therefore more favourable.

We now investigate the role the different substrates play in determining the reaction pathway energies. Firstly, we calculated the free energy reaction pathways for CoPc and CoTPP which are upright covalently immobilisation on pristine graphene and SWCNT (4,0) substrates, see figure 4.16. For the CoPc reaction pathway the rate determining step (RDS) is CoPc + CO_2 + $\frac{1}{2}H_2$ $\longrightarrow$ CoPc-COOH which is shown as an endothermic step, which at 0 V potential is ~ 1 eV, at 0.5 V potential it is ~ 0.6 eV and at 1 V potential it flattens out to ~ 0.1 eV. The CO_2 adsorption step is also shown and found to have an adsorption free energy of ~ 0.1

eV, similar to the RDS step at 1 V. While the homogeneous (free molecule) system shows the first reaction step (the RDS) to be slightly exothermic at -0.02 eV which is calculated with solvation entropy and implicit water (solvation-phase), unlike the immobilised systems which are limited to vibrational entropy in gas-phase. Figure 4.16 is also shown in figure B7 of appendix B except the homogeneous reaction pathway free energies are calculated in gas-phase and using vibrational entropy, the same free energy calculation method for the immobilised systems. In this case the homogeneous system's RDS is also endothermic with negligible energy differences between the homogeneous, graphene and SWCNT systems, while for the reaction pathway as a whole the homogeneous system closely mirrors that of the SWCNT system. Coming back to figure 4.16, at 1 V potential it is possible that the kinetics of some of the molecules in the system will be able to overcome the 0.1 eV RDS energy since an average kinetic energy of ~ 0.04 eV at a temperature of 298.15 K is determined from $KE = \frac{3}{2}k_{\mathrm{B}}T$ from kinetic theory and the ideal gas law. This means an electrode potential of 1.1 V or more would change the RDS step from endothermic to exothermic for the immobilised systems due to the higher e concentration. This could also be facilitated with a lower pH level (more acidic) giving a larger H^+ concentration. The second CoPc-COOH + $\frac{1}{2}H_2 \longrightarrow$ CoPc-CO + H_2O step is already exothermic at 0 V electrode potential and becomes more so at larger potentials with an energy difference of ~ 1 eV for an electrode potential of 1 V. For the final step we find the homogeneous systems show slight exothermic behaviour (caused by more detailed entropy contributions shown in equation 4.5, associated with a 'free molecule' and the inclusion of implicit water) with an energy difference of ~ -0.06 eV, while immobilised systems show an endothermic energy difference of ~ 0.06 eV. These small energy differences point to the desorption of CO from the cobalt centre of CoPc being spontaneous.

There does not seem to be an agreed upon reaction mechanism for CoPc. Some studies propose it to be similar to CoTPP, with the exception of the cobalt centre charge state associated with some steps [**19**, **24**, **207**]. In the intermediate adsorption section (section 6) we observed CO_2 does not bond as strongly to the cobalt centre of CoPc in gas-phase (-0.17 eV) compared to CoTPP (-0.25 eV), as seen in figure 4.9, although stronger bonding occurs in an implicit water environment (see figure B3 in appendix B). For the CoPc reaction pathways in this

section the CO_2 and H adsorption on CoPc giving CoPc-COOH may occur in one concerted step [**19**] possibly similar to CoTPP [**4**], but in other studies cobalt porphyrin (CoP) like molecules have been proposed to have two steps: CO_2 adsorbs on CoTPP giving CoTPP-CO_2, then H adsorption results in CoTPP-COOH as shown in figure 4.15 [**188**,**190**,**243**,**244**]. Given the uncertainty surrounding the reaction mechanisms we include the CO_2 adsorption step in our free energy reaction pathway figures as it is still a point of interest. For CoTPP we will follow the mechanism proposed by the recent work of Marianov *et al* in which CoTPP + CO_2 +H_2 $\longrightarrow$ CoTPP-COOH + $\frac{1}{2}H_2$ occurs as a concerted step (CO_2 adsorption step will still be shown) with the co-adsorption of CO_2 + H on CoTPP [**4**].

The CoTPP reaction pathways are also shown in figure 4.16 and we find that the transition to the final state (CoTPP + CO + H_2O) remains the most endothermic with the desorption of CO requiring $\sim$0.3 eV for immobilised CoTPP. Figure 4.15 and the CoTPP plot of figure 4.16 show a 0.34 eV and 0.22 eV difference between vibrational entropy free energy and solvation entropy with implicit water free energy values, respectively. However, if it were possible to calculate solvation entropy and efficiently utilise implicit water for the immobilised systems this step maybe closer to an exothermic reaction. In figure B7 of appendix B the homogeneous reaction free energy pathway is calculated in gas-phase using vibrational entropy for the immobilised CoTPP systems and solvation entropy for the intermediate free energies. The homogeneous CoTPP reaction free energies in Figure B7 shows similar reaction free energies to the same homogeneous system in figure 4.16 except for the final step which in figure 4.16 becomes exothermic due to an implicit water contribution. The type of substrate used to immobilise CoTPP has a slight effect on the reaction pathway; we see CO_2 and CO_2+H adsorption is clearly grouped into three energies depending on the substrate or lack there of. The reaction step CoTPP-COOH + $\frac{1}{2}H_2$ $\longrightarrow$ CoTPP-CO + H_2O is always exothermic even at 0 V electrode potential showing similar behaviour compared to CoPc. While the concerted reaction step CoTPP + CO_2 + H_2 $\longrightarrow$ CoTPP-COOH + $\frac{1}{2}H_2$ is only exothermic when a 1 V electrode potential is used with energy differences between -0.2 eV to -0.4 eV depending on the substrate. CO_2 adsorption free energy is found to only be exothermic for the graphene system with an energy of ~ -0.1 eV, while the homogeneous and SWCNT systems show endothermic adsorption free energies of ~ 0.2 eV. Therefore, the immobilised CoTPP (and

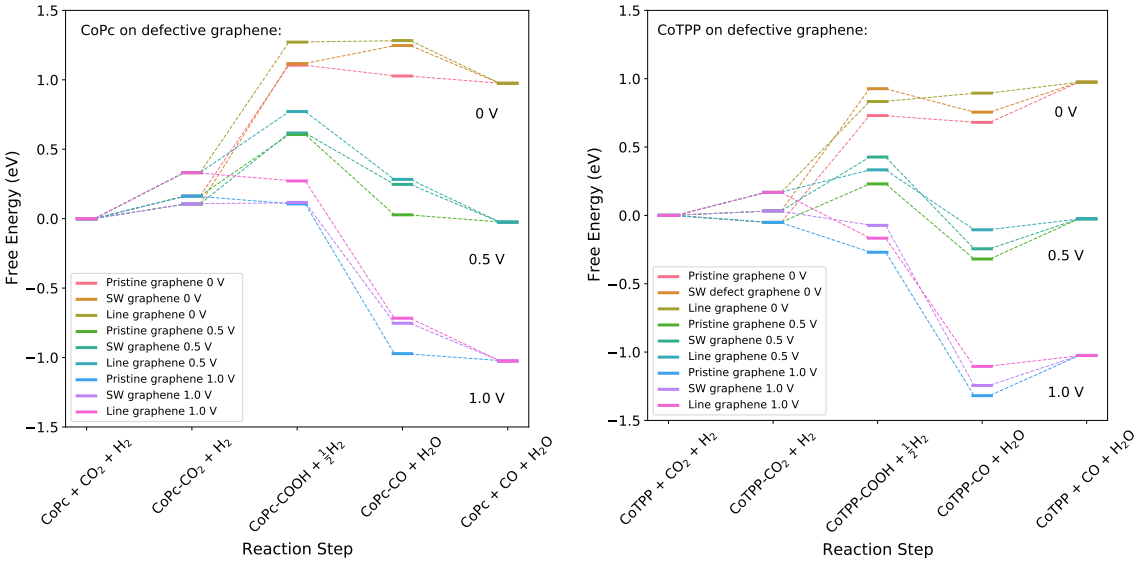

FIGURE 4.17. Reaction pathways of the CO_2ERR for upright CoPc and CoTPP on pristine, and defective graphene. The reaction pathways are calculated for the 0 V, 0.5 V and 1 V electrode potentials for H^++e^- transfer steps. A pH value of 7 has been assumed for all steps that undergo a H^++e^- transfer. Free energies of immobilised systems are calculated using vibration only entropy while free molecules such as CO and H_2O have the free energies calculated using solvation entropy, also both immobilised and free systems are calculated in gas-phase.

CoPc) systems show little difference between each other with the pristine graphene substrate being only slightly more favourable compared to the pristine SWCNT substrate. If it were possible to include solvation entropy for the graphene substrate systems along with implicit water (which would be computationally very expensive) then we might find the CO desorption free energy become exothermic as expected.

4.3.5.3 Defect Comparison

We have considered reaction pathway calculation methods and immobilisation substrates, now we look at the effect immobilising over different defects has on the reaction pathway behaviour. Figure 4.17 compares the reaction pathway of CoPc and CoTPP immobilised on pristine graphene, SW defect in graphene and the octagon-pentagon line defect in graphene. The choice of defect sites has been reduced relative to the intermediate adsorption section due to the long and expensive vibration calculations. We have chosen to consider the SW and

line defects because they are representative of common defect sites in graphene, SW having low formation energy and high migration energy (see table B1 in appendix B) and the line defect occurring at graphene sheet boundaries will have a large surface area increasing the probability of immobilisation on such a site. Starting with CoPc we find the RDS for CO_2+H adsorption to be slightly endothermic (~ 0.1 eV) when immobilised on pristine graphene and a SW defect in graphene, while the CoPc immobilised on an octagon-pentagon line defect in graphene shows more significant endothermic behaviour (~ 0.3 eV). The CO_2 adsorption free energies are shown to be similar to the RDS step as a whole. This indicates a higher over potential may be required to initiate CO_2ERR for CoPc immobilised on a graphene line defect, the cause of which is possibly linked to the size of the defect and its tendency to accumulate charge [**226**]. The CO desorption step is found to be more exothermic for defective graphene compared to pristine graphene substrates with desorption energies of -0.3 eV and -0.05 eV respectively, this is also reflected in the adsorption energies see figure 4.6. The intermediate step forming H_2O and leaving CO bonded on CoPc is strongly exothermic for both 0.5 V and 1 V electrode potentials indicating this step would have little effect on the reaction rate, the same behaviour of this step is found for CoTPP and all other CO_2ERR systems investigated in this study. From the three substrates CoPc immobilised on a SW defect in graphene shows the best performance with relatively low CO_2+H adsorption and favourable CO desorption.

Slightly different behaviour is found for CoPc immobilised on defective SWCNT shown in figure 4.18 with pristine SWCNT showing the most favourable reaction pathway. This is because pristine SWCNT shows a more favourable RDS step (CoPc-COOH formation) by -0.2 eV, the subsequent H_2O formation step is also more exothermic on the pristine system by ~ 0.1 eV, while only a 0.05 eV difference in energy is found between the pristine and SW systems for the final CO desorption step.

For CoTPP in figure 4.17, we observe for pristine and defective substrates the first step of CO_2+H adsorption on CoTPP is exothermic unlike CoPc. This indicates CoPc may require higher electrode potentials for CO_2ERR onset. This is a pattern we also find in table B2 of appendix B which summarises experimental performances of recently studied cobalt-centred catalysts where we see CoPc tends to have slightly higher electrode potentials compared to

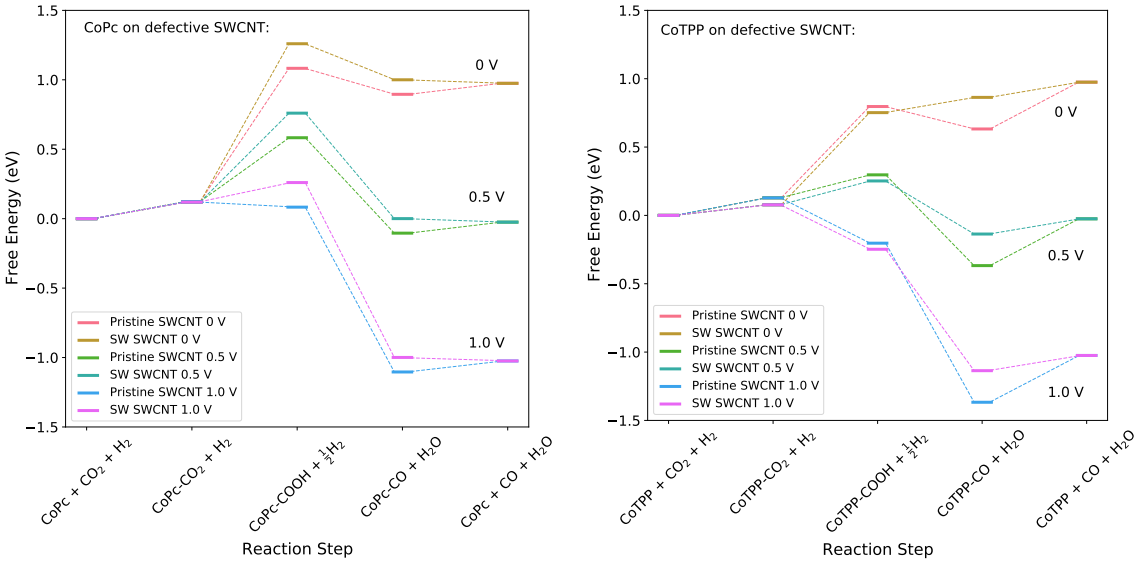

FIGURE 4.18. Reaction pathways of the CO_2ERR reaction for upright CoPc and CoTPP on pristine and defective single-walled carbon nanotube (SWCNT). The reaction pathways are calculated for the 0 V, 0.5 V and 1 V electrode potentials. A pH value of 7 has been assumed for all steps that undergo a H^++e^- transfer. Free energies of immobilised systems are calculated using vibration only entropy while free molecules such as CO and H_2O have there free energies calculated using solvation entropy, also both immobilised and free systems are calculated in gas-phase.

CoTPP. For example upright immobilised CoTPP uses an electrode potential of -1.05 V vs. NHE [**21**], while immobilised CoPc use electrode potentials between -1.1 V to -1.2 V vs. NHE [**245**, **246**]. The pristine substrate shows the strongest adsorption free energy of -0.27 eV for CO_2+H (-0.05 eV for CO_2), for the line defect we get -0.17 eV (0.03 eV for CO_2) and the SW defect gives -0.07 eV (0.17 eV for CO_2). The final CO desorption step is endothermic (different from CoPc which shows exothermic behaviour) with pristine and SW defect substrates showing endothermic desorption energies between $0.2 - 0.3$ eV, while the desorption energy for the line defect is 0.08 eV making it less endothermic and more likely to occur. For the case of CoTPP the best performance is found to come from CoTPP immobilised on an octagon-pentagon line defect showing relatively strong exothermic behaviour for the first and second steps with the final CO desorption step only being slightly endothermic. Considering these calculations were only performed for gas-phase with vibrational entropy contributions for the free energies, similar calculations in implicit water and using solvation

entropy for the free energies may show the final step to be exothermic as per the relations shown in figure 4.15.

Interestingly, the SW defect system for CoTPP immobilised on SWCNT shows the most favourable reaction pathway for CoTPP in figure 4.18. There is only a slight difference in the first (RDS) step with the SW system being slightly more exothermic by -0.04 eV, the second step is however more exothermic for pristine SWCNT resulting in a larger endothermic value for the final CO desorption step which is 0.34 eV for pristine and 0.1 eV for SW, indicating CO desorption would occur more efficiently for the SW defect system.

4.3.5.4 Linker and Multi-defect Systems

Next we look at linker and multi-defect systems, which include CoPc immobilisation on both graphene and SWCNT using a pyridine linker as shown in figure 4.9, multiple defect sites (see figure B8 in appendix B) [**24**, **231**] and CoTPP immobilised via an atomic oxygen linker on a SWCNT (see figure 4.12) [**23**]. Recently, experimental and theoretical studies have been carried out for CoPc where it was proposed CoPc could be covalently immobilised over a dense region of defects in graphene consisting of two single vacancy defect and two double vacancy defect under the four ligands along with a double vacancy defect under the cobalt centre, creating a stable and highly selective CO_2ERR catalyst which we refer to as the 'multi-defect' system [**231**]. However no experimental justification was given for why this particular set of defects were chosen to represent the substrate. The first CO_2 adsorption step is dependent on the system since it does not involve a H^++e^- transfer and thus no electrode potential term which is why we see 4 distinct energies, these are 0.15 eV, 0.1 eV, 0.02 eV and -0.12 eV for multi-defect, O-linker, pyridine on SWCNT and pyridine on graphene systems, respectively. This shows that CoPc immobilised via pyridine on graphene shows exothermic behaviour for CO_2 adsorption, this may also be the case on SWCNT as well given the borderline endothermic energy for CO_2 adsorption of 0.02 eV. Considering the accuracy of these calculations this step could be exothermic for the SWCNT system if implicit water and/or the solvation entropy were able to be included. The CO_2+H $\longrightarrow$ COOH adsorption step at an electrode potential of 1 V shows the reaction is exothermic for

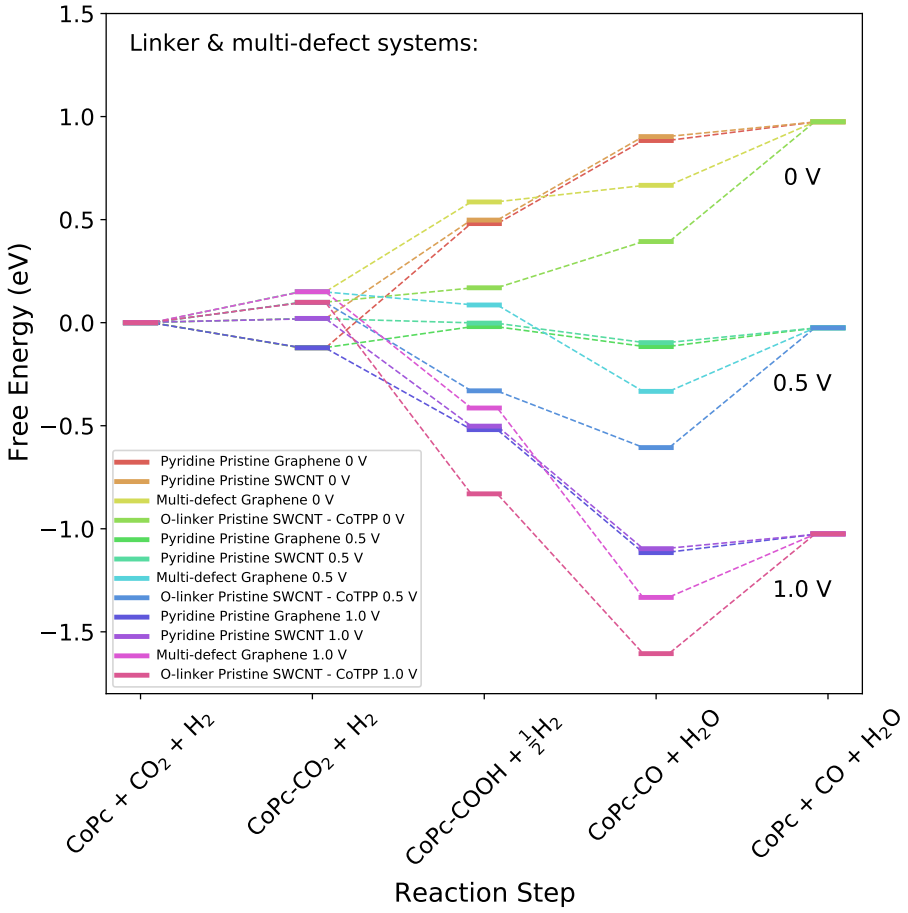

FIGURE 4.19. Reaction pathways of the CO_2ERR reaction for immobilised CoPc and CoTPP on graphene and SWCNT (4,0). The O-linker system corresponds to immobilised CoTPP. The reaction pathways are calculated for the 0 V, 0.5 V and 1 V electrode potentials. A pH value of 7 has been assumed for all steps that undergo a H^++e^- transfer. The multi-defect system correspond to the system studied in Ref [**231**].

all systems, even without the CO_2 adsorption step, free energies are between -0.4 eV to -0.8 eV. Systems showing endothermic behaviour for CO_2 adsorption maybe more likely to have a concerted step for CO_2+H adsorption. The step for H_2O formation leaving CO bonded to CoPc is strongly exothermic for all systems as expected, with free energies between -0.6 eV to -0.8 eV. The final step of CO desorption is endothermic for all systems, but least so for the pyridine linkers which show an almost identical desorption energy of ~ 0.1 eV, while the O-linker and multi-defect systems show much stronger endothermic behaviour with desorption energies of 0.6 eV and 0.3 eV, respectively. Its clear from figure 4.19 that

the CoPc-pyridine systems show the most favourable reaction pathways with the graphene substrate system possibly outperforming the SWCNT substrate system due to energetically favourable CO_2 adsorption. The experimental performance of these systems are consistent with figure 4.19 with CoPc-pyridine on CNTs having a turn over frequency (ToF) of 34.5 s^{-1} [**24**], the multi-defect system has a ToF of 3.9 s^{-1} [**231**] and the O-linker system has a ToF of 1.37 s^{-1} [**23**].

Comparing CoPc immobilised via pyridine on graphene and CoTPP immobilised on a line defect in graphene we find both systems to have a triplet spin state. The CoPc pyridine system has the spin density profile mainly localised on the pyridine nitrogen atom and CoPc cobalt centre as shown in figure B6 of appendix B. For CoTPP immobilised on a graphene line defect the spin density profile is localised on the line defect itself with charge depletion from the cobalt centre which may contribute the relatively more endothermic CO_2 adsorption free energy in figure 4.17. This shows two different spin density profiles, one which originates from the nitrogen-cobalt bonding of the pyridine linker and CoPc catalyst, and one which is defect and substrate localised.

Based on the favourable CO_2ERR reaction pathway of CoPc immobilised via pyridine linker on graphene in figure 4.19 we compare the effect that different graphene defects have on this system, see figure 4.20. The CO_2 adsorption step for the systems is centred around 0 eV making it difficult to accurately determine the direction of this step (i.e. whether it is endothermic or exothermic) given calculations are in gas-phase and with only a vibrational description of entropy. We observe that this step is slightly exothermic on the pristine graphene, and borderline in the SW case, with adsorption free energies of -0.12 eV and -0.02 eV respectively. While for the line defect this step is slightly endothermic with an adsorption free energy of 0.08 eV. The RDS step creating CoPc-COOH and the step for H_2O formation leaving CoPc-CO, we find both steps are strongly exothermic (between -0.4 eV to -0.6 eV) as expected given the results from the previous free energy pathways we have investigated. The final CO desorption step shows slight, or borderline, endothermic behaviour with the pristine graphene exhibiting the strongest such behaviour (~ -0.1 eV) and the line defect the weakest (-0.002 eV). In general, we do not see significant differences

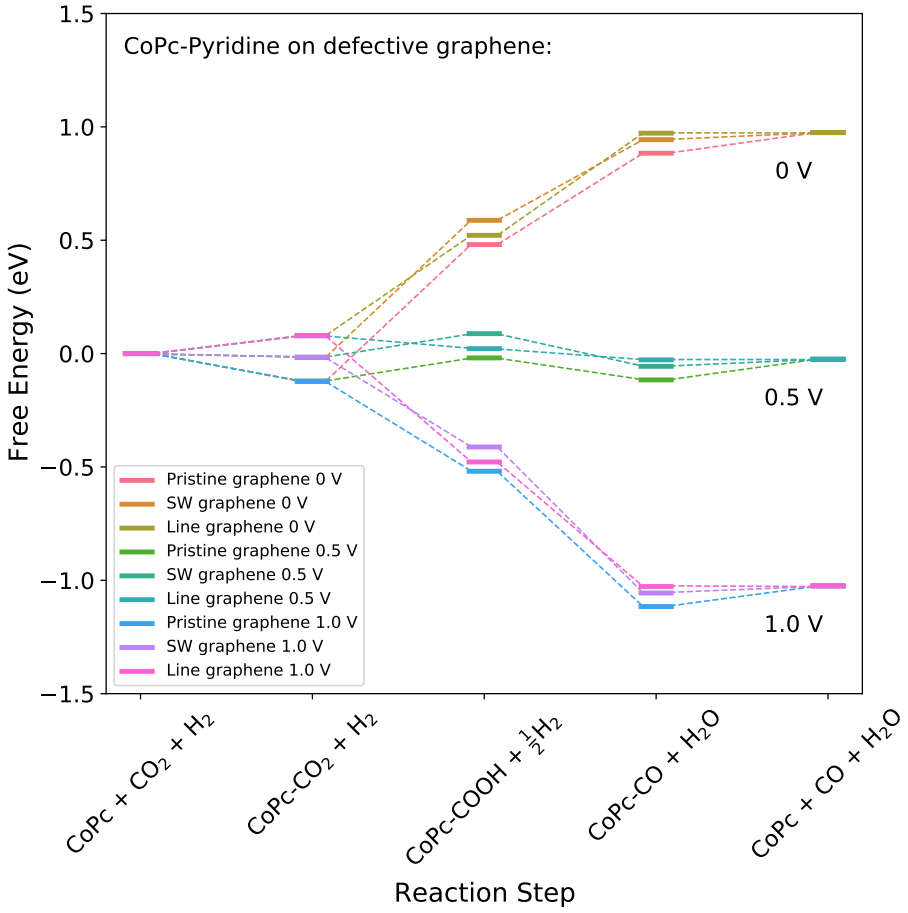

FIGURE 4.20. Reaction pathways of the CO_2ERR reaction for CoPc immobilised via pyridine linker on different graphene defects. Reaction-pathways have been calculated for 0 V, 0.5 V and 1 V electrode potentials. A pH value of 7 is assumed for all H^++e^- transfer steps. Free energies of immobilised systems are calculated using vibration entropy while free molecules such as CO and H_2O have the free energies calculated using solvation entropy, also both immobilised and free systems are calculated in gas-phase.

in the reaction pathway for CoPc immobilised on graphene via a pyridine linker for different defect sites with the CO_2 adsorption step showing the largest free energy difference of 0.2 eV. Therefore, it is difficult to conclude on a most favourable pathway but it should be noted that the pristine graphene system follows the most exothermic pathway until the final CO desorption step which as previously mentioned is slightly endothermic.

4.4 Summary

We have conducted a consistent and comparative density functional theory (DFT) investigation of covalently immobilised cobalt-centred phthalocyanine (CoPc) and cobalt-centred tetraphenylporphyrin (CoTPP) catalysts used to facilitate the CO_2 electroreduction reaction (CO_2ERR) on carbon substrates. Defective and non-defective covalent immobilisation sites on substrates are investigated to establish their effect on CO_2ERR and to provide a realistic interpretation of a carbon electrode. We find little difference between the bonding energies of CoTPP and CoPc on the same substrate particularly on stable defect sites such as the Stone-Wales (SW) defect and the octagon-pentagon line defect. Narrow SWCNTs and defective substrates show the strongest bonding energies compared to graphene and pristine substrates respectively. Atomic charge results show higher charge localisation on immobilised CoPc compared to immobilised CoTPP possibly caused by the rigid structure of CoPc. While SWCNT substrates have higher charge localisation by $\sim -0.3e$ compared to graphene meaning SWCNT defect sites only attract little additional charge from the catalyst compared to graphene. Adsorption energies of upright-immobilised CoPc and CoTPP are similar to their homogeneous systems, in contrast the pyridine-immobilised CoPc shows stronger CO_2 adsorption of -0.4 eV while CoTPP immobilised via oxygen linker shows much weaker CO_2 adsorption of -0.2 eV. SW and line defect sites are found to weaken (relative to pristine sites) the adsorption energies of CO for both upright-immobilised CoPc by 0.2 eV and oxygen linker-immobilised CoTPP by 0.15 eV. The line defect site is also found to weaken the CO_2 adsorption energy on CoPc immobilised via pyridine linker by 0.15 eV.

Finally, covalently immobilised CoPc and CoTPP show similar or improved reaction performance compared to their homogeneous counterparts. It is found that CoTPP bonded to an octagon-pentagon line defect and CoPc bonded to a Stone-Wales defect in graphene show the best performing reaction pathways compared to other defect or pristine sites on graphene. These systems show both a favourable rate determining step (COOH formation on CoPc/CoTPP) and a final CO desorption step, particularly the latter which shows an ~ -0.2 eV improvement relative to pristine graphene. The best performing CO_2ERR system is found to be CoPc immobilised on graphene using a pyridine linker, which exhibits an almost

complete exothermic reaction path with only a slight endothermic step for final CO desorption. This performance improvement is linked to strong CO_2 binding facilitated by the unoccupied spin down elements of the d_{z^2} orbital with energies just above the Fermi level. Considering that the free energies are calculated using vibration entropy for the immobilised systems (due to the large size), it is possible the final CO desorption step could be exothermic if more detailed but prohibitively computationally expensive implicit water and solvation entropy contributions are used for the immobilised systems. Relative reaction pathway performance of the linker and multi-defect systems match the experimental performances particularly for turn over frequency. Reaction pathways between CoPc and CoTPP are similar but CoTPP generally presents a more favourable rate determining step. The covalent immobilisation of such metal-organic complexes crosses the divide separating homogeneous to heterogeneous catalysis. This bridge is an important and relatively unexplored interface topic in chemistry. Thus, we believe the present paper is also valuable to broader, more fundamental chemistry.

CHAPTER 5

First Principles Investigation of Cobalt-Phthalocyanine Active Site Tuning via Atomic Linker Immobilisation for CO_2 Electroreduction

---

We investigate the CO_2 electroreduction reaction (CO_2ERR) using first principles calculations, for the active site tuning of cobalt-centred phthalocyanine (CoPc) via distinct atomic linker species which immobilise CoPc on a carbon nanotube (CNT) substrate. Eight different linker species are studied, along with the effect of linker hydrogenation. Superior reaction performance is predicted for the NH, S and PH linkers, which show activated CO_2 adsorption. This results from spin polarization causing unoccupied d_{z^2} spin-down states of the cobalt active site at, or above, the Fermi level. Using an 'on-catalyst' reaction scheme, calculated activation barriers for COOH formation and CO desorption are lower for the CoPc-PH-CNT system compared to the CoPc-NH-CNT system and CoPc remains well grafted to PH-CNT throughout the reaction. We thus expect the PH linker system to have similar or better CO_2ERR performance compared to the NH and S linker systems but at a slightly higher electrode potential.

5.1 Introduction

The landscape of CO_2 reduction catalysts is vast, ranging from surface catalysts such as copper, to metal-organic frameworks, to molecular catalysts such as cobalt-centred phthalocyanine (CoPc) [**7**, **9**, **247**]. Three criteria that need to be satisfied for a catalyst to be considered for scaled practical applications are stability for long term operation, performance for high product creation volume at low energy input and material cost of the catalyst. In this study we

investigate, using first principles calculations, the performance of axially immobilised CoPc molecular catalysts via an atomic linker on single-walled carbon nanotubes.

Molecular catalyst enhancement through ligand functionalisation is a heavily investigated and effective method for tuning catalytic performance [**4**, **245**, **248**, **249**]. However, directly modifying the active site is expected to provide more significant performance change since one can directly tune the electronic properties of the active site.

Recent experimental studies have shown molecular catalysts such as organometallic complexes immobilised via an atomic linker are viable and have shown promising CO_2 electroreduction reaction (CO_2ERR) performance. A study by Zhu *et al.* demonstrates the viability and high selectivity (up to 98% Faradaic efficiency) of an atomic oxygen linker immobilising cobalt porphyrin on a carbon nanotube (CNT) with a turnover frequency (TOF) of 2.1s^{-1} at a potential of -0.65 V vs. RHE (at pH = 7.3) with all loaded cobalt catalyst considered active [**23**]. More recently a study by Li *et al.* has shown strong CO_2ERR performance for CoPc immobilised using a NH_2 linker with Faradaic efficiency of $>96\%$ and TOF of 31.4s^{-1} at -0.6 V vs. RHE (at pH = 7.2) with all loaded cobalt catalyst considered active [**27**]. Comparing these two studies we see a significant performance difference in TOF between the oxygen and NH_2 linker studies. This is a direct result of the linker bonded directly to the cobalt (Co) centre, changing the electronic properties of the cobalt active site. Previously, it has been shown experimentally and theoretically in our earlier work, for a pyridine linker immobilising CoPc via its cobalt-centre on a CNT, that a high TOF and relatively strong CO_2 adsorption on the cobalt active site can be achieved which is caused by unoccupied d_{z^2} states close to the Fermi level [**24–26**, **250**]. These Co-N_5 complexes have been shown to achieve Faradaic efficiencies of up to 99.4% which is remarkably selective [**251**]. However, direct performance tuning of the cobalt active-site is relatively unexplored compared to performance tuning via ligand functionalisation, and further performance enhancement maybe achieved from different atomic linker species and configurations.

In this study we investigate, using density functional theory (DFT) calculations, atomic linkers used to covalently immobilise CoPc via its cobalt active site on single-walled carbon nanotubes (SWCNT) and their impact on reaction performance. Axial immobilisation just

like ligand immobilisation allows for fast electron transport from the electrode to the catalyst, but also directly influences the electronic character of the active site. We have conducted a screening test of non-metallic and metalloid elements (with the exception of Al) as atomic-style linkers, investigating the effect on the electronic, structural and reaction properties of the immobilised CoPc catalyst. Furthermore, activation barriers are calculated for each reaction step, assuming an 'on-catalyst' reaction scheme, in which all CO_2ERR steps occur on the CoPc catalyst. Our results show that out of all the linker systems considered, the NH and S linker systems are expected to have similar reaction performance compared to the previously mentioned pyridine linker system, while the PH linker may have superior reaction performance at a higher electrode potential.

5.2 Method

The DFT calculations are performed using the Vienna Ab initio Software Package (VASP) version 5.4.4 [**28**, **29**]. For all calculations the generalized gradient approximation of Perdew, Burke and Ernzerhof (PBE) is taken as the exchange-correction functional [**30**] and the Becke-Johnson damping D3(BJ) dispersion correction is included [**31**–**33**]. Calculations are spin polarized and use an energy cutoff of 500 eV which is determined from convergence tests [**242**]. Only the gamma point is used for the k-point sampling due to the large catalyst and substrate systems. The supercell size for the CoPc-SWCNT systems is $30 \times 25 \times 25.65$ Å orthorhombic. The SWCNT is in the (6,0) zig-zag configuration and lies along the z-axis, due to the SWCNTs small radius we expect it to have a metallic electronic character [**209**]. The Methfessel-Paxton scheme for smearing at the Fermi level is used for systems containing metal atoms, while for systems with only non-metal atoms, Gaussian smearing is used. The systems are relaxed until all forces on all atoms are below 0.01 eV/Å. The electronic convergence criteria is set at 10^{-6} eV. For systems with a net charge, the additional charge is included by increasing the number of valence electrons in the supercell. Atomic charges are calculated using the Bader charge method with charge densities calculated in VASP [**252**–**255**]. Calculations that involve implicit water make use of the VASPSol polarized continuum model extension for VASP [**152**, **153**]. A relative permittivity value of 78.4 is used to simulate

implicit water. A finite system could also be used to model the system as done in our previous study for cobalt centred tetraphenylporphyrin (CoTPP) [**4**], but with the periodic nature of the SWCNT a periodic system is computationally efficient and does not require end capping of the SWCNT.

Adsorption energies in this study are calculated using equation 5.1 where $E_{\text{CoPc-COxx}}$ is the total energy of the catalyst-substrate plus adsorbate (e.g. intermediates, reactants) system. E_{CoPc} is the total energy of the catalyst-substrate system and E_{COxx} is the total energy of the free, isolated adsorbate (intermediates, reactants) system as calculated in a large supercell.

$$E_{\text{ads}} = E_{\text{CoPc-COxx}} - E_{\text{CoPc}} - E_{\text{COxx}} \tag{5.1}$$

5.2.1 CHE Model

In order to determine the reaction pathways we calculate the reaction free energies using the computational hydrogen electrode (CHE) model by Norskov *et al.* which is given in equation 5.2 [**34**].

$$\Delta G = \Delta E_{\text{DFT}} + \Delta E_{\text{ZPE}} - T\Delta S + eU + G_{\text{pH}} \tag{5.2}$$

In equation 5.2, ΔG is the change in free energy, ΔE_{DFT} is the change in DFT ground state energy, ΔE_{ZPE} is the change in zero-point energy (ZPE), and T is the temperature which is set to 298.15 K for all calculations. ΔS is the change in entropy energy contribution which we calculate using a combination of two methods. The first entropy method applies to immobilised substrate systems for which we only consider the vibrational entropy contribution since the translational and rotational contributions are likely negligible compared to a free molecule. The second entropy method applies to free molecules (e.g. CO, CO_2) which includes translational, rotational, vibrational and cavitational contributions corrected for solvation effects using the method of Garza [**47**,**242**]. eU is the chosen electrode potential and $G_{\text{pH}} = k_{\text{B}}T\ln(10)\text{pH}$ is a pH correction term that is considered when pH values are greater than zero. Both of these terms are only applied for H + e reaction steps since there is not

simple way of modelling the pH dependence of reaction steps such as CO_2 adsorption [**190**]. For all our calculations an electrode potential of -1.0 V and a pH value of 7 is used, which gives $eU = -1.0$ eV and $G_{\text{pH}} = 0.41$ eV.

5.3 Results

5.3.1 Assessment of Linker Immobilisation

Linkers offer a covalent bridge between a substrate and a catalyst and in some cases these linkers can directly affect the reaction performance of a catalyst. Here, we investigate metal, metalloid and non-metallic atomic linkers (specifically, Al, As, B, Ge, N, P, S, Si linker species) which bond directly to the active site of CoPc anchoring it to a SWCNT substrate. These linkers will change the electronic structure of the cobalt active site of CoPc, in turn changing the CO_2ERR performance for better or worse. We also look at linker hydrogenation for bond termination of linker species which tend to form more than two bonds (e.g. N, P and Si linker species). It is also likely that these linker fragments will not exist in their atomic form and would have to be H terminated.

We determine the energetically most favourable bonding site of the linkers on the SWCNT substrate, where the top, bridge and hollow sites are considered. The results are listed in table 5.1, with energies of each species being given relative to the most favourable non-hydrogenated system. The hydrogenated systems have relative energies calculated using equation 5.3.

$$E_{\text{Rel}} = E_{\text{Sys}} - E_{\text{Fav}} - \frac{1}{2} N E_{\text{H}_2} \tag{5.3}$$

In equation 5.3, E_{Rel} is the relative system energy, E_{Sys} is the system energy of interest. E_{Fav} is the energy of the most favourable (non-hydrogenated) system. N is the number of hydrogenating H atoms and E_{H_2} is the energy of H_2.

It is discovered that linker species further along the periodic table form weaker bonds either with the CoPc catalyst or the SWCNT substrate as shown in figure 5.1. The exception is the As linker which bonds to both the SWCNT substrate and CoPc catalyst, albeit tilted

Linker species	Initial site	Final site	Hydrogenated	E_{Rel} (eV)	Used
Al	Top	Bridge	No	0.64	No
	Hollow	Hollow	No	0.00	Yes
	Bridge	Bridge	No	0.65	No
As	Top	Bridge	No	1.03	No
	Hollow	Hollow	No	1.06	No
	Bridge	Bridge	No	0.00	Yes
		Bridge	Yes (1)	0.27	No
B	Top	Top	No	1.05	No
	Hollow	Hollow	No	0.86	No
	Bridge	Bridge	No	0.00	Yes
Ge	Top	Hollow	No	0.29	No
	Hollow	Hollow	No	0.02	No
	Bridge	Hollow	No	0.00	No
		Hollow	Yes (1)	0.10	Yes
		Top	Yes (2)	-0.48	No
N	Top	Top	No	1.61	No
		Bridge	Yes (1)	-0.89	Yes
		Top	Yes (2)	-1.09	No†
	Hollow	Bridge	No	0.00	Yes
	Bridge	Bridge	No	0.58	No
P	Top	Bridge	No	1.63	No
		Bridge	Yes (1)	0.27	Yes
	Hollow	Hollow	No	1.43	No
	Bridge	Bridge	No	0.00	No
S	Top	Bridge	No	0.00	No‡
	Top	Top	Yes (1)	0.30	No
	Hollow	Top	No	0.27	No
	Bridge	Bridge	No	0.00	Yes
Si	Top	Bridge	Yes (2)	-1.88	No
	Hollow	Hollow	Yes (1)	-1.11	No
		Hollow	No	0.00	No
	Bridge	Bridge	Yes (1)	-1.47	Yes
		Bridge	No	0.26	No

TABLE 5.1. Bonding sites and relative energies (in eV) for the various CoPc-linker-SWCNT systems considered. Energies are relative to the most favourable non-hydrogenated system and calculated using equation 5.3. 'Initial site' is the bonding site of the linker on the SWCNT before relaxation. 'Final site' is the bonding site after relaxation. 'Yes' or 'No' for 'Hydrogenation' indicates whether H is bonded to the linker structure and the number in brackets is the degree of hydrogenation. 'Used' indicates whether the system is further considered. All systems are in a neutral charge state. †Relaxed geometry changes significantly when a net charge is introduced. ‡Initial top site S-linker relaxes to identical bridge site as the initial bridge system.

relative the SWCNT. The arsenic (As) linker forms a bond length of 2.32 Å to the cobalt centre, and is close to reported experimental values between 2.42-2.43 Å found in As_n ligand complexes [**256**]. A similar bonding behaviour is observed between germanium (Ge) and the cobalt centre with a Ge-Co bond length of 2.27 Å. The Ge linker shows weak bonding to the SWCNT substrate with a Ge-C distance of 2.42 Å, while experimental Ge-C bond lengths are found to be between 1.95-2.0 Å in Ge tricoordinate complexes [**257**]. The hydrogenated sulfur linker (SH) shows a different behaviour, with the SH linker remaining bonded to the

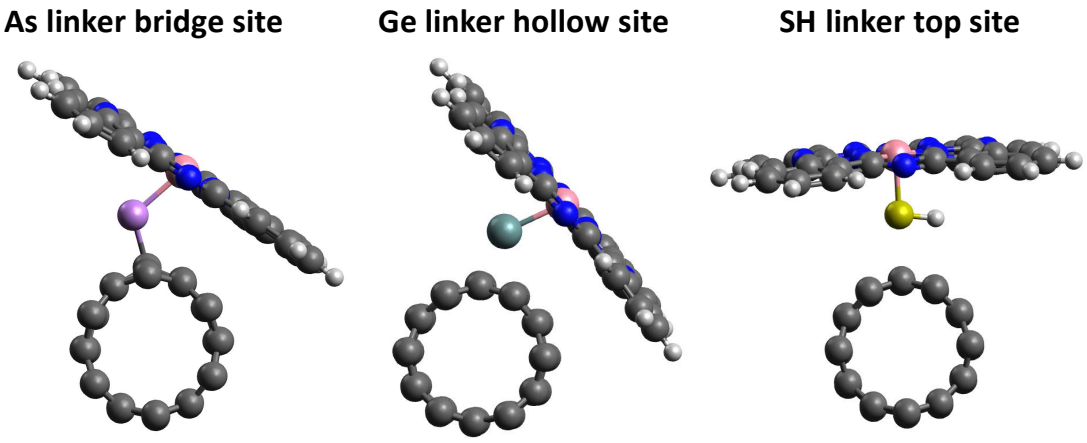

FIGURE 5.1. Relaxed geometries of weakly immobilised CoPc-linker-SWCNT systems and third row linker species. All system geometries have been calculated with a net neutral charge. White, grey, blue, pink, purple, spruce and yellow spheres are hydrogen, carbon, nitrogen, cobalt, arsenic, germanium and sulfur atoms respectively.

cobalt centre, but becomes weakly bonded to the SWCNT substrate. This is a result of the SH linker only having a single unpaired electron in the 3p orbital. The bond length between the SWCNT substrate and the S linker increases from 1.87 Å to 2.46 Å with hydrogenation, while the S-Co bond distance decreases from 2.24 Å to 2.19 Å. In figure 5.1 the As linker system performance is still investigated in later sections of this study, but for the SH linker, the inclusion of hydrogenation impacts the ability of the linker to bond with the SWCNT substrate, so the S linker is further studied without hydrogenation. Similarly, the GeH linker system is investigated instead of the Ge linker system due to its weak bonding to the substrate.

We expect the PH and S linkers to be promising linker candidates with the PH linker expected to have two unpaired electrons in the 3p orbital just like the S linker. Both these linkers immobilise over SWCNT bridge sites with the PH linker having a calculated P-Co bond length of 2.16 Å. This is within the 2.00-2.22 Å range calculated in a previous study for a (PPP)CoPMe$_3$ complex [**258**]. All other linker systems show good bonding geometry between the catalyst, linker and substrate. Only systems that show good SWCNT-linker-CoPc

System component	Net Bader charge (e)	
	Net charge: neutral	Net charge: $-3e$
CoPc	-0.13	-0.95
NH_2 linker	-0.26	-0.26
SWCNT	0.39	-1.79

TABLE 5.2. Net Bader charge analysis (in units of e) of the CoPc, NH_2-Linker and SWCNT substrate system components for the neutral and $-3e$ net charge systems.

bonding geometries as indicated in the 'Used' column of table 5.1 are further investigated in subsequent sections.

5.3.1.1 Nitrogen Linker

Particular attention has been paid to the nitrogen linkers since these systems create an N_5 complex around the cobalt active site which has demonstrated experimentally high turnover frequency performance reflected in favourable reaction pathway calculations [**24**, **27**, **250**]. We find a significant change in the geometry of the NH_2 linker system between a net neutral charge and a net negative charge of $-3e$, where the $-3e$ charge state is required to reduce the CoPc-Linker-SWCNT system for CO_2ERR, see table 5.2. In the reduced state the CoPc catalyst has a net charge of -0.95 and the SWCNT substrate has a large negative net charge of $-1.79e$. As shown in figure 5.2, we observe that the CoPc catalyst no longer bonds to the NH_2 linker in the $-3e$ charge state, with the bond length increasing from 2.32 Å for the neutral system to 2.83 Å. This Co-N bond breaking occurs due to filling of the Co d_{z^2} state under reduced conditions which no longer becomes available for bonding with the NH_2 linker. This is evident by comparing the d_{z^2} orbital in both the PDoS and HOMO orbitals of the neutral and reduced systems in figures C14 and C15 of appendix C, respectively. In figure C14 the neutral system has an unoccupied d_{z^2} component close to the Fermi level, but this disappears for the reduced system. However, previous studies have shown that a complete occupation of the d_{z^2} orbital does not occur for the pyridine linker (another N_5 coordinated CoPc system) which remains bonded to both the catalyst and CNT support under reduced conditions [**24**, **250**, **259**]. This means that CoPc is more weakly bound to the NH_2 linker compared to the pyridine linker.

The experimental study that incorporated the NH_2 linker implies that the CoPc-linker-SWCNT remains stable under CO_2ERR environments, different to what is indicated by our calculations [**27**]. This could mean one of two things: firstly the NH_2 linker-system previously experimentally studied could actually be in a different configuration, such as an NH linker instead of a NH_2 [**27**]; or secondly, there are environmental effects present in the experiment but not reproduced in our model such as non-ideal/defective supports or solvation energies which play an important role in the immobilisation and stability of the charged system. Therefore, given the discrepancy between our calculations and previous experimental results, the NH_2 linker is not further considered in this study.

The bottom two systems in figure 5.2 are the NH and N linker systems which are investigated further in subsequent sections. The NH linker bonds to the SWCNT substrate over a bridge site and remains bonded to both the substrate and catalyst under reduced conditions. Only a slight increase in the bond length from 2.04 Å for the net neutral charge to 2.11 Å for the $-3e$ net charged system is found. We observe that the N linker system (bottom right) inserts itself between one of the C-C bonds of the SWCNT, forming a protruding pryidinic structure on the SWCNT surface. This adsorption behaviour has been previously reported for single N atom adsorption on SWCNT [**260**]. The atomic N-linker bonds to the cobalt centre with a bond length of 2.01 Å and 2.14 Å for the net neutral and $-3e$ net charged systems, respectively.

5.3.2 Redox Potentials

To check the validity of our model we have calculated the redox potentials of CoPc immobilised directly via pyridine linker on SWCNT (4,0). As mentioned in the introduction, CoPc immobilised on CNT has been studied experimentally but due to low catalyst loading they could not accurately measure the reduction potential of their system [**24**]. However, a similar system recently studied does report the reduction potentials of -0.34 V and -1.10 V for the first and second reduction of CoPc immobilised via pyridine in an encapsulated-polymer P4VP [**259**]. Even though they use a different support they have the same CoPc-pyridine complex, so we expect the reduction potentials to be similar between the P4VP and CNT supports. A recent study by Calle-Vallejo and co-workers provides a method of correcting GGA DFT

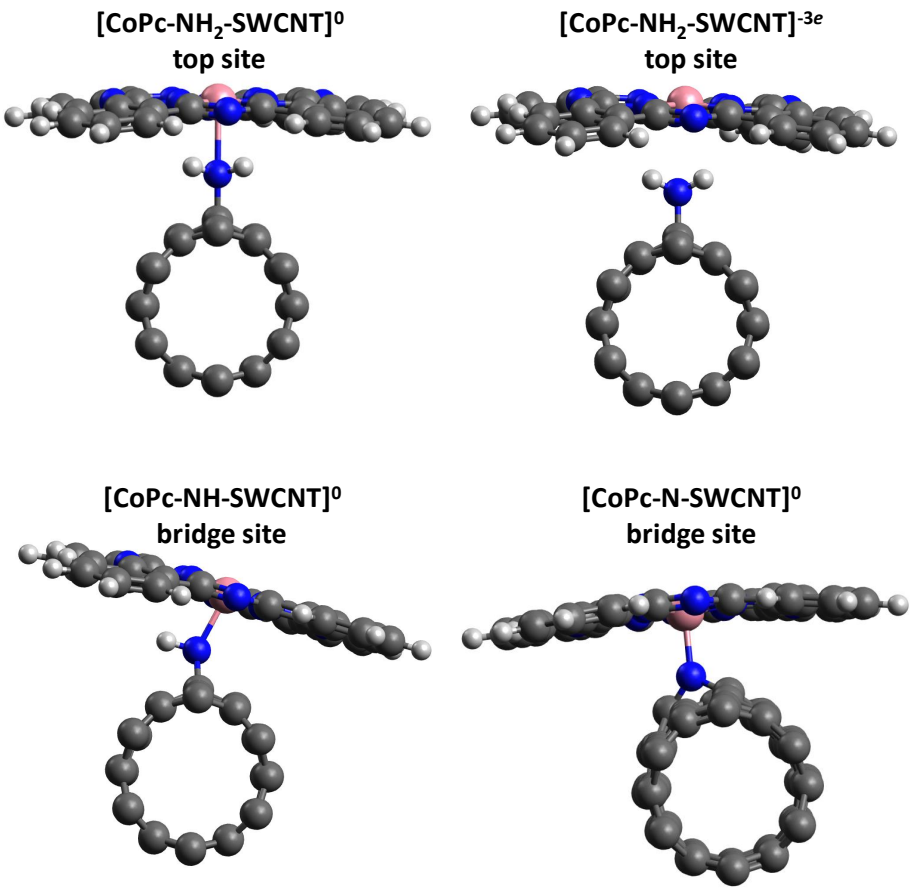

FIGURE 5.2. Relaxed geometries of CoPc immobilised via nitrogen linker on SWCNT. The top two systems show the NH_2 linker for the net neutral charge (left) and $-3e$ net negative charge (right). Bottom two systems have a net neutral charge and show the NH linker (left) and N linker (right).

methods via empirical corrections to the standard free energies of formation. This means we expect to have an approximate error of ± 0.2 eV in our redox potential calculations [**261**].

We have used the Nernst equation in its free energy form as per previous studies, equation 5.4, to calculate the redox potentials [**20**, **262**, **263**]. In equation 5.4, ΔG is the change in free energy (in eV) of the initial and final states of the redox reaction. n_e is the number of electrons transferred and U_{ref} is the reference electrode taken to be the standard hydrogen electrode (SHE) with a value of -4.6 V [**264**]. Equation 5.4 calculates the redox potentials vs. reversible hydrogen electrode (RHE) with a pH value of 7 used.

charge	SWCNT calc. (V)	expt. [**259**] (V)
$-1e$	0.14	-0.34
$-2e$	-0.56	-1.15
$-3e$	-1.06	

TABLE 5.3. Comparison of calculated and experimental redox potentials of CoPc-pyridine immobilised on a SWCNT (4,0) and P4VP support, respectively. All calculated and experimental redox potentials are vs. RHE.

$$U_{\text{redox}} = -\frac{\Delta G}{n_e} - U_{\text{ref}} + 0.059\text{pH} \tag{5.4}$$

From table 5.3 we find that calculated SWCNT redox potentials are close to the experimentally measured redox potentials. It is more appropriate to compare $-2e$/$-3e$ calculated redox potentials with the $-1e$/$-2e$ experimental redox potentials. This is because experimentally the CO_2ERR onset potential is reported to occur when the system is doubly reduced [**259**]. The onset potential is best reflected in the $-3e$ charge state of our calculated system. This is where we have strong (activated) CO_2 bonding to the Co active site. We found that increasing to additional charges beyond $-3e$ does not change the CO_2 adsorption energy significantly [**250**].

Following this relation, we see that the singly reduced ($-2e$ for calc.) SWCNT redox potentials is slightly larger 0.22 V compared to experiment while the doubly reduced is very close, just 0.09 V less compared to experiment. Previous studies for homogeneous (free) CoPc catalyst have found this method calculates much more negative redox potentials compared to experiment [**20**]. The present SWCNT model, however, is found to reproduce the redox potentials relatively accurately, supporting our choice of CNT model.

5.3.3 CO_2ERR Pathways

Having established the subset of favourable CoPc-linker-SWCNT systems, we now investigate their CO_2ERR pathway performance. The reaction pathways are calculated using the CHE model described in section 2.1, allowing us to estimate the electrode potential and pH correction energy contributions.

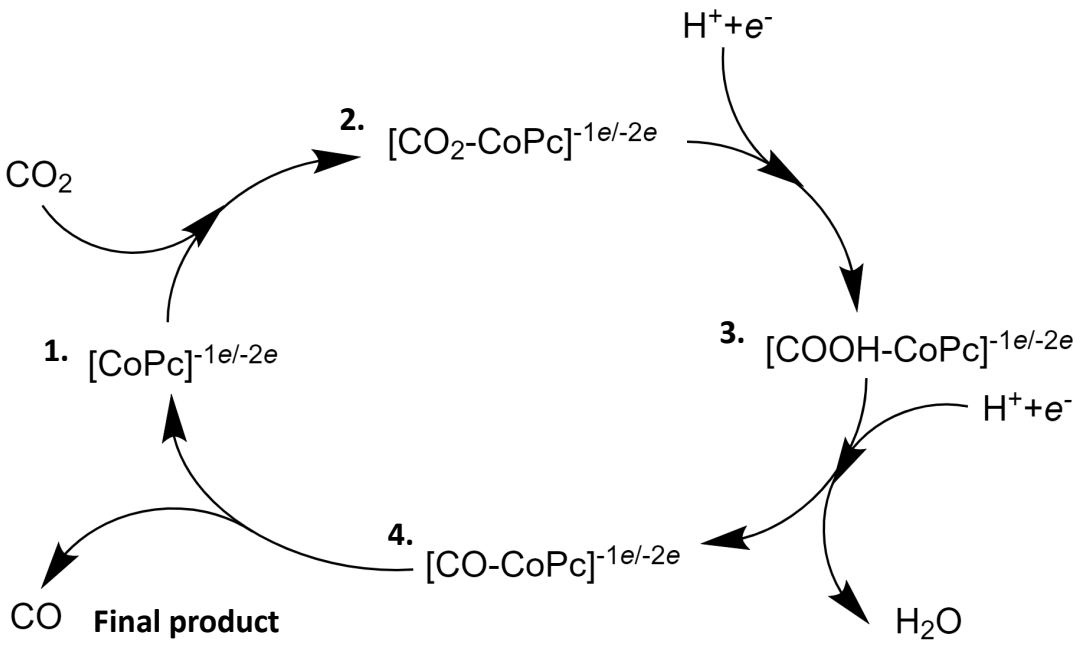

FIGURE 5.3. The 'simplified' CO_2ERR reaction mechanism used in this study. The reaction cycle is split into four steps as indicated by numbers one to four. Both $-1e$ and $-2e$ reduced states are considered for homogeneous CoPc.

To investigate the CO_2ERR pathways, we follow the mechanistic approach of Marianov *et al.* which was applied to cobalt-centred tetraphenylporphyrin (CoTPP), which is structurally similar to CoPc with a cobalt and N macro-cycle centre [**4**, **21**]. This means CoTPP is likely to have a CO_2ERR mechanism akin to that of CoPc. It should be noted, CoPc is the sole catalyst of interest in this study and CoTPP is only included in this section for comparison. In this reaction scheme the rate-determining step is the concerted H^++e^- transfer step of CoPc+CO_2+H^++e^- $\longrightarrow$ CoPc-COOH, which in the 'simplified' scheme, shown in figure 5.3 and used in figure 5.4 and figure 5.5, is CoPc+CO_2+H_2 $\longrightarrow$ CoPc-COOH+$\frac{1}{2}H_2$. In figure 5.4 and figure 5.5 the concerted step is split to include the CO_2 adsorption step, which if strong may indicate a fast rate-determining step. CoPc has been shown experimentally to produce CH_3OH at a selectivity of 44% and at higher electrode potentials than CO production. In the present work we focus on the initial CO2ERR as CoPc is more desirable for CO production. All systems need to be in a reduced state to be 'active' catalysts which means increasing the number of valence electrons in the supercell. We followed our method from our previous study by which we find CoPc-linker-substrate systems require $-3e$ net charge to match the

$-1e$ net charge of a homogeneous (isolated, non-immobilised) CoPc catalyst [**250**]. The $-2e$ net charge for the Homogeneous CoPc system is also considered because there is no consensus regarding the charge of the active anionic state of CoPc [**17–20**].

5.3.3.1 Linker Reaction Pathway Screening

Figure 5.4 shows the calculated CO_2ERR pathways for the CoPc-linker-SWCNT systems selected in section 3.1. We also show for reference the reaction pathway for the homogeneous CoPc systems of $-1e$ and $-2e$ net charge. Favourable pathways are those with the least endothermic and most exothermic reaction steps. The PH, NH and S linker systems show the most favourable reaction pathways and have strong CO_2 bonding. The next most favourable is the SiH linker system. For the PH linker, only the CO_2 adsorption step is slightly endothermic with an adsorption free energy of 0.08 eV; for the NH linker, the same is similar at 0.06 eV. The COOH formation step is more exothermic for the NH linker compared to the PH linker with free energies of -0.35 eV and -0.05 eV, respectively. The H_2O formation step (CoPc-COOH+$\frac{1}{2}H_2 \longrightarrow$ CoPc-CO+H_2O) shows less significant change between linker systems. The free energy for CoPc-CO+H_2O is clustered around -0.50 eV, but the GeH and N linkers are outliers with energies of -0.30 eV and -0.70 eV, respectively. The final CO desorption step is only exothermic for the GeH and PH linker systems with desorption free energies of -0.14 eV and -0.04 eV, respectively. Unlike the PH linker system, the NH linker system has an endothermic final step of 0.13 eV, similar to most of the other linker systems.

At the chosen 1V electrode potential the homogeneous, Al, B, SiH and GeH linker systems all show an endothermic COOH formation step (first H^++e^- transfer step). The SiH linker system shows the least endothermic free energy of 0.01 eV. Given their relatively poor performance we do not think these linkers would make good candidates for experimental investigations. The N linker system shows the strongest endothermic COOH formation step with a value of -0.40 eV but a relatively large endothermic final CO desorption step of ~ 0.3 eV. Therefore, we do not consider the N linker as a potential candidate.

This leaves us with just the NH, S and PH linkers which we also compare to our previous work where we investigated CoTPP immobilised via an oxygen linker and CoPc immobilised

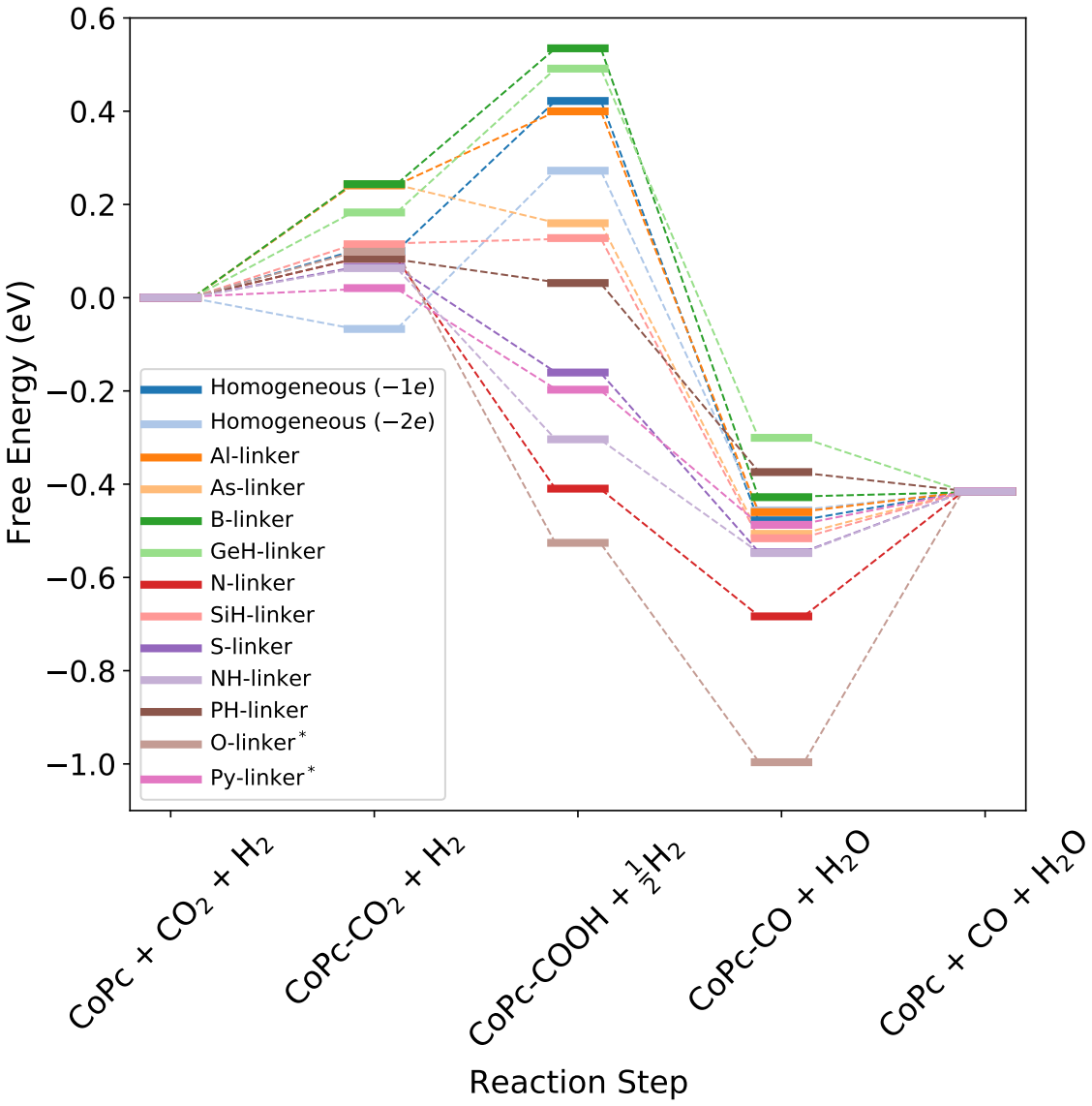

FIGURE 5.4. Comparison of CO_2ERR free energy pathways for the considered CoPc-linker-SWCNT systems. 'Homogeneous' is the reaction pathway for free CoPc. Atomic linkers which are hydrogenated are labeled with H, e.g. NH, PH. The Homogeneous system has been considered with a net charge of $-1e$ and $-2e$ and the other linker systems have a net charge of $-3e$. *CO_2ERR reaction pathways from our previous study for the oxygen and pyridine linker [**250**].

via pyridine linker on SWCNT [**250**]. These CO_2ERR pathways are included in figure 5.4 for comparison with the present CoPc-linker-SWCNT systems as the 'O-linker' and 'Py-linker' pathways. We observe the pyridine linker has the least endothermic CO_2 adsorption free

energy of 0.02 eV which is ~ 0.05 eV less than the NH and PH linker systems. The NH linker system is still found to be more exothermic for the COOH formation step by -0.10 eV compared to the Py-linker. While, the CO desorption step for the NH linker remains slightly endothermic with a desorption free energy of 0.11 eV unlike the PH linker system which has an exothermic desorption energy of -0.04 eV. The O-linker CoTPP system clearly has a favourable COOH formation step but a significantly endothermic CO desorption free energy of 0.58 eV likely caused by the electronegative nature of the O atom and reflected in low experimental turnover frequencies [**23**]. Therefore we expect the NH and S linkers to have a similar reaction performance to the pyridine linker which has shown excellent experimental performance [**24**]. While the PH linker may have superior reaction performance but at a higher electrode potential around -1.2 V.

5.3.3.2 Solvation Effects

For the best performing linker systems, the PH and NH linkers, we have further compared gas-phase (from figure 5.4) and solvation-phase (including implicit water) in figure 5.5. The addition of implicit water causes the free energies of the NH linker system to become more exothermic for the CO_2 adsorption, COOH and H_2O formation steps. The CO_2 adsorption free energy becomes more favourable by -0.16 eV and goes from being endothermic by 0.06 eV in gas-phase to exothermic by -0.10 eV in solvation-phase. The COOH formation step shows a more significant exothermic free energy difference of -0.36 eV, going from -0.30 eV in gas-phase to -0.66 eV in solvation-phase. The final CO desorption step becomes more endothermic by 0.22 eV for solvation-phase when comparing gas-phase in figure 5.4.

The PH linker shows an opposite trend to the NH linker, becoming more endothermic for the CO_2 adsorption step by 0.07 eV when comparing gas-phase to solvation-phase. In solvation-phase the C-Co bond length from the adsorbed CO_2 to the Co active site are almost identical between the PH and NH linkers with bond lengths of 2.10 Å and 2.09 Å, respectively. Comparing the change in CO_2 bond length from gas-phase to solvation-phase the PH-linker and NH-linker systems see a shortening of the bond by 0.19 Å and 0.13 Å, respectively. In solvation-phase the Co-P bond length immobilising CoPc to the PH linker is 2.57 Å,

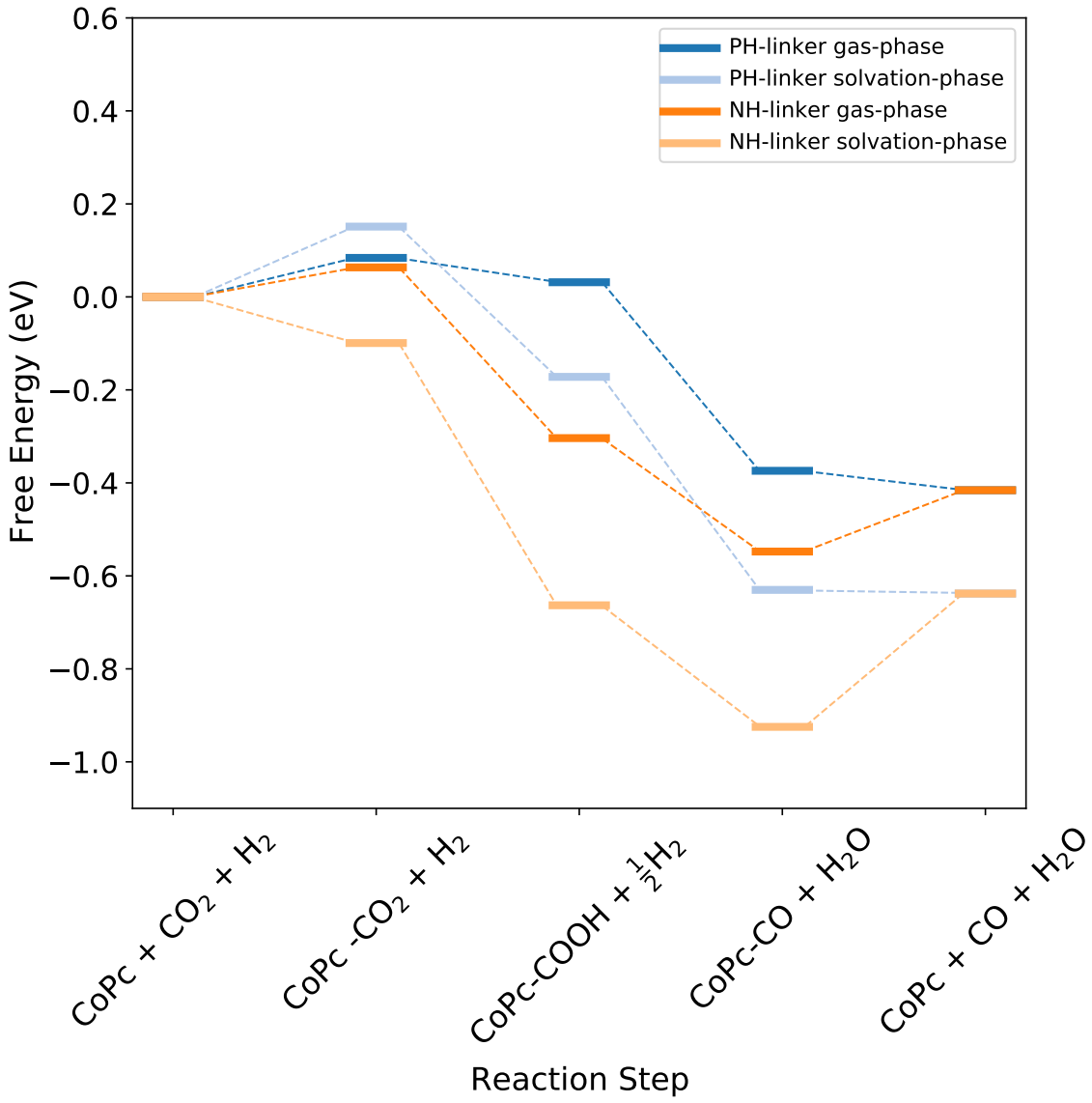

FIGURE 5.5. CO_2ERR free energy pathways in gas-phase and solvation-phase for the PH and NH linker systems.

0.17 Å longer than the Co-N bond length of the NH linker system. This means the change in CO_2 adsorption free energy must be related to the implicit water models effect on both the linker and adsorbed CO_2 region. The COOH and H_2O formation steps show the same strengthening of exothermic behaviour as the NH linker system. Although the change in exothermic behaviour going from gas-phase to solvation phase is ~ -0.20 eV which is ~ 0.15 eV weaker compared to the NH linker. The final CO desorption step shows the same

slight exothermic behaviour in both gas-phase and solvation-phase. Overall, the reaction pathways for the NH and PH linkers becomes more exothermic under solvation conditions but retains the same relative reaction behaviour observed in gas-phase.

The large systems investigated in this study has meant that using more accurate explicit water models, which include the effect of hydrogen bonding interactions between the solvent and intermediate-catalyst systems, would be computationally prohibitive. Therefore, we used an implicit water model simulating the bulk solution as a polarised continuum which is computationally more efficient but provides only an 'average' solvation effect. Polarised continuum models for water are considered well established and have been shown to give a good description [**265**, **266**]. The CO_2 adsorption free energy on homogeneous CoPc has been reported to be ~ -0.5 eV using an explicit model of water calculated using standard DFT methods, which is quite close to our calculated value obtained using the implicit solvation model of -0.35 eV for the same system [**18**].

5.3.4 Density of States

To determine why some CoPc-linker-SWCNT systems show superior performance relative to other systems, we investigate and compare the partial density of states (PDoS) of the cobalt active site. We have selected a subset of systems from figure 5.4 and calculated the PDoS of the cobalt centre *d*-states which are shown in figure 5.6. Some of the systems selected show weak CO_2 physisorption, while others show a more significant interaction as indicated by the bent nature of CO_2, and shorter C-Co bond length between the CO_2 and CoPc.

From figure 5.6 we find linker systems with weak (linear) CO_2 physisorption (Al and B linkers) show a low density of states, at or above, the Fermi level. While those systems with strong (bent) CO_2 bonding (PH, NH and S linkers) show a high density of states, at or just above, the Fermi level. An exception to this trend is found with the N linker system, which shows a relatively high density of states just above the Fermi level, but only weak (linear) CO_2 physisorption. From the decomposition of the cobalt centre d-state into its orbital components (see figure C16 in appendix C), we find a mixed orbital state just above the Fermi level with

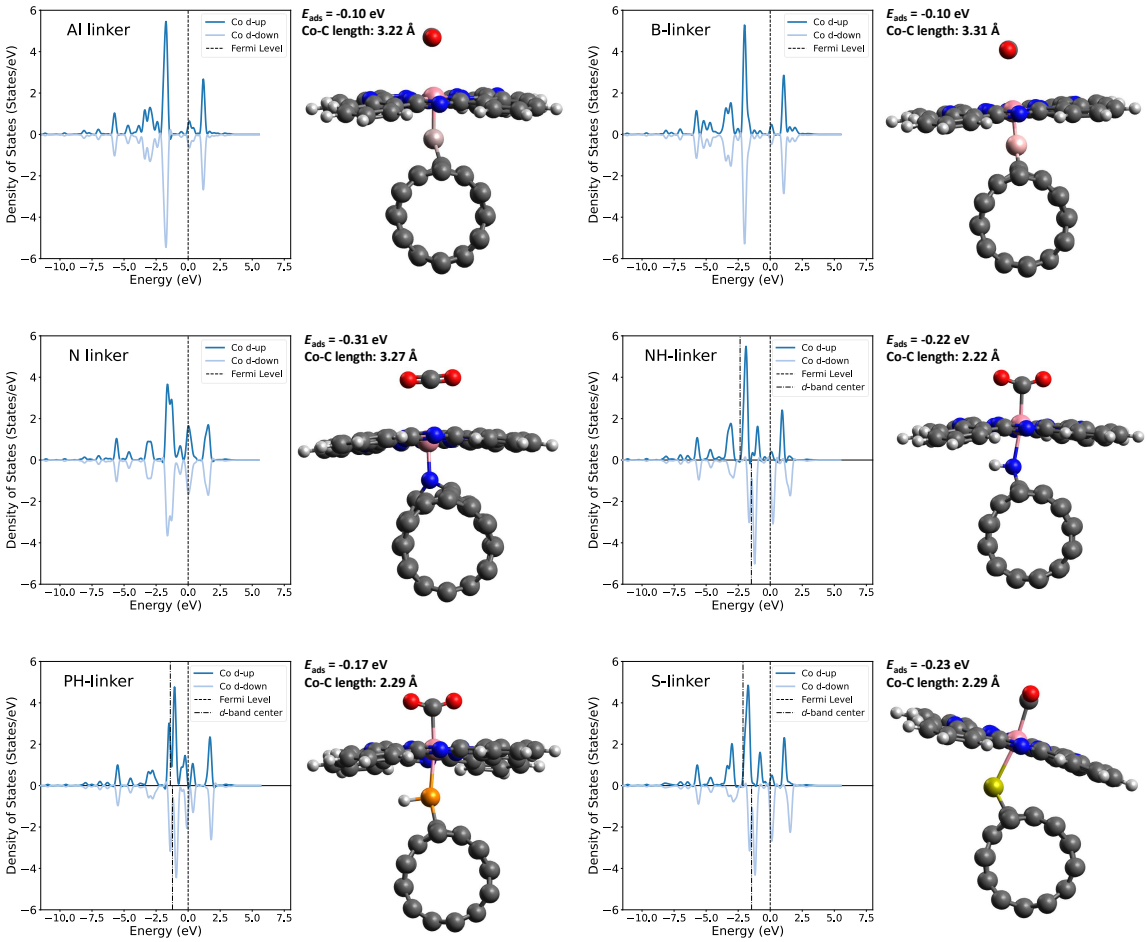

FIGURE 5.6. The partial density of states with respect to the Fermi level (black dashed line at the energy zero) of CoPc-linker-SWCNT systems before CO_2 adsorption, and the corresponding atomic geometries when CO_2 is adsorbed, where the adsorption energy E_{ads}, and Co-C bond lengths are given. PDoS are the total d-states of the cobalt active site, with dot-dashed lines showing the spin-up and spin-down d-band centres. All systems have a $-3e$ net charge. The top two and bottom right systems have the CO_2 intermediate rotated 90°. Grey (top left), light pink (top right), orange (bottom left), yellow (bottom right) and red atoms are Al, B, P, S and O species respectively. The small white, blue, and dark grey spheres represent H, N and C atoms, respectively.

$d_{x^2-y^2}$ having the largest contribution of > 1 state/eV for the NH and PH linker systems. The S linker systems shows the same trend, but with the d_{xy} being the largest component. The N linker on the other hand shows a broader density of states just above the Fermi level and the d-state break down shows a more equal spread of component contributions, all of which are < 1 state/eV.

We notice catalyst systems exhibiting a stronger (bent) CO_2 interaction, have a magnetic moment. In particular, asymmetry of the spin up and spin down PDoS in the NH and S linker systems is a result of both the systems being spin polarized in a doublet state with magnetic moments of 1.4 μ_B and 1 μ_B, respectively. The PH linker systems exhibits a smaller spin polarization with a magnetic moment of 0.2 μ_B. That is, all systems with strong CO_2 adsorption show some degree of spin polarization. This is explained by orbital reordering of the cobalt active site as a result of the linker by which the d_{z^2} orbital is moved (at least in part) to a higher energy state and the d_{xy} is moved to a lower energy state. This is shown in figure C17 and has been previously reported [**25**, **26**]. Once the d_{z^2} orbital exists in a higher energy level the spin-down component is unoccupied and makes up $\sim 20\%$ of a mixed orbital just above the Fermi level, see figure C16 and figure C18 of appendix C. Examination of the PDoS (in figure C17 of appendix C) for CoPc immobilised via pyridine linker on both graphene and SWCNT supports show a significant difference in the orbital ordering. The spin-down d_{z^2} orbital is almost completely unoccupied when using a graphene support but becomes mostly occupied when using a SWCNT support, leaving a mixed orbital with approximately $\sim 20\%$ d_{z^2} component. Given these significant changes in the spin-down occupancy of the d_{z^2} orbital, we do not obtain a significant difference in the CO_2 adsorption energy which is only -0.15 eV stronger using a graphene support. Previous studies have also reported $\sim 20\%$ d_{z^2} component being sufficient for strong CO_2 adsorption [**26**, **190**].

5.3.5 Reaction Barriers

We now investigate the activation barriers associated with each reaction step. Reaction barriers on homogeneous and heterogeneous CoPc catalysts have scarcely been reported and only for a couple of select reaction steps [**20**]. Firstly we calculate the activation barriers of homogeneous CoPc, then we calculate the activation barriers of the best performing CoPc-NH-SWCNT and CoPc-PH-SWCNT linker systems. In section 3.2 CoPc was considered with $-1e$ and $-2e$ net charge, for the calculation of homogeneous CoPc reaction barriers we take CoPc to have a $-2e$ net charge. This is because CoPc with $-2e$ net charge has stronger CO_2 adsorption and has recently been proposed as the anionic charge state of homogeneous

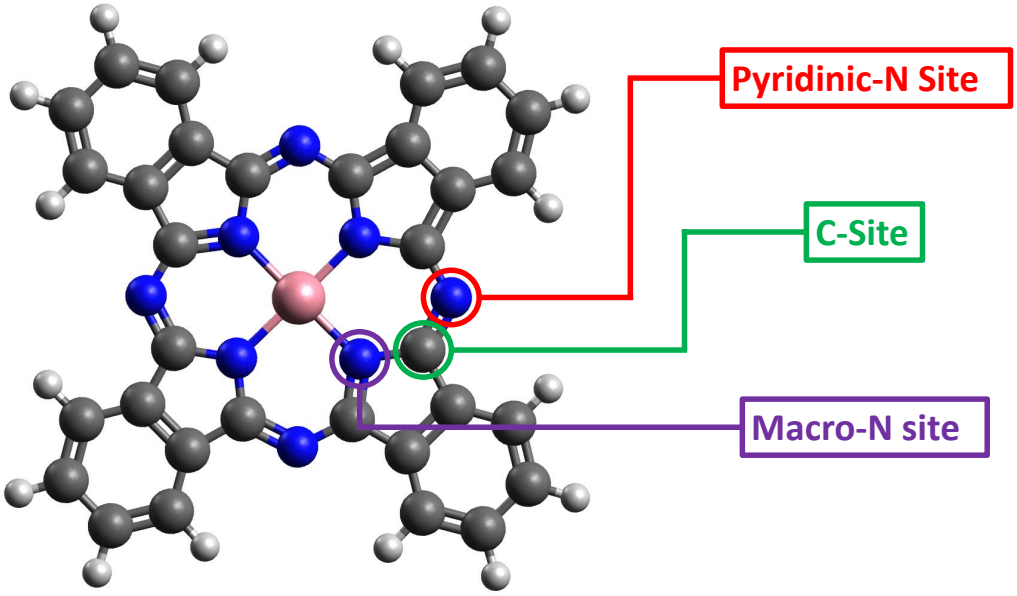

FIGURE 5.7. Identification of CoPc H adsorption sites considered for the transition state calculations.

CoPc for CO_2ERR [**20**, **267**]. We take H to already be adsorbed on CoPc meaning no H^++e^- transfer occurs from the bulk solution and therefore the CHE model used in section 3.2 is not required. H atoms are adsorbed on three unique CoPc sites close to the cobalt active site as highlighted in figure 5.7. This allows us to consider an 'on-catalyst' reaction scheme for activation barrier calculations, which instead of H coming from the bulk solution as a H^++e^- transfer it comes from an already adsorbed H atom on one of three designated CoPc sites. The 'on-catalyst' reaction scheme is discussed further in section 3.4.1.

5.3.5.1 Hydrogenation of CoPc

We start by testing H adsorption sites on isolated homogeneous CoPc, as indicated in figure 5.7, and find H adsorption on one of the pyridinic-N atoms is the most favourable as shown in figure 5.8, highlighted by the green box. The energies in figure 5.8 are total energies (E) relative to the most favourable system, which is H adsorbed on a pyridinic-N site. H adsorption on the C-site closest to the Co-centre shows the next lowest energy by 0.16 eV followed by the Co-centre by 0.37 eV and the macro-N site by 0.81 eV. We observe that

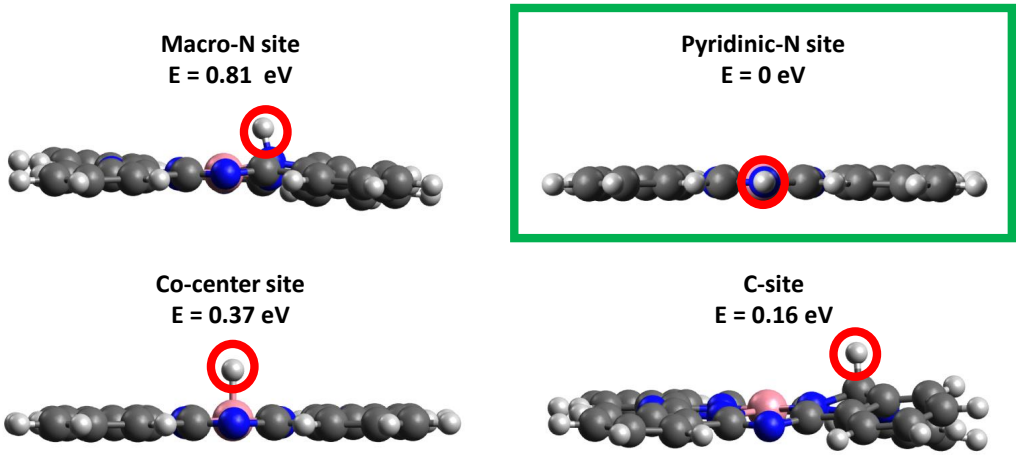

FIGURE 5.8. Relaxed geometries of H adsorption on different CoPc sites. The adsorbed H atoms are highlighted in the red circle. The system highlighted in green is the most favourable H adsorption site and is the energy reference (E) by which all other systems are compared. Each system has a $-2e$ net charge.

H adsorption on the C-site significantly deforms the CoPc molecule by twisting its ligand structure. A similar protonation approach on cobalt-centred porphyrin has been studied by Yao *et al.* which assumed H adsorbed on a macro-N site [**188**].

Next we investigate the CO_2 adsorption behaviour on CoPc with H co-adsorbed on the different sites as shown in figure 5.9 with adsorption energies calculated using equation 5.1. We find CO_2 achieves the strongest adsorption energy when H is co-adsorbed on the macro-N site of CoPc. However, the macro-N site is also the system with the least favourable energy as shown in figure 5.8. CO_2 adsorbed on CoPc with H on a pyridinic-N site still shows the lowest total system energy, with a CO_2 adsorption energy half that of the macro-N system. CO_2 adsorption with H on the C-site shows similar adsorption energies to having H on the pyridinic-N site. It is clear from figure 5.9 that H co-adsorption on sites near the cobalt active site help facilitate CO_2 adsorption.

Given we have found H adsorption is favourable on the pyridinic-N site, it is possible that all pyridinic-N sites are hydrogenated under experimental conditions. This would leave only C-sites and macro-N sites as potential H adsorption sites. When all pyridinic-N sites on CoPc are saturated with H, we obtain a strong CO_2 adsorption energy of -0.61 eV, which is close to

the H on macro-N system. If we include an additional H on a C-site when all the pyridinic-N sites are hydrogenated, we obtain an adsorption energy of -0.56 eV, slightly less compared to having no additional H on the C-site. The case when all pyridinic-N sites are hydrogenated and there is an additional H on a macro-N site has not been included in figure 5.9 since, on relaxation, the system immediately forms COOH.

Previous studies have shown hydrogenation of the pyridinic-N sites of CoPc results in significant changes in the electronic structure and geometry of the CoPc molecule [**268**–**271**]. We find the Co-N bond lengths of CoPc increase by ~ 0.03 Å when one pyridinic-N site is hydrogenated and by ~ 0.06 Å when all four pyridinic-N sites are hydrogenated, as previously reported [**271**]. CoPc also experiences a change in magnetic moment upon hydrogenation. In-particular, hydrogenation of a single pyridinic-N site increases the magnetic moment by $0.2\mu_{\mathrm{B}}$ and when all pyridinic-N sites are hydrogenated the magnetic moment decreases by $0.4\mu_{\mathrm{B}}$ resulting in noticeable spin quenching of the system relative to unhydrogenated CoPc.

5.3.5.2 Off-centre CO_2 Adsorption

A previous study by Marianov *et al.* discovered off-centre CO_2 binding on cobalt-centred tetraphenylporphyrin (CoTPP) was more favourable compared to directly adsorbing on the cobalt centre [**4**]. In figure 5.10, however, off-centre binding of CO_2 on CoPc is much less favourable (by $\sim$1.0 eV) compared to CO_2 adsorption on the cobalt centre. This is likely due to the rigidity of the CoPc molecule which prefers to remain planar, different to CoTPP which prefers a saddle geometry. We do not expect off-centre binding of CO_2 to play a role in the CO_2ERR pathway of CoPc. Therefore, the less favourable off-centre binding of CO_2 on CoPc leads to its better stability compared to CoTPP.

Another off-centre binding scenario has recently been proposed by Xia *et al.* for the same system studied here [**246**]. In this scenario COOH was determined to bond on a macro-cycle N site before moving to the cobalt active site where OH cleavage occurs, leaving the CO product. We considered this scenario for COOH on a macro-cycle N site and found COOH experienced a strong repulsion along the z-axis, away from the CoPc catalyst, see figure 5.11. The same repulsive behaviour was found when the system had a net neutral and net negative

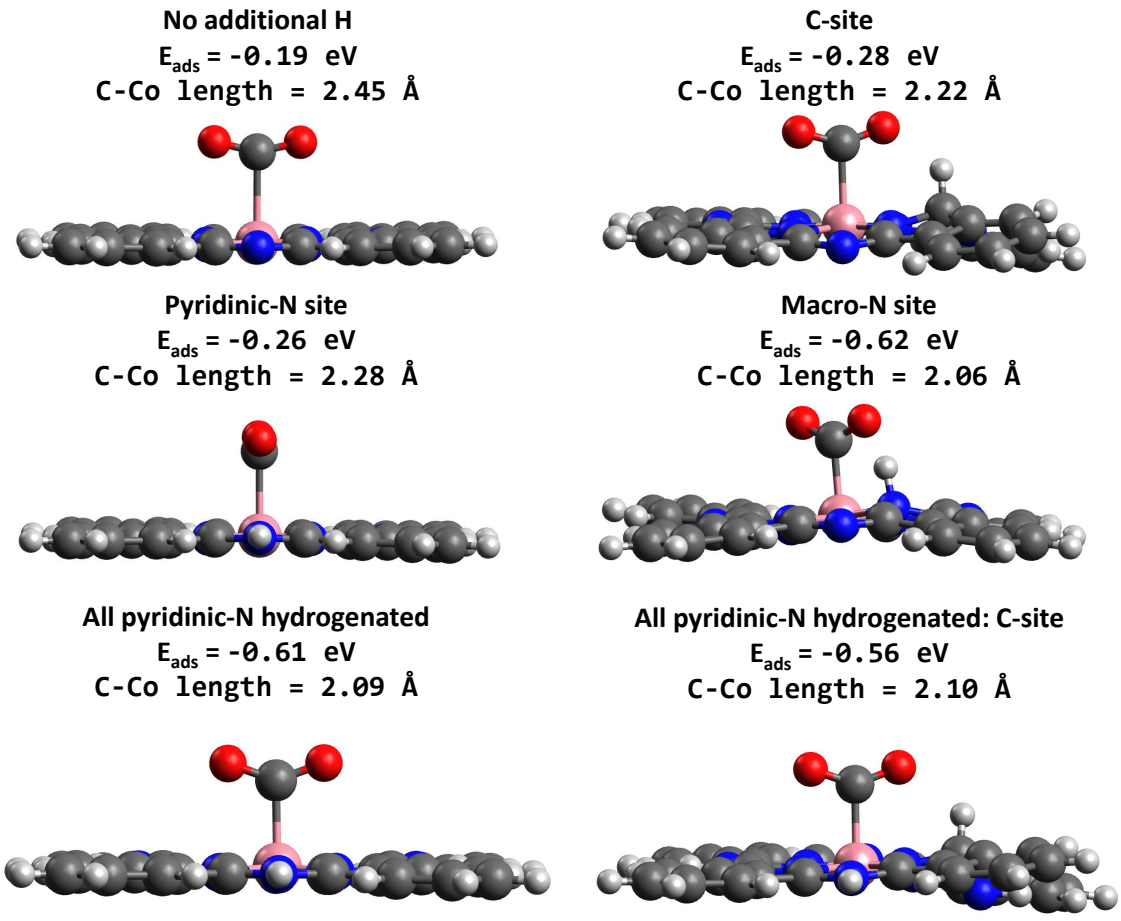

FIGURE 5.9. CO_2 adsorption geometries, energies and bond lengths on CoPc for different H co-adsorption sites. The pyridinic-N system has been rotated 90°, for better visibility of the additional H atom. The net charge on each of these systems is $-2e$.

$(-2e)$ charge. It is interesting that we find such a discrepancy between our calculation and those of Xia *et al.*. This could be a result of different calculation methods, in that Xia *et al.* used the Amsterdam Density Functional (ADF) code [**272**] with a TZP basis set [**273**] and PBE exchange-correlation functional, without periodic boundary conditions. Another explanation could be the geometry found by Xia *et al.* was used to calculate spectra which closely matched their experimental x-ray spectra.

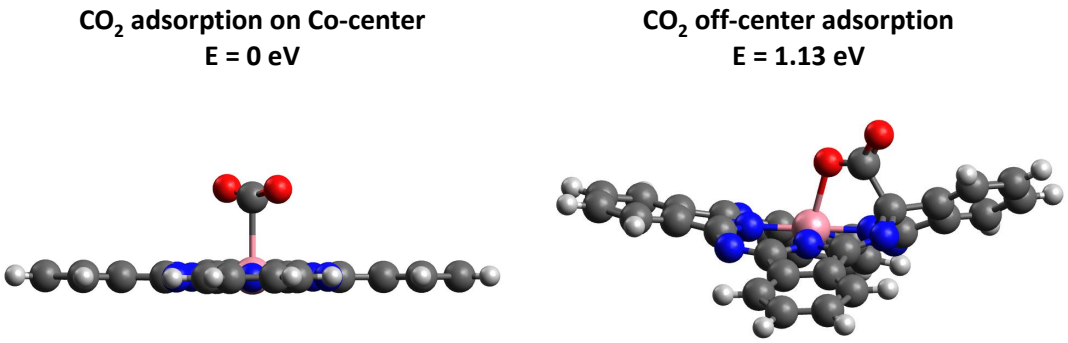

FIGURE 5.10. The cobalt centre and off-centre adsorption of CO_2 on CoPc. The energy is in eV, and is given with reference to CO_2 adsorbed on the Co-centre for the system which has the lowest energy. The net charge on each of these systems is $-2e$.

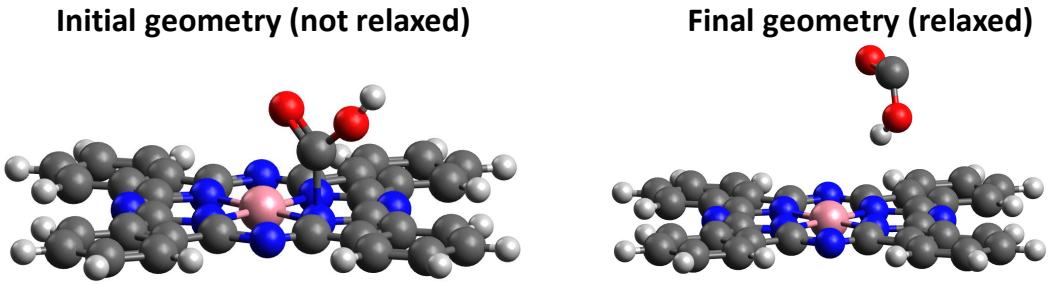

FIGURE 5.11. Initial and final (relaxed) geometries of COOH over a macro-cycle N-site of CoPc. The system has a net charge of $-2e$.

5.3.5.3 Activation Barriers of Homogeneous CoPc

In the following we calculate the reaction barriers for COOH formation and subsequent cleavage into adsorbed OH and CO over the homogeneous molecular catalyst CoPc. These reaction steps for which the barriers are calculated, follow the reaction schemes for CoPc proposed in previous studies [**18**, **20**, **267**]. An 'on-catalyst' reaction, meaning all reactions steps occur on the CoPc catalyst (excluding the initial CO_2 adsorption and final CO desorption steps), has been assumed for the calculation of these barriers without the need for expensive molecular dynamics calculations. All species involved in the CO_2ERR remain in the system

(or supercell), different to the CHE method used in section 3.2 which requires separate adsorbent and adsorbate systems to calculate reaction pathways.

As the initial step we consider the adsorption of CO_2 onto the cobalt active site with H atoms adsorbed on the sites indicated in figure 5.7. For each H adsorption site the barriers will be different for the CO_2 adsorption and COOH formation steps, while, the OH cleavage and CO desorption steps do not depend on the initial H adsorption site on CoPc. In all barrier calculations the cobalt centre of CoPc is fixed. For CO_2 adsorption from the gas-phase onto CoPc the C atom of CO_2 is fixed for specific distances from the cobalt centre and all other atoms relaxed. The results are shown in figure 5.12. We find there is no barrier to CO_2 adsorption when CoPc is in a reduced state with a net charge of $-2e$. The CoPc system with H adsorbed on a pyridinic-N site has the lowest energy (most favourable configuration) with a relatively flat adsorption potential. This is followed by the CoPc system with H on the C-site which shows a slightly steeper adsorption potential. The system with H on the macro-cycle N site shows an adsorption energy variation for CO_2 that is an order of magnitude steeper compared to the other systems due to the stronger adsorption energy and shorter bond lengths as shown in figure 5.9.

To calculate the reaction barriers for COOH formation, we fix the position of H at each step of its transition towards the O atom of CO_2 adsorbed at the cobalt centre. This is shown in figure 5.13. We find almost no barrier to COOH formation (only a slight barrier of 0.09 eV) when H is adsorbed on a macro-N site (green curve), although the starting geometry with H on the macro N-site is less favourable compared to the C and pyridinic-N sites. COOH formation, when H is on the C-site, shows the highest activation barrier of 0.68 eV. This is likely caused by the significant bending and twisting of the CoPc catalyst when H is adsorbed on this site, which is further exacerbated when H moves towards adsorbed CO_2. When the initial position of H is on a pyridinic-N site of CoPc and it moves towards the centre of the catalyst to form COOH, we obtain a relatively low barrier of 0.30 eV. During this pathway the CoPc catalyst remains in a planar configuration without experiencing any significant twisting/deformation. Interestingly, adsorption of H on the pyridinic-N site has the most favourable energy, even more energetically favourable (by -0.19 eV) compared to forming the COOH intermediate.

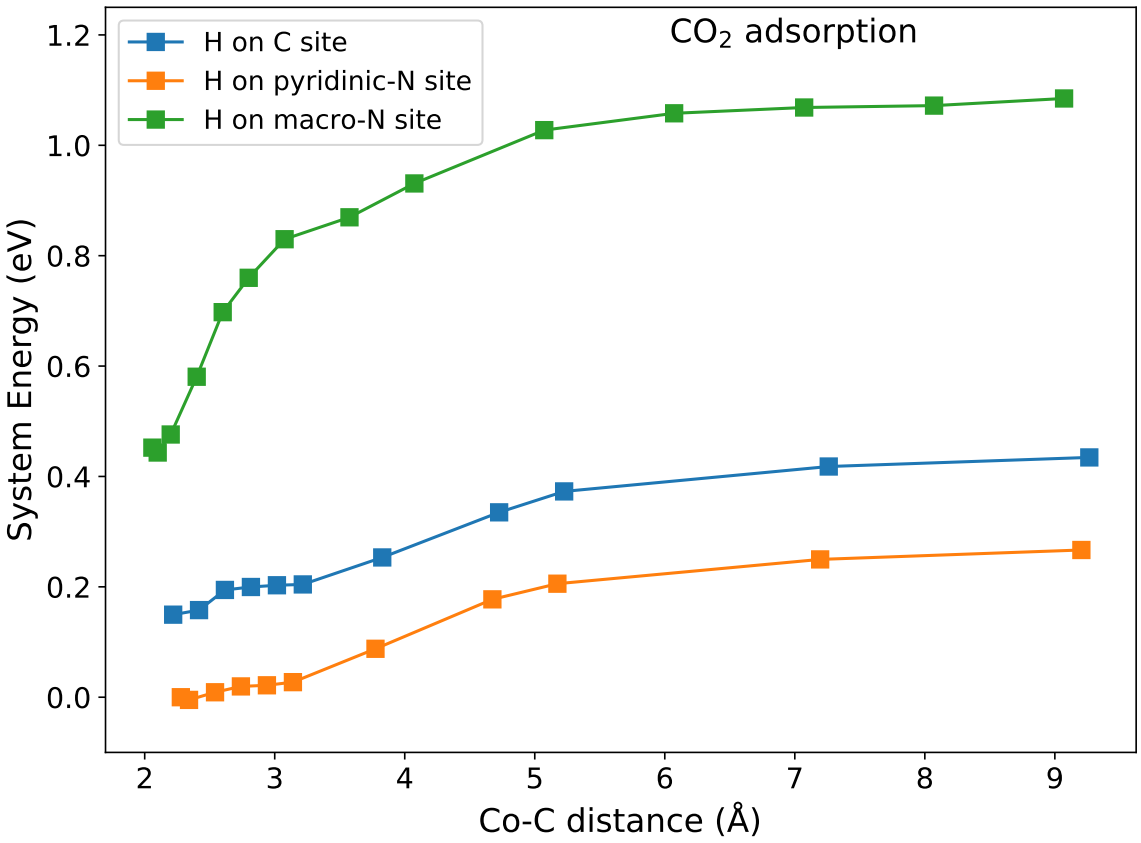

FIGURE 5.12. Calculated energy pathways for CO_2 adsorption on the cobalt centre of CoPc. All energies are calculated relative to the final CoPc-H-CO_2 system with H adsorbed on a pyridinic-N site. All systems have been calculated with a $-2e$ net charge.

This further supports our statement in section 3.4.1 that the pyridinic-N sites could become hydrogenated under experimental conditions.

In figure 5.14 both OH cleavage and CO desorption reaction barriers are calculated. The OH cleavage barrier has been calculated for OH desorption into the solution and for OH adsorption to a C site on CoPc. For both scenarios we fix the position of the O atom of OH at each step and relax all other atoms except the cobalt centre. For OH desorption into the solution we also fix the position of the C atom of COOH. We see the OH moving into the solution scenario shows the highest energy barrier of 2.30 eV. For OH co-adsorption on CoPc, the reaction barrier is lower, 1.44 eV. To the best of our knowledge there have been no first principles calculations on the cleavage of OH from COOH over similar molecular

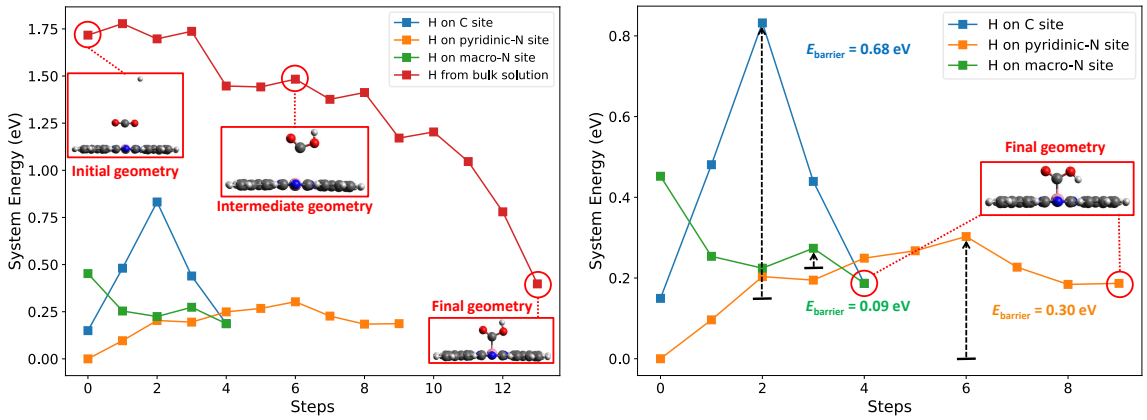

FIGURE 5.13. Calculated activation barriers for COOH formation. The left plot shows the COOH formation barrier and pathway energies for H coming from bulk solution (red), or with H already adsorbed on CoPc. The right plot is an enlarged figure showing the activation barriers for COOH formation when H is initially adsorbed on the different CoPc sites shown in figure 5.9. All energies are relative to CO_2-CoPc-H with H on a pyridinic-N site of CoPc (the zero energy). The black arrows indicate the barrier heights. Red circles highlight the steps of the shown geometries. All systems have been calculated with a $-2e$ net charge.

catalysts, but a previous study has calculated the reaction barrier of C-OH cleavage from methylcyclohexanol to be ~ 1.70 eV [**274**]. A recent study of CO_2ERR on transition metal clusters have found the COOH $\longrightarrow$ CO+OH barrier to be ~ 0.50 eV [**275**]. The difference in barrier energies results from stronger attractive interactions over a metal surface compared to our molecular metallorganic CoPc catalyst.

The CO desorption step is found to have a barrier of 0.61 eV, as seen in the right plot of figure 5.14. To calculate the barrier we fixed the position of C at each step away from the surface and relaxed all other atoms except the cobalt centre. This is slightly less than the experimental CO desorption energy of 0.90 eV from a Co(0001) surface [**276**]. A recent DFT study by Chen *et al.* found CO desorption from CoPc would experience spin cross over from a quartet to doublet state when reduced by $-2e$, with a comparative energy barrier of ~ 0.50 eV [**267**]. We did not observe any spin cross over in our calculations of CO desorption, possibly due to differences in calculation methods.

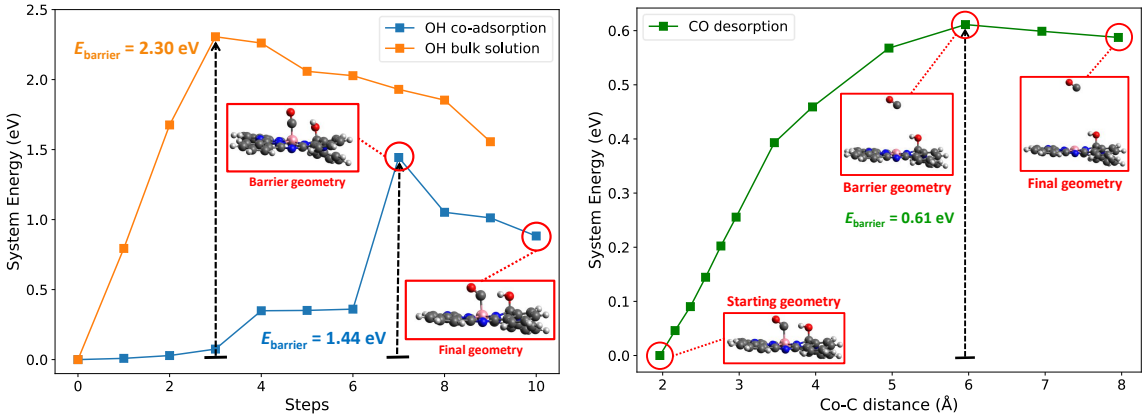

FIGURE 5.14. Calculated activation barriers of OH cleavage (left) and CO desorption (right). OH cleavage barriers are calculated for OH going to the bulk solution (orange) and OH re-adsorbing on CoPc (blue). The CO desorption step has only been calculated for CO desorption when OH is re-adsorbed on CoPc. Energies of the left plot are shown with respect to the initial CoPc-COOH system. The energies of the right plot are with respect to the CoPc-CO system. Black lines indicate reaction barriers and red circles highlight the geometries at particular steps or distances. All systems have been calculated with a net charge of $-2e$.

It is interesting to consider which 'on-catalyst' pathway CO_2ERR is likely to take on CoPc. If we go by figures 5.12-5.14 the H on pyridinic-N site is the lowest energy configuration with a relatively small barrier of 0.30 eV for COOH formation. Under experimental conditions when H^+ and e^- are abundant, these pyridinic-N sites may be saturated with H, leaving only H adsorption on other C and macro-N sites. Given the higher COOH formation barrier of 0.68 eV when H is on the C-site, it is likely this pathway is not competitive. This leaves the two N-sites as potential 'on-catalyst' H sources for COOH formation. Two scenarios then exist for on catalyst COOH formation, either one of the N site pathways dominate or both pathways are competitive with each other. Looking at the initial states, we would expect pyridinic-N sites to become saturated with H followed by C-sites and then macro-N sites. This could mean H adsorption on an macro-N site is statistically less likely to occur, but it does give rise to an almost barrierless reaction pathway for COOH formation. OH adsorption on the CoPc catalyst is assumed for our 'on-catalyst' scenario, but under experimental conditions it is expected that OH^- goes into the solution and remains as OH^- or forms H_2O (depending on the pH of the solution) [**4**, **18**, **20**, **248**].

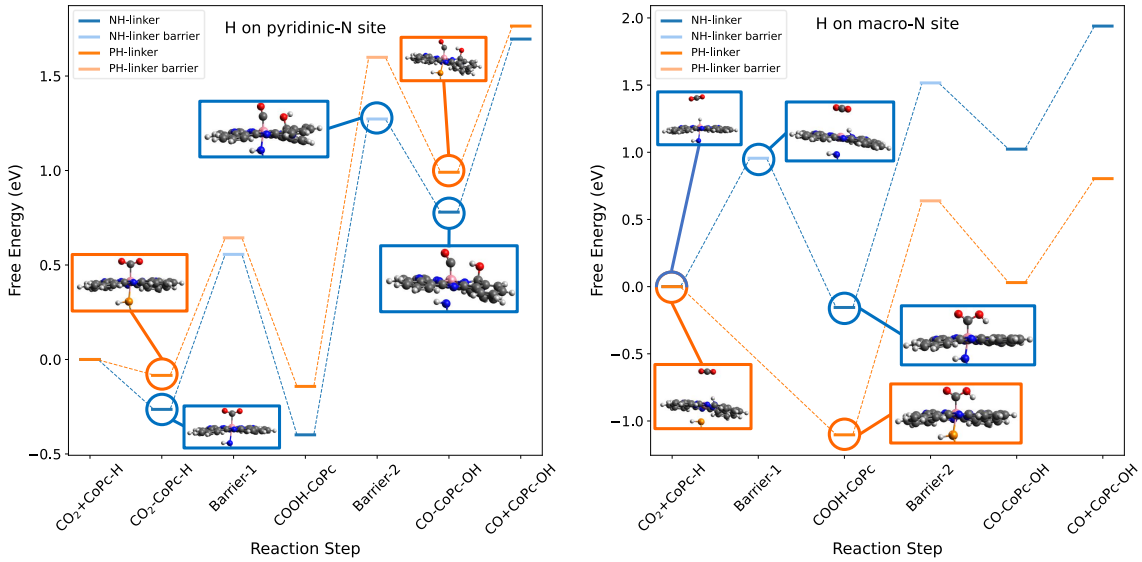

FIGURE 5.15. Comparison of reaction pathways including activation barriers for the NH and PH linker systems. The CO_2ERR pathway is calculated for H both initially on a pyridinic-N site and macro-N site. Steps and geometries of interest are highlighted in red.

Under experimental conditions the 'on-catalyst' formation of COOH may be out competed by H^++e^- transfer from the bulk solution. In the left plot of figure 5.13, COOH is formed above the CoPc catalyst without a barrier as H is brought from solution closer to the weakly adsorbed CO_2. This points to the CoPc+CO_2+H^++e^- $\longrightarrow$ CoPc-COOH step likely being concerted, and as mentioned in section 3.2, is proposed as the rate-determining step [**4**, **19**, **20**, **267**]. In the following section, we will investigate 'on-catalyst' pathways and activation barriers for CO_2ERR over the best performing CoPc-linker systems identified in sections 3.2-3.3, through which the effect of the molecular catalyst being immobilised on the support can be determined.

5.3.5.4 Linker System Activation Barriers

In sections 3.2-3.3 we found both the PH and NH linker systems demonstrated the best CO_2ERR performance based on the reaction pathways in figure 5.4. We now investigate the 'on-catalyst' reaction pathway and activation barriers for these systems. The results are shown in figure 5.15 where we have calculated the 'on-catalyst' CO_2ERR pathways for H on

a pyridinic-N site and macro-N site. For H on pyridinic-N the CO_2 adsorption free energy is -0.26 eV on the NH linker, stronger compared to (-0.08 eV) the PH linker system. The barrier to COOH formation is 0.82 eV and 0.72 eV for the NH linker and PH linker systems, respectively which are considerably higher than the 0.30 eV barrier of the homogeneous system (see figure 5.13). We believe this is due to bending of the CoPc geometry and not due to strengthening of the H-N bond (see figure 5.16) because the H adsorption energy is similar (only a 0.05 eV difference) to the homogeneous CoPc system. The barrier to OH cleavage and adsorption on a CoPc C-site is 1.67 eV and 1.74 eV for the NH and PH linker systems, respectively. These values are ~ 0.30 larger than the homogeneous system in figure 5.14. We notice that the CO-CoPc-OH geometry becomes detached from the NH linker, with a Co-N bond length of 2.48 Å, increasing by 0.35 Å compared to the COOH-CoPc step. This is also reflected by a more exothermic step going from 'Barrier-2' to CO-CoPc-OH by -0.10 eV for the PH linker system compared to the NH linker system given the Co-P bond remains in tack for the CO-CoPc-OH geometry. It is therefore possible that the NH linker system could become detached from the CoPc catalyst at high pH levels given the adsorption of OH^- on CoPc.

For H on a macro-N site, the initial step shows a detachment of the CoPc-H complex from the PH linker, increasing the Co-P bond length by ~ 0.20 Å (relative to the COOH-CoPc-PH-CNT system), resulting in a physisorbed interaction. This weaker CoPc-linker interaction may result in catalyst leaching. For the NH linker, the H atom initially does not bond to the macro-N site, instead bonding to the Co-centre which is energetically more favourable, see figure 5.8. Once the CO_2 intermediate is brought closer to the Co-centre, H bonds to the macro-N site the forms COOH with a 0.96 eV barrier. The PH linker does not have a barrier since H remains on the macro-N site, spontaneously forming COOH once CO_2 adsorbs on the Co-centre. This results in a strongly exothermic energy for COOH formation of -1.10 eV on the PH linker system, compared to -0.16 eV (with the aforementioned barrier) for the NH linker system. The formation of COOH shortens the CoPc-linker bond for both systems, since the H atom is no-longer bonded to the macro-N site. The OH cleavage step is identical to the H on pyridinic-N scenario. Finally, the CO desorption energies are approximately the same for both linker systems, around ~ 0.90 eV.

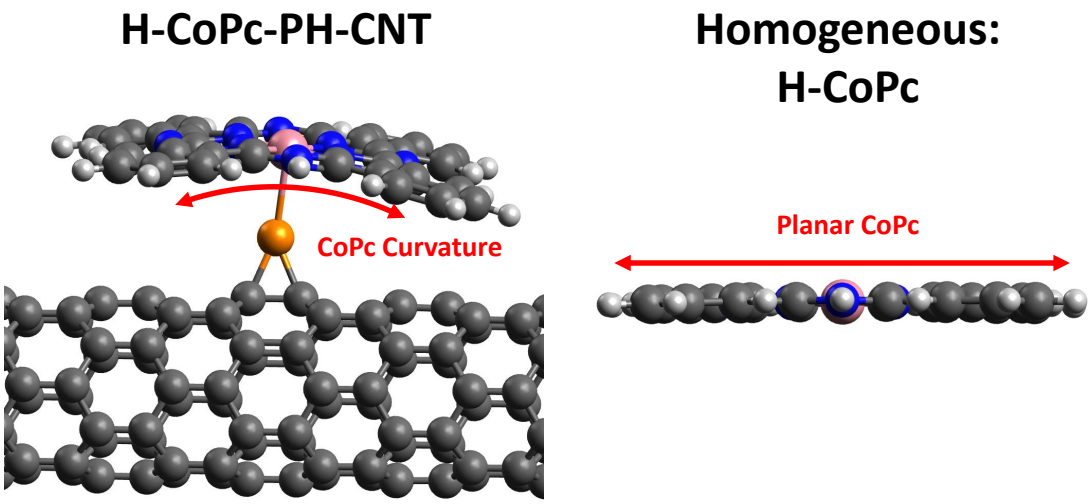

FIGURE 5.16. Relaxed geometries of the H-CoPc-PH-SWCNT system and H-CoPc system where H is on a pyridinic-N site. Structural nature of the CoPc catalyst is marked in red.

On considering which linker system shows the better performance, we observed that the PH linker has a smaller barrier to COOH formation when H is on a pyridinic-N site and no barrier, unlike the NH linker, when H is on a macro-N site. Also, when H is on a macro-N site, the PH linker system shows a more 'concerted' and exothermic reaction step for COOH formation. Furthermore, the P-Co bond for the PH linker system remains intact when OH is adsorbed on a CoPc C site, unlike for the NH linker system. This implies that the PH linker system would have better 'on-catalyst' CO_2ERR performance and robustness and thereby propose it as a potentially promising linker for CoPc immobilisation for the CO_2ERR.

5.4 Summary

We have studied the effect of different linker species used to tune the performance of active-site immobilised CoPc on single-walled carbon nanotubes (SWCNT). We discover that out of the eight linkers investigated the NH, S and PH linkers show the best CO_2 electroreduction reaction (CO_2ERR) performance. These linker systems are spin polarized and found

to have a high density of spin-down d-states close to the Fermi level, including a d_{z^2} component reordered to a higher energy level providing an attractive interaction between the CO_2 intermediate and cobalt active site. Calculated redox potentials of our system with a pyridine linker shows good agreement with experimental reduction potentials of similar systems. Furthermore, 'on-catalyst' pathways are compared and activation barriers calculated. It is estimated that an 'on-catalyst' CO_2ERR pathway would involve H on a pyridinic-N or macro-N CoPc site. Comparing the 'on-catalyst' performance between the favoured NH and PH linker systems, we conclude, based on activation barriers and the CoPc-linker bonding, that the PH linker presents the best CO_2ERR catalyst candidate.

CHAPTER 6

Summary and Outlook

This thesis investigates three main themes, namely, improved methods to calculate solvation entropy which are required to determine accurate free energy reaction pathways, the properties of directly immobilised metal-organic catalysts on carbon supports used in the CO_2 electroreduction reaction (CO_2ERR) and linker immobilised metal-organic catalysts on carbon nanotubes for the CO_2ERR. With regard to the first theme, we considered various methods including scaling of gas-phase entropy, Langevin dipoles and solvation corrections to gas-phase entropy to calculate solvation entropy values [**42–47**, **49–51**]. Such approaches allow us to calculate solvation entropy values without the need to conduct expensive *ab initio* molecular dynamics calculations. The molecular size dependence of these solvation entropy methods have hitherto not been studied, with bench marking sets usually restricted to smaller solute molecules. Having developed the methodology to accurately and efficiently calculate solvation entropy values for molecules over a range of sizes, we were then able to include the effect of entropy in the reaction pathways calculated using density functional theory to obtain accurate free energy reaction diagrams which were used to assess and predict the CO_2ERR performance of the considered catalysts. We firstly investigated the direct immobilisation of cobalt-centred tetraphenylporphyrin (CoTPP) and cobalt-centred phthalocyanine (CoPc) on carbon supports, namely, graphene and carbon nanotubes (CNTs). The impact of immobilising CoTPP and CoPc at intrinsic defect sites in the carbon supports has not previously been studied theoretically or experimentally despite the fact that defects such as vacancies can significantly change the electronic properties. The immobilisation of metal-organic catalysts can also be achieved by using atomic-style linkers (via their cobalt active site) on carbon supports such as CNTs. Some of these systems have demonstrated superior reaction rate performance compared to homogeneous (free molecular catalysts) and directly immobilised

catalysts [**23**, **24**, **27**, **249**]. In view of this we performed a series study to investigate which species of atomic-style linkers 'tunes' the electronic properties of the cobalt active site to improve the catalyst performance.

The results of these investigations were described in detail in the various chapters, specifically, chapter 3 reports our effective approach to calculating solvation entropies required for obtaining accurate free energy reaction pathways. The excellent performance was demonstrated via a bench marking study of the solvation entropy methods investigated. We found that the method of correcting each entropy contribution for solvation (method of Garza *et al*) provided the most accurate solvation entropy values when using the box-packing method for cavity formation entropy [**47**]. This method also gave a mean average error (MAE) of 0.07 eV compared to MAE's of 0.32 eV and 0.43 eV for the dipole (ChemSol 2.1) method and vibrational entropy, respectively. This method showed the same linear trend in molecular van der Waals volume vs. solvation entropy as the experimental results and was also found to give more accurate CO binding energies of -0.24 eV, compared to the experimental value of -0.26 eV [**189**].

In chapter 4 we used the developed solvation entropy approach of chapter 3 (in conjunction with the computational hydrogen electrode model (CHE)) to study the immobilisation of CoTPP and CoPc on carbon supports and study the effect that intrinsic defects in the carbon support have in facilitating CoTPP and CoPc immobilisation and their impact on the CO_2ERR performance. Interestingly, we found that defects act like 'charge-sinks', drawing charge away from the immobilised molecule. Both graphene and single walled carbon nanotubes (SWCNTs) are used to model the electrode-catalyst interface with local and semi-local defects considered. We found that upright immobilised catalysts CoTPP on an octagon-pentagon line defect and CoPc on a Stone-Wales (SW) defect had the most favourable free energy reaction pathways compared to pristine graphene and the other graphene defects considered. In particular CO desorption on both CoTPP and CoPc was more favourable by ~ -0.2 eV compared to the pristine graphene system. However, superior CO_2ERR performance was found for CoPc immobilised via pyridine linker which bonds directly to the cobalt active of CoPc. This causes all spin-down d_{z^2} states to shift to higher energy levels just above

the Fermi level, becoming unoccupied. These unoccupied d_{z^2} states are axially coordinated which help facilitate strong CO_2 adsorption shown by the activated/bent geometry of CO_2. It was observed that the relative free energy reaction pathway performances corresponded with experimental turn over frequency (TOF) performances reported in previous studies [**21**,**23**,**24**]. This study bridges the divide between homogeneous and heterogeneous catalysts, which to date has been relatively unexplored.

In chapter 5 we undertake a systematic study of CoPc immobilisation via its cobalt active site on CNT supports using 'atomic-style' linkers. We found in chapter 4 that CoPc immobilised via the pyridine linker to its active site (forming an N_5 complex) gave superior CO_2ERR performance and stronger CO_2 adsorption, owing to the spin-down d_{z^2} states becoming unoccupied. Our aim was to determine if similar, or superior, CO_2ERR performance can be achieved by changing the species and hydrogenation of the atomic-style linker which immobilises CoPc on a CNT support. We studied eight different atomic style linker species and started by testing how well they immobilised CoPc on the CNT, and how much linker hydrogenation is required. The set of eight linkers we found gave the strongest immobilisation of CoPc on the CNT were: Al, As, B, GeH, N, NH, PH, SiH. The free energy reaction pathways were obtained and showed that both the NH and S linkers would likely have similar reaction performance to the pyridine linker, while PH may have superior reaction performance but at higher electrode potentials. This is because the PH linker has a slightly less favourable COOH formation step by ~ 0.2 eV compared to the NH and S linker systems. However, the CO desorption step is exothermic for the PH linker, while for the NH and S linkers it is endothermic by 0.1 eV. Redox potentials for the pyridine linker system were calculated and found to show good agreement with experiment [**259**]. Activation barriers were obtained for the NH and PH linker systems where the catalyst is pre-hydrogenated on a pyridinic-N and macro-N site. It was found that PH linker exhibited better structural stability and lower reaction barriers compared to the NH linker. On the basis of these promising results, we therefore, propose that the NH, S and PH linker systems would be interesting candidates for future experimental studies.

The road to an industrially applicable catalysts for CO_2ERR is still being forged. The criteria for an industrially scalable catalyst includes being more than 90% selective, having a charge density of at least 200 mA/cm^{-1} and long-term stability [**277**]. Metal-organic catalysts offer a promising pathway to this goal with selectivity of $> 99\%$ being exhibited and long term stability has been shown for covalently immobilised catalysts [**9**]. However, covalent catalyst immobilisation is still experimentally difficult to achieve and more research is required. There is still a need for further studies on different types of molecular catalysts, linkers and supports to get a clearer understanding of the CO_2ERR mechanisms and performance over a range of catalysts. Here *ab initio* simulations play an important role allowing one to probe the atomic structure, adsorption behaviour of the reactants, the reaction barriers and mechanisms, and thus predict performance. As further motivation for this field, recently a cobalt tetra-(4-N,N,N-trimethylanilinium)phthalocyanine (CoTMAPc) catalyst has been able to achieve (experimentally) charge densities > 200 mA/cm^{-1}, selectivity $> 90\%$ and high reaction rate [**278**]. This demonstrates the promise of metal-organic complexes as CO_2ERR catalysts for industrially scalable catalysts.

References

[1] Oleksandr S. Bushuyev, Phil De Luna, Cao Thang Dinh, Ling Tao, Genevieve Saur, Jao van de Lagemaat, Shana O. Kelley, and Edward H. Sargent. What Should We Make with CO_2 and How Can We Make It? *Joule*, 2(5):825–832, 2018.

[2] Axel Groß. Challenges in the modeling of elementary steps in electrocatalysis. *Curr Opin Electrochem*, 37:101170, February 2023.

[3] Yuvraj Y. Birdja, Jing Shen, and Marc T. M. Koper. Influence of the metal center of metalloprotoporphyrins on the electrocatalytic co_2 reduction to formic acid. *Catal*, 288:37–47, 2017.

[4] Aleksei N. Marianov, Alena S. Kochubei, Tanglaw Roman, Oliver J. Conquest, Catherine Stampfl, and Yijiao Jiang. Resolving Deactivation Pathways of Co Porphyrin-Based Electrocatalysts for CO_2 Reduction in Aqueous Medium. *ACS Catal.*, 11(6):3715–3729, March 2021.

[5] Ruud Kortlever, Jing Shen, Klaas Jan P. Schouten, Federico Calle-Vallejo, and Marc T. M. Koper. Catalysts and Reaction Pathways for the Electrochemical Reduction of Carbon Dioxide. *J. Phys. Chem. Lett*, 6(20):4073–4082, 2015.

[6] Robert Francke, Benjamin Schille, and Michael Roemelt. Homogeneously Catalyzed Electroreduction of Carbon Dioxide—Methods, Mechanisms, and Catalysts. *Chem. Rev*, 118(9):4631–4701, 2018.

[7] Sheng Zhang, Qun Fan, Rong Xia, and Thomas J. Meyer. CO2 Reduction: From Homogeneous to Heterogeneous Electrocatalysis. *Acc. Chem. Res*, 53(1):255–264, 2020.

[8] Nathan Corbin, Joy Zeng, Kindle Williams, and Karthish Manthiram. Heterogeneous molecular catalysts for electrocatalytic co_2 reduction. *Nano Res.*, 12(9):2093–2125, 2019.

[9] Libo Sun, Vikas Reddu, Adrian C. Fisher, and Xin Wang. Electrocatalytic reduction of carbon dioxide: Opportunities with heterogeneous molecular catalysts. *Energy Environ. Sci.*, 13(2):374–403, 2020.

[10] Fang Lv, Na Han, Yuan Qiu, Xijun Liu, Jun Luo, and Yanguang Li. Transition metal macrocycles for heterogeneous electrochemical co_2 reduction. *Coord. Chem. Rev*,

422:213435, 2020.

[11] Chenhuai Yang, Shuyu Li, Zhicheng Zhang, Haiqing Wang, Huiling Liu, Fei Jiao, Zhenguo Guo, Xiaotao Zhang, and Wenping Hu. Organic–inorganic hybrid nanomaterials for electrocatalytic co_2 reduction. *Small*, 16(29):2001847, 2020.

[12] Iqbal Bhugun, Doris Lexa, and Jean-Michel Savéant. Catalysis of the Electrochemical Reduction of Carbon Dioxide by Iron(0) Porphyrins: Synergystic Effect of Weak Brönsted Acids. *J. Am. Chem. Soc.*, 118(7):1769–1776, 1996.

[13] Lingjing Chen, Zhenguo Guo, Xi-Guang Wei, Charlotte Gallenkamp, Julien Bonin, Elodie Anxolabéhère-Mallart, Kai-Chung Lau, Tai-Chu Lau, and Marc Robert. Molecular Catalysis of the Electrochemical and Photochemical Reduction of CO_2 with Earth-Abundant Metal Complexes. Selective Production of CO vs HCOOH by Switching of the Metal Center. *J. Am. Chem. Soc.*, 137(34):10918–10921, 2015.

[14] Alon Chapovetsky, Thomas H. Do, Ralf Haiges, Michael K. Takase, and Smaranda C. Marinescu. Proton-Assisted Reduction of CO_2 by Cobalt Aminopyridine Macrocycles. *J. Am. Chem. Soc.*, 138(18):5765–5768, 2016.

[15] Xin-Ming Hu, Magnus H. Rønne, Steen U. Pedersen, Troels Skrydstrup, and Kim Daasbjerg. Enhanced catalytic activity of cobalt porphyrin in co_2 electroreduction upon immobilization on carbon materials. *Angew. Chem. Int.*, 56(23):6468–6472, 2017.

[16] Maryam Abdinejad, Ali Seifitokaldani, Caitlin Dao, Edward H. Sargent, Xiao-an Zhang, and Heinz Bernhard Kraatz. Enhanced electrochemical reduction of co_2 catalyzed by cobalt and iron amino porphyrin complexes. *ACS Appl. Energy Mater.*, 2(2):1330–1335, 2019.

[17] Na Han, Yu Wang, Lu Ma, Jianguo Wen, Jing Li, Hechuang Zheng, Kaiqi Nie, Xinxia Wang, Feipeng Zhao, Yafei Li, Jian Fan, Jun Zhong, Tianpin Wu, Dean J. Miller, Jun Lu, Shuit-Tong Lee, and Yanguang Li. Supported cobalt polyphthalocyanine for high-performance electrocatalytic CO_2 reduction. *Chem*, 3(4):652–664, 2017.

[18] Zheng Zhang, Jianping Xiao, Xue-Jiao Chen, Song Yu, Liang Yu, Rui Si, Yong Wang, Suheng Wang, Xianguang Meng, Ye Wang, Zhong-Qun Tian, and Dehui Deng. Reaction Mechanisms of Well-Defined Metal–N4 Sites in Electrocatalytic CO_2 Reduction. *Angew. Chem. Int.*, 57(50):16339–16342, 2018.

[19] Minghui Zhu, Ruquan Ye, Kyoungsuk Jin, Nikifar Lazouski, and Karthish Manthiram. Elucidating the Reactivity and Mechanism of CO_2 Electroreduction at Highly Dispersed Cobalt Phthalocyanine. *ACS Energy Lett.*, 3(6):1381–1386, 2018.

[20] Hengyu Li, Jie Wei, Xuya Zhu, Lin Gan, Tao Cheng, and Jia Li. Stimulating the precatalyst redox reaction and the proton-electron transfer process of cobalt phthalocyanine for CO_2 electroreduction. *J. Phys. Chem. C*, 126(23):9665–9672, 2022.

[21] Aleksei N. Marianov and Yijiao Jiang. Covalent ligation of Co molecular catalyst to carbon cloth for efficient electroreduction of CO_2 in water. *Appl. Catal. B*, 244:881–888, 2019.

[22] Mingming Huai, Zhenglei Yin, Fengyuan Wei, Gongwei Wang, Li Xiao, Juntao Lu, and Lin Zhuang. Electrochemical CO_2 reduction on heterogeneous cobalt phthalocyanine catalysts with different carbon supports. *Chem. Phys. Lett.*, 754:137655, 2020.

[23] Minghui Zhu, Jiacheng Chen, Libei Huang, Ruquan Ye, Jing Xu, and Yi-Fan Han. Covalently Grafting Cobalt Porphyrin onto Carbon Nanotubes for Efficient CO_2 Electroreduction. *Angew. Chem. Int.*, 58(20):6595–6599, 2019.

[24] Minghui Zhu, Jiacheng Chen, Rong Guo, Jing Xu, Xiangchen Fang, and Yi-Fan Han. Cobalt phthalocyanine coordinated to pyridine-functionalized carbon nanotubes with enhanced CO_2 electroreduction. *Appl. Catal. B*, 251:112–118, 2019.

[25] W. W. Kramer and C. C. L. McCrory. Polymer coordination promotes selective CO_2 reduction by cobalt phthalocyanine. *Chem. Sci.*, 7(4):2506–2515, 2016.

[26] Jianyu Han, Pengfei An, Shuhu Liu, Xiaofei Zhang, Dawei Wang, Yi Yuan, Jun Guo, Xueying Qiu, Ke Hou, Lin Shi, Yin Zhang, Shenlong Zhao, Chang Long, and Zhiyong Tang. Reordering d orbital energies of single-site catalysts for CO_2 electroreduction. *Angew. Chem., Int. Ed.*, 58(36):12711–12716, 2019.

[27] Hongdong Li, Yue Pan, Zuochao Wang, Yaodong Yu, Juan Xiong, Haoyang Du, Jianping Lai, Lei Wang, and Shouhua Feng. Coordination engineering of cobalt phthalocyanine by functionalized carbon nanotube for efficient and highly stable carbon dioxide reduction at high current density. *Nano Res.*, 2021.

[28] G. Kresse and J. Furthmüller. Efficient iterative schemes for *Ab Initio* total-energy calculations using a plane-wave basis set. *Phys. Rev. B*, 54(16):11169–11186, October 1996.

[29] G. Kresse and J. Furthmüller. Efficiency of *Ab-Initio* total energy calculations for metals and semiconductors using a plane-wave basis set. *Comput. Mater. Sci.*, 6(1):15–50, 1996.

[30] John P. Perdew, Kieron Burke, and Matthias Ernzerhof. Generalized Gradient Approximation Made Simple. *Phys. Rev. Lett.*, 77(18):3865–3868, 1996.

[31] Axel D. Becke and Erin R. Johnson. A density-functional model of the dispersion interaction. *J. Chem. Phys.*, 123(15):154101, October 2005.

[32] Stefan Grimme, Jens Antony, Stephan Ehrlich, and Helge Krieg. A consistent and accurate ab initio parametrization of density functional dispersion correction (DFT-D) for the 94 elements H-Pu. *J. Chem. Phys.*, 132(15):154104, April 2010.

[33] Stefan Grimme, Stephan Ehrlich, and Lars Goerigk. Effect of the damping function in dispersion corrected density functional theory. *J. Comput. Chem.*, 32(7):1456–1465, 2011.

[34] J. K. Nørskov, J. Rossmeisl, A. Logadottir, L. Lindqvist, J. R. Kitchin, T. Bligaard, and H. Jónsson. Origin of the overpotential for oxygen reduction at a fuel-cell cathode. *J. Phys. Chem. B*, 108(46):17886–17892, 2004.

[35] David J. Giesen, Christopher J. Cramer, and Donald G. Truhlar. Entropic Contributions to Free Energies of Solvation. *J. Phys. Chem*, 98(15):4141–4147, 1994.

[36] Shunzhou Wan, Roland H. Stote, and Martin Karplus. Calculation of the aqueous solvation energy and entropy, as well as free energy, of simple polar solutes. *J. Chem. Phys.*, 121(19):9539–9548, 2004.

[37] Michael R. Shirts and Vijay S. Pande. Solvation free energies of amino acid side chain analogs for common molecular mechanics water models. *J. Chem. Phys.*, 122(13):134508, 2005.

[38] Tod A. Pascal, Shiang-Tai Lin, and William A. Goddard Iii. Thermodynamics of liquids: Standard molar entropies and heat capacities of common solvents from 2PT molecular dynamics. *Phys. Chem. Chem. Phys.*, 13(1):169–181, 2010.

[39] Shiang-Tai Lin, Prabal K. Maiti, and William A. Goddard. Two-Phase Thermodynamic Model for Efficient and Accurate Absolute Entropy of Water from Molecular Dynamics Simulations. *The Journal of Physical Chemistry B*, 114(24):8191–8198, 2010.

[40] Cui Zhang, Leonardo Spanu, and Giulia Galli. Entropy of Liquid Water from Ab Initio Molecular Dynamics. *J. Phys. Chem. B*, 115(48):14190–14195, 2011.

[41] Miguel A. Caro, Tomi Laurila, and Olga Lopez-Acevedo. Accurate schemes for calculation of thermodynamic properties of liquid mixtures from molecular dynamics simulations. *J. Chem. Phys.*, 145(24):244504, 2016.

[42] Jacopo Tomasi, Benedetta Mennucci, and Roberto Cammi. Quantum Mechanical Continuum Solvation Models. *Chem. Rev.*, 105(8):2999–3094, 2005.

[43] Zhi-Xiang Yu and K. N. Houk. Intramolecular 1,3-Dipolar Ene Reactions of Nitrile Oxides Occur by Stepwise 1,1-Cycloaddition/Retro-Ene Mechanisms. *J. Am. Chem. Soc.*, 125(45):13825–13830, 2003.

[44] R. Erik Plata and Daniel A. Singleton. A Case Study of the Mechanism of Alcohol-Mediated Morita Baylis–Hillman Reactions. The Importance of Experimental Observations. *J. Am. Chem. Soc.*, 137(11):3811–3826, 2015.

[45] Michinori Sumimoto, Naoki Iwane, Tomohiko Takahama, and Shigeyoshi Sakaki. Theoretical Study of Trans-metalation Process in Palladium-Catalyzed Borylation of Iodobenzene with Diboron. *J. Am. Chem. Soc.*, 126(33):10457–10471, 2004.

[46] C. Tony Liu, Christopher I. Maxwell, David R. Edwards, Alexei A. Neverov, Nicholas J. Mosey, and R. Stan Brown. Mechanistic and Computational Study of a Palladacycle-Catalyzed Decomposition of a Series of Neutral Phosphorothioate Triesters in Methanol. *J. Am. Chem. Soc.*, 132(46):16599–16609, 2010.

[47] Alejandro J. Garza. Solvation Entropy Made Simple. *J. Chem. Theory Comput.*, 15(5):3204–3214, 2019.

[48] Dean J. Tantillo. Portable Models for Entropy Effects on Kinetic Selectivity. *J. Am. Chem. Soc.*, 144(31):13996–14004, 2022.

[49] Jan Florián and Arieh Warshel. Langevin Dipoles Model for ab Initio Calculations of Chemical Processes in Solution: Parametrization and Application to Hydration Free Energies of Neutral and Ionic Solutes and Conformational Analysis in Aqueous Solution. *J. Phys. Chem. B*, 101(28):5583–5595, 1997.

[50] Jan Florián and Arieh Warshel. Calculations of Hydration Entropies of Hydrophobic, Polar, and Ionic Solutes in the Framework of the Langevin Dipoles Solvation Model. *J. Phys. Chem. B*, 103(46):10282–10288, 1999.

[51] Jan Florián, Jiří Šponer, and Arieh Warshel. Thermodynamic Parameters for Stacking and Hydrogen Bonding of Nucleic Acid Bases in Aqueous Solution: Ab Initio/Langevin Dipoles Study. *J. Phys. Chem. B*, 103(5):884–892, 1999.

[52] V. Fock. Näherungsmethode zur Lösung des quantenmechanischen Mehrkörperproblems. *Zeitschrift für Physik*, 61(1):126–148, 1930.

[53] Douglas Rayner Hartree and W. Hartree. Self-consistent field, with exchange, for beryllium. *Proceedings of the Royal Society of London. Series A - Mathematical and Physical Sciences*, 150(869):9–33, 1935.

[54] J. C. Slater. A Simplification of the Hartree-Fock Method. *Physical Review*, 81(3):385–390, 1951.

[55] David S. Sholl and Janice A. Steckel. *Density Functional Theory: A Practical Introduction*. John Wiley & Sons, Inc., Hoboken, New Jersey, first edition, 2009.

[56] Edward Nelson. Feynman Integrals and the Schrödinger Equation. *J. Math. Phys.*, 5(3):332–343, 1964.

[57] Spyros Efthimiades. Derivation of the Schrodinger Equation. *Il Nuovo Cimento B*, page 118, 2003.

[58] Hiroshi Nakatsuji. Discovery of a general method of solving the schrödinger and dirac equations that opens a way to accurately predictive quantum chemistry. *Acc. Chem. Res.*, 45(9):1480–1490, 2012.

[59] Max Born, Kun Huang, and M. Lax. *Dynamical Theory of Crystal Lattices*. Oxford Univeristy Press, Oxford, England, first edition, 1954.

[60] Eric J. Heller. *The Semiclassical Way to Dynamics and Spectroscopy*. Princeton University Press, Princeton New Jersey, United States, first edition, 2018.

[61] Stephen Wolfram. *A New Kind of Science*. Wolfram Media, Champaign, Il, USA, 2002.

[62] Karl F. Sundman. Mémoire sur le problème des trois corps. *Acta Mathematica*, 36:105–179, 1913.

[63] D Belorizky. Application pratique des méthodes de m. sundman à un cas particulier du problème des trois corps. *Bulletin Astronomique*, 6:417–434, 1930.

[64] June Barrow-Green. *Poincar{\'e} and the Three Body Problem*, volume 11. American Mathematical Society, Providence, Rhode Island, first edition, 1997.

[65] Philip G Breen, Christopher N Foley, Tjarda Boekholt, and Simon Portegies Zwart. Newton versus the machine: Solving the chaotic three-body problem using deep neural networks. *MNRAS*, 494(2):2465–2470, 2020.

[66] Hiroyuki Nakashima and Hiroshi Nakatsuji. Solving the Schrödinger equation for helium atom and its isoelectronic ions with the free iterative complement interaction (ICI) method. *J. Chem. Phys.*, 127(22):224104, 2007.

[67] D. R. Hartree. The Wave Mechanics of an Atom with a Non-Coulomb Central Field. Part I. Theory and Methods. *Math. Proc. Cambridge Philos. Soc.*, 24(1):89–110, 1928.

[68] D. R. Hartree. The Wave Mechanics of an Atom with a Non-Coulomb Central Field. Part II. Some Results and Discussion. *Math. Proc. Cambridge Philos. Soc.*, 24(1):111–132, January 1928.

[69] David J. Griffiths. *Introduction to Quantum Mechanics*. Prentice Hall, Inc., Upper Saddle River, New Jersey, first edition, 1995.

[70] J. J. Sakurai and Jim Napolitano. *Modern Quantum Mechanics*. Cambridge University Press, Great Britian, third edition, 2020.

[71] Avi Rauk. *Orbital Interaction Theory of Organic Chemistry*. John Wiley & Sons, New York, United States, second edition, 2000.

[72] C. C. J. Roothaan. New Developments in Molecular Orbital Theory. *Rev Mod Phys*, 23(2):69–89, 1951.

[73] G. G. Hall and John Edward Lennard-Jones. The molecular orbital theory of chemical valency VIII. A method of calculating ionization potentials. *Proceedings of the Royal Society of London. Series A. Mathematical and Physical Sciences*, 205(1083):541–552,

1951.

[74] June Gunn Lee. *Computational Materials Science: An Introduction*. Taylor & Francis Group, LLC, Boca Raton, Florida, second edition, 2017.

[75] Shuo Ma, Yingjin Ma, Baohua Zhang, Yingqi Tian, and Zhong Jin. Forecasting System of Computational Time of DFT/TDDFT Calculations under the Multiverse Ansatz via Machine Learning and Cheminformatics. *ACS Omega*, 6(3):2001–2024, 2021.

[76] P. Hohenberg and W. Kohn. Inhomogeneous Electron Gas. *Physical Review*, 136(3B):B864–B871, 1964.

[77] Wolfram Koch and Max C. Holthausen. *A Chemist's Guide to Density Functional Theory*. Wiley, New York, United States, second edition, 2001.

[78] W. Kohn and L. J. Sham. Self-Consistent Equations Including Exchange and Correlation Effects. *Physical Review*, 140(4A):A1133–A1138, 1965.

[79] Robert G Parr and Yang Weitao. *Density-Functional Theory of Atoms and Molecules*. Oxford University Press, Oxford, United Kingdom, 1995.

[80] Oleg Gritsenko, Robert van Leeuwen, and Evert Jan Baerends. Analysis of electron interaction and atomic shell structure in terms of local potentials. *J. Chem. Phys.*, 101(10):8955–8963, 1994.

[81] O. V. Gritsenko, P. R. T. Schipper, and E. J. Baerends. Exchange and correlation energy in density functional theory: Comparison of accurate density functional theory quantities with traditional hartree–fock based ones and generalized gradient approximations for the molecules li_2,n_2,f_2. *J. Chem. Phys.*, 107(13):5007–5015, 1997.

[82] J. P. Perdew and Alex Zunger. Self-interaction correction to density-functional approximations for many-electron systems. *Phys. Rev. B*, 23(10):5048–5079, 1981.

[83] W. Kohn and L. J. Sham. Self-Consistent Equations Including Exchange and Correlation Effects. *Physical Review*, 140(4A):A1133–A1138, 1965.

[84] D. M. Ceperley and B. J. Alder. Ground state of the electron gas by a stochastic method. *Phys. Rev. Lett.*, 45(7):566–569, 1980.

[85] SH Vosko, L. Wilk, and M. Nusair. Accurate spin-dependent electron liquid correlation energies for local spin density calculations: A critical analysis. *Canadian Journal of Physics*, 58(8):1200–1211, 1980.

[86] John P. Perdew and Yue Wang. Accurate and simple analytic representation of the electron-gas correlation energy. *Phys. Rev. B*, 45(23):13244–13249, 1992.

[87] Bharat Medasani, Maciej Haranczyk, Andrew Canning, and Mark Asta. Vacancy formation energies in metals: A comparison of MetaGGA with LDA and GGA exchange–correlation functionals. *Comput. Mater. Sci.*, 101:96–107, 2015.

[88] A. D. Becke. Density functional calculations of molecular bond energies. *J. Chem. Phys*, 84(8):4524–4529, 1986.

[89] John P. Perdew. Density-functional approximation for the correlation energy of the inhomogeneous electron gas. *Phys. Rev. B*, 33(12):8822–8824, 1986.

[90] A. D. Becke. Density-functional exchange-energy approximation with correct asymptotic behavior. *Phys. Rev. A*, 38(6):3098–3100, 1988.

[91] John P. Perdew, Kieron Burke, and Yue Wang. Generalized gradient approximation for the exchange-correlation hole of a many-electron system. *Phys. Rev. B*, 54(23):16533–16539, 1996.

[92] John P. Perdew and Karla Schmidt. Jacob's ladder of density functional approximations for the exchange-correlation energy. *AIP Conference Proceedings*, 577(1):1–20, 2001.

[93] A. D. Becke and M. R. Roussel. Exchange hholes in inhomogeneous systems: A coordinate-space model. *Phys. Rev. A*, 39(8):3761–3767, April 1989.

[94] Carlo Adamo, Matthias Ernzerhof, and Gustavo E. Scuseria. The meta-GGA functional: Thermochemistry with a kinetic energy density dependent exchange-correlation functional. *J. Chem. Phys*, 112(6):2643–2649, 2000.

[95] Jianwei Sun, Adrienn Ruzsinszky, and JohnP. Perdew. Strongly Constrained and Appropriately Normed Semilocal Density Functional. *Phys. Rev. Lett.*, 115(3):036402, 2015.

[96] Haowei Peng, Zeng-Hui Yang, John P. Perdew, and Jianwei Sun. Versatile van der Waals Density Functional Based on a Meta-Generalized Gradient Approximation. *Phys. Rev. X*, 6(4):041005, 2016.

[97] Albert P. Bartók and Jonathan R. Yates. Regularized SCAN functional. *J. Chem. Phys*, 150(16):161101, 2019.

[98] Axel D. Becke. A new mixing of Hartree–Fock and local density-functional theories. *J. Chem. Phys*, 98(2):1372–1377, 1993.

[99] P. J. Stephens, F. J. Devlin, C. F. Chabalowski, and M. J. Frisch. Ab Initio Calculation of Vibrational Absorption and Circular Dichroism Spectra Using Density Functional Force Fields. *J. Chem. Phys*, 98(45):11623–11627, 1994.

[100] Aliaksandr V. Krukau, Oleg A. Vydrov, Artur F. Izmaylov, and Gustavo E. Scuseria. Influence of the exchange screening parameter on the performance of screened hybrid functionals. *J. Chem. Phys*, 125(22):224106, 2006.

[101] Sérgio Filipe Sousa, Pedro Alexandrino Fernandes, and Maria João Ramos. General Performance of Density Functionals. *J. Phys. Chem. A*, 111(42):10439–10452, 2007.

[102] Poul Georg Moses, Maosheng Miao, Qimin Yan, and Chris G. Van de Walle. Hybrid functional investigations of band gaps and band alignments for AlN, GaN, InN, and InGaN. *J. Chem. Phys*, 134(8):084703, 2011.

[103] Stefan Grimme. Density functional theory with london dispersion corrections. *WIREs Computational Molecular Science*, 1(2):211–228, 2011.

[104] Bogumil Jeziorski, Robert Moszynski, and Krzysztof Szalewicz. Perturbation theory approach to intermolecular potential energy surfaces of van der waals complexes. *Chem. Rev.*, 94(7):1887–1930, 1994.

[105] Stefan Grimme. Accurate description of van er waals complexes by density functional theory including empirical corrections. *J. Comput. Chem.*, 25(12):1463–1473, 2004.

[106] B. M. Axilrod and E. Teller. Interaction of the van der waals type between three atoms. *J. Chem. Phys.*, 11(6):299–300, 1943.

[107] H. B. G. Casimir and D. Polder. The influence of retardation on the london-van der waals forces. *Phys. Rev.*, 73(4):360–372, 1948.

[108] George Starkschall and Roy G. Gordon. Calculation of coefficients in the power series expansion of the long-range dispersion force between atoms. *The Journal of Chemical Physics*, 56(6):2801–2806, 1972.

[109] Stefan Grimme. Semiempirical GGA-type density functional constructed with a long-range dispersion correction. *J. Comput. Chem*, 27(15):1787–1799, 2006.

[110] Jeng-Da Chai and Martin Head-Gordon. Long-range corrected hybrid density functionals with damped atom–atom dispersion corrections. *Phys. Chem. Chem. Phys*, 10(44):6615–6620, 2008.

[111] Yi Liu and William A. III Goddard. A Universal Damping Function for Empirical Dispersion Correction on Density Functional Theory. *Mater. Trans.*, 50(7):1664–1670, 2009.

[112] Erin R. Johnson and Axel D. Becke. A post-hartree-fock model of intermolecular interactions: Inclusion of higher-order corrections. *The Journal of Chemical Physics*, 124(17):174104, 2006.

[113] Weine Olovsson. Running VASP in parallel – guidelines and results, 2022.

[114] Axel D. Becke. Perspective: Fifty years of density-functional theory in chemical physics. *J. Chem. Phys.*, 140(18):18A301, 2014.

[115] Alejandro J. Garza, Alexis T. Bell, and Martin Head-Gordon. Nonempirical meta-generalized gradient approximations for modeling chemisorption at metal surfaces. *J. Chem. Theory Comput.*, 14(6):3083–3090, 2018.

[116] Fabien Tran, Julia Stelzl, and Peter Blaha. Rungs 1 to 4 of dft jacob's ladder: Extensive test on the lattice constant, bulk modulus, and cohesive energy of solids. *J. Chem. Phys.*, 144(20):204120, 2016.

[117] Rafael B. Araujo, Gabriel L. S. Rodrigues, Egon Campos dos Santos, and Lars G. M. Pettersson. Adsorption energies on transition metal surfaces: Towards an accurate and balanced description. *Nat. Commun.*, 13(1):6853, 2022.

[118] Jianwei Sun, Adrienn Ruzsinszky, and JohnP. Perdew. Strongly constrained and appropriately normed semilocal density functional. *Phys. Rev. Lett.*, 115(3):036402, 2015.

[119] Dalar Nazarian, P. Ganesh, and David S. Sholl. Benchmarking density functional theory predictions of framework structures and properties in a chemically diverse test set of metal–organic frameworks. *J. Mater. Chem. A.*, 3(44):22432–22440, 2015.

[120] Indrani Choudhuri and Donald G. Truhlar. Improved predictive tools for structural properties of metal–organic frameworks. *Molecules*, 25(7):1552, 2020.

[121] Léo Chaussy, Denis Hagebaum-Reignier, Stéphane Humbel, and Paola Nava. Accurate computed singlet–triplet energy differences for cobalt systems: Implication for two-state reactivity. *Phys. Chem. Chem. Phys.*, 24(36):21841–21852, 2022.

[122] Alexander Wolfram, Quratulain Tariq, Cynthia C. Fernández, Maximilian Muth, Martin Gurrath, Daniel Wechsler, Matthias Franke, Federico J. Williams, Hans-Peter Steinrück, Bernd Meyer, and Ole Lytken. Adsorption energies of porphyrins on mgo(100): An experimental benchmark for dispersion-corrected density-functional theory. *Surf. Sci.*, 717:121979, 2022.

[123] Benedikt P. Klein, Juliana M. Morbec, Markus Franke, Katharina K. Greulich, Malte Sachs, Shayan Parhizkar, François C. Bocquet, Martin Schmid, Samuel J. Hall, Reinhard J. Maurer, Bernd Meyer, Ralf Tonner, Christian Kumpf, Peter Kratzer, and J. Michael Gottfried. Molecule–Metal Bond of Alternant versus Nonalternant Aromatic Systems on Coinage Metal Surfaces: Naphthalene versus Azulene on Ag(111) and Cu(111). *J. Phys. Chem. C.*, 123(48):29219–29230, 2019.

[124] Stefan R. Kachel, Benedikt P. Klein, Juliana M. Morbec, Maik Schöniger, Mark Hutter, Martin Schmid, Peter Kratzer, Bernd Meyer, Ralf Tonner, and J. Michael Gottfried. Chemisorption and Physisorption at the Metal/Organic Interface: Bond Energies of Naphthalene and Azulene on Coinage Metal Surfaces. *J. Phys. Chem. C.*, 124(15):8257–8268, 2020.

[125] Felix Bloch. Über die Quantenmechanik der Elektronen in Kristallgittern. *Zeitschrift für Physik*, 52(7):555–600, 1929.

[126] Neil Ashcroft and David Mermin. *Solid State Physics*. Holt, Rinehart and Winston, New York, USA, 1976.

[127] Hendrik J. Monkhorst and James D. Pack. Special points for brillouin-zone integrations. *Phys. Rev. B*, 13(12):5188–5192, 1976.

[128] G. Kresse and D. Joubert. From ultrasoft pseudopotentials to the projector augmented-wave method. *Phys. Rev. B*, 59(3):1758–1775, 1999.

[129] P. E. Blöchl. Projector augmented-wave method. *Phys. Rev. B*, 50(24):17953–17979, 1994.

[130] K. Lejaeghere, V. Van Speybroeck, G. Van Oost, and S. Cottenier. Error Estimates for Solid-State Density-Functional Theory Predictions: An Overview by Means of the Ground-State Elemental Crystals. *Crit. Rev. Solid State Mater. Sci*, 39(1):1–24, 2014.

[131] R. P. Feynman. Forces in Molecules. *Physical Review*, 56(4):340–343, 1939.

[132] William H. Press, Brian P. Flannery, Saul A. Teukolsky, and William T. Vetterling. *Numerical Recipes: The Art of Scientific Computing*. Cambridge University Press, New York, United States, third edition, 1987.

[133] Kang-Gyu Lee, Mani Balamurugan, Sunghak Park, Heonjin Ha, Kyoungsuk Jin, Hongmin Seo, and Ki Tae Nam. Importance of Entropic Contribution to Electrochemical Water Oxidation Catalysis. *ACS Energy Lett.*, 4(8):1918–1929, August 2019.

[134] Arianna Savini, Alberto Bucci, Gianfranco Bellachioma, Luca Rocchigiani, Cristiano Zuccaccia, Antoni Llobet, and Alceo Macchioni. Mechanistic Aspects of Water Oxidation Catalyzed by Organometallic Iridium Complexes. *Eur. J. Inorg. Chem.*, 2014(4):690–697, 2014.

[135] Ferran Acuña-Parés, Zoel Codolà, Miquel Costas, Josep M. Luis, and Julio Lloret-Fillol. Unraveling the Mechanism of Water Oxidation Catalyzed by Nonheme Iron Complexes. *Chem. Eur. J*, 20(19):5696–5707, 2014.

[136] Marek Strajbl, Yuk Y. Sham, Jordi Villà, Z.-T. Chu, and Arieh Warshel. Calculations of Activation Entropies of Chemical Reactions in Solution. *J. Phys. Chem. B*, 104(18):4578–4584, 2000.

[137] Nidhi Singh and Arieh Warshel. A comprehensive examination of the contributions to the binding entropy of protein–ligand complexes. *Proteins: Struct., Funct., Bioinf.*, 78(7):1724–1735, 2010.

[138] Diego Ardura, Ramón López, and Tomás L. Sordo. Relative Gibbs Energies in Solution through Continuum Models: Effect of the Loss of Translational Degrees of Freedom in

Bimolecular Reactions on Gibbs Energy Barriers. *J. Phys. Chem. B*, 109(49):23618–23623, 2005.

[139] Raphael F. Ribeiro, Aleksandr V. Marenich, Christopher J. Cramer, and Donald G. Truhlar. Use of Solution-Phase Vibrational Frequencies in Continuum Models for the Free Energy of Solvation. *J. Phys. Chem. B*, 115:14556–14562, 2011.

[140] F. M. Floris, M. Selmi, A. Tani, and J. Tomasi. Free energy and entropy for inserting cavities in water: Comparison of Monte Carlo simulation and scaled particle theory results. *J. Chem. Phys.*, 107(16):6353–6365, 1997.

[141] Caterina Benzi, Maurizio Cossi, Roberto Improta, and Vincenzo Barone. Building cavities in a fluid of spherical or rod-like particles: A contribution to the solvation free energy in isotropic and anisotropic polarizable continuum model. *J. Comput. Chem.*, 26(11):1096–1105, 2005.

[142] Bonnie O. Leung, Darren L. Reid, David A. Armstrong, and Arvi Rauk. Entropies in Solution from Entropies in the Gas Phase. *J. Phys. Chem. A*, 108(14):2720–2725, 2004.

[143] Robert A. Pierotti. A scaled particle theory of aqueous and nonaqueous solutions. *Chem. Rev.*, 76(6):717–726, 1976.

[144] H. Reiss, H. L. Frisch, and J. L. Lebowitz. Statistical Mechanics of Rigid Spheres. *J. Chem. Phys.*, 31(2):369–380, 1959.

[145] A. Warshel and M. Levitt. Theoretical studies of enzymic reactions: Dielectric, electrostatic and steric stabilization of the carbonium ion in the reaction of lysozyme. *J. Mol. Biol.*, 103(2):227–249, 1976.

[146] Arieh. Warshel. Calculations of chemical processes in solutions. *J. Phys. Chem*, 83(12):1640–1652, 1979.

[147] Arieh Warshel and Stephen T. Russell. Calculations of electrostatic interactions in biological systems and in solutions. *Q. Rev. Biophys.*, 17(3):283–422, 1984.

[148] S. T. Russell and A. Warshel. Calculations of electrostatic energies in proteins: The energetics of ionized groups in bovine pancreatic trypsin inhibitor. *J. Mol. Biol.*, 185(2):389–404, 1985.

[149] Eva Španinger and Urban Bren. Carcinogenesis of -Propiolactone: A Computational Study. *Chem. Res. Toxicol.*, 33(3):769–781, 2020.

[150] Gregor Hostnik, Martin Gladović, and Urban Bren. Tannin Basic Building Blocks as Potential Scavengers of Chemical Carcinogens: A Computational Study. *J. Nat. Prod.*, 82(12):3279–3287, 2019.

[151] Aleksandr V. Marenich, Christopher J. Cramer, and Donald G. Truhlar. Universal Solvation Model Based on Solute Electron Density and on a Continuum Model of the Solvent Defined by the Bulk Dielectric Constant and Atomic Surface Tensions. *J. Phys. Chem. B*, 113(18):6378–6396, 2009.

[152] Kiran Mathew, Ravishankar Sundararaman, Kendra Letchworth-Weaver, T. A. Arias, and Richard G. Hennig. Implicit solvation model for density-functional study of nanocrystal surfaces and reaction pathways. *J. Chem. Phys.*, 140(8):084106, 2014.

[153] Kiran Mathew, V. S. Chaitanya Kolluru, Srinidhi Mula, Stephan N. Steinmann, and Richard G. Hennig. Implicit self-consistent electrolyte model in plane-wave density-functional theory. *J. Chem. Phys.*, 151(23):234101, 2019.

[154] Witold Brostow, Jean-Pierre Dussault, and Bennett L Fox. Construction of Voronoi polyhedra. *J. Comput. Phys.*, 29(1):81–92, 1978.

[155] F. Matthias Bickelhaupt, Nicolaas J. R. van Eikema Hommes, Célia Fonseca Guerra, and Evert Jan Baerends. The CarbonLithium Electron Pair Bond in (CH3Li)n (n = 1, 2, 4). *Organometallics*, 15(13):2923–2931, 1996.

[156] Célia Fonseca Guerra, Jan-Willem Handgraaf, Evert Jan Baerends, and F. Matthias Bickelhaupt. Voronoi deformation density (VDD) charges: Assessment of the Mulliken, Bader, Hirshfeld, Weinhold, and VDD methods for charge analysis. *J. Comput. Chem.*, 25(2):189–210, 2004.

[157] Donald A. McQuarrie. *Statistical Mechanics*. Harper & Row, New York, N.Y., first edition edition, 1976.

[158] Antonio Fernández-Ramos, Benjamin A. Ellingson, Rubén Meana-Pañeda, Jorge M. C. Marques, and Donald G. Truhlar. Symmetry numbers and chemical reaction rates. *Theor. Chem. Acc.*, 118(4):813–826, 2007.

[159] Michael K. Gilson and Karl K. Irikura. Symmetry Numbers for Rigid, Flexible, and Fluxional Molecules: Theory and Applications. *J. Phys. Chem. B*, 114(49):16304–16317, 2010.

[160] Stefan Grimme. Supramolecular Binding Thermodynamics by Dispersion-Corrected Density Functional Theory. *Chem. Eur. J.*, 18(32):9955–9964, 2012.

[161] Jeng-Da Chai and Martin Head-Gordon. Long-range corrected hybrid density functionals with damped atom–atom dispersion corrections. *Phys. Chem. Chem. Phys.*, 10(44):6615–6620, 2008.

[162] Yan Zhao and Donald G. Truhlar. Computational characterization and modeling of buckyball tweezers: Density functional study of concave–convex interactions. *Phys. Chem. Chem. Phys.*, 10(19):2813–2818, 2008.

[163] Richard B. McClurg, Richard C. Flagan, and William A. Goddard III. The hindered rotor density-of-states interpolation function. *J. Chem. Phys.*, 106(16):6675–6680, 1997.

[164] Lynza H. Sprowl, Charles T. Campbell, and Líney Árnadóttir. Hindered Translator and Hindered Rotor Models for Adsorbates: Partition Functions and Entropies. *J. Phys. Chem. C*, 120(18):9719–9731, 2016.

[165] Xiao-Long Zhang, Yong-Tao Ma, Yu Zhai, and Hui Li. Analytic Morse/long-range potential energy surfaces and "adiabatic-hindered-rotor" treatment for a symmetric top-linear molecule dimer: A case study of CH_3F–H_2. *J. Chem. Phys.*, 148(12):124302, 2018.

[166] Manjeera Mantina, Adam C. Chamberlin, Rosendo Valero, Christopher J. Cramer, and Donald G. Truhlar. Consistent van der Waals Radii for the Whole Main Group. *J. Phys. Chem. A*, 113(19):5806–5812, 2009.

[167] A. Bondi. van der Waals Volumes and Radii. *J. Chem. Phys.*, 68(3):441–451, 1964.

[168] Yuan H. Zhao, Michael H. Abraham, and Andreas M. Zissimos. Fast Calculation of van der Waals Volume as a Sum of Atomic and Bond Contributions and Its Application to Drug Compounds. *J. Org. Chem.*, 68(19):7368–7373, 2003.

[169] Calvin R. Chen and George I. Makhatadze. ProteinVolume: Calculating molecular van der Waals and void volumes in proteins. *BMC Bioinform*, 16(1):101, 2015.

[170] Miquel Garcia-Ratés and Frank Neese. Effect of the Solute Cavity on the Solvation Energy and its Derivatives within the Framework of the Gaussian Charge Scheme. *J. Comput. Chem.*, 41(9):922–939, 2020.

[171] David H. Wertz. Relationship between the gas-phase entropies of molecules and their entropies of solvation in water and 1-octanol. *J. Am. Chem. Soc.*, 102(16):5316–5322, 1980.

[172] David L. Mobley, Ken A. Dill, and John D. Chodera. Treating Entropy and Conformational Changes in Implicit Solvent Simulations of Small Molecules. *J. Phys. Chem. B*, 112(3):938–946, 2008.

[173] Philipp Pracht and Stefan Grimme. Calculation of absolute molecular entropies and heat capacities made simple. *Chem. Sci.*, 12(19):6551–6568, 2021.

[174] M Osinga. Rigidity, lipophilicity, and henry's constant. *J. Am. Chem. Soc.*, 101(6):1621–1622, 1979.

[175] Emo Welzl. *Smallest Enclosing Disks (Balls and Ellipsoids)*, volume 555 of *New Results and New Trends in Computer Science*. Springer, Berlin, Heidelberg, Germany, 1991.

[176] A.M Odlyzko and N.J.A Sloane. New bounds on the number of unit spheres that can touch a unit sphere in n dimensions. *J. Comb. Theory Ser. A.*, 26(2):210–214, 1979.

[177] C Bradford Barber, David P Dobkin, and Hannu Huhdanpaa. The quickhull algorithm for convex hulls. *ACM Trans. Math. Softw.*, 22(4):469–483, 1996.

[178] V. P. Voloshin, A. V. Anikeenko, N. N. Medvedev, and A. Geiger. An algorithm for the calculation of volume and surface of unions of spheres. application for solvation shells. In *2011 Eighth International Symposium on Voronoi Diagrams in Science and Engineering*, pages 170–176, 2011.

[179] Chaoyu Quan and Benjamin Stamm. Mathematical analysis and calculation of molecular surfaces. *J. Comput. Phys.*, 322:760–782, 2016.

[180] Robert L Berg and Cecil E Vanderzee. Thermodynamics of carbon dioxide and carbonic acid: (a) the standard enthalpies of solution of Na_2CO_3(s), $NaHCO_3$(s), and CO_2(g) in water at 298.15 K; (b) the standard enthalpies of formation, standard Gibbs energies of formation, and standard entropies of CO_2(aq), HCO_3(aq), CO_32(aq), $NaHCO_3$(s), Na_2CO_3(s), $Na_2CO_3{\cdot}H_2O$(s), and $Na_2CO_3{\cdot}10H_2O$(s). *J. Chem. Thermodyn.*, 10(12):1113–1136, 1978.

[181] Robert N. Goldberg and Yadu B. Tewari. Thermodynamic and Transport Properties of Carbohydrates and their Monophosphates: The Pentoses and Hexoses. *J. Phys. Chem. Ref. Data*, 18(2):809–880, 1989.

[182] Juliana Boerio-Goates, Michael R. Francis, Robert N. Goldberg, Manuel A. V. Ribeiro da Silva, Maria D. M. C. Ribeiro da Silva, and Yadu B. Tewari. Thermochemistry of adenosine. *J. Chem. Thermodyn.*, 33(8):929–947, 2001.

[183] Yizhak Marcus. Tetraalkylammonium Ions in Aqueous and Non-aqueous Solutions. *J. Solution Chem.*, 37(8):1071, 2008.

[184] *NIST Chemistry WebBook Standard Reference Database*. (accessed date 10-22-2021).

[185] Robert A. Alberty. Standard molar entropies, standard entropies of formation, and standard transformed entropies of formation in the thermodynamics of enzyme-catalyzed reactions. *J. Chem. Thermodyn.*, 38(4):396–404, 2006.

[186] Christoph Bannwarth, Sebastian Ehlert, and Stefan Grimme. GFN2-xTB—An Accurate and Broadly Parametrized Self-Consistent Tight-Binding Quantum Chemical Method with Multipole Electrostatics and Density-Dependent Dispersion Contributions. *J. Chem. Theory Comput.*, 15(3):1652–1671, 2019.

[187] Annia Galano and Juan Raúl Alvarez-Idaboy. Kinetics of radical-molecule reactions in aqueous solution: A benchmark study of the performance of density functional methods. *J. Comput. Chem.*, 35(28):2019–2026, 2014.

[188] Cang Lang Yao, Jian Chen Li, Wang Gao, and Qing Jiang. Cobalt-porphine catalyzed CO_2 electro-reduction: A novel protonation mechanism. *Phys. Chem. Chem. Phys.*, 19(23):15067–15072, 2017.

[189] Ida M. B. Nielsen and Kevin Leung. CobaltPorphyrin Catalyzed Electrochemical Reduction of Carbon Dioxide in Water. 1. A Density Functional Study of Intermediates. *J. Phys. Chem. A*, 114(37):10166–10173, 2010.

[190] Jing Shen, Manuel J. Kolb, Adrien J. Göttle, and Marc T. M. Koper. DFT Study on the Mechanism of the Electrochemical Reduction of CO_2 Catalyzed by Cobalt Porphyrins. *J. Phys. Chem. C*, 120(29):15714–15721, 2016.

[191] Barbara Chiavarino, Maria Elisa Crestoni, Simonetta Fornarini, and Carme Rovira. Unravelling the Intrinsic Features of NO Binding to Iron(II)- and Iron(III)-Hemes. *Inorg. Chem.*, 47(17):7792–7801, 2008.

[192] Axel D. Becke. A new mixing of Hartree–Fock and local density-functional theories. *J. Chem. Phys.*, 98(2):1372–1377, 1993.

[193] Chengteh Lee, Weitao Yang, and Robert G. Parr. Development of the Colle-Salvetti correlation-energy formula into a functional of the electron density. *Phys. Rev. B*, 37(2):785–789, 1988.

[194] Volker Blum, Ralf Gehrke, Felix Hanke, Paula Havu, Ville Havu, Xinguo Ren, Karsten Reuter, and Matthias Scheffler. Ab initio molecular simulations with numeric atom-centered orbitals. *Comput. Phys. Commun.*, 180(11):2175–2196, 2009.

[195] M. J. Frisch, G. W. Trucks, H. B. Schlegel, G. E. Scuseria, M. A. Robb, J. R. Cheeseman, Montgomery, Jr., J. A. and T. Vreven, K. N. Kudin, J. C. Burant, J. M. Millam, S. S. Iyengar, J. Tomasi, V. Barone, B. Mennucci, M. Cossi, G. Scalmani, N. Rega, G. A. Petersson, H. Nakatsuji, M. Hada, M. Ehara, K. Toyota, R. Fukuda, J. Hasegawa, M. Ishida, T. Nakajima, Y. Honda, O. Kitao, H. Nakai, M. Klene, X. Li, J. E. Knox, H. P. Hratchian, J. B. Cross, V. Bakken, C. Adamo, J. Jaramillo, R. Gomperts, R. E. Stratmann, O. Yazyev, A. J. Austin, R. Cammi, C. Pomelli, J. W. Ochterski, P. Y. Ayala, K. Morokuma, G. A. Voth, P. Salvador, J. J. Dannenberg, V. G. Zakrzewski, S. Dapprich, A. D. Daniels, M. C. Strain, O. Farkas, D. K. Malick, A. D. Rabuck, K. Raghavachari, J. B. Foresman, J. V. Ortiz, Q. Cui, A. G. Baboul, S. Clifford, J. Cioslowski, B. B. Stefanov, G. Liu, A. Liashenko, P. Piskorz, I. Komaromi, R. L. Martin, D. J. Fox, T. Keith, M. A. Al-Laham, C. Y. Peng, A. Nanayakkara, M. Challacombe, P. M. W. Gill, B. Johnson, W. Chen, M. W. Wong, C. Gonzalez, J. A. Pople. Gaussian, Inc., Wallingford, CT, *Gaussian 03*, Revision C.02 edition, 2004.

[196] R. Ditchfield, W. J. Hehre, and J. A. Pople. Self-Consistent Molecular-Orbital Methods. IX. An Extended Gaussian-Type Basis for Molecular-Orbital Studies of Organic Molecules. *J. Chem. Phys.*, 54(2):724–728, January 1971.

[197] W. J. Hehre, R. Ditchfield, and J. A. Pople. Self—Consistent Molecular Orbital Methods. XII. Further Extensions of Gaussian—Type Basis Sets for Use in Molecular Orbital Studies of Organic Molecules. *J. Chem. Phys.*, 56(5):2257–2261, March 1972.

[198] P. C. Hariharan and J. A. Pople. The influence of polarization functions on molecular orbital hydrogenation energies. *Theor. Chim. Acta*, 28(3):213–222, September 1973.

[199] Vitaly A. Rassolov, John A. Pople, Mark A. Ratner, and Theresa L. Windus. 6-31G* basis set for atoms K through Zn. *J. Chem. Phys.*, 109(4):1223–1229, 1998.

[200] G. te Velde, F. M. Bickelhaupt, E. J. Baerends, C. Fonseca Guerra, S. J. A. van Gisbergen, J. G. Snijders, and T. Ziegler. Chemistry with ADF. *J. Comput. Chem.*, 22(9):931–967, 2001.

[201] B. Hammer, L. B. Hansen, and J. K. Nørskov. Improved adsorption energetics within density-functional theory using revised Perdew-Burke-Ernzerhof functionals. *Phys. Rev. B*, 59(11):7413–7421, 1999.

[202] Bo-Tao Teng, Xiao-Dong Wen, Maohong Fan, Feng-Min Wu, and Yulong Zhang. Choosing a proper exchange–correlation functional for the computational catalysis on surface. *Phys. Chem. Chem. Phys.*, 16(34):18563–18569, 2014.

[203] Abhirup Patra, Haowei Peng, Jianwei Sun, and John P. Perdew. Rethinking CO adsorption on transition-metal surfaces: Effect of density-driven self-interaction errors. *Phys. Rev. B*, 100(3):035442, 2019.

[204] Adrien J. Göttle and Marc T. M. Koper. Determinant role of electrogenerated reactive nucleophilic species on selectivity during reduction of co_2 catalyzed by metalloporphyrins. *J. Am. Chem. Soc.*, 140(14):4826–4834, 2018.

[205] Haoqian Zhou, Xiaolong Zou, Xi Wu, Xin Yang, and Jia Li. Coordination engineering in cobalt–nitrogen-functionalized materials for co_2 reduction. *J. Phys. Chem. Lett.*, 10(21):6551–6557, 2019.

[206] Stephen Paul, Yi-Lin Kao, Lingmei Ni, Rayko Ehnert, Iris Herrmann-Geppert, Roel van de Krol, Robert W. Stark, Wolfram Jaegermann, Ulrike I. Kramm, and Peter Bogdanoff. Influence of the metal center in m–n–c catalysts on the co_2 reduction reaction on gas diffusion electrodes. *ACS Catal.*, 11(9):5850–5864, 2021.

[207] Na Han, Yu Wang, Lu Ma, Jianguo Wen, Jing Li, Hechuang Zheng, Kaiqi Nie, Xinxia Wang, Feipeng Zhao, Yafei Li, Jian Fan, Jun Zhong, Tianpin Wu, Dean J. Miller, Jun Lu, Shuit-Tong Lee, and Yanguang Li. Supported Cobalt Polyphthalocyanine for High-Performance Electrocatalytic CO_2 Reduction. *Chem*, 3(4):652–664, 2017.

[208] Mahmood Aliofkhazraei, Nasar Ali, W. Milne, Cengiz Ozkan, S. Mitura, and Juana Gervasoni. *Graphene Science Handbook: Electrical and Optical Properties*. CRC Press, Florida, United States of America, 1st ed edition, 2016.

[209] X. Blase, Lorin X. Benedict, Eric L. Shirley, and Steven G. Louie. Hybridization effects and metallicity in small radius carbon nanotubes. *Phys. Rev. Lett.*, 72(12):1878–1881, 1994.

[210] N. Wang, Z. K. Tang, G. D. Li, and J. S. Chen. Single-walled 4 Å carbon nanotube arrays. *Nature*, 408(6808):50–51, 2000.

[211] Shin-ichi Sawada and Noriaki Hamada. Energetics of carbon nano-tubes. *Solid State Commun.*, 83(11):917–919, 1992.

[212] Jeroen W. G. Wilder, Liesbeth C. Venema, Andrew G. Rinzler, Richard E. Smalley, and Cees Dekker. Electronic structure of atomically resolved carbon nanotubes. *Nature*, 391(6662):59–62, 1998.

[213] J.-C. Charlier. Defects in carbon nanotubes. *Acc. Chem. Res.*, 35(12):1063–1069, December 2002.

[214] Axel Gross. *Theoretical Surface Science: A Microscopic Perspective*. Springer, Ulm, Germany, 2009.

[215] L. G. Zhou and S. Q. Shi. Adsorption of foreign atoms on Stone–Wales defects in carbon nanotube. *Carbon*, 41(3):613–615, 2003.

[216] Nirupama Chakrapani, Yiming M. Zhang, Saroj K. Nayak, James A. Moore, David L. Carroll, Yoon Y. Choi, and Pulickel M. Ajayan. Chemisorption of Acetone on Carbon Nanotubes. *J. Phys. Chem. B*, 107(35):9308–9311, 2003.

[217] S. Santucci, S. Picozzi, F. Di Gregorio, L. Lozzi, C. Cantalini, L. Valentini, J. M. Kenny, and B. Delley. NO_2 and CO gas adsorption on carbon nanotubes: Experiment and theory. *J. Chem. Phys.*, 119(20):10904–10910, 2003.

[218] Xin Lu, Zhongfang Chen, and Paul v. R. Schleyer. Are StoneWales Defect Sites Always More Reactive Than Perfect Sites in the Sidewalls of Single-Wall Carbon Nanotubes? *J. Am. Chem. Soc.*, 127(1):20–21, 2005.

[219] Holger F. Bettinger. The Reactivity of Defects at the Sidewalls of Single-Walled Carbon Nanotubes: The StoneWales Defect. *J. Phys. Chem. B*, 109(15):6922–6924, 2005.

[220] Seong Ho Yang, Weon Ho Shin, Jung Woo Lee, Se Yun Kim, Seong Ihl Woo, and Jeung Ku Kang. Interaction of a Transition Metal Atom with Intrinsic Defects in Single-Walled Carbon Nanotubes. *J. Phys. Chem. B*, 110(28):13941–13946, 2006.

[221] Annia Galano, Misaela Francisco-Marquez, and Ana Martínez. Influence of Point Defects on the Free-Radical Scavenging Capability of Single-Walled Carbon Nanotubes. *J. Phys. Chem. C*, 114(18):8302–8308, 2010.

[222] Philip G. Collins. *Defects and Disorder in Carbon Nanotubes*, volume 2. Oxford Univ. Press, Oxford, England, first edition edition, 2010.

[223] Florian Banhart, Jani Kotakoski, and Arkady V. Krasheninnikov. Structural defects in graphene. *ACS Nano*, 5(1):26–41, 2011.

[224] Yuanyue Liu and Boris I. Yakobson. Cones, Pringles, and Grain Boundary Landscapes in Graphene Topology. *Nano Lett.*, 10(6):2178–2183, 2010.

[225] Jayeeta Lahiri, You Lin, Pinar Bozkurt, Ivan I. Oleynik, and Matthias Batzill. An extended defect in graphene as a metallic wire. *Nat. Nanotechnol.*, 5(5):326–329, 2010.

[226] Daniel Berger and Christian Ratsch. Line defects in graphene: How doping affects the electronic and mechanical properties. *Phys. Rev. B*, 93(23):235441, 2016.

[227] Xianbao Wang, Yunqi Liu, Wenfeng Qiu, and Daoben Zhu. Immobilization of tetra-tert -butylphthalocyanines on carbon nanotubes : A first step towards the development of new nanomaterials. *J. Mater. Chem.*, 12(6):1636–1639, 2002.

[228] Gema de la Torre, Werner Blau, and Tomas Torres. A survey on the functionalization of single-walled nanotubes. The chemical attachment of phthalocyanine moieties. *Nanotechnology*, 14(7):765–771, 2003.

[229] Bolade O. Agboola and Kenneth I. Ozoemena. Self-assembly and heterogeneous electron transfer properties of metallo-octacarboxyphthalocyanine complexes on gold electrode. *Phys. Chem. Chem. Phys.*, 10(17):2399–2408, 2008.

[230] Fernando C. Moraes, Lucia H. Mascaro, Sergio A. S. Machado, and Christopher M. A. Brett. Direct electrochemical determination of carbaryl using a multi-walled carbon nanotube/cobalt phthalocyanine modified electrode. *Talanta*, 79(5):1406–1411, 2009.

[231] Jing-Jing Ma, Hong-Lin Zhu, Yue-Qing Zheng, and Miao Shui. An Insight into Anchoring of Cobalt Phthalocyanines onto Carbon: Efficiency of the CO_2 Reduction Reaction. *ACS Appl. Energy Mater.*, 4(2):1442–1448, 2021.

[232] Haidong Zhang, Shixiong Min, Fang Wang, and Zhengguo Zhang. Immobilizing cobalt phthalocyanine into a porous carbonized wood membrane as a self-supported heterogenous electrode for selective and stable CO_2 electroreduction in water. *Dalton Trans.*, 49(44):15607–15611, 2020.

[233] Hong-Lin Zhu, Lin-Chang Liu, Zhong-Yi Li, Jing-Jing Ma, Yue-Qing Zheng, and Miao Shui. Insight into the Active Site in Electrochemical CO_2 Reduction of Self-Supported Cobalt Phthalocyanine Anchored on $ZnIn_2S_4$ Nanoarrays. *ACS Appl. Energy Mater.*, 4(7):6616–6623, 2021.

[234] Shanhe Gong, Wenbo Wang, Xinxin Xiao, Jun Liu, Chundu Wu, and Xiaomeng Lv. Elucidating influence of the existence formation of anchored cobalt phthalocyanine on electrocatalytic CO_2-to-CO conversion. *Nano Energy*, 84:105904, 2021.

[235] Takuya Hayashi, Yoong Ahm Kim, Toshiharu Matoba, Masaya Esaka, Kunio Nishimura, Takayuki Tsukada, Morinobu Endo, and Mildred S. Dresselhaus. Smallest

Freestanding Single-Walled Carbon Nanotube. *Nano Lett.*, 3(7):887–889, 2003.

[236] Madhu Menon, Antonis N. Andriotis, and George E. Froudakis. Curvature dependence of the metal catalyst atom interaction with carbon nanotubes walls. *Chem. Phys. Lett.*, 320(5):425–434, 2000.

[237] Federico Franco, Clara Rettenmaier, Hyo Sang Jeon, and Beatriz Roldan Cuenya. Transition metal-based catalysts for the electrochemical CO_2 reduction: from atoms and molecules to nanostructured materials. *Chem. Soc. Rev*, 49(19):6884–6946, 2020.

[238] Vitaliy A. Kislenko, Sergey V. Pavlov, and Sergey A. Kislenko. Influence of defects in graphene on electron transfer kinetics: The role of the surface electronic structure. *Electrochim. Acta*, 341:136011, 2020.

[239] Rafia Ahmad and Abhishek K. Singh. Simultaneous Site Adsorption Shift and Efficient CO Oxidation Induced by V and Co in Pt Catalyst. *J. Phys. Chem. C*, 121(23):12807–12816, 2017.

[240] Matthew T. Darby, E. Charles H. Sykes, Angelos Michaelides, and Michail Stamatakis. Carbon Monoxide Poisoning Resistance and Structural Stability of Single Atom Alloys. *Top Catal*, 61(5):428–438, 2018.

[241] Satadeep Bhattacharjee, Umesh V. Waghmare, and Seung-Cheol Lee. An improved d-band model of the catalytic activity of magnetic transition metal surfaces. *Sci. Rep.*, 6(1):35916, 2016.

[242] Oliver J. Conquest, Tanglaw Roman, Aleksei Marianov, Alena Kochubei, Yijao Jiang, and Catherine Stampfl. Calculating Entropies of Large Molecules in Aqueous Phase. *J. Chem. Theory Comput.*, 17(12):7753–7771, 2021.

[243] Kevin Leung, Ida M. B. Nielsen, Na Sai, Craig Medforth, and John A. Shelnutt. CobaltPorphyrin Catalyzed Electrochemical Reduction of Carbon Dioxide in Water. 2. Mechanism from First Principles. *J. Phys. Chem. A*, 114(37):10174–10184, 2010.

[244] Jing Shen, Ruud Kortlever, Recep Kas, Yuvraj Y. Birdja, Oscar Diaz-Morales, Youngkook Kwon, Isis Ledezma-Yanez, Klaas Jan P. Schouten, Guido Mul, and Marc T. M. Koper. Electrocatalytic reduction of carbon dioxide to carbon monoxide and methane at an immobilized cobalt protoporphyrin. *Nat. Commun.*, 6(1):8177, 2015.

[245] Alberto De Riccardis, Michelle Lee, Roman V. Kazantsev, Alejandro J. Garza, Guosong Zeng, David M. Larson, Ezra L. Clark, Peter Lobaccaro, Paul W. W. Burroughs, Ermelinda Bloise, Joel W. Ager, Alexis T. Bell, Martin Head-Gordon, Giuseppe Mele, and Francesca M. Toma. Heterogenized Pyridine-Substituted Cobalt(II) Phthalocyanine Yields Reduction of CO_2 by Tuning the Electron Affinity of the Co Center. *ACS Appl. Mater. Interfaces*, 12(5):5251–5258, 2020.

[246] Yujian Xia, Stepan Kashtanov, Pengfei Yu, Lo-Yueh Chang, Kun Feng, Jun Zhong, Jinghua Guo, and Xuhui Sun. Identification of dual-active sites in cobalt phthalocyanine for electrochemical carbon dioxide reduction. *Nano Energy*, 67:104163, 2020.

[247] Dae-Hyun Nam, Phil De Luna, Alonso Rosas-Hernandez, Arnaud Thevenon, Fengwang Li, Theodor Agapie, Jonas C Peters, Osama Shekhah, Mohamed Eddaoudi, and Edward H Sargent. Molecular enhancement of heterogeneous CO_2 reduction. *Nat. Mater.*, 19(3):266–276, 2020.

[248] Huiying Tian, Kai Wang, Ziyi Shui, Muhammad Ali Raza, Hang Xiao, Meidan Que, Liangliang Zhu, and Xi Chen. Enhanced CO_2 electroreduction on co active site of cobalt phthalocyanine by electronic effect. *Mater. Lett.*, 310:131482, 2021.

[249] Huajian Xu, Huizhu Cai, Linxia Cui, Limei Yu, Rui Gao, and Chuan Shi. Molecular modulating of cobalt phthalocyanines on aminofunctionalized carbon nanotubes for enhanced electrocatalytic CO_2 conversion. *Nano Research*, 2022.

[250] Oliver J. Conquest, Tanglaw Roman, Aleksei Marianov, Alena Kochubei, Yijiao Jiang, and Catherine Stampfl. *Ab Initio* investigation of covalently immobilized cobalt-centered metal-organic catalysts for CO_2 reduction: The effect of the substrate on the reaction energetics. *J. Phys. Chem. C*, 126(24):10081–10100, 2022.

[251] Yuan Pan, Rui Lin, Yinjuan Chen, Shoujie Liu, Wei Zhu, Xing Cao, Wenxing Chen, Konglin Wu, Weng-Chon Cheong, Yu Wang, Lirong Zheng, Jun Luo, Yan Lin, Yunqi Liu, Chenguang Liu, Jun Li, Qi Lu, Xin Chen, Dingsheng Wang, Qing Peng, Chen Chen, and Yadong Li. Design of single-atom co-n_5 catalytic site: A robust electrocatalyst for co2 reduction with nearly 100% co selectivity and remarkable stability. *J. Am. Chem. Soc.*, 140(12):4218–4221, 2018.

[252] Graeme Henkelman, Andri Arnaldsson, and Hannes Jónsson. A fast and robust algorithm for Bader decomposition of charge density. *Comput. Mater. Sci.*, 36(3):354–360, 2006.

[253] Edward Sanville, Steven D. Kenny, Roger Smith, and Graeme Henkelman. Improved grid-based algorithm for Bader charge allocation. *J. Comput. Chem.*, 28(5):899–908, 2007.

[254] W. Tang, E. Sanville, and G. Henkelman. A grid-based Bader analysis algorithm without lattice bias. *J. Phys. Condens. Matter*, 21(8):084204, 2009.

[255] Min Yu and Dallas R. Trinkle. Accurate and efficient algorithm for Bader charge integration. *J. Chem. Phys.*, 134(6):064111, 2011.

[256] C. Grabl, M. Bodensteiner, M. Zabel, and M. Scheer. Synthesis of arsenic-rich As_n ligand complexes from yellow arsenic. *Chem. Sci.*, 6(2):1379–1382, 2015.

[257] Kim M. Baines and William G. Stibbs. The molecular structure of organogermanium compounds. *Coord. Chem. Rev.*, 145:157–200, 1995.

[258] Andrew M. Poitras, Sadie E. Knight, Mark W. Bezpalko, Bruce M. Foxman, and Christine M. Thomas. Addition of H_2 across a cobalt-phosphorus bond. *Angew. Chem., Int. Ed.*, 57(6):1497–1500, 2018.

[259] Yingshuo Liu, Aniruddha Deb, Kwan Yee Leung, Weixuan Nie, William S. Dean, James E. Penner-Hahn, and Charles C. L. McCrory. Determining the coordination environment and electronic structure of polymer-encapsulated cobalt phthalocyanine under electrocatalytic CO_2 reduction conditions using in situ x-ray absorption spectroscopy. *Dalton Trans.*, 49(45):16329–16339, 2020.

[260] Mingwen Zhao, Yueyuan Xia, James P. Lewis, and Ruiqin Zhang. First-principles calculations for nitrogen-containing single-walled carbon nanotubes. *J. Appl. Phys.*, 94(4):2398–2402, 2003.

[261] Laura P. Granda-Marulanda, Alejandra Rendón-Calle, Santiago Builes, Francesc Illas, Marc T. M. Koper, and Federico Calle-Vallejo. A semiempirical method to detect and correct dft-based gas-phase errors and its application in electrocatalysis. *ACS Catalysis*, 10(12):6900–6907, 2020.

[262] Hagen Neugebauer, Fabian Bohle, Markus Bursch, Andreas Hansen, and Stefan Grimme. Benchmark study of electrochemical redox potentials calculated with semiempirical and dft methods. *J. Phys. Chem. A*, 124(35):7166–7176, 2020.

[263] Cheng-Nan Chang, Hong-Bang Cheng, and Allen C. Chao. Applying the nernst equation to simulate redox potential variations for biological nitrification and denitrification processes. *J. Phys. Chem. A*, 38(6):1807–1812, 2004.

[264] Kiran Mathew, V. S. Chaitanya Kolluru, Srinidhi Mula, Stephan N. Steinmann, and Richard G. Hennig. Implicit self-consistent electrolyte model in plane-wave density-functional theory. *J. Chem. Phys.*, 151(23):234101, 2019.

[265] Jin Zhang, Haiyang Zhang, Tao Wu, Qi Wang, and David van der Spoel. Comparison of implicit and explicit solvent models for the Calculation of solvation free energy in organic solvents. *J. Chem. Theory Comput.*, 13(3):1034–1043, 2017.

[266] Péter Pál Fehér and András Stirling. Assessment of reactivities with explicit and implicit solvent models: QM/MM and gas-phase evaluation of three different ag-catalysed furan ring formation routes. *New J. Chem.*, 43(39):15706–15713, 2019.

[267] Xiaoyu Chen, Dongli Wei, and Marten S. G. Ahlquist. Aggregation and significant difference in reactivity therein: Blocking the CO_2-to-CH_3OH reaction. *Organometallics*, 40(17):3087–3093, 2021.

[268] Leonidas Tsetseris. Hydrogen- and oxygen-related effects in phthalocyanine crystals: Formation of carrier traps and a change in the magnetic state. *Phys. Chem. Chem. Phys.*, 16(7):3317–3322, 2014.

[269] Jian-Qiang Zhong, Zhunzhun Wang, Jia Lin Zhang, Christopher A. Wright, Kaidi Yuan, Chengding Gu, Anton Tadich, Dongchen Qi, He Xing Li, Min Lai, Kai Wu, Guo Qin Xu, Wenping Hu, Zhenyu Li, and Wei Chen. Reversible tuning of interfacial and intramolecular charge transfer in individual mnpc molecules. *Nano Lett.*, 15(12):8091–8098, 2015.

[270] A. Sarasola, M. Abadia, C. Rogero, and A. Garcia-Lekue. Theoretical insights into unexpected molecular core level shifts: Chemical and surface effects. *J. Phys. Chem. Lett.*, 8(23):5718–5724, 2017.

[271] Yu Wang, Xiaoguang Li, and Jinlong Yang. Electronic and magnetic properties of copc and fepc molecules on graphene: The substrate, defect, and hydrogen adsorption effects. *Phys. Chem. Chem. Phys.*, 21(10):5424–5434, 2019.

[272] G. te Velde, F. M. Bickelhaupt, E. J. Baerends, C. Fonseca Guerra, S. J. A. van Gisbergen, J. G. Snijders, and T. Ziegler. Chemistry with adf. *Phys. Chem. Chem. Phys.*, 22(9):931–967, 2001.

[273] E. Van Lenthe and E. J. Baerends. Optimized slater-type basis sets for the elements 1-118. *J. Comput. Chem.*, 24(9):1142–1156, 2003.

[274] Geun Ho Gu, Charles A. Mullen, Akwasi A. Boateng, and Dionisios G. Vlachos. Mechanism of dehydration of phenols on noble metals via first-principles microkinetic modeling. *ACS Catal.*, 6(5):3047–3055, 2016.

[275] Vivianne K. Ocampo-Restrepo, Lucas G. Verga, and Juarez L. F. Da Silva. Ab initio study of the c-o bond dissociation in CO_2 reduction by redox and carboxyl routes on 3d transition metal systems. *J. Phys. Chem. C*, 125(48):26296–26306, 2021.

[276] J Lahtinen, J Vaari, A Taio, A Vehanen, and P Hautojarvi. Adsorption and desorption measurements of co and O_2 on cobalt. *Vacuum*, 41(1):112–114, 1990.

[277] Dezhi Xu, Kangkang Li, Baohua Jia, Wenping Sun, Wei Zhang, Xue Liu, and Tianyi Ma. Electrocatalytic CO_2 reduction towards industrial applications. *Carbon Energy*, 5(1):e230, 2023.

[278] Jianjun Su, Jun-Jie Zhang, Jiacheng Chen, Yun Song, Libei Huang, Minghui Zhu, Boris I. Yakobson, Ben Zhong Tang, and Ruquan Ye. Building a stable cationic molecule/electrode interface for highly efficient and durable CO_2 reduction at an industrially relevant current. *Energy Environ. Sci*, 14(1):483–492, 2021.

[279] Elif Ertekin, D. C. Chrzan, and Murray S. Daw. Topological description of the Stone-Wales defect formation energy in carbon nanotubes and graphene. *Phys. Rev. B*,

79(15):155421, 2009.

[280] V. Ongun Özçelik, H. Hakan Gurel, and S. Ciraci. Self-healing of vacancy defects in single-layer graphene and silicene. *Phys. Rev. B*, 88(4):045440, 2013.

[281] Stephen T. Skowron, Irina V. Lebedeva, Andrey M. Popov, and Elena Bichoutskaia. Energetics of atomic scale structure changes in graphene. *Chem. Soc. Rev*, 44(10):3143–3176, 2015.

[282] Gun-Do Lee, C. Z. Wang, Euijoon Yoon, Nong-Moon Hwang, Doh-Yeon Kim, and K. M. Ho. Diffusion, Coalescence, and Reconstruction of Vacancy Defects in Graphene Layers. *Phys. Rev. Lett.*, 95(20):205501, 2005.

[283] J. Kotakoski, A. V. Krasheninnikov, U. Kaiser, and J. C. Meyer. From Point Defects in Graphene to Two-Dimensional Amorphous Carbon. *Phys. Rev. Lett.*, 106(10):105505, 2011.

[284] Xing Zhang, Zishan Wu, Xiao Zhang, Liewu Li, Yanyan Li, Haomin Xu, Xiaoxiao Li, Xiaolu Yu, Zisheng Zhang, Yongye Liang, and Hailiang Wang. Highly selective and active co_2 reduction electrocatalysts based on cobalt phthalocyanine/carbon nanotube hybrid structures. *Nature Communications*, 8(1):1–8, 2017.

[285] Hong-Lin Zhu, Yue-Qing Zheng, and Miao Shui. Synergistic Interaction of Nitrogen-Doped Carbon Nanorod Array Anchored with Cobalt Phthalocyanine for Electrochemical Reduction of CO_2. *ACS Appl. Energy Mater.*, 3(4):3893–3901, 2020.

[286] Zhongjie Yang, Xiaofei Zhang, Chang Long, Shuhao Yan, Yanan Shi, Jianyu Han, Jing Zhang, Pengfei An, Lin Chang, and Zhiyong Tang. Covalently anchoring cobalt phthalocyanine on zeolitic imidazolate frameworks for efficient carbon dioxide electroreduction. *CrystEngComm*, 22(9):1619–1624, 2020.

[287] Shengshen Gu, Aleksei N. Marianov, Yuxiang Zhu, and Yijiao Jiang. Cobalt porphyrin immobilized on the TiO_2 nanotube electrode for CO_2 electroreduction in aqueous solution. *J. Energy Chem.*, 55:219–227, 2021.

1 Appendix A

Solvent	**Relative Permittivity** ϵ_r	**Acentric Factor** (ω)	**Molar Mass** M_S **(kg/mol)**	**Density of Solvent Medium** ρ **(kg/m^3)**
H_2O	80	0.344	0.018	997
CH_2Cl_2	8.9	0.2	0.085	1330

TABLE A1. The solvent-dependent physical constants used in the solvation entropy model for equations 17, 20 and 23.

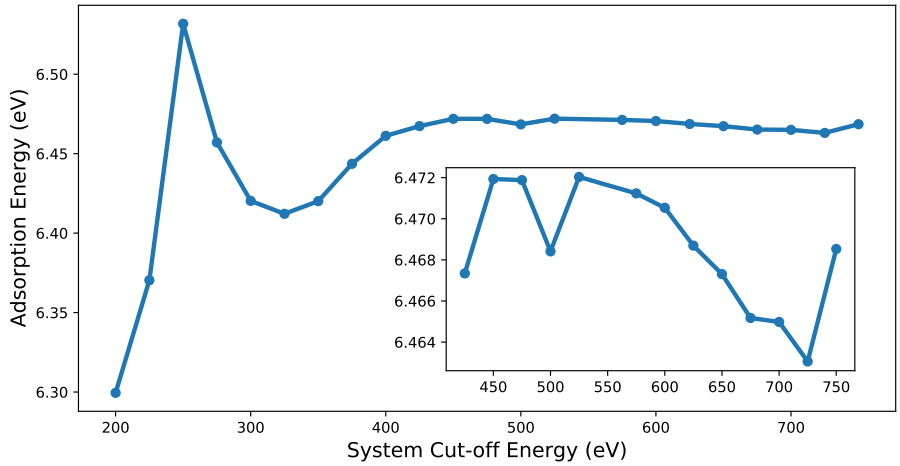

FIGURE A1. Adsorption energy of a Co atom in the center of the porphine structure as a function of energy cut-off. The inset plot shows the results for energy cut-off values between 400 eV to 750 eV.

Species	**Empirical**^{I}	**Group Element**^{II}	**Probe vdW**^{III}	**Probe Total**^{III}	**Convex Hull**^{IV}	**Expt.**
CO (Carbon Monoxide)	0.00115	0.00125	0.00125	0.00125	0.00126	0.00109^{α}
H_2 (Hydrogen Molecule)	0.00071		0.00071	0.00071	0.00071	0.00060^{α}
O_2 (Oxygen Molecule)	0.00136	0.00137	0.00136	0.00136	0.00136	0.00115^{α}
CO_2 (Carbon Dioxide	0.00139	0.00141	0.00140	0.00140	0.00141	0.00124^{γ}
H_2O (Water)	0.00127	0.00122	0.00122	0.00122	0.00122	0.00072^{β}
H_2S (Hydrogen Sulfide)	0.00131	0.00127	0.00128	0.00128	0.00128	0.00127^{α}

H_2O_2 (Hydrogen Peroxide)	0.00200	0.00197	0.00196	0.00196	0.00164	0.00149^{α}
NH_3 (Ammonia)	0.00130	0.00122	0.00124	0.00124	0.00124	0.00115^{α}
HCOOH (Formic Acid)	0.00177	0.00176	0.00176	0.00176	0.00175	0.00170^{β}
HNO_3 (Nitric Acid)	0.00191	0.00191	0.00190	0.00190	0.00188	0.00152^{α}
CH_4 (Methane)	0.00114	0.00112	0.00114	0.00114	0.00114	0.00089^{α}
C_2H_3N (Acetonitrile)	0.00165	0.00163	0.00165	0.00165	0.00164	0.00171^{δ}
C_2H_4 (Ethylene)	0.00144	0.00140	0.00142	0.00142	0.00141	0.00129^{δ}
H_2CO_3 (Carbonic Acid)	0.00186	0.00185	0.00185	0.00185	0.00183	0.00194^{β}
CH_3OH (Methanol)	0.00168	0.00163	0.00164	0.00164	0.00163	0.00138^{α}
C_2H_4O (Acetaldehyde)	0.00189	0.00186	0.00187	0.00187	0.00185	0.00135^{δ}
CH_3COOH (Acetic Acid)	0.00192	0.00184	0.00190	0.00189	0.00186	0.00183^{δ}
C_2H_6 (Ethane)	0.00154	0.00147	0.00150	0.00149	0.00147	0.00123^{α}
CH_4N_2O (Urea)	0.00190	0.00185	0.00187	0.00187	0.00184	0.00183^{α}
C_2H_5OH (Ethanol)	0.00196	0.00189	0.00191	0.00190	0.00186	0.00156^{δ}
C_3H_6O (Acetone)	0.00198	0.00193	0.00195	0.00194	0.00190	0.00183^{δ}
$C_2H_5NO_2$ (Glycine)	0.00230	0.00225	0.00226	0.00225	0.00220	0.00165^{α}
$C_4H_4O_4$ (Fumaric Acid)	0.00273	0.00273	0.00273	0.00271	0.00262	0.00271^{α}
C_3H_8O (Isopropanol)	0.00182	0.00211	0.00214	0.00212	0.00206	0.00213^{δ}
C_3H_8O (Propanol)	0.00189	0.00217	0.00220	0.00218	0.00213	0.00190^{δ}
$C_3H_7NO_2$ (Alanine)	0.00265		0.00260	0.00258	0.00251	0.00165^{α}
$H_4P_2O_7$ (Pyrophosphoric Acid)	0.00313		0.00310	0.00307	0.00296	0.00227^{α}
$C_4H_8O_2$ (Ethyl acetate)	0.00237	0.00229	0.00232	0.00230	0.00219	0.00276^{α}
$C_4H_6O_4$ (Succinic Acid)	0.00284	0.00288	0.00281	0.00279	0.00271	0.00280^{α}
$C_5H_5N_5$ (Adenine)	0.00266	0.00248	0.00252	0.00250	0.00245	0.00226^{α}

$C_4H_{10}O$ (Butanol)	0.00254	0.00243	0.00246	0.00244	0.00237	0.00223^{δ}
C_5H_{10} (Cyclopentane)	0.00191	0.00173	0.00177	0.00175	0.00168	0.00174^{δ}
C_8H_7N (Indole)	0.00244	0.00231	0.00232	0.00230	0.00224	0.00182^{α}
$C_4H_8N_2O_3$ (Asparagine)	0.00278	0.00271	0.00274	0.00270	0.00257	0.00248^{α}
$C_4H_8N_2O_3$ (Glycylglycine)	0.00287		0.00281	0.00278	0.00263	0.00339^{α}
$C_4H_{12}N$ (Tetramethyl-ammonium)	0.00215	0.00198	0.00205	0.00201	0.00195	0.00190^{ϵ}
C_6H_{12} (Cyclohexane)	0.00187	0.00167	0.00171	0.00170	0.00161	0.00172^{δ}
$C_5H_{11}NO_2$ (Valine)	0.00291	0.00280	0.00284	0.00279	0.00268	0.00206^{α}
$C_5H_{10}O_5$ (D-Ribose)	0.00321	0.00310	0.00307	0.00303	0.00292	0.00258^{α}
$C_5H_{10}O_5$ (D-Ribulose)	0.00336	0.00327	0.00329	0.00325	0.00312	0.00241^{α}
$C_5H_{10}N_2O_3$ (Glutamine)	0.00309	0.00298	0.00302	0.00297	0.00279	0.00262^{α}
$C_5H_{10}O_5$ (L-Arabinose)	0.00327	0.00311	0.00313	0.00308	0.00298	0.00190^{α}
$C_6H_{13}NO_2$ (Leucine)	0.00295	0.00282	0.00287	0.00281	0.00266	0.00322^{α}
$C_6H_{12}O_6$ (D-Fructose)	0.00361		0.00345	0.00340	0.00325	0.00290^{ζ}
$C_6H_{12}O_6$ (D-Galactose)	0.00346	0.00327	0.00330	0.00325	0.00309	0.00283^{α}
$C_6H_{12}O_6$ (D-Glucose)	0.00369		0.00353	0.00347	0.00329	0.00281^{ζ}
$C_6H_{12}O_6$ (D-Mannose)	0.00340	0.00322	0.00324	0.00319	0.00302	0.00274^{α}
$C_{11}H_{12}N_2O_2$ (Tryptophan)	0.00344		0.00328	0.00321	0.00296	0.00280^{α}
$C_8H_{20}N$ (Tetraethylammonium)	0.00326	0.00302	0.00310	0.00305	0.00290	0.00264^{ϵ}
$C_{10}H_12N_4O_5$ (Inosine)	0.00400		0.00372	0.00365	0.00322	0.00373^{α}
$C_{10}H_13N_5O_4$ (Adenosine)	0.00395	0.00410	0.00367	0.00360	0.00310	0.00378^{η}

$C_{10}H_1N_5O_7P$ (Adenosine Monophosphate)	0.00497		0.00463	0.00453	0.00375	0.00434^{α}
$C_{12}H_{22}O_{11}$ (Lactose)	0.00498	0.00469	0.00465	0.00450	0.00391	0.00416^{α}
$C_{12}H_{22}O_{11}$ (Maltose)	0.00497	0.00468	0.00465	0.00451	0.00407	0.00425^{α}
$C_{12}H_{22}O_{11}$ (Sucrose)	0.00490		0.00460	0.00445	0.00397	0.00451^{ζ}
$C_{16}H_{36}N$ (Tetrabutylammonium)	0.00443	0.00398	0.00413	0.00401	0.00296	0.00394^{ϵ}

TABLE A2. Entropy values for different molecular vdW (van der Waal) volume calculation methods using the solvation entropy model. All values have been calculated using the box packing method of the previous study [**47**]. References for the experimental values are given as follows: α [**185**],β [**184**],γ [**180**],δ [**47**],ϵ [**183**], ζ [**181**] and η [**182**]

Species	**Gas Phase**	**SPT Method**	**AF: BP**	**AF: SP**	**AF: RP**	**AF: CHP**	**AF: SES**	**Expt.**
H_2 (Hydrogen Molecule)	0.00135	0.00097	0.00071	0.00075	0.00071	0.00074	0.00074	0.00060^{α}
H_2O (Water)	0.00196	0.00164	0.00122	0.00130	0.00122	0.00128	0.00127	0.00072^{β}
NH_3 (Ammonia)	0.00200	0.00170	0.00124	0.00133	0.00124	0.00130	0.00130	0.00115^{α}
O_2 (Oxygen Molecule)	0.00213	0.00182	0.00136	0.00143	0.00136	0.00141	0.00141	0.00115^{α}
CH_4 (Methane)	0.00193	0.00166	0.00114	0.00124	0.00115	0.00121	0.00121	0.00089^{α}
CO (Carbon Monoxide)	0.00205	0.00177	0.00125	0.00135	0.00125	0.00132	0.00132	0.00109^{α}

H_2O_2 (Hydrogen Peroxide)	0.00271	0.00227	0.00196	0.00239	0.00214	0.00203	0.00193	0.00149^{α}
H_2S (Hydrogen Sulfide)	0.00210	0.00185	0.00128	0.00140	0.00129	0.00137	0.00137	0.00127^{α}
CO_2 (Carbon Dioxide)	0.00222	0.00195	0.00140	-0.05595	0.00140	0.00145	0.00145	0.00124^{γ}
CH_3OH (Methanol)	0.00248	0.00224	0.00164	0.00174	0.00164	0.00171	0.00171	0.00138^{α}
C_2H_4 (Ethylene)	0.00227	0.00205	0.00142	0.00152	0.00144	0.00149	0.00149	0.00129^{δ}
HCOOH (Formic Acid)	0.00261	0.00238	0.00176	0.00184	0.00175	0.00182	0.00182	0.00170^{β}
C_2H_6 (Ethane)	0.00237	0.00216	0.00149	0.00159	0.00150	0.00156	0.00156	0.00123^{α}
HNO_3 (Nitric Acid)	0.00278	0.00257	0.00190	-0.61809	0.00189	0.00196	0.00196	0.00152^{α}
C_2H_3N (Acetonitrile)	0.00253	0.00232	0.00165	0.00132	0.00164	0.00171	0.00171	0.00171^{δ}
C_2H_4O (Acetaldehyde)	0.00276	0.00257	0.00187	0.00170	0.00187	0.00193	0.00193	0.00135^{δ}
H_2CO_3 (Carbonic Acid)	0.00274	0.00255	0.00185	0.00192	0.00184	0.00191	0.00191	0.00194^{β}

C_2H_5OH (Ethanol)	0.00281	0.00264	0.00190	0.00198	0.00189	0.00196	0.00196	0.00156^{δ}
CH_4N_2O (Urea)	0.00278	0.00261	0.00187	0.00194	0.00185	0.00193	0.00193	0.00183^{α}
CH_3COOH (Acetic Acid)	0.00282	0.00266	0.00189	- 4.37167	0.00188	0.00195	0.00196	0.00183^{δ}
C_3H_6O (Acetone)	0.00291	0.00278	0.00194	0.00179	0.00193	0.00200	0.00200	0.00183^{δ}
$C_2H_5NO_2$ (Glycine)	0.00322	0.00310	0.00225	0.00068	0.00224	0.00230	0.00231	0.00165^{α}
C_3H_8O (Propanol)	0.00316	0.00303	0.00218	0.00222	0.00218	0.00223	0.00224	0.00190^{δ}
C_3H_8O (Isopropanol)	0.00312	0.00301	0.00212	0.00223	0.00210	0.00219	0.00219	0.00213^{δ}
C_5H_{10} (Cyclopentane)	0.00282	0.00276	0.00175	0.00187	0.00176	0.00183	0.00183	0.00174^{δ}
$C_3H_7NO_2$ (Alanine)	0.00363	0.00357	0.00258	0.00267	0.00256	0.00264	0.00264	0.00165^{α}
$C_4H_{10}O$ (Butanol)	0.00346	0.00338	0.00244	0.00244	0.00243	0.00248	0.00248	0.00223^{δ}
$C_4H_8O_2$ (Ethyl acetate)	0.00335	0.00329	0.00230	0.00230	0.00229	0.00234	0.00235	0.00276^{α}
$C_4H_{12}N$ (Tetramethylammonium)	0.00314	0.00312	0.00201	0.00215	0.00204	0.00210	0.00210	0.00190^{ϵ}
$C_4H_4O_4$ (Fumaric Acid)	0.00378	0.00374	0.00271	0.00228	0.00269	0.00275	0.00275	0.00271^{α}

C_6H_{12} (Cyclohexane)	0.00282	0.00281	0.00170	0.00179	0.00171	0.00176	0.00176	0.00172^{δ}
$C_4H_6O_4$ (Succinic Acid)	0.00382	0.00377	0.00279	0.00278	0.00279	0.00280	0.00280	0.00280^{α}
$C_5H_5N_5$ (Adenine)	0.00364	0.00364	0.00250	0.00245	0.00249	0.00255	0.00255	0.00226^{δ}
$H_4P_2O_7$ (Pyrophosphoric Acid)	0.00422	0.00423	0.00307	0.00314	0.00306	0.00312	0.00313	0.00227^{α}
C_8H_7N (Indole)	0.00346	0.00347	0.00230	0.00083	0.00228	0.00235	0.00236	0.00182^{α}
$C_4H_8N_2O_3$ (Asparagine)	0.00386	0.00389	0.00270	0.00268	0.00268	0.00274	0.00275	0.00248^{α}
$C_4H_8N_2O_3$ (Glycylglycine)	0.00387	0.00387	0.00278	0.00276	0.00278	0.00279	0.00279	0.00339^{α}
$C_5H_{11}NO_2$ (Valine)	0.00400	0.00404	0.00279	0.00288	0.00278	0.00286	0.00286	0.00206^{α}
$C_5H_{10}O_5$ (D-Ribose)	0.00426	0.00433	0.00303	0.00312	0.00301	0.00309	0.00309	0.00258^{α}
$C_5H_{10}O_5$ (L-Arabinose)	0.00432	0.00438	0.00308	0.00316	0.00307	0.00314	0.00314	0.00190^{α}
$C_5H_{10}O_5$ (D-Ribulose)	0.00444	0.00450	0.00325	0.00329	0.00324	0.00328	0.00328	0.00241^{α}
$C_5H_{10}N_2O_3$ (Glutamine)	0.00414	0.00419	0.00297	0.00298	0.00296	0.00298	0.00298	0.00262^{α}
$C_6H_{13}NO_2$ (Leucine)	0.00407	0.00416	0.00281	0.00288	0.00280	0.00286	0.00286	0.00322^{α}

$C_6H_{12}O_6$ (D-Fructose)	0.00472	0.00485	0.00340	0.00347	0.00339	0.00345	0.00345	0.00290^{ζ}
$C_6H_{12}O_6$ (D-Galactose)	0.00454	0.00466	0.00325	0.00330	0.00323	0.00328	0.00328	0.00283^{α}
$C_6H_{12}O_6$ (D-Mannose)	0.00449	0.00461	0.00319	0.00323	0.00318	0.00322	0.00323	0.00274^{α}
$C_6H_{12}O_6$ (D-Glucose)	0.00476	0.00488	0.00347	0.00351	0.00345	0.00349	0.00349	0.00281^{ζ}
$C_8H_{20}N$ (Tetraethyl-ammonium)	0.00443	0.00458	0.00305	0.00314	0.00303	0.00311	0.00312	0.00264^{ϵ}
$C_{11}H_{12}N_2O_2$ (Tryptophan)	0.00461	0.00482	0.00321	0.00321	0.00320	0.00322	0.00322	0.00280^{α}
$C_{10}H_{12}N_4O_5$ (Inosine)	0.00501	0.00525	0.00365	0.00363	0.00369	0.00360	0.00360	0.00373^{α}
$C_{10}H_{13}N_5O_4$ (Adenosine)	0.00501	0.00526	0.00360	0.00357	0.00364	0.00357	0.00356	0.00378^{η}
$C_{10}H_{14}N_5O_7P$ (Adenosine Monophos-phate)	0.00581	0.00610	0.00453	0.00463	0.00478	0.00445	0.00440	0.00434^{α}
$C_{16}H_{36}N$ (Tet-rabutylam-monium)	0.00565	0.00605	0.00401	0.00414	0.00412	0.00399	0.00397	0.00394^{ϵ}
$C_{12}H_{22}O_{11}$ (Maltose)	0.00618	0.00659	0.00451	0.00440	0.00455	0.00446	0.00446	0.00425^{α}
$C_{12}H_{22}O_{11}$ (Sucrose)	0.00625	0.00668	0.00445	0.00444	0.00445	0.00444	0.00444	0.00451^{ζ}

$C_{12}H_{22}O_{11}$ (Lactose)	0.00614	0.00655	0.00450	0.00439	0.00455	0.00444	0.00443	0.00416$^{\alpha}$

TABLE A3. Entropy values in units eV/K calculated using the solvation entropy model for different packing methods, cavity descriptions. The acentric factor (AF) packing methods included in this table are the box packing (BP), spherical packing (SP), rectangular packing (RP), convex hull packing (CHP) and the solvent excluded surface packing (SES). Gas phase and experimental entropies for aqueous phase are also included. References for the experimental values are given as follows: α [**185**],β [**184**],γ [**180**],δ [**47**],ϵ [**183**], ζ [**181**] and η [**182**]

Packing Method	**Molecular Size Category**			
	All	Small	Medium	Large
SPT	0.383	0.230	0.368	0.568
Box	0.092	0.062	0.097	0.121
Rectangular Prism	0.094	0.065	0.096	0.124
Spherical	0.117	0.091	0.129	0.129
Convex Hull	0.102	0.077	0.109	0.124
SES	0.102	0.076	0.109	0.123

TABLE A4. Mean Absolute Error (MAE) of calculated $T\Delta S$ values (eV) relative to experiment. These values complement those in the bar plot of figure 6. The packing methods are given in the first column with scaled particle theory (SPT) and solvent excluded surface (SES). *All* is the MAE of all molecules the *Small*, *Medium* and *Large* categories.

Species	Scaled Gas Phase	Vibrational Entropy	Solvation Model	Solvation Model with Correction	ChemSol
H_2 (Hydrogen Molecule)	0.00084	0.00000	0.00071	0.00050	0.00054
H_2O (Water)	0.00121	0.00000	0.00122	0.00100	0.00055
NH_3 (Ammonia)	0.00124	0.00000	0.00124	0.00103	0.00061
O_2 (Oxygen Molecule)	0.00132	0.00000	0.00136	0.00114	0.00064

CH_4 (Methane)	0.00120	0.00000	0.00114	0.00093	0.00080
CO (Carbon Monoxide)	0.00127	0.00000	0.00125	0.00104	0.00062
H_2O_2 (Hydrogen Peroxide)	0.00168	0.00001	0.00196	0.00175	0.00059
H_2S (Hydrogen Sulfide)	0.00130	0.00000	0.00128	0.00107	0.00064
CO_2 (Carbon Dioxide)	0.00138	0.00004	0.00140	0.00119	0.00069
CH_3OH (Methanol)	0.00154	0.00008	0.00164	0.00143	0.00076
C_2H_4 (Ethylene)	0.00141	0.00003	0.00142	0.00121	0.00089
HCOOH (Formic Acid)	0.00162	0.00004	0.00176	0.00155	0.00073
C_2H_6 (Ethane)	0.00147	0.00009	0.00149	0.00128	0.00092
HNO_3 (Nitric Acid)	0.00172	0.00010	0.00190	0.00169	0.00072
C_2H_3N (Acetonitrile)	0.00157	0.00011	0.00165	0.00144	0.00090
C_2H_4O (Acetaldehyde)	0.00171	0.00017	0.00187	0.00166	0.00092
H_2CO_3 (Carbonic Acid)	0.00170	0.00012	0.00185	0.00164	0.00071
C_2H_5OH (Ethanol)	0.00175	0.00022	0.00190	0.00169	0.00089
CH_4N_2O (Urea)	0.00173	0.00016	0.00187	0.00165	0.00096
CH_3COOH (Acetic Acid)	0.00175	0.00013	0.00189	0.00168	0.00089
C_3H_6O (Acetone)	0.00180	0.00027	0.00194	0.00172	0.00106
$C_2H_5NO_2$ (Glycine)	0.00200	0.00043	0.00225	0.00204	0.00086
C_3H_8O (Propanol)	0.00196	0.00044	0.00218	0.00197	0.00100
C_3H_8O (Isopropanol)	0.00193	0.00040	0.00212	0.00191	0.00098
C_5H_{10} (Cyclopentane)	0.00175	0.00024	0.00175	0.00154	0.00124
$C_3H_7NO_2$ (Alanine)	0.00225	0.00077	0.00258	0.00237	0.00101
$C_4H_{10}O$ (Butanol)	0.00214	0.00065	0.00244	0.00223	0.00108
$C_4H_8O_2$ (Ethyl acetate)	0.00208	0.00048	0.00230	0.00209	0.00120
$C_4H_{12}N$ (Tetramethylammonium)	0.00194	0.00056	0.00201	0.00180	0.00065
$C_4H_4O_4$ (Fumaric Acid)	0.00234	0.00081	0.00271	0.00250	0.00116
C_6H_{12} (Cyclohexane)	0.00175	0.00018	0.00170	0.00148	0.00131
$C_4H_6O_4$ (Succinic Acid)	0.00237	0.00083	0.00279	0.00258	0.00111

$C_5H_5N_5$ (Adenine)	0.00226	0.00062	0.00250	0.00229	0.00124
$H_4P_2O_7$ (Pyrophosphoric Acid)	0.00262	0.00120	0.00307	0.00286	0.00122
C_8H_7N (Indole)	0.00214	0.00049	0.00230	0.00209	0.00143
$C_4H_8N_2O_3$ (Asparagine)	0.00240	0.00084	0.00270	0.00249	0.00118
$C_4H_8N_2O_3$ (Glycylglycine)	0.00240	0.00083	0.00278	0.00257	0.00130
$C_5H_{11}NO_2$ (Valine)	0.00248	0.00103	0.00279	0.00258	0.00114
$C_5H_{10}O_5$ (D-Ribose)	0.00264	0.00122	0.00303	0.00282	0.00119
$C_5H_{10}O_5$ (L-Arabinose)	0.00268	0.00126	0.00308	0.00287	0.00127
$C_5H_{10}O_5$ (D-Ribulose)	0.00275	0.00135	0.00325	0.00304	0.00122
$C_5H_{10}N_2O_3$ (Glutamine)	0.00257	0.00105	0.00297	0.00276	0.00140
$C_6H_13NO_2$ (Leucine)	0.00253	0.00104	0.00281	0.00260	0.00125
$C_6H_{12}O_6$ (D-Fructose)	0.00293	0.00159	0.00340	0.00319	0.00122
$C_6H_{12}O_6$ (D-Galactose)	0.00282	0.00140	0.00325	0.00304	0.00133
$C_6H_{12}O_6$ (D-Mannose)	0.00278	0.00135	0.00319	0.00298	0.00143
$C_6H_{12}O_6$ (D-Glucose)	0.00295	0.00162	0.00347	0.00325	0.00144
$C_8H_{20}N$ (Tetraethylammonium)	0.00275	0.00140	0.00305	0.00284	0.00068
$C_{11}H_{12}N_2O_2$ (Tryptophan)	0.00286	0.00140	0.00321	0.00300	0.00181
$C_{10}H_{12}N_4O_5$ (Inosine)	0.00311	0.00169	0.00365	0.00343	0.00173
$C_{10}H_{13}N_5O_4$ (Adenosine)	0.00311	0.00169	0.00360	0.00339	0.00191
$C_{10}H_{14}N_5O_7P$ (Adenosine Monophosphate)	0.00360	0.00236	0.00453	0.00432	0.00203
$C_{16}H_{36}N$ (Tetrabutylammonium)	0.00350	0.00232	0.00401	0.00380	0.00087
$C_{12}H_{22}O_{11}$ (Maltose)	0.00383	0.00278	0.00451	0.00430	0.00176
$C_{12}H_{22}O_{11}$ (Sucrose)	0.00387	0.00286	0.00445	0.00424	0.00174
$C_{12}H_{22}O_{11}$ (Lactose)	0.00381	0.00273	0.00450	0.00428	0.00197

TABLE A5. Table of calculated entropy values in units of eV/K based on current [**47**] and previous scaling [**43**, **44**], vibration only [**45**, **46**] and the ChemSol program (version 2.1) [**49**–**51**] methods.

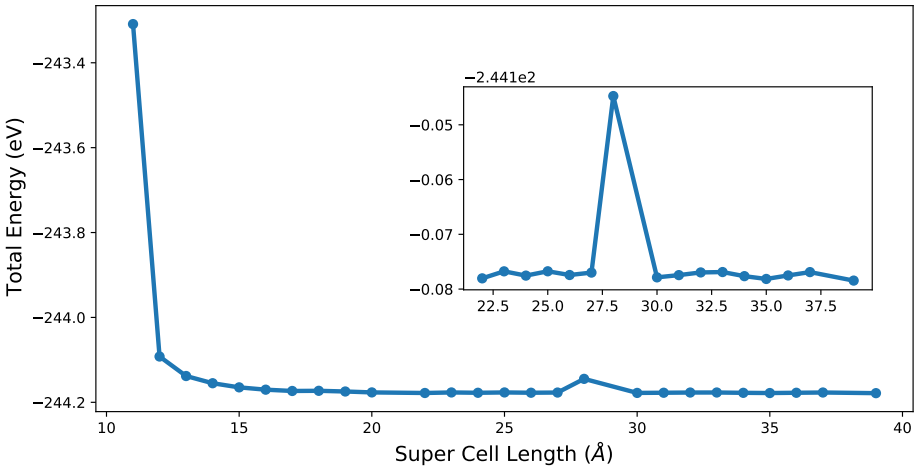

FIGURE A2. Total energy of the cobalt porphine as a function of the side length of an orthorhombic supercell. The inset plot shows the energy between 20 Å and 39 Å.

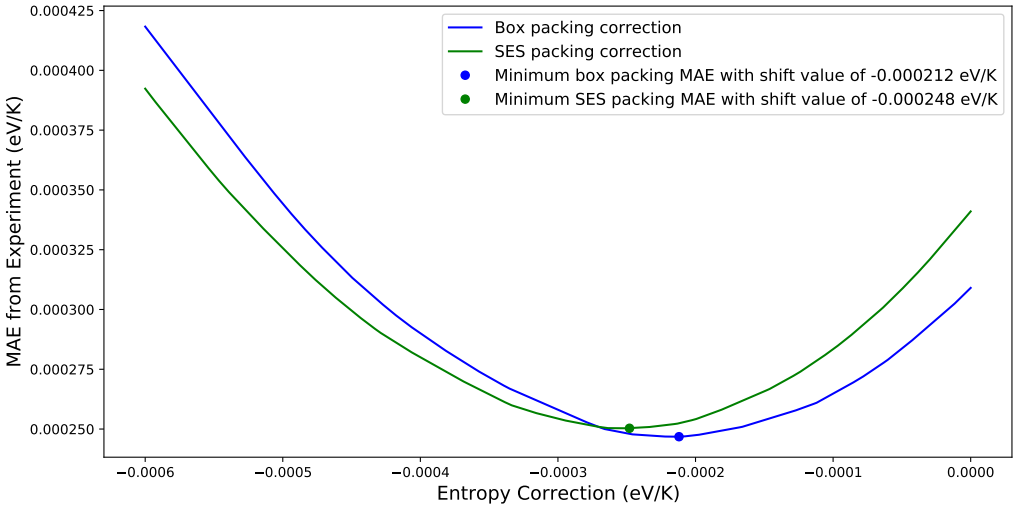

FIGURE A3. Minimisation of the mean absolute error (MAE) to determine the empirical correction factors for the solvation entropy model using the box packing method (blue) and SES packing method (green).

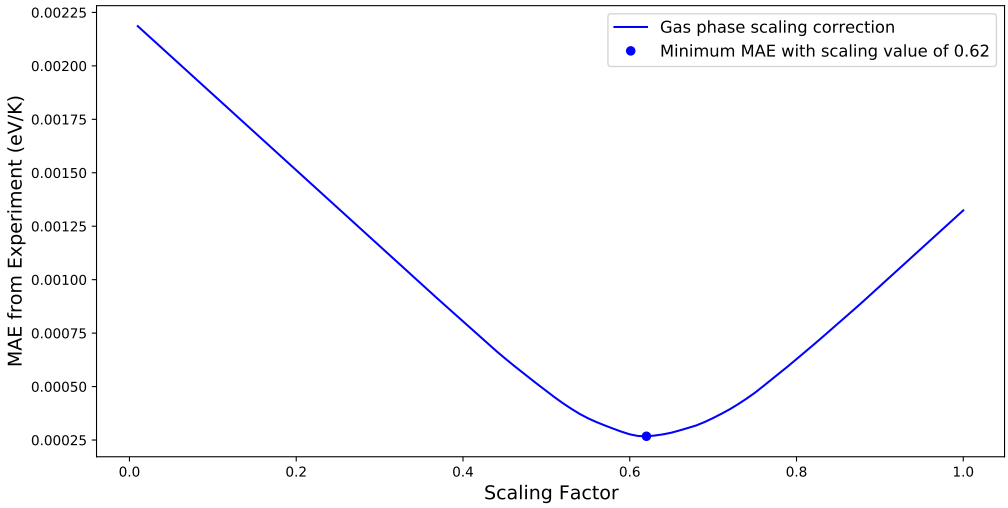

FIGURE A4. Optimal gas phase scaling value to achieve entropy values close to experimental solvation entropies.

	PBE+D3	**SCAN+rVV10***	**SCAN+rVV10**
Uncorrected	0.056	0.058	0.057
Corrected	0.036	0.037	0.040

TABLE A6. Mean absolute error (MAE) entropy values relative to experiment for a subset of 17 small molecules determined using the solvation model with different functionals and the box packing method. The corrected MAE values have the $S_{\text{corr-box}} = 0.000212$ eV/K term included in there calculations at a temperature of 298.15 K. The *SCAN+rVV10** MAE entropy values have had their geometries relaxed using the SCAN+rV110 functional but vibrational frequencies are calculated using the PBE+D3 functional. for the other columns geometries and vibrational frequencies are calculated using the same functional identified by the column title.

System	**Gas-Phase Adsorption Energy (eV)**		**Solvation-Phase Adsorption Energy (eV)**	
	PBE	PBE+D3(BJ)	PBE	PBE+D3(BJ)
Co^0P-CO_2	-0.08	-0.31	-0.49	-0.7
Co^0P-COOH	-1.39	-1.57	-1.28	-1.51
Co^IP-CO_2	-0.06	-0.27	-0.22	-0.44
Co^IP-COOH	-1.36	-1.61	-1.11	-1.37
$Co^{II}P$-CO_2	-0.15	-0.12	-0.10	-0.09
$Co^{II}P$-COOH	-2.17	-2.29	-2.05	-2.20

TABLE A7. Adsorption energies of CO_2 and COOH adsorption on neutral (Co^{II}), negative -1e (Co^I) and negative -2e (Co^0) charge cobalt-centered porphine (CoP) for the gas-phase and solvation-phase. Calculations are conducted using the PBE functional with and without the dispersion correction D3(BJ) [**31**–**33**].

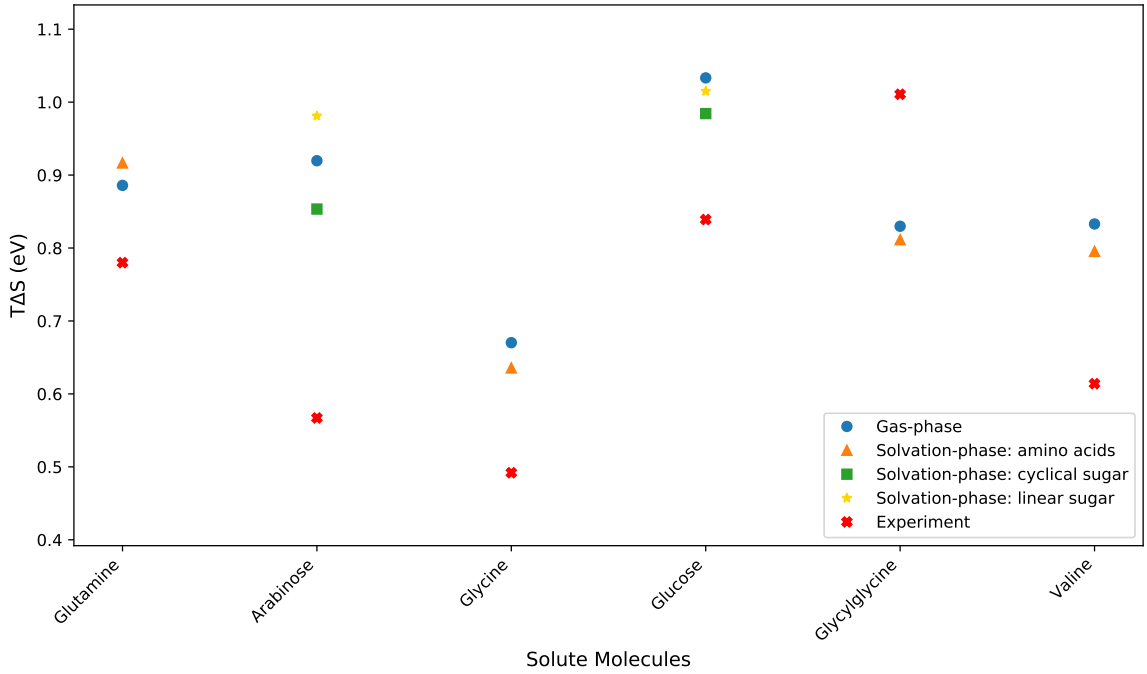

FIGURE A5. TΔS values using the box packing method for select amino acids and sugars deemed to be outliers (see figures 6 and 7). Blue points are gas-phase calculations used in figures 6 and 7, with amino acids in non-zwitteronic form and sugars in cyclical form. Orange points are amino acid structures calculated in impicit water and in their zwitteronic form. Green points are sugar structures calculated in implicit water and in cyclical form. Yellow points are sugar structures calculated in implicit water and in linear form. Red points are experimental aqueous phase entropy values.

2 Appendix B

Defect	E_F **graphene (eV)**	E_F **CNT(4,0)** (eV)	E_F **CNT(4,4) (eV)**	E_F **literature (eV)**	**Refs**
Stone-Wales	4.99	0.36	2.21	4 - 5.4	[**223**, **279**]
Single Vacancy	7.73	3.53	5.63	7.5 - 7.9	[**223**, **280**]
Double Vacancy (5-8-5)	7.50	2.03	2.83	7.2–8.7	[**223**, **281**]
Double Vacancy (555-777)	6.79	2.53	3.28	6.4-7.5	[**223**, **282**]
Double Vacancy (5555-6-7777)	7.42	2.97	4.10	7	[**223**, **283**]

TABLE B8. Graphene defect formation energies which for vacancy defects have been calculated using the energy of a carbon atom in a graphene lattice. Carbon nanotube CNT columns are the defect formation energies in CNTs with (4,0) being a zig-zag CNT and (4,4) being an armchair CNT. Columns 2-4 have been calculated in this study, while column 5 *literature* are from calculations in the literature for graphene.

Catalyst	**Substrate**	**Linker**	**Potential (V vs. RHE)**	**Faradic efficiency (%)**	**Turn over frequency (s^{-1})**	**Electrolyte**	**Ref.**
CoPc	CNT	Pyridine	-0.63	>98%	34.5	0.5 M $NaHCO_3$	[**24**]
CoPP	CNT	Oxygen	-0.6	98.3%	1.37	0.5 M $KHCO_3$	[**23**]
CoPPc	CNT	MOF	-0.6	90%	1.36	0.5 M $NaHCO_3$	[**207**]
CoPc-CN	CNT	None - Noncov	-0.63	98%	4.1	0.1 M K_2CO_3	[**284**]
CoTPP	Carbon Cloth	Phenylene (ligand)	-1.05 (vs. NHE)	67%	8.3	0.5 M $KHCO_3$	[**21**]
CoPc-Py	Carbon Cloth	None - Noncov	-0.7	95%	6.9	0.05 M K_2CO_3	[**245**]
CoPc	Carbon Cloth	None - Noncov	-0.7	86%	3.5	0.05 M K_2CO_3	[**245**]
CoPc	Carbon Cloth	None - Noncov	-0.8	99%	-	0.1 M K_2CO_3	[**246**]
CoPc	Graphene (N-doped)	None - Noncov	-0.7	85.3%	11.35	0.1 M $KHCO_3$	[**285**]
CoTAPc	Zeolite (ZIF-90)	Imine Bonding	-0.97	90%	0.3	0.5 M $NaHCO_3$	[**286**]
CoTPP	TiO_2 Nanotube	Pyridine	-1.10 (vs. NHE)	41.5%	1.11	0.5 M $KHCO_3$	[**287**]

TABLE B9. Recent experimental results from the literature investigating the CO_2ERR using cobalt centred complexes as the catalyst. The *Catalyst* column indicates the catalyst used (for brevity full names are not included, see references). The *Substrate* column indicates the substrate on which the catalyst is immobilized. The *Linker* column indicates the type of linker used if covalently immobilized, *None - Noncov* is when the catalyst is not covalently immobilized and instead immobilized by $\pi - \pi$ interaction, while *MOF* stands for metal organic framework. *Potential* indicates the electrode potential (V) applied vs. RHE (reversible hydrogen electrode) unless otherwise specified. *Faradaic Efficiency* column shows how selective the catalyst is at producing the CO product. *Turn Over Frequency* indicates how much CO product is produced per active site, per second. The *Electrolyte* column indicates the amount and type of electrolyte used in the aqueous solution. The last column indicates the references for each row.

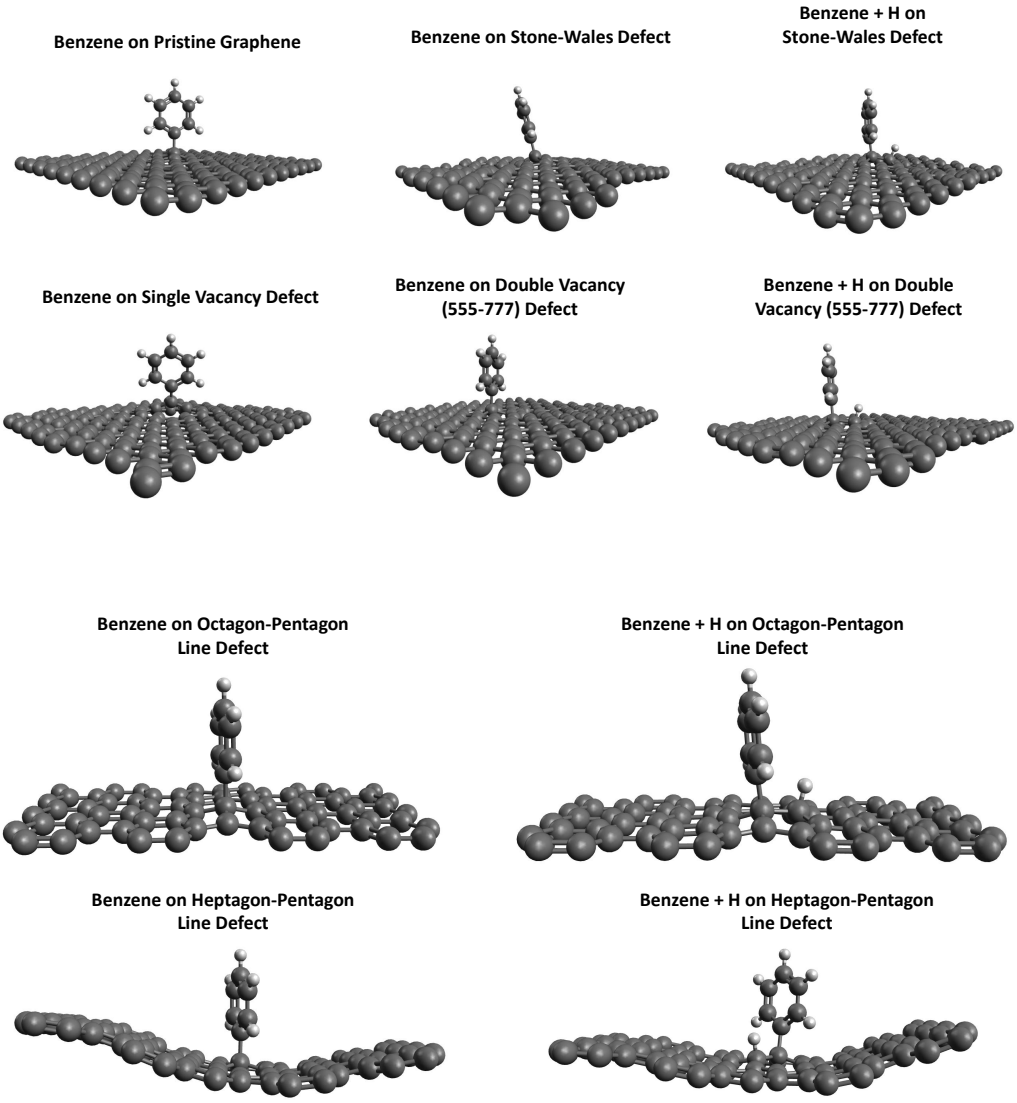

FIGURE B6. The geometries of the favorable benzene-graphene bonded systems determined in table 1. Benzene bonded on pristine, Stone-Wales (SW), single vacancy (SV), double vacancy (DV) in the 555-777 configuration (see table B1 above) and the line defects: octagon-pentagon and heptagon-pentagon. As per table 1 we consider the scenario where dissociated hydrogen from benzene forms free H_2 and the scenario where H adsorbs on graphene.

Site	Benzene (eV)	CoPc (eV)
1	0.76	0.39
2	0.90	0.63
3	1.79	1.16
4	1.09	1.03

TABLE B10. Bonding energy of benzene and CoPc on graphene octagon-pentagon line defect sites. The adsorption sites are shown in figure 1 and benzene adsorption energies are from table 1.

Defect	**Bonding site**	**Bonding energy (eV)**
Stone-Wales	On-defect	0.55
	Off-defect	2.23
Double-vacancy	Site 1	1.47
	Site 2	1.45
Line: octagon-pentagon	Site 1	0.75
	Site 2	0.91
	Off-defect	2.17
Line: heptagon-pentagon	Site 1	1.37
	Site 2	1.5
	Off-defect	2.34

TABLE B11. Bonding energies of benzene and its dissociated hydrogen on and off graphene defect sites. Bonding energies are shown for the Stone-Wales defect, double vacancy defect, octagon-pentagon line defect and heptagon-pentagon line defect sites. The bonding site indicated is that of benzene with hydrogen adsorbed on a neighboring atom of the defect and are shown on figure 1.'Off Defect' only applies to benzene; hydrogen always adsorbs on the defect site. Bonding energies have been calculated using $E_{\text{bond}} = E_{\text{graphene-benzene-H}} - E_{\text{graphene}} - E_{\text{benzene}}$.

System	Bonding energy (eV)	CNT Diameter (Å)
Benzene-CNT (3,3)	0.03	4.07
Benzene-CNT (4,0)	-0.62	3.13
Benzene-CNT (4,4)	0.59	5.42
Benzene-CNT (5,0)	-0.25	3.92
Benzene-CNT (5,1)	0.29	4.36
Benzene-CNT (5,5)	1.04	6.78
Benzene-CNT (6,0)	0.15	4.70
Benzene-CNT (6,6)	1.24	8.14
Benzene-CNT (8,0)	0.98	6.26
Benzene-CNT (8,8)	1.43	10.85
Benzene-CNT (10,0)	1.25	7.83
Benzene-CNT (10,10)	1.53	13.56
Graphene	1.96	-

TABLE B12. Bonding energies of benzene on different sized single-walled carbon nanotubes (SWCNT). The type of SWCNT is indicated by its (m, n) integers, $(m, 0)$ indicates a zig-zag SWCNT and (m, m) indicates an armchair SWCNT. These results are plotted in figure 2.

Platform	**Bonding energy (eV)**		
	CoTPP	CoPc	Benzene
Graphene pristine	1.96	1.87	1.96
SWCNT (4,4) pristine	0.53	0.50	-
SWCNT (4,0) pristine	-0.89	-0.73	-
Graphene single vacancy	-1.14	-3.48	-1.33
SWCNT (4,4) single vacancy	-2.09	-2.08	-
SWCNT (4,0) single vacancy	-2.31	-2.39	-
Graphene Stone-Wales	0.58	1.01	0.67
SWCNT (4,4) Stone-Wales	-0.03	-0.07	-
SWCNT (4,0) Stone-Wales	-0.30	-0.11	-
Graphene line defect	0.23	0.81	0.76
Graphene double vacancy 555-777 off-centre	0.18	0.57	0.49
SWCNT (4,4) double vacancy 555-777 off-centre	0.44	0.41	-
SWCNT (4,0) double vacancy 555-777 off-centre	-0.55	-0.45	-
Graphene double vacancy 555-777 centre	1.25	1.83	1.64
SWCNT (4,4) double vacancy 555-777 centre	0.42	0.33	-
SWCNT (4,0) double vacancy 555-777 centre	-0.07	-0.05	-

TABLE B13. Bonding energies of CoTPP (cobalt-tetraphenylporphyrin), CoPc (cobalt-phthalocyanine) and benzene on pristine and defective single layer graphene and SWCNT substrates. Bonding energies have been calculated using equation 1 in the main text.

Homogeneous

[CoPc]$^{-1e}$ [CoPc]$^{-2e}$

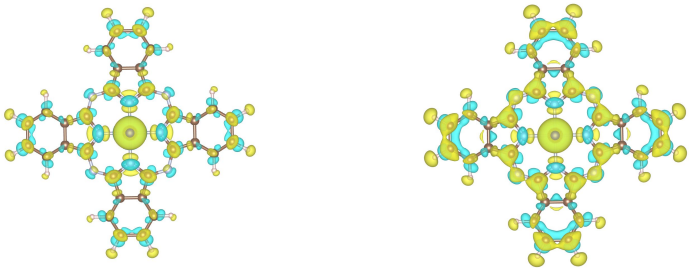

Homogeneous

[CoTPP]$^{-1e}$ [CoTPP]$^{-2e}$

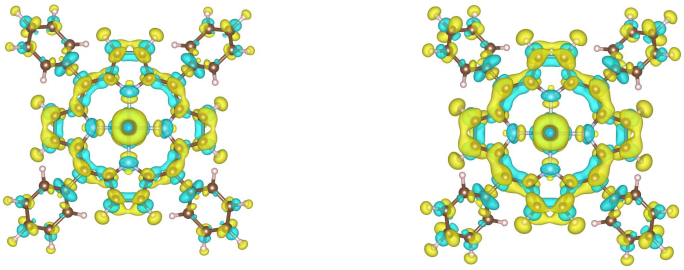

Pristine

[CoPc]$^{-1e}$ [CoPc]$^{-2e}$ [CoPc]$^{-3e}$

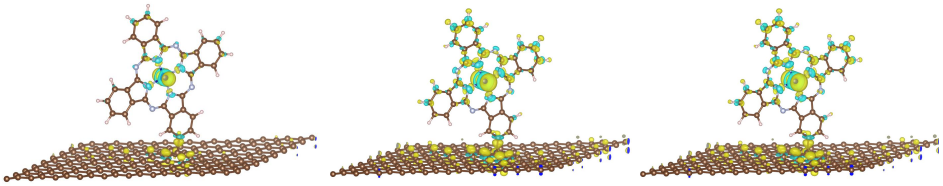

Pristine

[CoTPP]$^{-1e}$ [CoTPP]$^{-2e}$ [CoTPP]$^{-3e}$

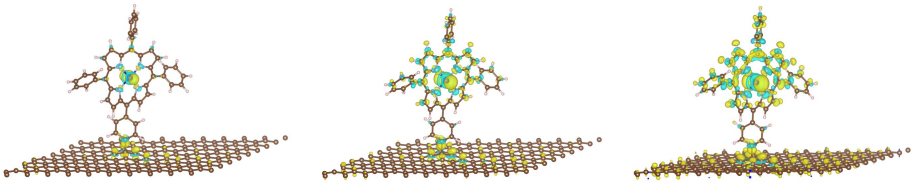

Defect: Stone-Wales

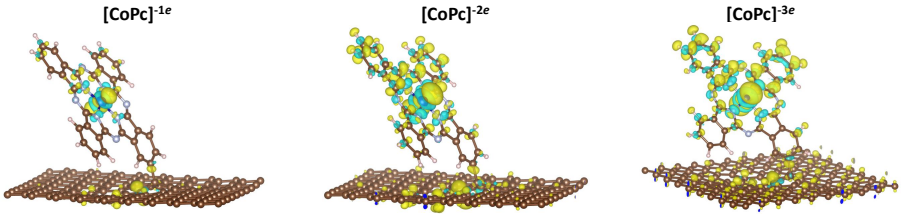

Defect: Stone-Wales

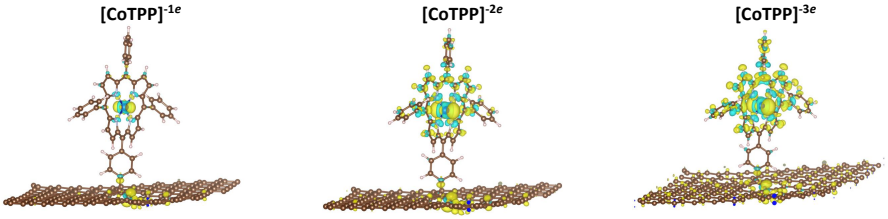

Defect: Line oct-pent

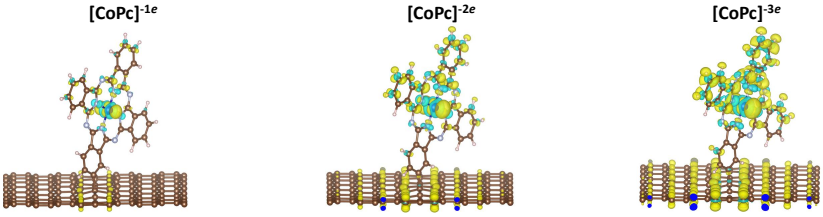

Defect: Line oct-pent

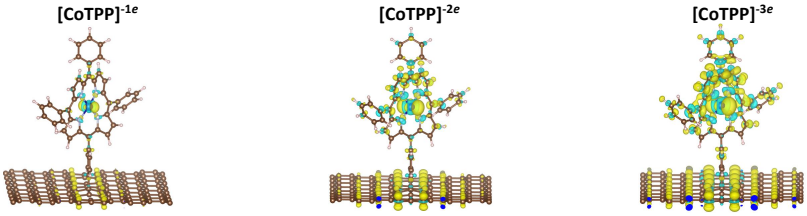

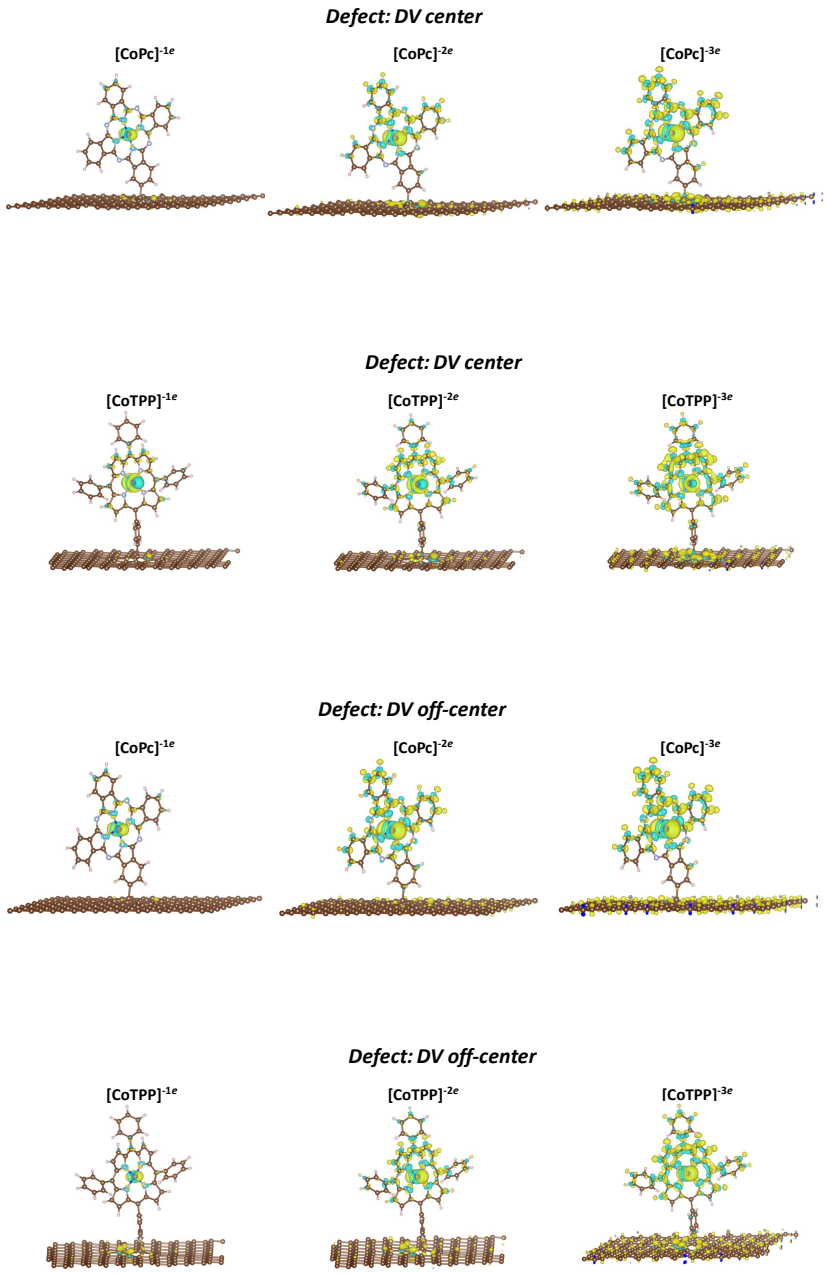

FIGURE B7. Charge density difference figures for free and immobilized CoPc and CoTPP molecules on pristine and defective graphene. All charge density differences are taken relative to the neutral charge density of each system, for example the charge density difference of $[CoPc]^{-1e}$ is calculated by subtracting the neutral charge density of $[CoPc]^{0}$ from the -1e charge density of $[CoPc]^{-1e}$. Charge density differences are calculated for systems with net charges of -1e, -2e and -3e.

Defect	CoPc/CoTPP	Intermediate	-1e net charge : adsorption energy (eV)	-3e net charge : adsorption energy (eV)
Homogeneous	CoTPP	CO	-0.37	-
		CO_2	-0.24	-
		COOH	-1.70	-
	CoPc	CO	-0.21	-
		CO_2	-0.19	-
		COOH	-1.38	-
Pristine	CoTPP	CO	-0.87	-0.40
		CO_2	-0.15	-0.25
		COOH	-2.41	-1.74
	CoPc	CO	-0.57	-0.28
		CO_2	-0.12	-0.17
		COOH	-1.96	-1.35
Stone-Wales	CoTPP	CO	-0.93	-0.41
		CO_2	-0.14	-0.23
		COOH	-2.31	-1.72
	CoPc	CO	-0.74	-0.05
		CO_2	-0.14	-0.15
		COOH	-2.12	-1.35
Double vacancy off-centre	CoTPP	CO	-0.96	-
		CO_2	-0.21	-0.24
		COOH	-2.34	-
	CoPc	CO	-0.94	-
		CO_2	-0.16	0.51
		COOH	-2.30	-
Double vacancy centre	CoTPP	CO	-0.76	-
		CO_2	-0.12	-0.18
		COOH	-2.15	-
	CoPc	CO	-0.74	-
		CO_2	-0.12	-0.17
		COOH	-2.14	-
Single vacancy	CoTPP	CO	-0.89	-
		CO_2	-0.15	-0.30
		COOH	-2.25	-
	CoPc	CO	-0.59	-
		CO_2	-0.14	-0.17
		COOH	-2.00	-
Line: Octagon-pentagon	CoTPP	CO	-0.93	-0.45
		CO_2	-0.15	-0.20
		COOH	-2.31	-1.79
	CoPc	CO	-0.74	-0.09
		CO_2	-0.15	-0.16
		COOH	-2.13	-1.43

TABLE B14. Adsorption energy of CO, CO_2 and COOH on cobalt-tetraphenylporpyrin (CoTPP) and cobalt-phthalocyanine (CoPc) which either free 'Homogeneous' or immobilized on pristine and defective graphene. '-' means calculations have not been conducted.

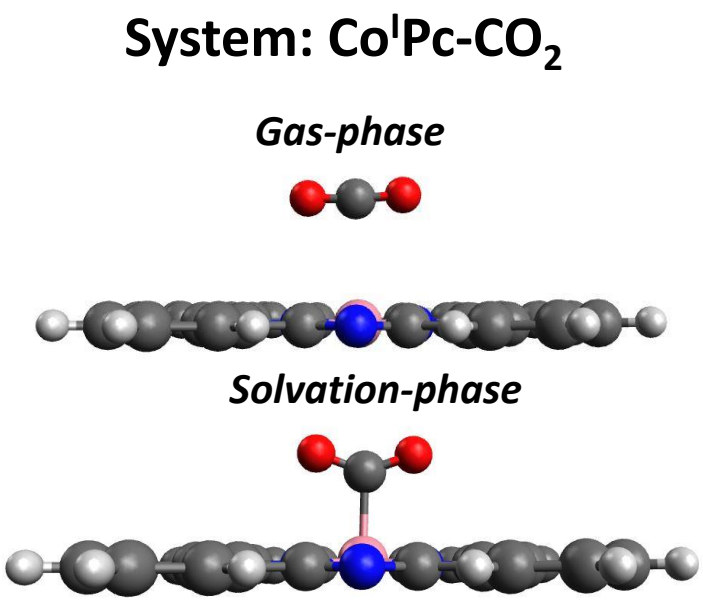

FIGURE B8. Relaxed geometry of Co^{I}Pc-CO$_2$ in both gas-phase and solvation-phase (using a polarised continuum model for implicit water).

System: Graphene-CoTPP-CO$_2$	
System charge	**Adsorption energy (eV)**
Neutral	-0.20
$-1e$	-0.15
$-2e$	-0.19
$-3e$	-0.25
$-4e$	-0.26
$-6e$	-0.27

TABLE B15. CO$_2$ adsorption energies on CoTPP which is immobilized on pristine graphene for a range of charge states from neutral to $-6e$. The $-5e$ charge has been excluded due to structural instability of the immobilized CoTPP molecule. Charge refers to the net charge or number of additional electrons included in the system, i.e. $-1e$ is one extra electron, $-2e$ is two extra electrons and so on.

Defect	Net charge	CoTPP/CoPc	Intermediate	CNT-4-0 adsorption energy (eV)	CNT-4-4 adsorption energy (eV)
Pristine	-1e	CoTPP	CO	-0.96	-0.87
			CO_2	-0.20	-0.16
			COOH	-2.33	-2.25
		CoPc	CO	-0.81	-0.51
			CO_2	-0.11	-0.14
			COOH	-2.20	-1.91
	-3e	CoTPP	CO	-0.47	-
			CO_2	-0.20	-
			COOH	-1.78	-
		CoPc	CO	-0.27	-
			CO_2	-0.17	-
			COOH	-1.39	-
SW	-1e	CoTPP	CO	-0.95	-
			CO_2	-0.16	-
			COOH	-2.32	-
		CoPc	CO	-0.81	-
			CO_2	-0.14	-
			COOH	-2.18	-
	-3e	CoTPP	CO	-0.47	-
			CO_2	-0.19	-
			COOH	-1.79	-
		CoPc	CO	-0.35	-
			CO_2	-0.26	-
			COOH	-1.42	-

TABLE B16. Adsorption energies of CO, CO_2 and COOH on cobalt-tetraphenylporpyrin (CoTPP) and cobalt-phthalocyanine (CoPc), for $-1e$ and $-3e$ net charges, which are immobilized on a pristine [4,0] zig-zag and [4,4] armchair carbon nanotube (CNT) and a Stone-Wales defect on a [4,0] CNT. '-' means no calculation was performed.

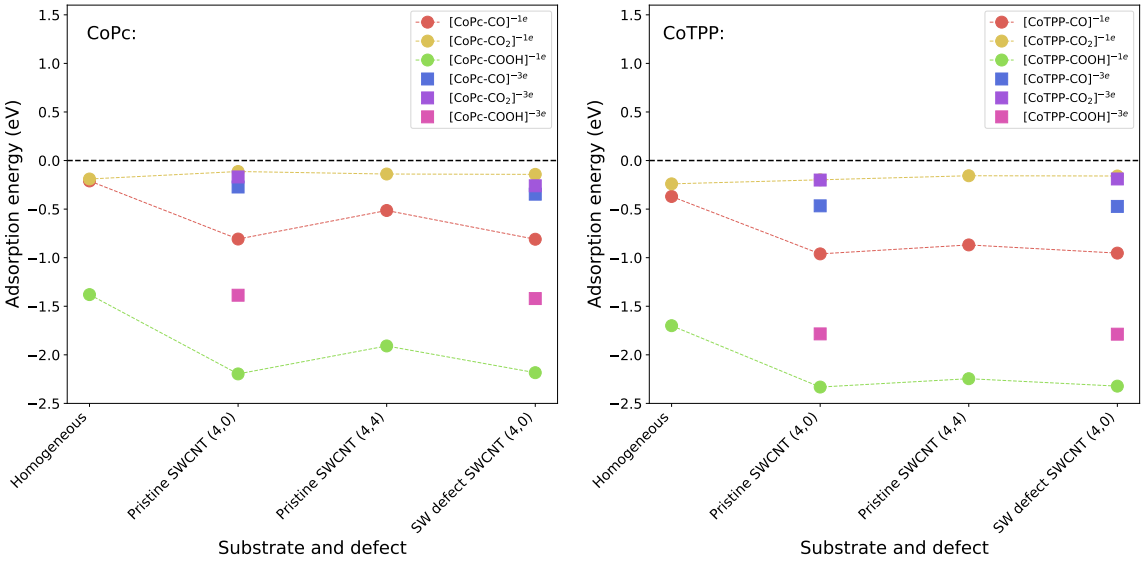

FIGURE B9. Adsorption energies of CO, CO_2 and COOH on CoPc and CoTPP which are immobilized on pristine and defective single-walled carbon nanotube (SWCNT) substrates. The *Homogeneous* case is when CoPc and CoTPP are not immobilized (free molecules). The -1e charge state and -3e charge state (one and three electrons added to the supercell respectively) are investigated based on the results from table 2. Both [CoPc/CoTPP-CO]$^{-3e}$ and [CoPc/CoTPP-COOH]$^{-3e}$ have only been calculated for the pristine graphene and SW defective graphene substrates for comparison to the $-1e$ charge state adsorption energies. For [CoPc/CoTPP-CO]$^{-3e}$ adsorption energies have been calculated for all substrates.

System charge	Defect	Intermediate	Adsorption energy (eV)
-1e	Pristine	CO	-0.39
		CO_2	-0.10
		COOH	-2.14
	Stone-Wales	CO	-0.39
		CO_2	-0.17
		COOH	-2.17
	Line	CO	-0.38
		CO_2	-0.11
		COOH	-2.14
-3e	Pristine	CO	-0.45
		CO_2	-0.41
		COOH	-2.18
	Stone-Wales	CO	-0.43
		CO_2	-0.42
		COOH	-2.13
	Line	CO	-0.43
		CO_2	-0.25
		COOH	-2.19

TABLE B17. Adsorption energy of CO, CO_2 and COOH on immobilized cobalt-phthalocyanine (CoPc) on pristine and defective graphene using a pyridine linker for $-1e$ and $-3e$ charge states.

Graphene defect	System charge	Co	CoPc	N (Pyridine)	Pyridine	Defect	Graphene
Pristine	Neutral	1.03	-0.27	-0.03	-0.28	N/A	0.32
	-1	1.02	-0.28	0.00	-0.38	N/A	-0.63
	-2	1.02	-0.27	-0.35	-0.38	N/A	-1.26
	-3	1.03	-0.29	-0.69	-0.45	N/A	-1.86
Stone-Wales	Neutral	1.04	-0.27	0.17	-0.29	0.03	0.12
	-1	1.01	-0.28	0.04	-0.32	-0.05	-0.71
	-2	1.01	-0.28	-0.35	-0.33	-0.10	-1.33
	-3	1.02	-0.28	-0.72	-0.32	-0.17	-1.96
Line: Oct-pent	Neutral	1.05	-0.27	0.18	-0.39	-0.21	0.21
	-1	1.03	-0.28	0.03	-0.40	-0.27	-0.63
	-2	1.03	-0.29	-0.13	-0.42	-0.53	-1.45
	-3	1.02	-0.29	-0.53	-0.41	-0.45	-2.06

TABLE B18. Net Voronoi charges (units of e) for atoms and structures of interest in the immobilized, via pyridine, CoPc molecule on pristine and defective graphene. Charge analysis has been done for the neutral, -1e, -2e and -3e net charges of all the systems. The *Co* column is the charge on the cobalt atom at the centre of the CoPc molecule. The *CoPc* column is the total charge of the immobilized CoPc molecule. The *N (Pyridine)* column is the charge on the N atom of the pyridine linker which bonds to the CoPc cobalt centre. The *Pyridine* column is the charge on the entire pyridine molecule. The *Defect* column is the total charge of the graphene defect. The *Graphene* column is the charge of the graphene sheet including the defect.

System charge	Defect	Intermediate	Adsorption energy (eV)
$-1e$	Pristine	CO	-1.33
		CO_2	-0.15
		COOH	-1.72
	SW	CO	-0.93
		CO_2	-0.14
		COOH	-2.25
$-3e$	Pristine	CO	-0.89
		CO_2	-0.19
		COOH	-2.28
	SW	CO	-0.75
		CO_2	-0.21
		COOH	-2.25

TABLE B19. Adsorption energy of CO, CO_2 and COOH on immobilized cobalt-tetraphenylporphyrin (CoTPP) on pristine and defective (4,0) zig-zag single-walled carbon nanotubes (SWCNT) using an oxygen linker.

SWCNT defect	Total charge	Co	CoTPP	O-Linker	Defect	SWCNT
Pristine	Neutral	1.16	0.40	-0.60	N/A	0.20
	-1	1.17	0.11	-0.62	N/A	-0.49
	-2	1.11	-0.23	-0.62	N/A	-1.14
	-3	1.08	-0.65	-0.57	N/A	-1.78
Stone-Wales	Neutral	1.10	0.08	-0.42	0.39	0.34
	-1	1.06	-0.28	-0.42	0.32	-0.30
	-2	1.04	-0.50	-0.43	0.20	-1.07
	-3	0.99	-0.85	-0.43	0.12	-1.71

TABLE B20. Net Voronoi charges (units of e) for atoms and structures of interest in the immobilized CoTPP molecule (via atomic oxygen linker) on pristine and defective SWCNT (4,0). Charge analysis has been done for the neutral, -1e, -2e and -3e net charges of all the systems. The *Co* column is the charge on the cobalt atom at the centre of the CoTPP molecule. The *CoTPP* column is the total charge of the immobilized CoTPP molecule. The *O-Linker* column is the charge on the O atom linker which bonds to the CoTPP cobalt centre. The *Defect* column is the charge of the SWCNT defect. The *SWCNT* column is the charge of the graphene sheet including the defect.

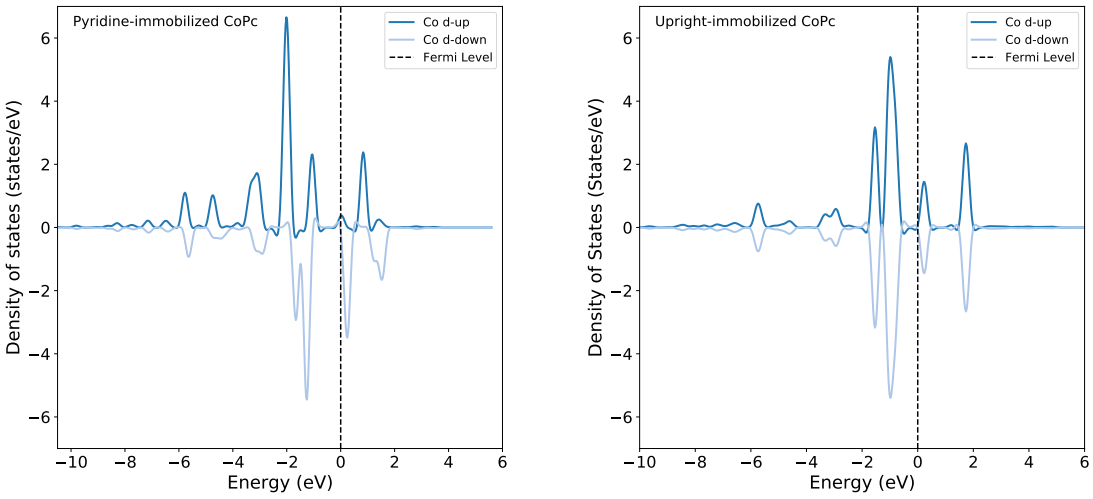

FIGURE B10. Partial density of states (PDoS) plots for the cobalt centre for CoPc immobilized on graphene via pyridine linker and CoPc directly immobilized upright to graphene via its ligand. The total d-orbital PDoS are shown. Spin polarised d-orbitals PDoS components are for the cobalt centre since these are the transition metal bonding orbitals. The plots have been zeroed to the Fermi level indicted by dashed black lines. Both systems have a total charge of $-3e$.

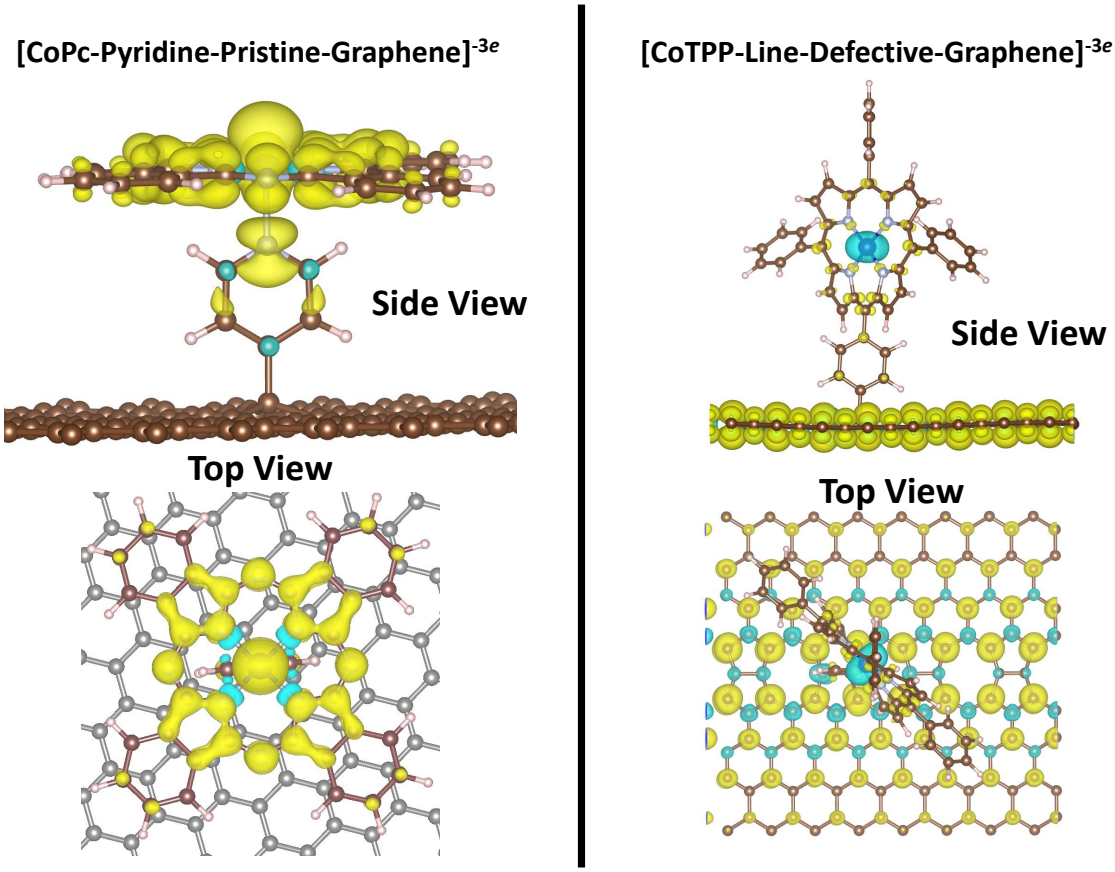

FIGURE B11. Spin charge density profiles of CoPc immobilized via pyridine linker on pristine graphene (left) and CoTPP immobilized on line defect in graphene (right). Spin charge densities are calculated by subtracting the spin-up and spin-down charge density components. Yellow shows regions of charge accumulation and blue shows regions of charge depletion. Silver and brown atoms are carbon atoms, silver is used to distinguish between the substrate carbon atoms and the CoPc carbon atoms. Dark blue atoms are cobalt, light blue are nitrogen and white are hydrogen.

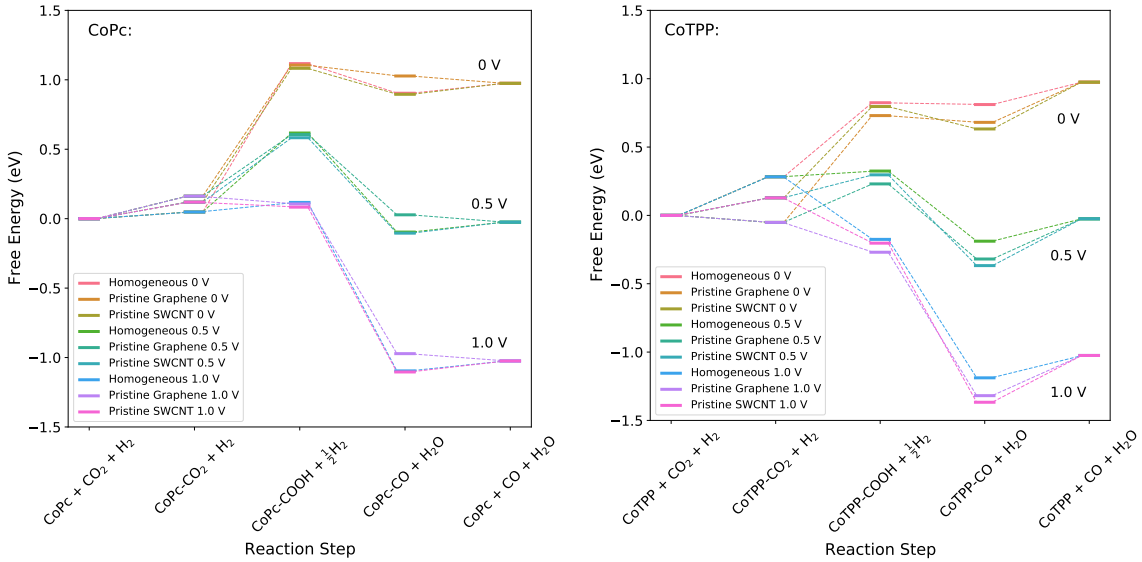

FIGURE B12. Reaction pathways of the CO_2RR reaction for CoPc (top) and CoTPP (bottom). Pristine graphene and pristine SWCNT (4,0) have CoPc and CoTPP immobilized upright. The reaction pathways are calculated for the 0 V, 0.5 V and 1 V electrode potentials for steps that include an e transfer. The Homogeneous systems have a total charge of $-1e$ and the immobilized systems have a total charge of $-3e$. *Homogeneous* indicates a non-immobilized or free CoPc/CoTPP molecule with free energies calculated in gas-phase and using vibrational entropy. Free energies of immobilized systems are calculated using vibration entropy while free molecules such as CO and H_2O have their free energies calculated using solvation entropy, while both immobilized and free systems are calculated in gas-phase. A pH value of 7 has been assumed for all steps that undergo a H^++e^- transfer.

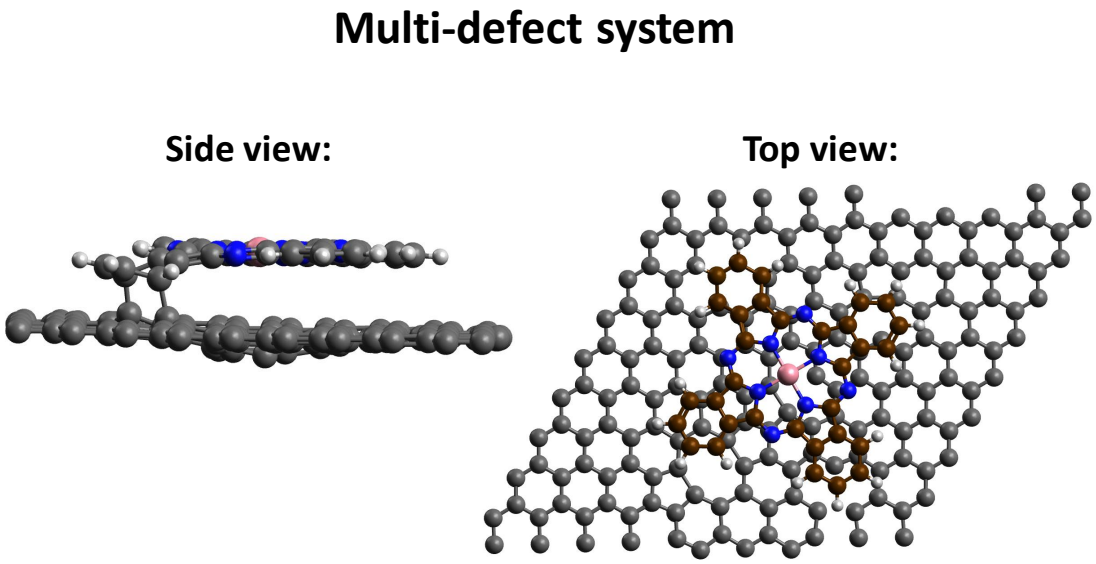

FIGURE B13. Top and side views of the multi defect system calculated in figure 17 and previously studied [**231**]. Shows CoPc covalently immobilized via its ligand over a double vacancy (DV) defect in graphene. The cobalt centre is over a DV defect along with two of the ligands, the other two ligands are over single vacancy (SV) defects. Grey and brown atoms are carbon, white atoms are hydrogen, blue atoms are nitrogen and pink atoms are cobalt. Brown is used to visually contrast CoPc carbon atoms with the carbon atoms of the graphene substrate.

3 Appendix C

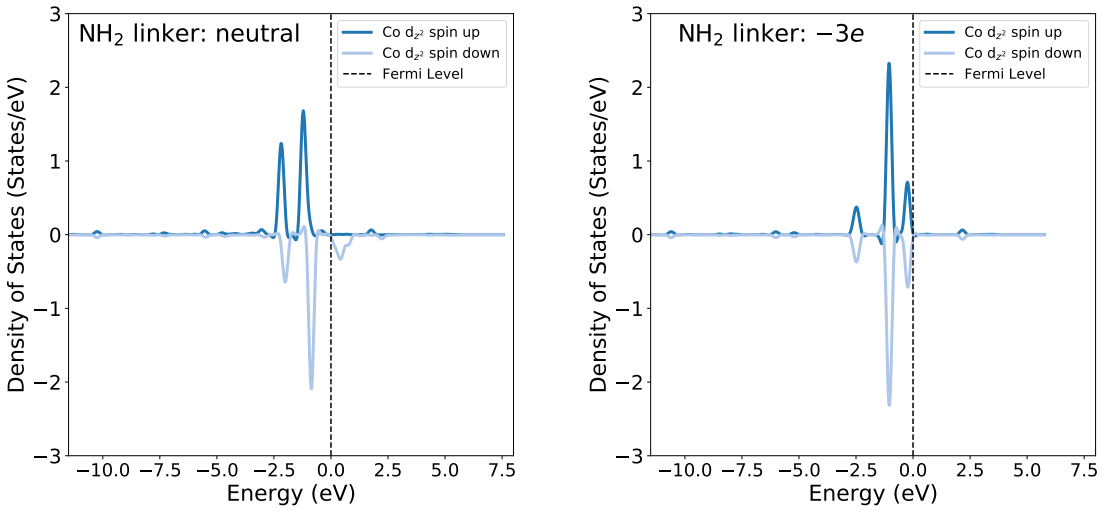

FIGURE C14. Spin polarised d_{z^2} PDoS of the Co active site for the NH_2 linker system in the neutral (left) and $-3e$ charged (right) states.

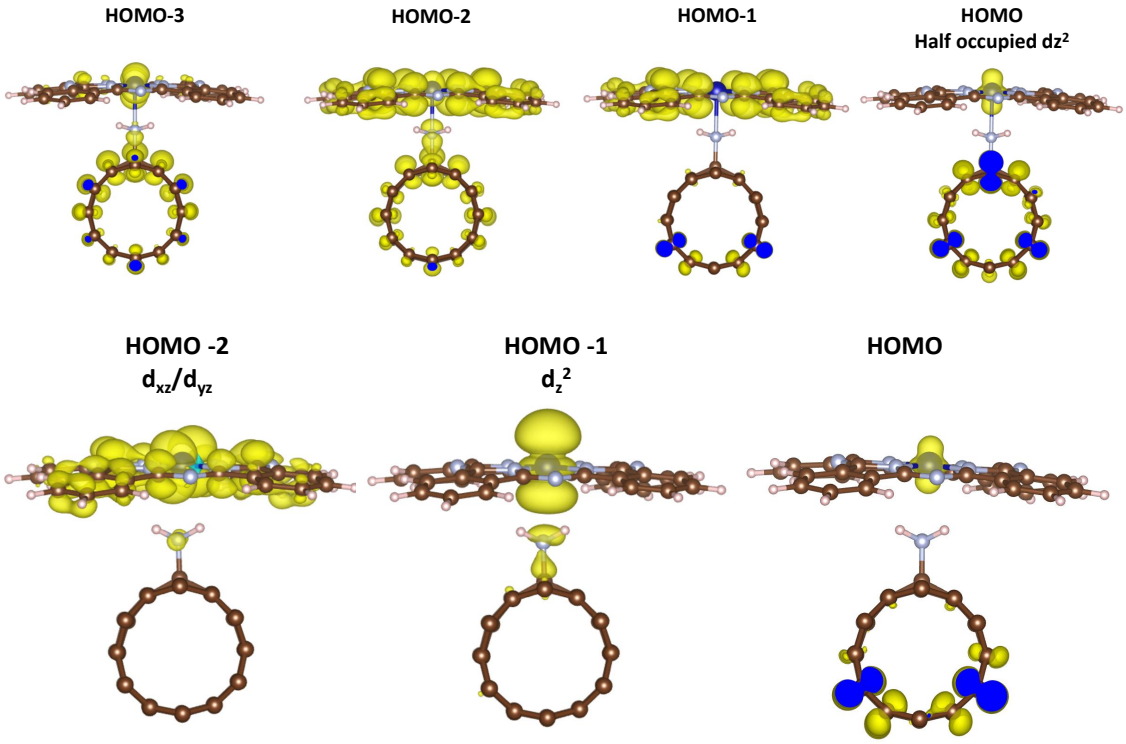

FIGURE C15. The HOMO orbitals of the NH_2 linker system in the neutral (top) and $-3e$ (bottom) charge states. An isosurface scaling of 0.001 e/Å^3 is used for all orbitals.

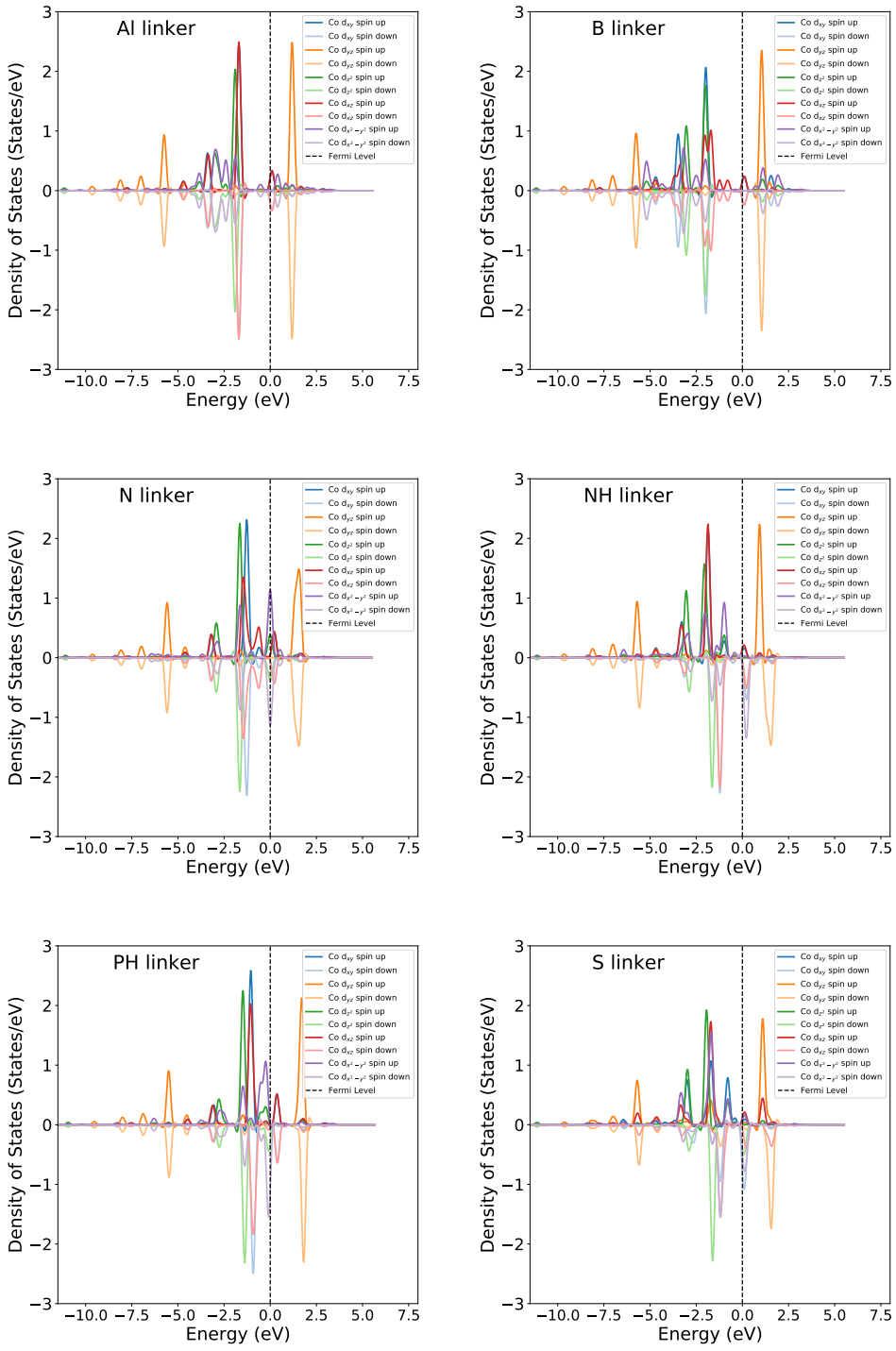

FIGURE C16. Cobalt active site decomposed d-states PDoS of the CoPc-linker-SWCNT systems in figure 6. All systems have a $-3e$ net charge.

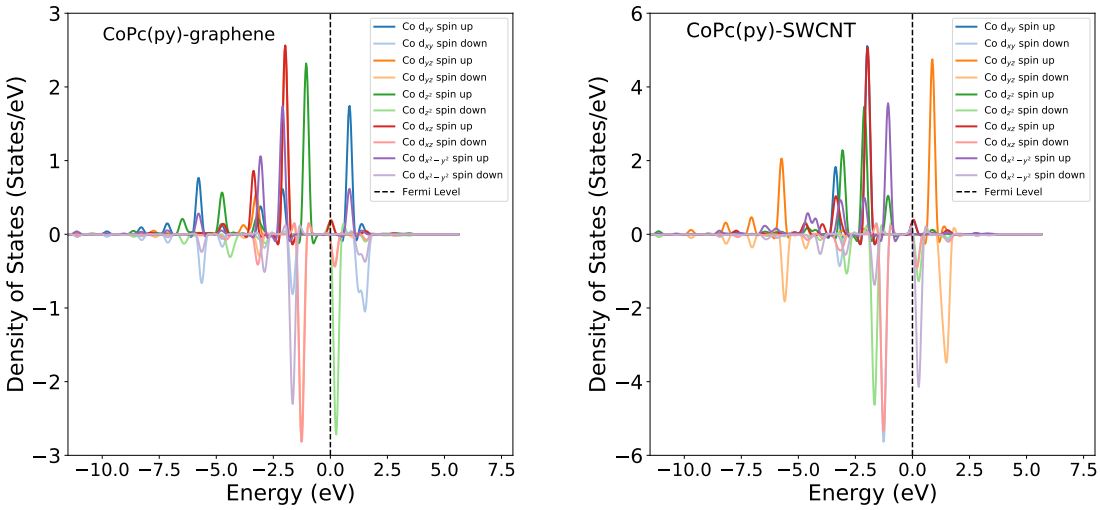

FIGURE C17. Cobalt active site d-states PDoS of CoPc(py)-Graphene (left) and CoPc(py)-SWCNT (4,0) (right). All systems have a $-3e$ net charge.

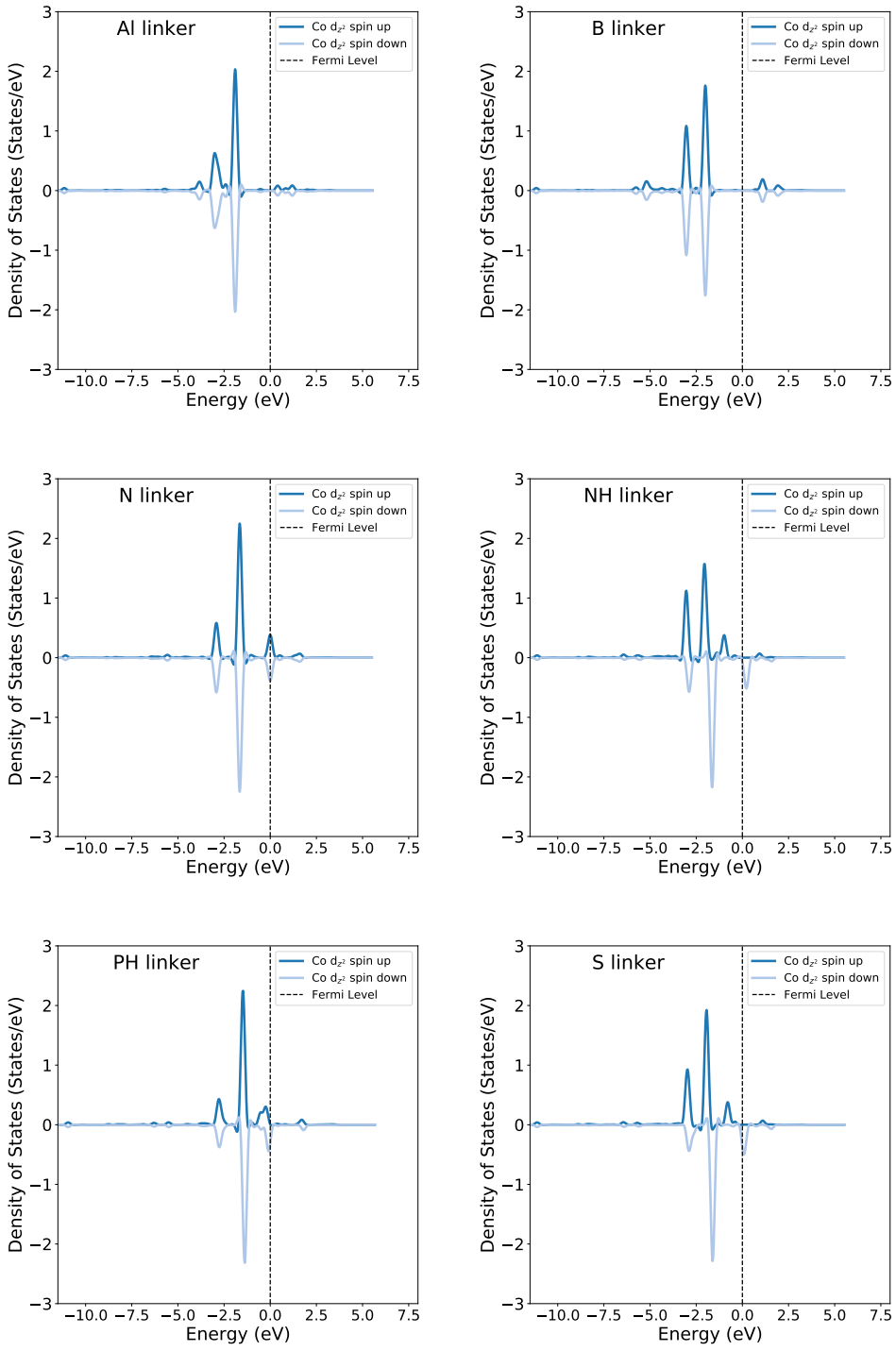

FIGURE C18. Cobalt active site d_{z^2}-orbital PDoS of the CoPc-linker-SWCNT systems in figure 6. All systems have a $-3e$ net charge.